

CO₂ capture by condensed rotational separation : thermodynamics and process design

Citation for published version (APA):

Benthum, van, R. J. (2014). *CO₂ capture by condensed rotational separation : thermodynamics and process design*. [Phd Thesis 1 (Research TU/e / Graduation TU/e), Mechanical Engineering]. Technische Universiteit Eindhoven. <https://doi.org/10.6100/IR762323>

DOI:

[10.6100/IR762323](https://doi.org/10.6100/IR762323)

Document status and date:

Published: 01/01/2014

Document Version:

Publisher's PDF, also known as Version of Record (includes final page, issue and volume numbers)

Please check the document version of this publication:

- A submitted manuscript is the version of the article upon submission and before peer-review. There can be important differences between the submitted version and the official published version of record. People interested in the research are advised to contact the author for the final version of the publication, or visit the DOI to the publisher's website.
- The final author version and the galley proof are versions of the publication after peer review.
- The final published version features the final layout of the paper including the volume, issue and page numbers.

[Link to publication](#)

General rights

Copyright and moral rights for the publications made accessible in the public portal are retained by the authors and/or other copyright owners and it is a condition of accessing publications that users recognise and abide by the legal requirements associated with these rights.

- Users may download and print one copy of any publication from the public portal for the purpose of private study or research.
- You may not further distribute the material or use it for any profit-making activity or commercial gain
- You may freely distribute the URL identifying the publication in the public portal.

If the publication is distributed under the terms of Article 25fa of the Dutch Copyright Act, indicated by the "Taverne" license above, please follow below link for the End User Agreement:

www.tue.nl/taverne

Take down policy

If you believe that this document breaches copyright please contact us at:

openaccess@tue.nl

providing details and we will investigate your claim.

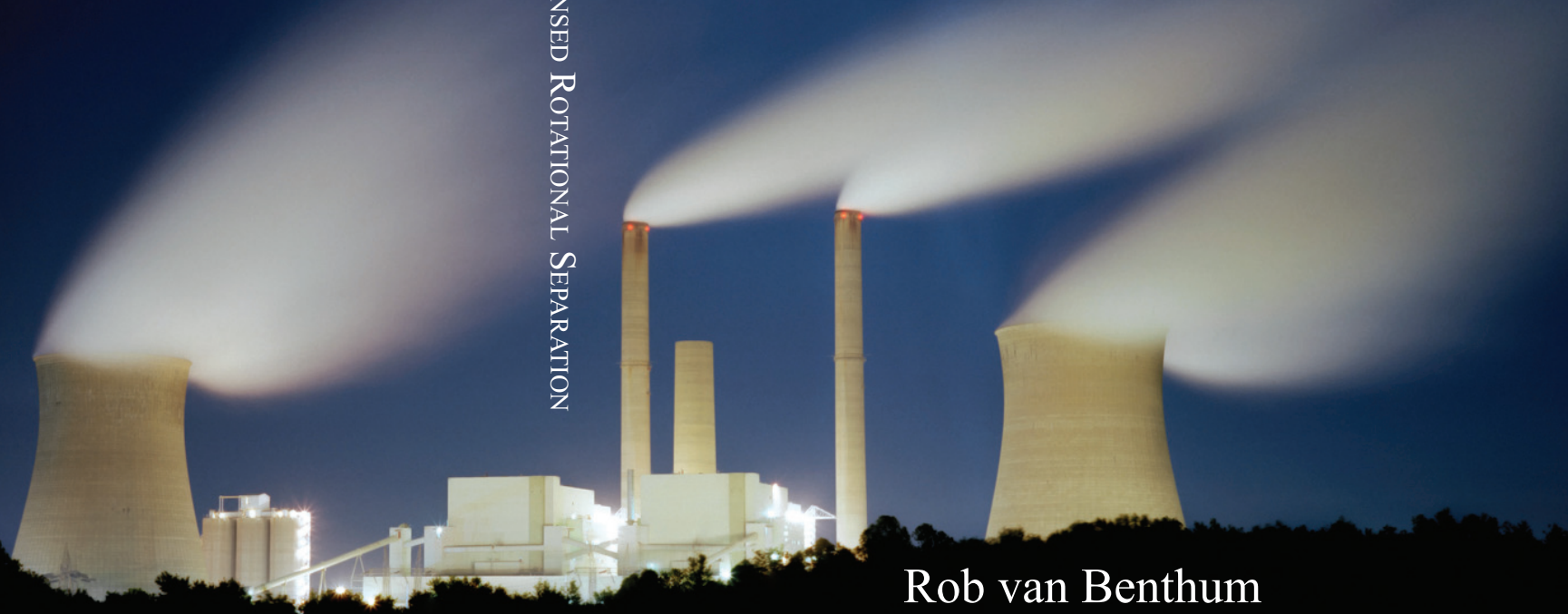
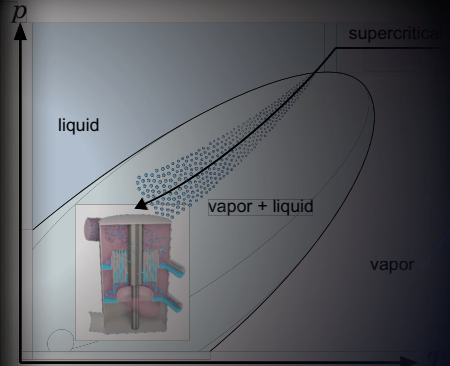
CO₂ CAPTURE

BY

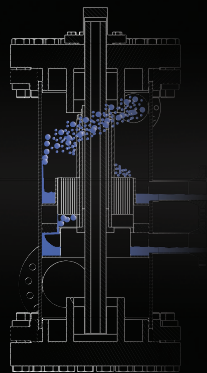
CONDENSED ROTATIONAL SEPARATION

Thermodynamics and Process Design

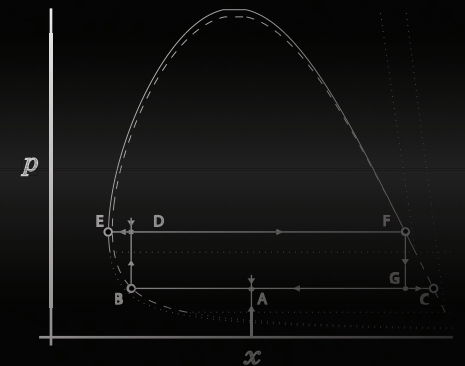
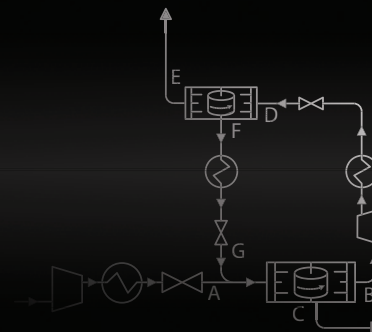
CO₂ CAPTURE BY CONDENSED ROTATIONAL SEPARATION



Rob van Benthum



Rob van Benthum



CO₂ Capture by Condensed Rotational Separation

Thermodynamics and Process Design

PROEFSCHRIFT

ter verkrijging van de graad van doctor aan de
Technische Universiteit Eindhoven, op gezag van de
rector magnificus, prof.dr.ir. C.J. van Duijn, voor een
commissie aangewezen door het College voor
Promoties in het openbaar te verdedigen
op dinsdag 7 januari 2014 om 16.00 uur

door

Rob Johannes van Benthum

geboren te Boxmeer

Dit proefschrift is goedgekeurd door de promotoren en de samenstelling van de promotiecommissie is als volgt:

voorzitter: prof.dr. H.J.H. Clercx
1^e promotor: prof.dr.ir. J.J.H. Brouwers
2^e promotor: prof.dr. M.E.Z. Golombok
copromotor: dr.ir. H.P. van Kemenade
leden: prof.dr.ir. D.M.J. Smeulders
prof.dr.-ing. K.R.G. Hein (Monash University, Universität Stuttgart)
prof.dr.-ing. R. Span (Ruhr-Universität Bochum)
adviseur: prof.dr. D.J.H. Smit (Shell, MIT, Chinese University of Petroleum)

This research is funded by Shell International Exploration & Production. Know-how and information on the Rotational Particle Separator and affiliated processes was provided by Romico Hold.

Cover photo: Daniel Shea
Cover design: Rob van Benthum
Printed by the Eindhoven University Press

A catalogue record is available from the Eindhoven University of Technology Library

ISBN: 978-90-386-3525-5

Copyright © 2013 by R.J. van Benthum

All rights reserved. No part of this publication may be reproduced, stored in a retrieval system, or transmitted, in any form, or by any means, electronic, mechanical, photocopying, recording, or otherwise, without the prior permission of the author.

To my lovely Laura

CO₂ Capture by Condensed Rotational Separation

Thermodynamics and Process Design

Coal is the most CO₂ producing fossil fuel and the biggest contributor to global emissions. We identify feasible CO₂ capture targets and apply them to the new CO₂ capture process of Condensed Rotational Separation (CRS). A phase equilibrium model is used to find optimal CRS separation conditions. We obtain the pure solid phase fugacity and introduce a stability criterion which we use to determine the 'nature preferred' stable phase equilibrium. By construction of horizontal tie-lines in the p - x phase diagram for pseudo binary mixtures, we determine the number of separation stages and their conditions, the process layout and the optimum feed stage. The effects of CRS deployment in narrow two-phase vapor-liquid regimes (i.e. where dew and bubble point lines are close) are highlighted, with the potential for application to multi-component mixtures. We assess the feasibility of CRS deployment in flue gas CO₂ capture on energy and volume. We postulate an overall package diameter for turbo-machinery, apply the NTU-effectiveness method to derive heat exchanger size and derive separator scale-up rules. CRS can only achieve a high recovery ($>70\%$) of high purity ($\geq 95\%_{vol}$) CO₂ if used in tandem with a technique that increases the CO₂ content in the flue gas. The CRS process is well-suited for final CO₂ purification of CO₂ enriched gas resulting from separation techniques that cannot by themselves meet CO₂ capture targets. We assessed CRS in combination with pre-enrichment by (partial) oxyfuel combustion and membrane CO₂ enrichment. The results were compared against today's mature post combustion CO₂ capture technology: chemical absorption by MEA. Energy costs of CO₂ capture are more than halved in comparison to chemical absorption by MEA. With a CO₂ capture penalty of only 6.5% HHV for 90% CO₂ removal, we find that the combination of CRS with today's feasible state-of-the-art membrane technology is a serious competitive candidate for flue gas CO₂ capture.

Contents

Abstract	vii
1 Introduction	1
1.1 Background	1
1.2 RPS Technology	3
1.3 Condensed Rotational Separation	5
1.4 Goal and Outline	7
2 Determination of Phase Equilibria	9
2.1 Introduction	9
2.2 Phase Equilibrium	10
2.3 Two-phase Fluid–Fluid Equilibria	12
2.3.1 Equation of State	12
2.3.2 Mixing rules	14
2.3.3 Fluid fugacity	15
2.3.4 Mass conservation in vapor-liquid equilibria	15
2.3.5 Governing equations and VLE-algorithm	18
2.4 Fluid–Multi-Solid Equilibria	21
2.4.1 Pure solid fugacity	21
2.4.2 Governing equations and VS/LS algorithm	26
2.4.3 Fluid phase identification	27
2.5 Multi-Fluid–Multi-Solid Equilibria	29
2.5.1 Mass conservation in multi-phase equilibria	29
2.5.2 Successive substitution for multi-fluid–multi-solid equilibria	33
2.6 Phase Stability	36
2.6.1 Excess Gibbs energy of a multi-phase mixture	36
2.6.2 Tangent plane stability calculations	37
2.6.3 The stable phase equilibrium calculation sequence	39
2.7 Model Verification	40
2.7.1 The CO ₂ /CH ₄ System	41
2.7.2 The CO ₂ /N ₂ System	43
2.7.3 The CO ₂ /CH ₄ /H ₂ S System	45
2.8 Conclusions and Recommendations	47

3	Preliminary Process Design	49
3.1	Single Stage CRS	49
3.2	Phase Diagrams	50
3.3	Natural Gas Sweetening	51
3.3.1	CO ₂ contaminated natural gas	52
3.3.2	Sour gas	56
3.4	CO ₂ Removal from Combustion Effluent	57
3.4.1	Effect of impurities	60
3.5	Separation in a Narrow Vapor-Liquid Regime	64
3.6	Separation of Multi-Component Mixtures	65
3.6.1	Effective separation of a single component	65
3.6.2	Separation of two or more pure components	66
3.7	Discussion	67
4	Energy and Sizing of Process Equipment:	69
4.1	Energy	69
4.1.1	Entropy and enthalpy	69
4.1.2	Temperature and pressure changer models	72
4.2	Equipment Sizing	75
4.2.1	Expanders	75
4.2.2	Compressors	80
4.2.3	Heat exchangers	84
4.2.4	Rotating Particle Separators	89
4.3	Summary and Conclusions	94
5	Coal Combustion CO₂ Capture	97
5.1	Capture Targets	98
5.2	Post Combustion CO ₂ Capture Technologies	99
5.2.1	Chemical absorption	100
5.2.2	Membranes	102
5.2.3	Low temperature processes	104
5.3	Oxyfuel CO ₂ Capture	105
5.3.1	Air Separation	106
5.3.2	CO ₂ purification	107
5.4	CO ₂ Compression	108
5.5	Flue Gas CO ₂ Purification by CRS	110
5.5.1	Combined isobaric and expansion cooling	111
5.5.2	CO ₂ stream purity	111
5.5.3	Energy costs and heat integration	114
5.5.4	Refrigeration	116
5.5.5	Equipment volume	117
5.6	CRS Pre-enrichment	119
5.6.1	Partial oxyfuel and CRS	119
5.6.2	Membranes and CRS	121
5.7	Comparison	124
5.8	Discussion	125

5.9	Closure	126
6	Conclusions	129
6.1	Modeling of Phase Equilibria	129
6.2	CRS: Thermodynamic Design, Energy and Sizing	130
6.3	CRS in Post-combustion CO ₂ Capture	131
6.4	Outlook for CRS	132
A	Thermodynamic Derivations	133
A.1	The Gibbs-Duhem Equation	133
A.2	Relations between chemical potential, fugacity and activity coefficient	134
A.3	Fluid Fugacity Coefficient	135
A.4	Departure Functions	138
B	Binary Interaction Parameters	141
C	Coal-fired Power Plant Model	143
D	Heat Transfer Coefficients for Coil-Wound Heat Exchangers	147
D.1	Shell side	148
D.2	Tube side	150
D.3	Estimation and selection of fluid properties	151
E	Membrane Models	153
E.1	The Infinitely Small Membrane	154
E.2	Cross-flow Membrane Modules	155
E.3	Counter-flow(-Sweep) Membranes	156
	Nomenclature	159
	Bibliography	163
	Dankwoord	173
	Curriculum Vitae	175

Introduction

1.1 Background

The world's energy demand is growing. From 1973 to 2010 the total world energy supply rose from 6107 Mtoe* a year to 12717 Mtoe a year (Fig. 1.1) [69], and has kept rising mainly due to the accelerated industrial revolution in large developing countries such as China and India. On the short term (the next 10–30 years) it is foreseen that the increasing energy demand will be covered by the utilization of fossil fuels (coal, oil and natural gas), supplemented by the development of renewable energy sources (geothermal, solar and wind energy) [69].

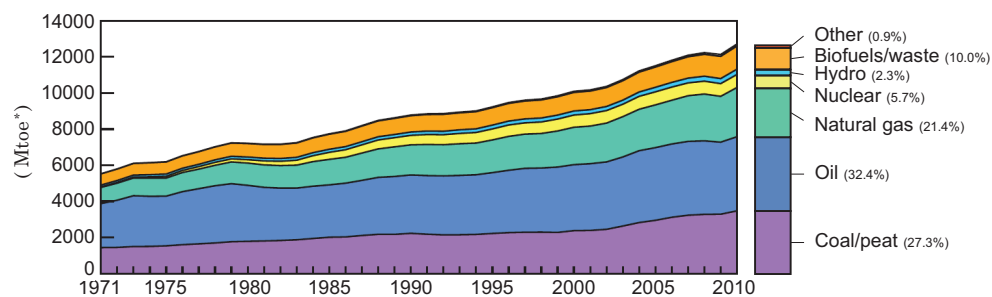


Figure 1.1: World energy consumption 1971 to 2010 by source. Reproduced from [69].

Fig. 1.2 shows the 2012-outlook on power generation change in TWh[†] from 2010 to 2035 divided over the western world and per energy source. On the short term, the power generation from coal in Europe and the USA is expected to decrease due to developments in unconventional oil and gas, such as Enhanced-Oil-Recovery and the production of shale gas [35]. In China and India, with their emerging economies, the energy demand rises quickly and will be covered largely by coal and renewable energy sources [141].

*Million tonnes oil equivalent: $1 \text{ Mtoe} = 4.1868 \cdot 10^{16} \text{ J}$

[†]1 TWh = $1 \cdot 10^9 \text{ kWh} = 3.6 \cdot 10^{15} \text{ J}$

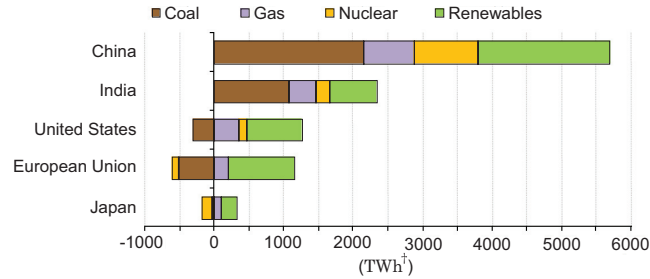


Figure 1.2: Outlook on the change in power generation, 2010–2035. Reproduced from [141].

Carbon dioxide (CO_2) released into the Earth’s atmosphere due to fossil fuel energy conversion, is believed to contribute significantly to the global climate change. Fig. 1.3 shows the world carbon dioxide emissions in million tonnes[‡] of CO_2 by fuel and its distribution in 2010. Almost half of the worldwide emitted CO_2 is due to the combustion of coal, about a third due to oil and a fifth due to natural gas. If compared to the total world energy supply, (Fig. 1.1), one fifth of the world supplied energy is related to natural gas, a third to oil and a quarter to coal. The high CO_2 emission to low energy content makes coal the most dirty fossil fuel available and the biggest contributor to global CO_2 emissions. The prospect of a significant increase in global coal consumption in the near future, caused by developing countries, is therefore a big concern for climate change. CO_2 emissions must therefore be reduced, starting with the major source: coal.

One of the options for short term reduction of CO_2 emissions is the capture and storage of CO_2 from fossil fuel derived flue gas (CCS). Capture, transport and storage of CO_2 comes unfortunately with a penalty in energy and installed process volume, which, if applied, increases the price of electricity and decreases the nett energy production. This penalty makes the application of CCS unattractive, especially for developing countries who want to increase their near term energy production against the cheapest price to feed their emerging economies.

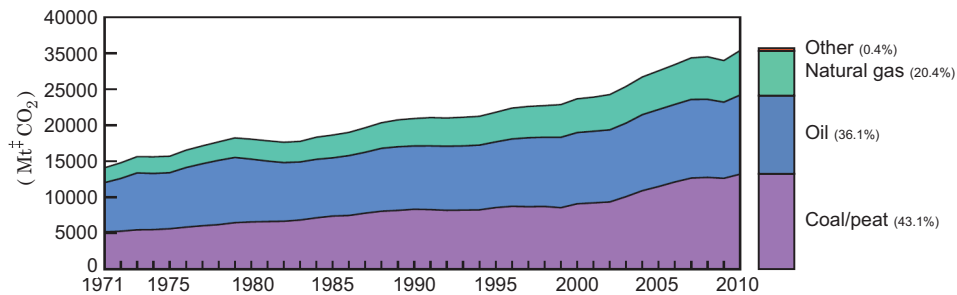


Figure 1.3: World CO_2 emissions from 1971 to 2010 by source. Reproduced from [69].

[‡]1 Mt = $1 \cdot 10^9$ kg

To limit CO₂ emissions, there is a need for novel compact energy efficient (cheap) carbon capture technology, especially for application in developing countries such as China and India. A novel fast, energy efficient and compact pressure-distillation process called 'Condensed Rotational Separation', addresses this need for novel cheap carbon-capture technology.

The process of Condensed Rotational Separation relies on two major innovations:

- Fast reduction of temperature and pressure of a gaseous mixture to a condition where the contaminant (CO₂) becomes a mist of micron sized droplets.
- Separation of the micron-size droplets from the gas by the unique Rotational Particle Separator (RPS).

These two innovations are further addressed in the following sections.

1.2 RPS Technology

Many examples can be found of processes that require the separation of fine particles or droplets from a fluid stream. Typical components include scrubbers, filters, cyclones and electrostatic precipitators. Separation techniques such as these are either constrained to solid particle removal, fail to remove (the smallest) micron-size particles or are energy intensive.

The development of the Rotational Particle Separator (RPS) [22] has overcome these limitations. The RPS is a compact centrifugal separator, consumes little energy ($\sim 2\%$ of entering gas pressure) and removes, with close to 100% efficiency, droplets (or particles) of micron diameter and larger.

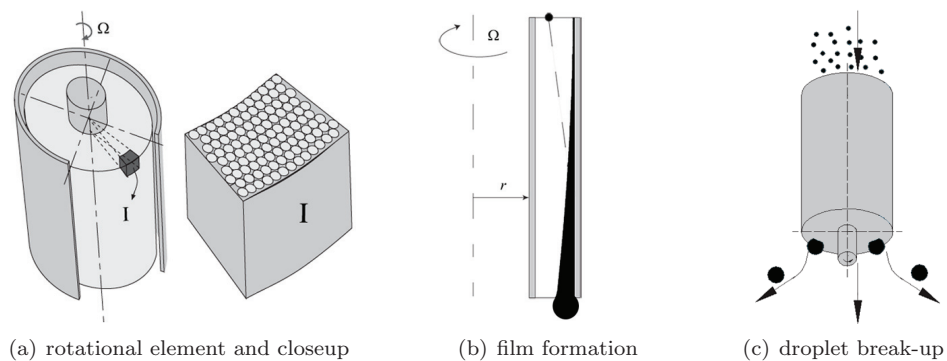


Figure 1.4: Principle of a rotating element

The core of the separation technique is an axially rotating element, which acts as a particle or droplet coagulator. The element consists of a large number of small axial channels contained in a cylinder (Fig. 1.4(a)). Particles or droplets entrained in the

fluid flowing through a channel collide with the channel wall due to centrifugal action where they form a layer of particle material or a liquid film (Fig. 1.4(b)). The layer or film exits a channel downstream by application of pressure pulses or by film breakup (Fig. 1.4(c)). The element provides the means to collect micron-sized particles under limited pressure drop and short residence time (compact energy efficient unit) [71].

The total RPS is basically an axial flow cyclone supplemented with the rotating element (Fig. 1.5). Three stages can be distinguished in the RPS: the pre-separator, the coagulator (rotating element) and the post-separator. The pre-separator contains a tangential inlet to provide rotational flow and is designed such that the diameter of the particles to be separated is well above the diameter of the particles collected in the element's channels. The pre-separator typically separates droplets from 20 μm upward. They are collected in a collection bucket and removed tangentially through the pre-separator outlet. Droplets down to 1 μm and below are collected by the rotating element and coagulated by film formation and break-up into particles of typically 50 μm or larger [25, 139]. These droplets enter the post-separator section. They move outward due to centrifugal action and form a liquid film on a co-rotating wall attached to the rotating element. The liquid film downstream of the co-rotating wall breaks-up again into large droplets. These droplets are in turn collected in the post-separator bucket and removed tangentially through the post-separator outlet. Clean gas leaves the RPS tangentially downstream of the post-separator.

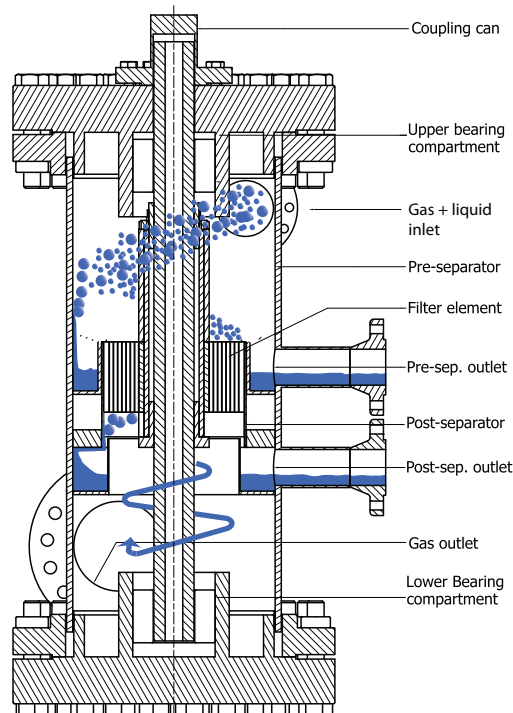


Figure 1.5: RPS as droplet catcher.

The element rotates at a speed comparable to a pump (tangential speed $30\text{--}40\text{ m}\cdot\text{s}^{-1}$). The drive of the filter element can be provided by either an electro motor or by the angular momentum of the tangential incoming flow. External shaft connections, affiliated sealing and the need for an electric connection can thus be omitted.

The ability of the RPS to separate droplets as small as $1\text{ }\mu\text{m}$, its compactness and its low pressure drop open the road to development of large throughput separation processes that make use of small droplet generation by means of partial condensation or evaporation.

1.3 Condensed Rotational Separation

Droplet wise partial condensation of gas mixtures is induced by fast pressure and temperature reduction (expansion) in a Joule-Thomson valve or a turbo expander. Fast expansion generates instant bulk cooling, which supersaturates the gas when expanded into a vapor-liquid two-phase region and drives condensation by means of nucleation and droplet growth. Within milliseconds, a mixture of vapor and micron sized droplets is obtained in concentrations according to thermodynamic phase equilibrium.

Droplet wise partial condensation by expansion for the purpose of gas separation makes only sense if it can be combined with a separation technique that accomplishes effective micron sized droplet separation, short residence time and low energy consumption. No other particle separation technique than the Rotational Particle Separator can fulfill all of these demands simultaneously.

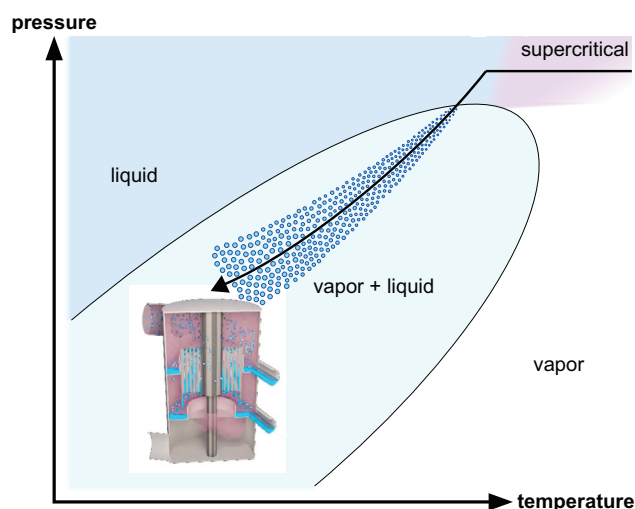


Figure 1.6: CRS principles: expansion cooling, droplet formation and gas-droplet separation by the RPS.

By a combination of isobaric cooling and expansion to a proper separation temperature and pressure in the vapor-liquid (or even a multi-phase) regime, and by separation of the resulting micron-sized droplets with an RPS (Fig. 1.6), selective separation can be achieved. The process can be repeated in series including internal looping for different separation pressures and temperatures to achieve maximum purification of both produced gas and liquid.

The only new equipment within the process of CRS is the RPS as droplet catcher. Other equipment, such as the expanders, a heat exchanger and eventually a compressor are conventional technology as applied in the oil and gas industry and can be purchased.

Development of the CRS principles started due to the need for an energy efficient technique to effectively remove condensable contaminants from severely contaminated natural gas. Research focused on key-elements of the process such as the thermodynamics of expansion, mist formation, fluid dynamics and centrifugal separation [10, 71, 139, 140].

Several tests have been performed to investigate the RPS as droplet catcher. A bench-scale RPS unit was designed and tested in a CO₂/CH₄ expansion test loop at the Shell laboratory in Amsterdam (-50°C, 40 bar, 50 kscfd⁻¹ (0.015 Nm³s⁻¹)) [139, 140]. Basic air/water separation performance was investigated on a large scale RPS, operating at atmospheric conditions at the Eindhoven University of technology (flow equivalent to 80 MMscfd⁻¹ (25 Nm³s⁻¹) at 40 bar) [71, 139]. An RPS capable of handling a flow of 4 MMscfd⁻¹ (1 Nm³s⁻¹) at 8 bar was tested at Eindhoven University of technology and subsequently installed in a slipstream of Enexis gas grid behind the pressure reduction section (40 to 8 bar). At the end of 2013, Enexis will install an upscale RPS to remove condensates from the entire flow downstream of the pressure reduction section (14 MMscfd⁻¹ (4 Nm³s⁻¹), 8 bar, -20°C).

Mist formation by Joule-Thompson expansion of CO₂/CH₄ mixtures under semi-cryogenic conditions was studied by Bansal [9, 10]. Mist with a particle size distribution ranging from 1 to 20 μm was experimentally identified on the expansion test loop at the Shell laboratory in Amsterdam.

Feasibility studies have been performed to applications of CRS in natural gas cleanup [66, 67], in CO₂ removal from flue gas [13, 127], and in CO₂ removal from syngas [20]. Other potential fields of application are for example air separation, nitrogen removal from natural gas in LNG (Liquid Natural Gas) processing and biogas upgrading. In general, CRS separation technology can be applied to all gas mixtures for which a vapor-liquid two-phase region can be created in which at least one of the phases can be obtained relatively pure.

In the development of CRS so far, two key issues remained unresolved:

- Identification of optimal process conditions and matching process layout.
- Determination of size and energy consumption of the whole process.

These issues are the key features of this work.

1.4 Goal and Outline

The focus in this thesis is on the thermodynamics and process design of the CRS process. A general method based on multi-phase thermodynamics is derived to identify optimal separation conditions and uncover the required process layout for maximum purification. Mathematical models of turbo-machinery, heat exchangers and the RPS are described for the evaluation of both the process size and energy consumption. The optimization method and process equipment models are subsequently applied in a feasibility study for the removal of CO₂ from coal-combustion derived flue gas by CRS.

In **Chapter 2** we discuss the thermodynamics of multi-phase equilibrium for multi-component mixtures and derive models for the determination of the different phase-equilibria. For the prediction of CRS process boundaries we develop a refined expression for pure solid phase fugacity. By introduction of phase stability theory and interaction with phase equilibrium calculations, a method is constructed to identify and determine stable phase equilibria. We show by comparison with experimental results in published literature, that accurate phase prediction can be accomplished.

In **Chapter 3** we develop a method for thermodynamic optimization of the purification and separation that can be achieved by CRS. We do this in the light of CO₂ removal from both severely contaminated natural gas and flue gas. We derive optimum separation conditions for these examples and evaluate the separation performance in the presence of impurities. We discuss the guidelines on how to evaluate the feasibility of deployment of CRS in certain applications. We show the effects of CRS deployment in narrow two-phase regimes (i.e. where dew and bubble point lines are close) and discuss how to separate more than one component from a multi-component mixture.

In **Chapter 4** we derive and discuss methods for the determination of energy consumption and process volume of different types of process equipment. Design methods are constructed based on compressible gas theory to obtain overall package volumes of turbo-machinery, the effectiveness-NTU correlation is introduced for size estimation of condensing multi-stream heat exchangers and RPS design equations are used to define useful scaling laws.

In **Chapter 5** we investigate the application of CRS in flue gas for post-combustion CO₂ capture. We identify CO₂ capture targets and discuss different CO₂ capture processes and their development status, followed by detailed design of the CRS process. Energy consumption and process volume of the CRS process are evaluated in detail. For a 500 MW_e coal-fired power plant, combinations of CRS with both oxyfuel technology and membranes are investigated and compared against the current standard on the basis of energy consumption, equipment volume and CO₂ product purity.

Determination of Phase Equilibria

2.1 Introduction

Correct and accurate prediction of multi-phase behavior is essential in the design of a separation process, such as Condensed Rotational Separation (CRS), that depends on multi-phase creation. Commercially available process simulation tools (computer software packages) such as Aspen-Plus and -Hysis and PRO/II are capable of calculating vapor-liquid equilibria within a process simulation environment, but disregard solid formation. Nevertheless, such commercial process simulation tools are often used in the design and performance evaluation of (semi-)cryogenic separation processes [14]. Thermodynamic multi-phase equilibria and property calculators such as Thermo-Calc and Multi-Flash are capable of predicting multi-phase behavior including solid phases, but cannot simulate process equipment in terms of energy and size and have limited software interaction capabilities with process simulation tools.

In the design of the CRS process, there is a need for correct determination of multi-phase existence and accurate calculation of corresponding multi-phase composition. Application of a phase equilibrium calculator in the development of the CRS process is not only restricted to optimization of separation/purification. It also serves the derivation of fluid properties under multi-phase conditions, the prediction of supersaturation due to rapid cooling of multi-component mixtures, and the calculation of entropy and enthalpy under multi-phase conditions. To that end, a flexible multi-phase equilibrium calculator is developed and described in this chapter, which:

1. includes phase prediction in both the fluid and solid phase regions,
2. predicts accurately high-pressure phase equilibria of mixtures with both non- and slightly-polar components,
3. checks the phase stability,
4. can be used in an open mathematical environment (e.g. MatLab),
5. and offers flexibility to utilization of different EoS models for description pVT behavior of different phases.

In Section 2.2, we discuss the background of phase equilibria, focussed on vapor-liquid coexistence. Section 2.3 presents the algorithm for two-phase fluid-fluid calculations. In Section 2.4, a new expression for pure component solid fugacity is derived and phase equilibrium involving one fluid phase and one or more pure component solid phases is discussed. Section 2.5 generalizes both models into a multi-fluid–multi-solid phase equilibrium model. Section 2.6 presents the phase stability problem, and describes the coupling between equilibrium and stability calculations. The final section of this chapter compares model predictions against experimental vapor-liquid (VLE), liquid-solid (LSE) and vapor-solid (VSE) equilibrium data of binary mixtures (CO₂/CH₄, CO₂/N₂) and a ternary mixture (CO₂/CH₄/H₂S).

2.2 Phase Equilibrium

Based on the first law of thermodynamics applied to a multi-component open system of variable composition, the change of Gibbs energy G can be written as:

$$\begin{aligned} dG &= V \cdot dp - S \cdot dT + \sum_{i=1}^N (\mu_i dn_i) \\ &= \left. \frac{\partial G}{\partial p} \right|_{T,n} dp - \left. \frac{\partial G}{\partial T} \right|_{p,n} dT + \sum_{i=1}^N \left(\left. \frac{\partial G}{\partial n_i} \right|_{T,p,n_{j \neq i}} dn_i \right), \end{aligned} \quad (2.1)$$

where n represents the total number of moles $n = \sum_{i=1}^N n_i$, T the temperature, p the pressure, S the entropy and V the volume. Eq. (2.1) is better known as the Gibbs-Duhem equation, and is the root of all phase calculations. A more thorough derivation of Eq. (2.1) can be found in Appendix A.1.

The last term in Eq. (2.1) is more commonly referred to as the chemical potential μ :

$$\mu_i = \left. \frac{\partial G}{\partial n_i} \right|_{T,p,n_{j \neq i}}. \quad (2.2)$$

Eqs. (2.1) and (2.2) can be applied to a medium with i components and no molecular particle exchange with the surroundings. Suppose the medium exists of two phases, A and B, which are in direct contact with each other, as shown in Fig. 2.1. In true thermodynamic equilibrium, pressure, temperature and Gibbs energy of the medium are constant, meaning there are no gradients (over time and position) which cause driving forces in heat and mass transfer. Molecules are however still capable of crossing the interface between the phases A and B, which denotes that the change of molecules of component i between phases A and B must be opposite and equal: $dn_i^A = -dn_i^B$. The result, if implemented in Eq (2.1), is the familiar criterion for phase equilibrium [48]:

$$\sum_{i=1}^N (\mu_i^A - \mu_i^B) dn_i^A = 0 \quad \text{or} \quad \mu_i^A - \mu_i^B = 0. \quad (2.3)$$

Eq. (2.3) is the basis for the Gibbs phase rule which relates the number of phases P and the number of components N to the number of degrees of freedom F in the multi-phase, multi-component system:

$$F = N - P + 2 \quad (2.4)$$

The number of degrees of freedom F represents the number of independent state variables that must be specified in order to describe the multi-phase, multi-component system [40].

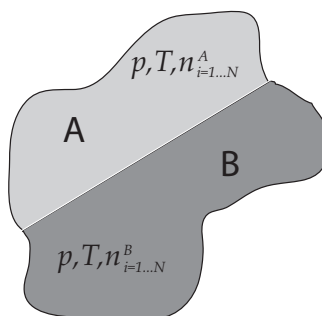


Figure 2.1: A medium consisting of i components and phases A and B which are in thermodynamic equilibrium at pressure p , temperature T and constant number of moles $n = \sum_i n^A + \sum_i n^B$.

With the introduction of the concept of fugacity (cf. Lewis [76]) the change in chemical potential of a component i between a reference state (p_0, T_0) and the actual state (p, T) is given as:

$$\mu_i - \mu_i^0 = RT \ln \left(\frac{f_i}{f_i^0} \right), \quad (2.5)$$

where f_i is the fugacity of component i , R the universal gas constant, y_i the molar concentration of component i . Scripts 0 and $_0$ indicate the reference state (cf. Appendix A.2). Using ideal gas behavior for the reference state ($f_i^0 = y_i p^0$) and reference conditions equal to the actual state ($p_0 = p, T_0 = T$), Eq. (2.5) transforms into:

$$\mu_i - \mu_i^0 = RT \ln(\phi_i) \quad \text{with} \quad \phi_i = \frac{f_i}{y_i p}, \quad (2.6)$$

where ϕ_i is the fugacity coefficient of component i .

Application of the relation between change in chemical potential and fugacity ratio (Eq. (2.5)) to the phase equilibrium condition, Eq. (2.3), results in the more workable criterion for phase equilibrium, which is often found in textbooks as [40, 99, 100]:

$$RT \ln \left(\frac{f_i^A}{f_i^B} \right) = 0 \quad \text{or} \quad f_i^A = f_i^B. \quad (2.7)$$

In calculation of equilibria with a vapor and a condensed phase, the vapor phase fugacity is traditionally derived from an equation of state. For the condensed phase the pure component saturated condition is traditionally taken as a reference, which results in the classical expression for equilibrium [100, 105]. For vapor-liquid equilibrium of a mixture, the classical expression is given as:

$$y_i p \phi_i^V = x_i \gamma_i^L p_i^{sat} \phi_i^{sat} \exp \left(\int_{p_i^{sat}}^p \frac{v_i^{L,sat}}{RT} dp' \right). \quad (2.8)$$

Superscripts ^V and ^L denote the vapor and liquid phase and ^{sat} refers to the pure component saturation condition. y_i and x_i are the vapor and liquid molar phase concentrations of component i . γ^L is the liquid phase activity coefficient with reference pressure p (cf. Appendix A). The integral in Eq. (2.8) is often denoted as the Poynting factor and acts as a correction in Gibbs energy for elevated pressure.

2.3 Two-phase Fluid–Fluid Equilibria

In prediction of vapor-liquid equilibria at low and moderate pressure, Eq. (2.8) is often used. With the assumptions of ideal gas behavior for vapor and saturated conditions, pure condensed phases and a pressure relatively close to the pure component saturation pressure (p^{sat}), Eq. (2.8) simplifies to Raoult’s law [116]. With elevated pressure however, assumptions of ideal gas behavior and constant liquid volume are no longer valid. A p vT-relation for each phase becomes a requirement in the accurate calculation of phase equilibria.

A simple but rigorous and physically founded relation to describe both liquid and vapor p vT-behavior in a single equation was first given by Johannes Diderick van der Waals who combined attractive and repulsive interactions between molecules with the assumption of hard sphere molecules into a pressure explicit equation of state of the cubic polynomial form in volume [132]. Since the development of the van-der-Waals (VdW) equation, many improvements have been suggested. The most successful improvements were proposed by Otto Redlich and J.N.S. Kwong [104], G.Soave [119] and D.Y. Peng and D.B. Robinson [97]. Their improvements especially focussed on the correct prediction of saturated conditions and the phase behavior of small molecular non- (and slightly-) polar fluids.

2.3.1 Equation of State

The Peng-Robinson equation of state (PR-EoS) has been applied in the oil and gas industry over more than three decades. Its exactness is verified and the parameters are documented for many components, both pure and in mixtures over a wide range of pressure and temperature [39, 77, 136].

The Peng-Robinson equation of state for pure components is defined as [97, 105]:

$$p = \frac{RT}{v - b} - \frac{a(T)}{v(v + b) + b(v - b)}, \quad (2.9)$$

where b represents the volume occupied in a medium by molecules which are assumed to be hard spherical objects. For the PR equation of state, a and b are empirically related through continuity of phases at critical conditions. b is given as:

$$b = \frac{0.0778 RT_c}{p_c}, \quad (2.10)$$

where T_c and p_c are the critical temperature and pressure. The term $a(T)$ represents the attractive forces between molecules. Peng and Robinson correlated the attractive term for their equation of state to the temperature and acentric factor ω by:

$$a(T) = \frac{0.45724 R^2 T_c^2}{p_c} \left(1 + f_\omega \left(1 - \sqrt{\frac{T}{T_c}} \right) \right) \quad (2.11)$$

with

$$f_\omega = 0.37464 + 1.54226 \omega - 0.26992 \omega^2$$

The acentric factor accounts to some extent for molecular shape differences (acentricity) in physical properties and is defined by Pitzer as [99]:

$$\omega = -\log_{10} \left[\frac{p_{sat}}{p} \right]_{(T/T_c)=0.7} - 1.0. \quad (2.12)$$

The Peng-Robinson equation of state is often presented dimensionless by the introduction of the compressibility factor Z :

$$Z^3 + (b' - 1) Z^2 + (-3b'^2 - 2b' + a') Z + b'^3 + b'^2 - a'b' = 0. \quad (2.13)$$

with:

$$b' = \frac{bp}{RT} \quad (2.14)$$

$$a' = \frac{a(T)p}{(RT)^2} \quad (2.15)$$

and the compressibility factor Z defined as:

$$Z = \frac{pv}{RT}, \quad (2.16)$$

which is a measure for non-ideal gas behavior and equals unity for ideal gas.

To give the unfamiliar reader a feeling for the typical behavior of a cubic EoS*, an example of a subcritical isotherm is illustrated in Fig. 2.2. The S-shape subcritical isotherm is characteristic for cubic equations of state. Three areas can be identified from the subcritical isotherm: a regime corresponding to liquid, a regime corresponding to vapor and an unphysical regime. The unphysical regime limits are defined by $\partial^2 p / \partial v^2|_T = 0$. When deriving the molar volume for a condition (p, T) of vapor-liquid coexistence, three roots are obtained. The vapor and liquid volumes are given by the largest and smallest root as indicated. The intermediate root has no physical meaning. The molecular volume cannot be smaller than the asymptotic limit, given by $v = b$ in case of the PR-EoS.

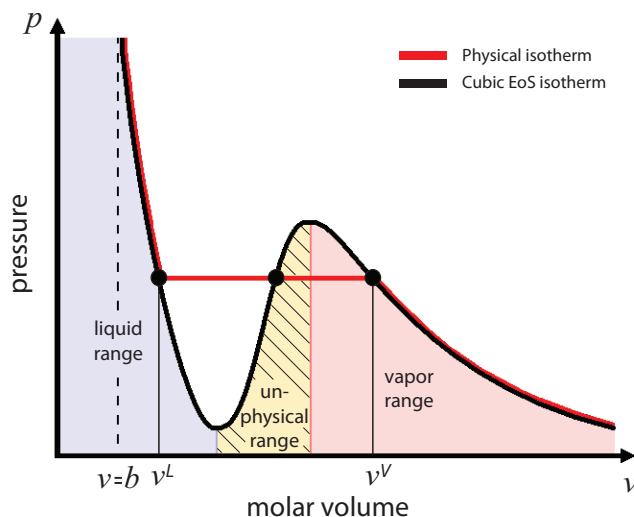


Figure 2.2: The shape of a typical isotherm of a cubic EoS for a pure component.

2.3.2 Mixing rules

Equations of state generally describe the behavior of pure fluids only. The application of an equation of state to a multi-component mixture introduces an additional thermodynamic variable; mixture composition. Mixture composition has to be taken into account due to different molecular interactions (van-der-Waals forces and hydrogen bonding) between similar and dissimilar molecules (different species).

Mixture composition is taken into account by the introduction of mixing rules, applied to the EoS parameters that relate to molecular properties (a and b in the PR-EoS). Peng and Robinson [97] showed that the van-der-Waals mixing rules are adequate for mixtures of small molecular and even slightly polar molecules. Harismiadis et al. [136] concluded that the VdW-mixing rules are reliable up to an eight-fold difference in the size of the component molecules.

*Equation Of State

The van-der-Waals one-fluid mixing rules for the Peng-Robinson EoS are given as:

$$a_m(T) = \sum_{i=1}^N \sum_{j=1}^N y_i y_j a_{ij}(T) \quad \text{with} \quad a_{ij} = [a_i(T)a_j(T)]^{0.5} (1 - k_{ij}) \quad (2.17)$$

$$b_m = \sum_{i=1}^N y_i b_i, \quad (2.18)$$

where y_i and y_j represent the concentrations of components i and j , a_i , a_j and b_i the pure component EoS parameters and k_{ij} the binary interaction parameter in the combining rule. For the pure component terms $i = j$, the binary interaction parameter is zero, resulting in the pure component parameter $a_{ii} = a_i$. For the cross terms, $i \neq j$, the binary interaction parameter is assumed to be symmetric, $k_{ij} = k_{ji}$, and is fitted as a constant to experimental data. Suggested values for some of the most encountered binary interactions are summarized in Appendix B.

2.3.3 Fluid fugacity

The simplicity of the Peng-Robinson EoS and the van-der-Waals mixing rules, and the validity for both vapor and liquid makes it possible to derive one single analytical expression for the fugacity coefficients of components in both fluid phases [105]. For the Peng–Robinson equation of state it can be shown (Appendix A.3) that the fugacity coefficient is expressed as:

$$\begin{aligned} \ln(\phi_i) = & \frac{b'_i}{b'_m} (Z - 1) - \ln(Z - b'_m) + \frac{1}{\sqrt{8}} \frac{a'_m}{b'_m} \dots \\ & \dots \left(\frac{2 \sum_j^N \left(y_j \sqrt{a'_i a'_j} (1 - k_{ij}) \right)}{a'_m} - \frac{b'_i}{b'_m} \right) \ln \left(\frac{Z + b'_m (1 - \sqrt{2})}{Z + b'_m (1 + \sqrt{2})} \right). \end{aligned} \quad (2.19)$$

Because of the capability of the cubic EoS to describe both liquids and gases, both fluid phases can be approached in a similar way. The equilibrium condition, as given in Eq. (2.8), becomes:

$$y_i p \phi_i^V = x_i p \phi_i^L. \quad (2.20)$$

In a similar way also liquid-liquid equilibria (LLE) can be described, in which subscripts ' V ' and ' L ' are replaced by a lighter and a heavier liquid phases ' L'_1 ' and ' L'_2 '.

2.3.4 Mass conservation in vapor-liquid equilibria

When a mixture with overall concentration z_i is split into a vapor and a liquid phase with vapor and liquid phase component concentrations y_i and x_i , they are related by

the molar vapor phase fraction, α^V by:

$$z_i = \alpha^V y_i + (1 - \alpha^V) x_i, \quad (2.21)$$

where the vapor fraction α^V describes the ratio between the total number of moles of overall mixture and the number of moles of all components in the vapor phase. In flash calculations, the molar vapor phase fraction is calculated from the mass balance, i.e., Eq. (2.21) by formation of 'so called 'objective functions'. Phase component concentrations (y_i, x_i) of the regarded mixture are found by using the mass balance after calculation of the molar vapor fraction α^V .

Objective functions are obtained by rewriting of Eq. (2.21) in expressions for x_i and y_i as a function of overall composition z_i , molar vapor fraction α^V and a K-factor, K_i , which is defined as the ratio between the vapor and liquid component concentrations ($K_i = y_i/x_i$). Combined with the concentration constraint ($\sum_{i=1}^N y_i = 1$), the obtained objection functions for x_i and y_i are:

$$\sum_{i=1}^N x_i = \sum_{i=1}^N \left(\frac{z_i}{1 + \alpha^V (K_i - 1)} \right) = 1, \quad (2.22)$$

$$\sum_{i=1}^N y_i = \sum_{i=1}^N \left(\frac{z_i K_i}{1 + \alpha^V (K_i - 1)} \right) = 1. \quad (2.23)$$

For known K-factors and feed concentration, the vapor-fraction can be solved from one of the objective functions, Eqs. (2.22)–(2.23), with use of an iterative Newton-Raphson method [48, 85].

To guarantee convergence of the Newton-Raphson method, a monotonic objection function is required for solving of the vapor fraction α^V , i.e. the sign of the function's derivative is not allowed to alter. Eqs. (2.22)–(2.23) are however not monotonic. A solution to this problem is to subtract Eq. (2.23) from Eq. (2.22) to obtain a new function, the Rachford-Rice objective function, that is monotonic [48, 138]:

$$f(\alpha^V) = \sum_{i=1}^N \left(\frac{z_i (K_i - 1)}{1 + \alpha^V (K_i - 1)} \right) = 0. \quad (2.24)$$

The objective functions (2.22) to (2.24) all have a number of singularities, equal to the number of components in the system. These are given by:

$$\alpha_{singular,i}^V = \frac{1}{1 - K_i}. \quad (2.25)$$

In Fig. 2.3 the new objective function (Eq. (2.24)) is shown as a function of the molar vapor fraction α^V for a binary mixture of CO₂/CH₄. In binary mixtures, there are only two singularities, indicated by 'A' and 'B'. Between these singularities, there is only one exact solution for the vapor fraction α^V that obeys the objective function

($f(\alpha^V) = 0$), indicated by 'c'. The solution domain of the iteration must be limited by the two singularities to guarantee convergence, otherwise the larger singularity might be crossed during Newton-Raphson iteration as shown by the dashed line 'D-E' in Fig. 2.3.

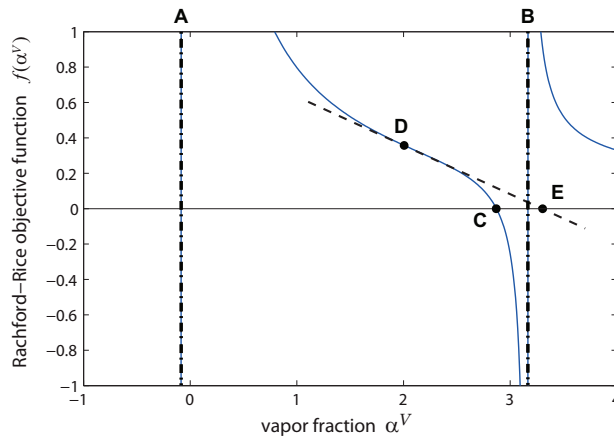


Figure 2.3: The Rachford-Rice objective function plotted for the CO_2/CH_4 binary mixture at 5 bar and 213 K. The singularities, as given by Eq. (2.25), are shown by the dash-dotted lines 'A' and 'B'. 'C' is the solution for the vapor fraction where $f(\alpha^V) = 0$.

In multi-component mixtures each additional component in the mixture contributes to an additional singularity and one more solution to the objective function. For positive K-factors, all singularities are however located outside the physical range of the vapor-fraction: $0 \leq \alpha^V \leq 1$. Singularities on both sides of the physical domain always occur. The search for the physically correct solution can therefore be limited by the smallest singularity greater than the physical range and the largest singularity smaller than the physical range; defined by the smallest and the largest K-factor [30]. Only in the case of a negative flash[†] it might be necessary to search outside this range [38]. In such case, one has to identify the region between two singularities in which the phase concentrations are all positive, holding:

$$1 + \alpha^V (K_i - 1) > 0 \quad i = 1, 2, \dots, N. \quad (2.26)$$

The sign of the left side of Eq. (2.26) changes only if a singularity value, Eq. (2.25), is crossed in the α^V interval. Locating the region that satisfies Eq. (2.26), will always give the correct solution domain for α^V even though the found solution might not physically exist.

[†]Negative flash: calculation of an unphysical phase equilibrium whereby positive phase concentrations, but one or more negative phase fractions are obtained. Negative flashes are typically used to obtain saturated mixture properties in the infinity of bubble and dew point conditions.

2.3.5 Governing equations and VLE-algorithm

The phase equilibrium criterion, the equation of state, the fugacity coefficient and the solving of the molar vapor phase fraction discussed in the previous sections result in the following set of equations that has to be solved to find the equilibrium conditions:

$$v^V = f(p, T, \mathbf{y}), \quad (2.27)$$

$$v^L = f(p, T, \mathbf{x}), \quad (2.28)$$

$$\phi_i^V = f(p, T, v^V, \mathbf{y}), \quad (2.29)$$

$$\phi_i^L = f(p, T, v^L, \mathbf{x}), \quad (2.30)$$

$$y_i \phi_i^V = x_i \phi_i^L, \quad (2.31)$$

$$x_i = \frac{z_i}{(1 + \alpha^V (K_i - 1))} \quad i = 1, 2, \dots, N, \quad (2.32)$$

$$\sum_{i=1}^N y_i = 1, \quad (2.33)$$

$$\alpha^V + \alpha^L = 1, \quad (2.34)$$

$$K_i = \frac{y_i}{x_i}. \quad (2.35)$$

\mathbf{x} and \mathbf{y} are thereby the vapor and liquid phase concentration vectors. Equations (2.27)–(2.28), describing the molar volume, result from the Peng-Robinson EoS, Eqs. (2.9)–(2.16), and the mixing rules, Eqs. (2.17)–(2.18). The fugacity coefficients for both fluid phases, Eqs. (2.29)–(2.30) are calculated according to Eq. (2.19). For N components, a set of $5N + 4$ equations is obtained that describes the equilibrium in the presence of $6N + 6$ variables. Prescription of pressure, temperature and the feed composition (a flash calculation) turns Eqs. (2.27)–(2.35) into a solvable set of equations.

As there are no analytical techniques for solving such sets of nonlinear coupled equations, iterative methods are used. The most successful and proven iterative method in phase calculation is the Successive Substitution Method (SSM) [48, 85]. SSM requires an initial guess for the K-factors to calculate the molar phase fractions and the phase component concentrations. These concentrations are used to calculate fugacity coefficients and fugacities. The phase equilibrium condition is checked, according Eqs. (2.20) and (2.31). If equilibrium is not satisfied, the ratio of liquid to vapor fugacities is used to update the K-factors according:

$$K_i^{(new)} = K_i^{(old)} \left(\frac{f_i^L}{f_i^V} \right)^q, \quad (2.36)$$

after which the iteration procedure is repeated. Updating the K-factors can sometimes be accelerated by a power $q > 1$. Methods for acceleration are described elsewhere [48] and not implemented in the model. Without acceleration, q is set to unity by default. The iteration procedure is stopped if satisfactory convergence is achieved; $\mathcal{O}(10^{-14})$. The iteration scheme of the SSM method is shown in Fig. 2.4.

Solving a phase equilibrium makes only sense if the solution converges to a physical meaningful solution within the region that satisfies Eq. (2.26), spanned by two singularities. A correction is taken into account when the new estimate for α^V crosses one of its nearby singularities as shown in Fig. 2.4. Converged solutions with a vapor phase fraction outside the physical domain are referred to as negative flashes, meaning that vapor-liquid equilibrium does not exist in the evaluated point according to model prediction.

Accurate estimation of initial K-factors is a requirement for convergence to a meaningful solution [85]. Initial K-factors can be estimated in various ways. Raoult's law combined with a vapor pressure correlation is the most simple way. An example of the latter for vapor-liquid equilibria is given by Wilson's correlation:

$$K_i = \frac{p_{c,i}}{p} \exp \left(5.37 (1 + \omega_i) \left(1 - \frac{T_{c,i}}{T} \right) \right). \quad (2.37)$$

Stability methods offer an alternative route to initiate K-factors for any kind of phase equilibrium. Examples are the rigorous stability analysis proposed by Michelsen [84] and the non-iterative stability analysis, where the K-values can be estimated directly from the ratio of mixture-vapor to pure-vapor fugacities [129]. Stability methods provide better estimates and are not limited to vapor-liquid equilibria, but take up to twice the computer time of Wilson's correlation [129].

With the increase of the number of components or the prediction of phase equilibrium far away from the lowest pure component saturation line, initiation with Wilson's correlation becomes inaccurate. Consequently the model can produce incorrect results. To prevent faults by inaccurate initiation, the flash calculations can be performed over a range of pressures at the flash temperature, starting from a pressure where the mixture is in the vapor-only phase, up to the desired flash pressure. In the vapor-only phase, Wilson's correlation can be used for estimation of the initial K-factors and the initial vapor-fraction equals one. As soon as the solution becomes two-phase, the initial vapor-fraction and K-factors for the next pressure can be taken directly from the converged solution of the actual pressure.

In mixtures with more than two components, a stepwise flashing method provides the insurance of the correct solving domain, as long as the number of steps is large enough, but comes, unfortunately, at a penalty of computing time. To omit a stepwise approach in pressure, we shall use stability analysis for the estimation of K-factors. This is further discussed in Section 2.6.

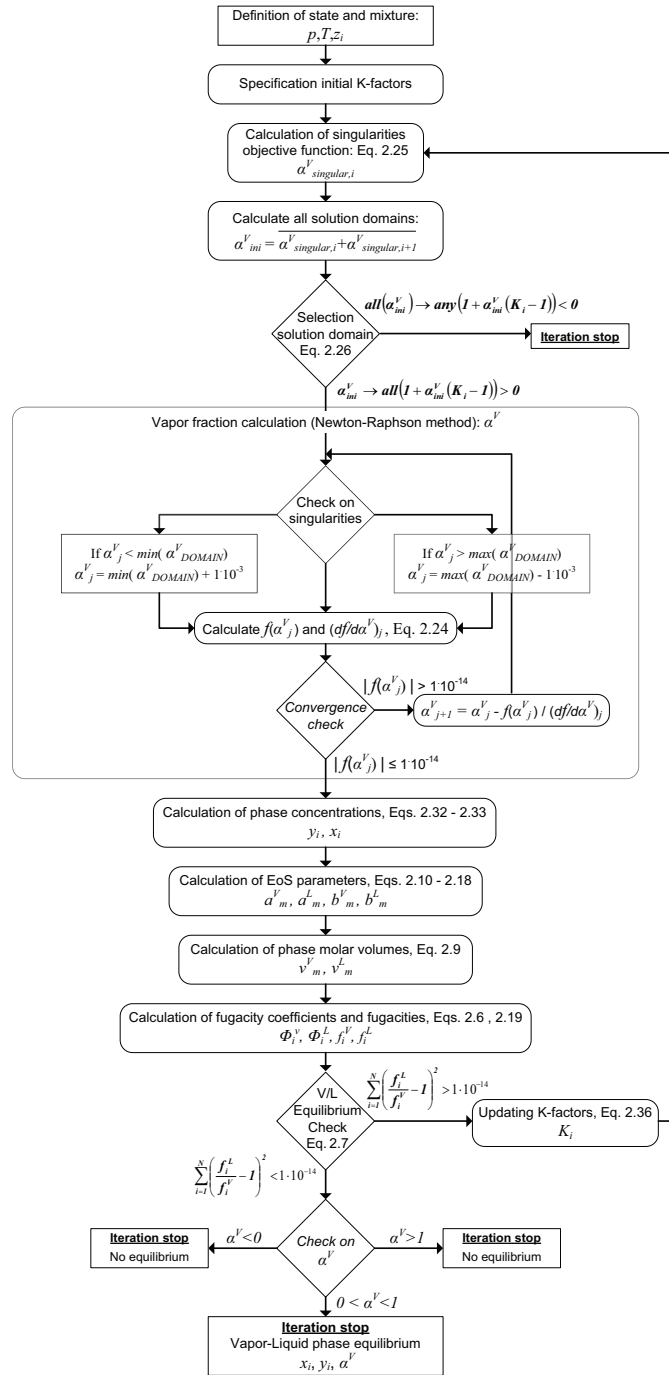


Figure 2.4: Iteration scheme of the Successive Substitution Method for solving the vapor-liquid phase equilibrium problem.

2.4 Fluid–Multi-Solid Equilibria

The accurate prediction of solid phase formation is of great importance in process engineering. In mixtures, one or more solid phases can exist in presence of one or more fluid phases. In this section we restrict to phase equilibria with a single fluid phase. We derive a more accurate expression for pure solid phase fugacity and describe the algorithm and equations for single-fluid–multi-solid phase equilibria.

In the case that there is a distinctive difference in pure component triple point temperatures of the different mixture components, it is legitimate to assume that the solid phase is formed as a pure component phase [98, 120]. The phase equilibrium condition for vapor-solid (VS) and liquid-solid (LS) equilibria can be written as:

$$f_{i^*}^S = \phi_{i^*}^V y_{i^*} p \quad \text{or} \quad f_{i^*}^S = \phi_{i^*}^L x_{i^*} p \quad \text{with} \quad i^* = 1, 2, \dots, N^*, \quad (2.38)$$

where i^* refers to a pure solid phase component, and N^* to the number of solid phases. Eq. (2.38) is the basis for solid–fluid equilibrium calculations, but requires an accurate relation for the fugacity of the solid phase.

2.4.1 Pure solid fugacity

The fugacity of a pure solid at conditions close to the sublimation line can be derived similarly to Eq. (2.8) and results in a comparable expression:

$$f_{i^*}^S = w_{i^*} \gamma_{i^*}^S p_{i^*}^{sub} \phi_{i^*}^{sub} \exp \left(\int_{p_{i^*}^{sub}}^p \frac{v_{i^*}^S}{RT} dp' \right), \quad (2.39)$$

where w_{i^*} is the concentration of component i^* in the solid phase, $p_{i^*}^{sub}$ the pure component sublimation pressure, $\phi_{i^*}^{sub}$ the pure component fugacity coefficient at sublimation pressure $p_{i^*}^{sub}$ and $v_{i^*}^S$ the solid molar volume, [98–100]. The solid activity coefficient $\gamma_{i^*}^S$ (cf. Eq. (2.5)) and component concentration w_{i^*} are per definition unity as a pure solid phase is assumed. The incompressibility of the solid phase justifies the assumption of a constant molar volume, even for pressures much higher than the pure component sublimation pressure. For the sublimation pressure, often correlations are used. The use of Eq. (2.39) becomes problematic when the solid molar volume or the sublimation pressure of the solid species is not available or when the sublimation pressure correlation is not accurate.

The alternative approach is given by Soave [120] and Prausnitz et al. [100] who related the fugacities of pure solid and pure subcooled liquid of component i^* with use of the change in molar Gibbs energy between the two phases at constant temperature:

$$\ln \left(\frac{f_{i^*}^L}{f_{i^*}^S} \right) = \frac{\Delta h^{fus}}{RT_{tr}} \left(\frac{T_{tr}}{T} - 1 \right) - \frac{c_p^L - c_p^S}{R} \left(\frac{T_{tr}}{T} - 1 \right) - \frac{c_p^L - c_p^S}{R} \ln \left(\frac{T_{tr}}{T} \right), \quad (2.40)$$

where Δh^{fus} refers to the heat of fusion of the solid pure component at the triple point and c_p^L and c_p^S to the isobaric heat capacities of both the liquid and solid phase.

Subscript '*tr*' denotes the triple point. Eq. (2.40) relies on both the heat of fusion and the triple point temperature reference state and corresponds to a thermodynamic path as shown in Fig. 2.5(a). Although Eq. (2.40) is often assumed to be more accurate than Eq. (2.39), it uses constant heat capacities and neither real gas effects nor pressure effects are included. Inaccurate values for solid phase fugacity can therefore be expected at high pressures and for temperatures away from the pure component tripple point.

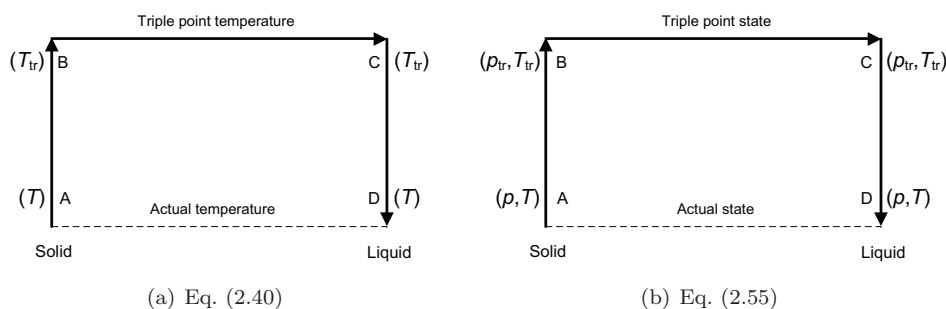


Figure 2.5: Thermodynamic path corresponding to the calculation of the ratio of solid to liquid fugacity of a pure component.

Real gas effects and the effect of pressure can be included, as is shown by Serin and Cézac for the application of sulphur precipitation in natural gas [29, 118]. They related the pure component solid phase fugacity to the pure component liquid phase fugacity at the fusion temperature under atmospheric pressure with use of residual enthalpy and the enthalpy difference between ideal gas and solid at the fusion temperature. They added a Poynting correction factor to correct for pressure effects (cf. Section 2.2).

Unfortunately for only a limited number of species both the heat of fusion and the solid heat capacity are available under atmospheric pressure. Furthermore, in case of many pure components, such as CO₂, transition of liquid to solid cannot be found at ambient pressure. In such a case the equations of Serin and Cézac are not applicable.

To come to a new expression for solid fugacity, we extend Eq. (2.40) in the remainder of this section to include real gas effects and pressure effects.

Starting from Eq. (2.5), a change in Gibbs energy is related to the change in fugacity by:

$$RT \int_L^S d \ln (f) = \int_L^S dg \rightarrow RT \ln \left(\frac{f^S}{f^L} \right) = g^S - g^L . \quad (2.41)$$

A change in Gibbs energy is rigourously expressed as:

$$\partial g = \partial h - T \partial s - s \partial T . \quad (2.42)$$

Because enthalpy, entropy and Gibbs energy are unique state functions, calculation of a difference in such a quantity is independent of the thermodynamic route of calculation. The described phase transition from liquid to solid is evaluated at constant temperature T . Therefore the third term on the right hand side of Eq. (2.42) must vanish. The change in Gibbs energy from liquid to solid in Eq. (2.41) can therefore be expressed as:

$$g_{(p,T)}^S - g_{(p,T)}^L = \left(h_{(p,T)}^S - h_{(p,T)}^L \right) - T \left(s_{(p,T)}^S - s_{(p,T)}^L \right), \quad (2.43)$$

where the involved state is indicated by the subscripts. Following a similar thermodynamic route as used for Eq. (2.40), but with both the triple point temperature T_{tr} and pressure p_{tr} as a fixed reference (Fig. 2.5(b)), the change in enthalpy can be expressed as:

$$\begin{aligned} h_{(p,T)}^S - h_{(p,T)}^L &= \left(h_{(p,T)}^S - h_{(p_{tr},T_{tr})}^S \right) \\ &+ \left(h_{(p_{tr},T_{tr})}^S - h_{(p_{tr},T_{tr})}^L \right) + \left(h_{(p_{tr},T_{tr})}^L - h_{(p,T)}^L \right). \end{aligned} \quad (2.44)$$

The second term in the RHS of Eq. (2.44) is given by the enthalpy of fusion:

$$h_{(p_{tr},T_{tr})}^S - h_{(p_{tr},T_{tr})}^L = -\Delta h_{(p_{tr},T_{tr})}^{fus}. \quad (2.45)$$

Similarly, with $\Delta S_{(p_{tr},T_{tr})}^{fus} = \Delta h_{(p_{tr},T_{tr})}^{fus}/T_{tr}$ the change in entropy becomes:

$$\begin{aligned} s_{(p,T)}^S - s_{(p,T)}^L &= \left(s_{(p,T)}^S - s_{(p_{tr},T_{tr})}^S \right) \\ &- \left(\frac{\Delta h_{(p_{tr},T_{tr})}^{fus}}{T_{tr}} \right) + \left(s_{(p_{tr},T_{tr})}^L - s_{(p,T)}^L \right). \end{aligned} \quad (2.46)$$

Combination of Eqs. (2.44)–(2.46) leads to:

$$\begin{aligned} g_{(p,T)}^S - g_{(p,T)}^L &= \Delta h_{(p_{tr},T_{tr})}^{fus} \left(\left(\frac{T}{T_{tr}} \right) - 1 \right) \dots \\ &+ \left(h_{(p_{tr},T_{tr})}^L - h_{(p,T)}^L \right) - T \left(s_{(p_{tr},T_{tr})}^L - s_{(p,T)}^L \right) \dots \\ &+ \left(h_{(p,T)}^S - h_{(p_{tr},T_{tr})}^S \right) - T \left(s_{(p,T)}^S - s_{(p_{tr},T_{tr})}^S \right). \end{aligned} \quad (2.47)$$

The entropy and enthalpy change of a non-ideal fluid can be calculated from a cubic EoS with a reference state satisfying ideal gas behavior and so called 'departure functions' (cf. Section 4.1.1), as described by Reid et al. [105]. The change in liquid enthalpy in Eq. (2.47) can be written as:

$$h_{(p_{tr},T_{tr})}^L - h_{(p,T)}^L = \int_{p_0}^{p_{tr}} \left. \frac{\partial h^L}{\partial p} \right|_{T_{tr}} dp' + \int_T^{T_{tr}} \left. \frac{\partial h}{\partial T} \right|_{p_0} dT' + \int_p^{p_0} \left. \frac{\partial h^L}{\partial p} \right|_T dp'. \quad (2.48)$$

The first and third term in the RHS of Eq. (2.48) are described by departure functions. The partial derivative in the second term is given by the ideal heat capacity c_p^o .

The ideal gas reference state is set at the evaluated temperature and sufficiently low pressure $\mathcal{O}(1)$ Pa. The solid phase enthalpy change can be expressed similarly:

$$h_{(p,T)}^S - h_{(p_{tr},T_{tr})}^S = \int_{p_0^*}^p \left. \frac{\partial h^S}{\partial p} \right|_T dp' + \int_{T_{tr}}^T c_p^{S*} dT' + \int_{p_{tr}}^{p_0^*} \left. \frac{\partial h^S}{\partial p} \right|_{T_{tr}} dp'. \quad (2.49)$$

The solid phase reference state is set at the evaluated temperature and can be set at ambient pressure, $\mathcal{O}(10^5)$ Pa, as for many species the solid phase heat capacity c_p^{S*} is available at ambient pressure. Solid heat capacities at other pressures can also be used, but the solid reference state pressure must be changed accordingly.

Entropy changes can be calculated similar to enthalpy changes (Eq. (2.49)), however with the change of entropy in the reference state given as:

$$\left. \frac{\partial s}{\partial T} \right|_{p_0} = \frac{c_p^o}{T}. \quad (2.50)$$

Combination of Eqs. (2.47)–(2.50) results into:

$$\begin{aligned} g_{(p,T)}^S - g_{(p,T)}^L &= \Delta h_{(p_{tr},T_{tr})}^{fus} \left(\left(\frac{T}{T_{tr}} \right) - 1 \right) \dots \\ &+ \int_{p_0}^{p_{tr}} \left. \frac{\partial g^L}{\partial p} \right|_{T_{tr}} dp' + \int_{p_{tr}}^{p_0^*} \left. \frac{\partial g^S}{\partial p} \right|_{T_{tr}} dp' \dots \\ &+ \int_T^{T_{tr}} c_p^o dT' - T \int_T^{T_{tr}} \frac{c_p^o}{T} dT' + \int_{T_{tr}}^T c_p^{S*} dT' - T \int_{T_{tr}}^T \frac{c_p^{S*}}{T} dT' \dots \\ &+ \int_p^{p_0} \left. \frac{\partial g^L}{\partial p} \right|_T dp' + \int_{p_0^*}^p \left. \frac{\partial g^S}{\partial p} \right|_T dp', \end{aligned} \quad (2.51)$$

with

$$\left. \frac{\partial g}{\partial p} \right|_T = \left. \frac{\partial h}{\partial p} \right|_T - T \left. \frac{\partial s}{\partial p} \right|_T. \quad (2.52)$$

For the liquid phase, the enthalpy and entropy change with pressure at constant temperature, and thus the change in Gibbs energy according Eq. (2.52), can be calculated with use of an EoS.

Generally applicable EoS models for solids do not exist. Calculation of the change of Gibbs energy of a solid with pressure is however possible from the conservation of energy at constant temperature:

$$dg = v^S dp - s^S dT \quad \rightarrow \quad \left. \frac{\partial g^S}{\partial p} \right|_T = v^S, \quad (2.53)$$

which means that either a constant solid molar volume or even a solid density correlation or expansion coefficient model can be used for calculation of the Gibbs energy change of the solid with pressure. For a constant molar volume the pure solid phase

departure functions (Eq. (2.51): 3th and 9th RHS term) can be combined and simplified with use of Eq. (2.53) to:

$$\int_{p_{tr}}^{p_0^*} \left. \frac{\partial g^S}{\partial p} \right|_{T_{tr}} dp' + \int_{p_0^*}^p \left. \frac{\partial g^S}{\partial p} \right|_T dp' = v^S (p - p_{tr}) . \quad (2.54)$$

Consequently, the solid phase reference state p_0^* drops out of the equation and the result can be interpreted as the Poynting correction for Eq. (2.40). Combination of Eqs. (2.41),(2.51) and (2.54) lead to the improved expression for the ratio of pure solid to pure liquid fugacity of a component that takes into account both pressure and non-ideal fluid effects:

$$RT \ln \left(\frac{f^S}{f^L} \right) = \Delta h_{(p_{tr}, T_{tr})}^{fus} \left(\left(\frac{T}{T_{tr}} \right) - 1 \right) + \int_{p_0}^{p_{tr}} \left. \frac{\partial g^L}{\partial p} \right|_{T_{tr}} dp' + \int_T^{T_{tr}} c_p^\circ dT' - \\ T \int_T^{T_{tr}} \frac{c_p^\circ}{T} dT' + \int_{T_{tr}}^T c_p^{S*} dT' - T \int_{T_{tr}}^T \frac{c_p^{S*}}{T} dT' + \int_p^{p_0} \left. \frac{\partial g^L}{\partial p} \right|_T dp' + v^S (p - p_{tr}) . \quad (2.55)$$

In case no subcooled liquid phase can be found from the EoS, which might occur for pressures below the extrapolated vapor-liquid saturation line, the vapor phase can be used instead of the subcooled liquid in Eq. (2.55). In such a case the heat of fusion must be replaced by the heat of sublimation, references to liquid state 'L' change into vapor state 'v' and the left hand side of Eq. (2.55) becomes the ratio of pure solid to pure vapor fugacity. If the heat of fusion or heat of sublimation is unknown in the triple point, but known at another fusion or sublimation condition, this condition can serve as reference instead.

Eq. (2.55) offers flexibility towards the reference condition at which the enthalpy of fusion or sublimation is known, and is independent of the pressure at which the solid heat capacity is available, which makes application to almost any species possible. Because of its higher accuracy and wider flexibility, Eq. (2.55) is the preferred equation in the calculation of solid-fluid equilibria.

2.4.2 Governing equations and vs/LS algorithm

Flash calculations involving a single fluid and one or more solid phases are somewhat distinctive from fluid–fluid equilibria, as a solid phase is assumed to be essentially pure. The equilibrium condition reduces therefore only to the components that become solid, Eq. (2.38). As the fluid phase can be described with the cubic EoS, the fluid phase fugacity coefficient can be calculated from Eq. (2.19). Single-fluid–multi-solid phase equilibria (On the example of vapor) can therefore be described by the following set of equations:

$$v^V = f(p, T, \mathbf{y}), \quad (2.56)$$

$$\phi_*^V = f(p, T, v^V, \mathbf{y}), \quad (2.57)$$

$$f_{i^*}^S = f(p, T) \quad i^* = 1, 2, \dots, N^*, \quad (2.58)$$

$$y_{i^*} = \frac{f_{i^*}^S}{\phi_{i^*}^V p}, \quad (2.59)$$

$$y_{i \neq i^*} = z_{i \neq i^*} \frac{1 - \sum y_{i^*}}{1 - \sum z_{i^*}} \quad i = 1, 2, \dots, (N - N^*), \quad (2.60)$$

$$\alpha_{i^*}^S = z_{i^*} - y_{i^*} \frac{1 - \sum z_{i^*}}{1 - \sum y_{i^*}}. \quad (2.61)$$

$$\alpha^V + \sum_{i^*=1}^{N^*} \alpha_{i^*}^S = 1, \quad (2.62)$$

Equation set (2.56)–(2.62) governs $N + 4$ equations for $2N + 6$ unknown parameters for an N -component mixture. Prescription of pressure p , temperature T and overall composition \mathbf{z} therefore defines the phase equilibrium conditions. As there is a similarity in fluid phase description between Eqs. (2.27)–(2.35) and Eqs. (2.56)–(2.62), a likewise successive substitution scheme can be used. The corresponding iteration scheme on the example of vapor–multi-solid equilibrium is given in Fig. 2.6.

Pure solid phase fugacities can be calculated outside the iteration. This is allowed as the solid phases are assumed to be pure and its fugacities therefore only depend on temperature and pressure. An initial guess for \mathbf{y} between the physical range $0 \geq \mathbf{y}^* \geq \mathbf{z}^*$ has to be taken to calculate the fluid phase molar volume and fluid phase partial fugacities of the solid components $i^* = 1, 2, \dots, N^*$. After fugacity calculation, the equilibrium condition is checked along Eq. (2.38). For insufficient convergence, the fluid phase concentration and the solid fraction are updated according Eqs. (2.59)–(2.61) and fluid phase molar volume and fugacity are calculated again in a new sequence.

2.4.3 Fluid phase identification

Solving of the compressibility factor or molar volume from the equation of state results in either one or three real solutions. In the calculation of fluid–solid equilibria, it is important to identify the correct root that belongs to the fluid phase regime (either vapor or liquid). In case of three real roots, identification with the correct fluid phase is straightforward. Existence of only one real root, often encountered for mixtures at pressures close to or above the critical pressure, is more problematic in fluid phase identification.

A cubic EoS has typically three regimes as explained in Section 2.3.1 and indicated in Fig. 2.2: a liquid, unphysical and vapor regime. The two boundaries between the three regimes are found by solving the first derivative of the third order polynomial EoS (Eq. (2.9) or Eq. (2.13)) to zero:

$$\left. \frac{\partial p(v_{m_{min}}^V, v_{m_{max}}^L)}{\partial v} \right|_T = 0 \quad \text{or} \quad \left. \frac{\partial f(Z_{m_{min}}^V, Z_{m_{max}}^L)}{\partial Z} \right|_{p,T} = 0, \quad (2.63)$$

where f is the cubic polynomial in terms of Z (Eq. (2.13)). $v_{m_{min}}^V$ or $Z_{m_{min}}^V$ and $v_{m_{max}}^L$ or $Z_{m_{max}}^L$ give the vapor and liquid region limits. For a pure component, there are always multiple real roots to be found in the two phase regime. Therefore the limits of the physical regions of the EoS, i.e. Eq. (2.63), are always real. For mixtures close to or above supercritical pressure, the solutions to Eq. (2.63) can become complex. In that case the absolutes of the complex limits give usable values for $v_{m_{min}}^V$ or $Z_{m_{min}}^V$ and $v_{m_{max}}^L$ or $Z_{m_{max}}^L$, which can be used to assign the root to the correct fluid phase.

In the iteration sequence (Fig. 2.6), the fluid phase is only identified by the smallest or largest root. Only after convergence the root of the fluid phase is checked on identity according Eq. (2.63). A solution with a fluid root that does not match with the solved type of equilibrium is discarded or denoted as the other type of fluid–multi–solid equilibrium. Such a check cannot be used as an early stopping criterion within the iteration as fluid composition, and thus description of fluid pVT behavior (includes also the critical conditions), change during iteration.

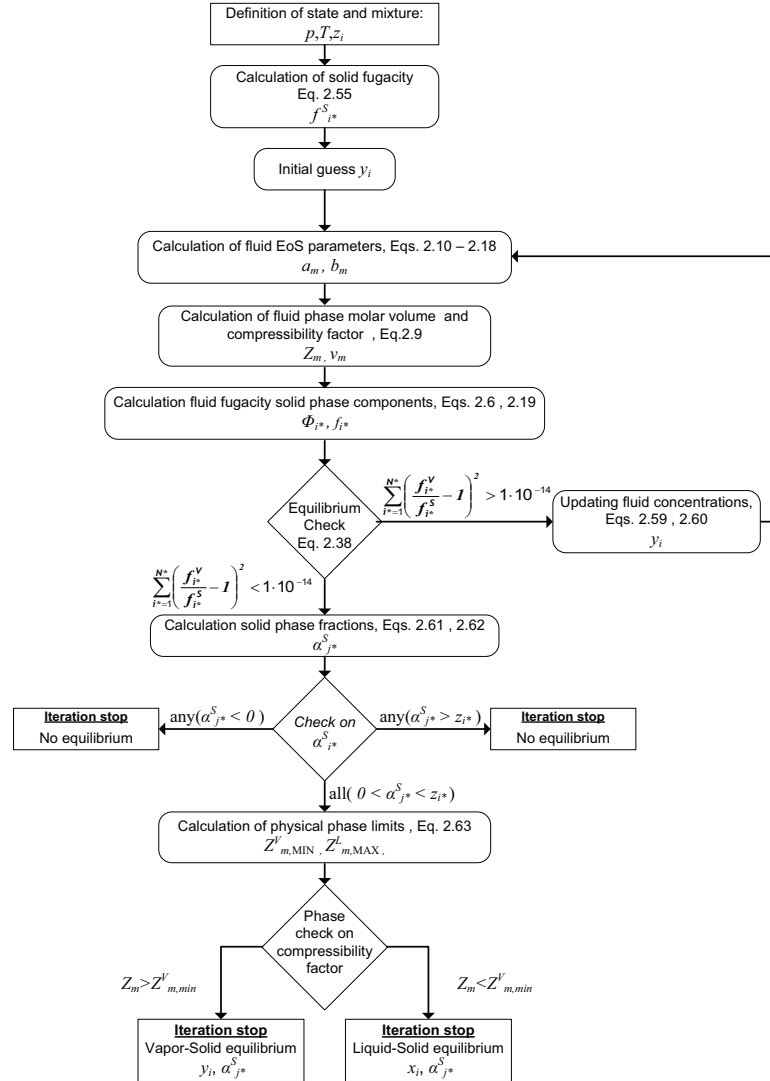


Figure 2.6: Iteration scheme of the Successive Substitution Method for solving the vapor–multi-solid phase equilibrium problem.

2.5 Multi-Fluid–Multi-Solid Equilibria

The previous sections described equilibria with two fluid phases (VLE and LLE) or one fluid phase with solid phases (VSE and LSE). For binary mixtures, these equilibria are sufficient to evaluate all possible kinds of phase behavior in a two-dimensional domain (e.g. in a p - T graph), as can be verified by the Gibbs phase rule, Eq. (2.4). In ternary mixtures, a maximum of three phases can coexist in thermodynamic equilibrium. Phase equilibria that have to be determined to be able to evaluate the complete phase behavior of ternary mixtures are: vapor-liquid-liquid equilibria (VLLE), vapor-liquid-solid equilibria (VLSE) and liquid-liquid-solid equilibria (LLSE). In this section we therefore construct a method for multi-component mixtures to determine equilibria with multiple fluid phases and eventually one or more solid phases.

The presence of each extra phase in a mixture puts an extra constraint on the phase equilibrium criteria. The equilibrium criteria can be described as:

$$\phi_{i,j} y_{i,j} p = \phi_{i,j+1} y_{i,j+1} p \quad i = 1, 2, \dots, N, \quad j = 1, \dots, P - N^* - 1, \quad (2.64)$$

$$\phi_{i^*,j} y_{i^*,j} p = f_{i^*,j}^S \quad i^* = 1^*, 2^*, \dots, N^*, \quad j = 1, \dots, j^* = i^*, \quad (2.65)$$

where y and ϕ denote the phase concentration and fugacity coefficient, j refers to the phase and i to the component involved. N^* and $P - N^*$ are the number of pure solid and fluid phases present in equilibrium. Note that the fluid phases equilibrium criterion, Eq. (2.64), holds for all components i , whereas the solid phase equilibrium criterion, Eq. (2.65), holds only for the components i^* that become a pure solid phase. Furthermore only one single fluid-solid criterion per component i^* , related to just one of the fluid phases is sufficient to describe the different solid phase criteria in multi-phase multi-component equilibrium.

2.5.1 Mass conservation in multi-phase equilibria

In line with Eq. (2.21), mass conservation in multi-phase equilibria is described by:

$$z_i = \sum_{j=1}^{P-1} \alpha_j y_{i,j} + \left(1 - \sum_{j=1}^{P-1} \alpha_j \right) y_{i,P} \quad i = 1, 2, \dots, N, \quad (2.66)$$

where α_j refers to the molar phase fraction of phase j . In 1995 it was first shown by Leibovici et al. [75] that the Rachford-Rice equation, Eq. (2.24), can be generally expanded to multi-phase multi-component mixtures by selection of a single reference phase:

$$f_j(\alpha_1, \alpha_2, \dots, \alpha_{P-1}) = \sum_{i=1}^N \frac{(K_{i,j} - 1) z_i}{1 + \sum_{m=1}^{P-1} (K_{m,i} - 1) \alpha_m} \quad j = 1, 2, \dots, P - 1, \quad (2.67)$$

where the K-factors are defined as:

$$K_{i,j} = \frac{y_{i,j}}{y_{i,ref}} \quad j = 1, 2, \dots, P - 1, \quad (2.68)$$

where subscript *'ref'* denotes the reference phase. In addition to Leibovici, it is of great importance to avert the use of a pure phase as a reference phase to prevent infinite K-factors.

Eq. (2.67) forms a set of $P - 1$ Rachford-Rice equations that can be solved according to a classical Newton procedure:

$$\alpha_j^{(k+1)} = \alpha_j^{(k)} + \lambda^{(k)} \Delta \alpha_j^{(k)}, \quad (2.69)$$

where λ is a deceleration parameter which is set to unity by default. During the Newton procedure, λ halves in value each time the solution domain is exceeded. For a vector $F(\boldsymbol{\alpha})$ containing all Rachford-Rice equations of the multi-phase system, the correction vector $\Delta \boldsymbol{\alpha}^{(k)}$, containing corrections $\Delta \alpha_j^{(k)}$, can be calculated by solving the system of equations:

$$\nabla F \cdot \Delta \boldsymbol{\alpha}^{(k)} = 0. \quad (2.70)$$

Similarly to two phase problems, the Rachford-Rice objective functions have as many singularities as components, which are equal for all Rachford-Rice equations contained in F . These singularities are given by the denominator of Eq. (2.67):

$$1 + \sum_{j=1}^{P-1} (K_{i,j} - 1) \alpha_j = 0 \quad i = 1, 2, \dots, N. \quad (2.71)$$

$$\alpha_{singular,i,P-1} = f(\alpha_1, \dots, \alpha_{P-2}, K_{i,1}, \dots, K_{i,P-1})$$

In contrast to two-phase fluid-fluid equilibria, the singularities are not described by points, but by straight hyperplanes in the $P - 1$ hyperspace. Fig. 2.7 shows the hyperplanes for a three-phase mixture, whereby the hyperplanes are lines in the two dimensions α_1 and α_2 . The different hyperplanes are not parallel. Their steepness depends on the different K-factors. Therefore the hyperplanes define regions in the hyperspace spanned by the $P - 2$ phase fractions α_j . By rewriting Eq. (2.71) into a straight hyperplane formation, Eq. (2.72), it can however be shown that no singularities cross the physical domain $0 < \alpha_j < 1$ as long as all K-factors are positive.

$$\alpha_{i,P-1} = b_i + \sum_{j=1}^{P-2} \alpha_j a_{i,j}, \quad b_i = \frac{1}{1 - K_{i,P-1}}, \quad a_{i,j} = \frac{K_{i,j \neq P-1} - 1}{1 - K_{i,P-1}}. \quad (2.72)$$

In Eq. (2.72) the b_i parameter describes the offset of a hyperplane in the dimension $P - 1$ at $\alpha_{j \neq P-1} = 0$. The $a_{i,j}$ parameter is the partial derivative $\partial \alpha_j / \partial \alpha_{P-1}$ and gives the steepness of the hyperplane in each dimension. Table 2.1 describes the behavior of the hyperplanes for real positive K-factors. Positive K-factors imply that offset and steepness are limited such that a hyperplane can only touch but not enter the physical phase fraction region $0 < \alpha_j < 1$, as can be derived from Eq. (2.72) and table 2.1.

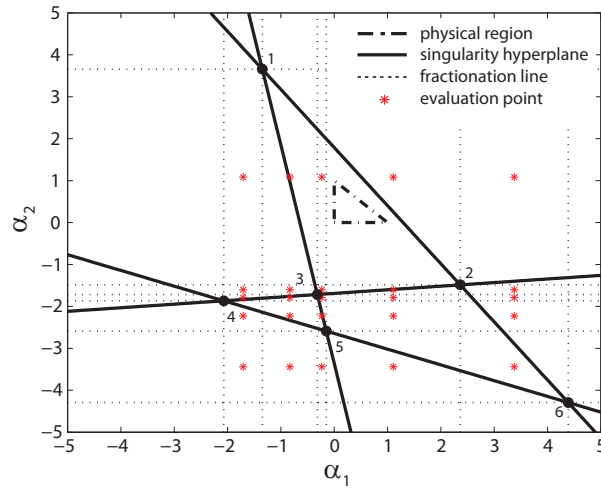
The correct solution domain of the Rachford-Rice equations, Eq. (2.67), must be enclosed by at least P different singularity hyperplanes. Consequently, if K-factors

Table 2.1: Behavior of the hyperplane parameters b_i and $a_{i,j}$ in Eq. (2.72) for positive K-factors.

	$0 \leq K_{i,j \neq P-1} \leq 1$	$K_{i,j \neq P-1} > 1$
$0 \leq K_{i,P-1} \leq 1 \rightarrow 1 \leq b_i \leq \infty \rightarrow$	$-b_i \leq a_{i,j} \leq 0$	$a_{i,j} > 0$
$K_{i,P-1} > 1 \rightarrow b_i < 0 \rightarrow$	$0 \leq a_{i,j} \leq -b_i$	$a_{i,j} < 0$

are positive and the number of phases equals the number of components, any arbitrary guess within the physical domain $0 < \alpha_j < 1$ is satisfactory to iteratively solve the Rachford-Rice equations.

When however the number of components exceeds the number of phases, $N > P$, the equations become multistable and limiting of the initial phase fractions within the physical domain becomes insufficient. In such case multiple enclosed regions between hyperplanes exist - see Fig. 2.7, which all contain a solution to the set of Rachford-Rice equations.

**Figure 2.7:** the singularity hyperplanes in the $P-1$ hyperspace for a 4 component mixture in the three phase regime with K-factors: $K_{11} = 2.55$, $K_{12} = 1.14$, $K_{13} = 0.23$, $K_{14} = 0.95$, $K_{21} = 1.30$, $K_{22} = 1.38$, $K_{23} = 0.44$, $K_{24} = 1.59$.

A transformation of the Rachford-Rice equations, Eq. (2.67), is an option to make the singularity hyperplanes and thus the regions parallel in the $P - 1$ hyperspace [142]. Such a transformation makes the identification and selection of the correct region and the calculation of the phase fractions a lot easier, but is complex and not necessarily required.

Instead of transformation of the equations, we developed a method to define the enclosed regions and identify the region that corresponds to only positive phase concentrations; $y_{i,j} > 0$, thereby also allowing for negative flashes:

To satisfy positive phase concentrations for all phases, mass conservation constrains that [75]:

$$1 + \sum_{j=1}^{P-1} (K_{i,j} - 1) \alpha_j > 0 \quad i = 1, 2, \dots, N. \quad (2.73)$$

Eq. (2.73) is also the expression defining the singularity conditions, cf. Eq. (2.71). Consequently, all phase component concentrations $y_{i,j}$ must be equal of sign in an enclosed region. By evaluation of Eq. (2.73) in a single point within each enclosed region, the correct physical region that satisfies positive phase component concentrations can be selected.

For conditions near phase boundaries, it is possible to encounter the region containing positive concentrations outside the physical phase fraction domain, depending on the accuracy of the initial K-factors. For these cases, but also if negative flashes have to be included (cf. Section 2.3.4), the regions enclosed by the singularity hyperplanes must be identified. An enclosed region in the $P - 1$ hyperspace is spanned by at least P crossings of $P - 1$ hyperplanes. All crossings can be identified by solving a set of $P - 1$ linear equations, defined by Eq. (2.71), for all unique combinations of $P - 1$ hyperplanes:

$$\begin{bmatrix} 1 \\ \vdots \\ 1 \end{bmatrix} + \begin{bmatrix} (K_{1,1} - 1) & \dots & (K_{P-1,1} - 1) \\ \vdots & \ddots & \vdots \\ (K_{1,P-1} - 1) & \dots & (K_{P-1,P-1} - 1) \end{bmatrix} \begin{bmatrix} \alpha_1 \\ \vdots \\ \alpha_{P-1} \end{bmatrix} = \begin{bmatrix} 0 \\ \vdots \\ 0 \end{bmatrix}. \quad (2.74)$$

Every dimension in the $P - 1$ hyperspace can be fragmented according to the positions of the crossings in that dimension, as shown in Fig. 2.7 for a 4-component mixture in the three phase region. The fractionating process defines hypercubes. The arbitrary points, in which Eq. (2.73) is evaluated, are chosen as the phase fraction average of each hypercube, depicted by the stars in Fig. 2.7.

Each region enclosed by hyperplanes contains at least one arbitrary evaluation point. The advantage of this method is that no enclosed regions can be skipped, no matter how many components and phases are present in the mixture and a phase fraction solution domain is always found.

2.5.2 Successive substitution for multi-fluid–multi-solid equilibria

The set of equations describing the phase equilibrium of a multi-fluid–multi-solid multi-component mixture is summarized by Eqs. (2.75)–(2.84). The set contains $2P + (3P - N^* - 1)N$ equations and $2(P + 1) + (3P - N^*)N$ variables. Prescribing $N+2$ variables (i.e. z , p and T) makes the system of equations defined and multistable for any arbitrary number of phases P , N^* and components N .

$$v_j = f_{unc}(p, T, \mathbf{y}_j) \quad j = 1, 2, \dots, P - N^*, \quad i = 1, 2, \dots, N, \quad (2.75)$$

$$\phi_{i,j} = f_{unc}(p, T, v_j, \mathbf{y}_j), \quad (2.76)$$

$$f_{i^*,j^*}^S = f_{unc}(p, T) \quad j^* = i^* = 1^*, 2^*, \dots, N^*, \quad (2.77)$$

$$y_{i,k-1} \phi_{i,k-1} = y_{i,k} \phi_{i,k} \quad k = 2, 3, \dots, P - N^*, \quad (2.78)$$

$$y_{i^*,1} \phi_{i^*,1}^S = f_{i^*,j^*}^S, \quad (2.79)$$

$$y_{i,ref} = \frac{z_i}{\left(1 + \sum_{m=1}^{P-1} \alpha_m (K_{i,m} - 1)\right)}, \quad (2.80)$$

$$y_{i^*,j^*} = 1, \quad y_{i,j^*} = 0, \quad (2.81)$$

$$\sum_{i=1}^N y_{i,j'} = 1 \quad j' = 1, 2, \dots, P - N^* - 1, \quad (2.82)$$

$$\sum_{m=1}^P \alpha_m = 1, \quad (2.83)$$

$$K_{i,j} = \frac{y_{i,j}}{y_{i,ref}}. \quad (2.84)$$

The system of equations (2.75)–(2.84) shows great similarity with the system of equations in two-phase fluid-fluid equilibria, cf. Eqs. (2.27)–(2.35). It is this similarity and the ability of extending the Rachford-Rice equations to multi-component-multi-phase mixtures that enables the expansion of the successive substitution method to mixtures with more than two components and multiple fluid or pure solid phases.

The iteration starts with a correct initial guess for the K-factors $K_{i,j}$ and the molar phase fractions α_j to start the Newton procedure for calculation of the phase fractions. The Newton procedure is followed by a calculation of the compressibility factors, fugacity coefficients and the component fugacities in each fluid phase. Just as in the fluid-fluid iteration, each K-factor is updated with the ratio of the reference to actual phase component fugacity:

$$K_{i,j}^{(new)} = K_{i,j}^{(old)} \left(\frac{f_{i,ref}}{f_{i,j}} \right)^q \quad i = 1, 2, \dots, N, \quad j = 1, 2, \dots, P - 1, \quad (2.85)$$

where the acceleration parameter q is, as explained in section 2.3.4, set to unity.

The presence of pure solid phases in the equilibrium requires modified initial values for the K-factors and a definition of the not-solid component fugacities in the solid phase:

$$K_{i \neq i^*, j^*} = 0 \quad , \quad f_{i \neq i^*, j^*}^S = f_{i \neq i^*, ref} \quad , \quad (2.86)$$

where $f_{i \neq i^*, ref}$ is the fugacity of the not-solid-components in the reference phase, chosen for the definition of the K-factors (cf. Eq. (2.68)). The constraints as given in Eq. (2.86) allow for the updating of only the solid phase solid component K-factor while the not-solid component K-factors of the solid phase remain zero. The assumption of Eq. (2.86) also prevents infinite values for the $P-1$ convergence criteria, described by Eq. (2.87):

$$\sum_{i=1}^N \left(\frac{f_{i, ref}}{f_{i, j}} - 1 \right)^2 \leq 10^{-14} \quad j = 1, 2, \dots, P-1 \quad . \quad (2.87)$$

The set of equations, assumptions, convergence criteria and constraints as discussed in this section, are all included in a successive substitution algorithm, which is schematically shown in figure 2.8.

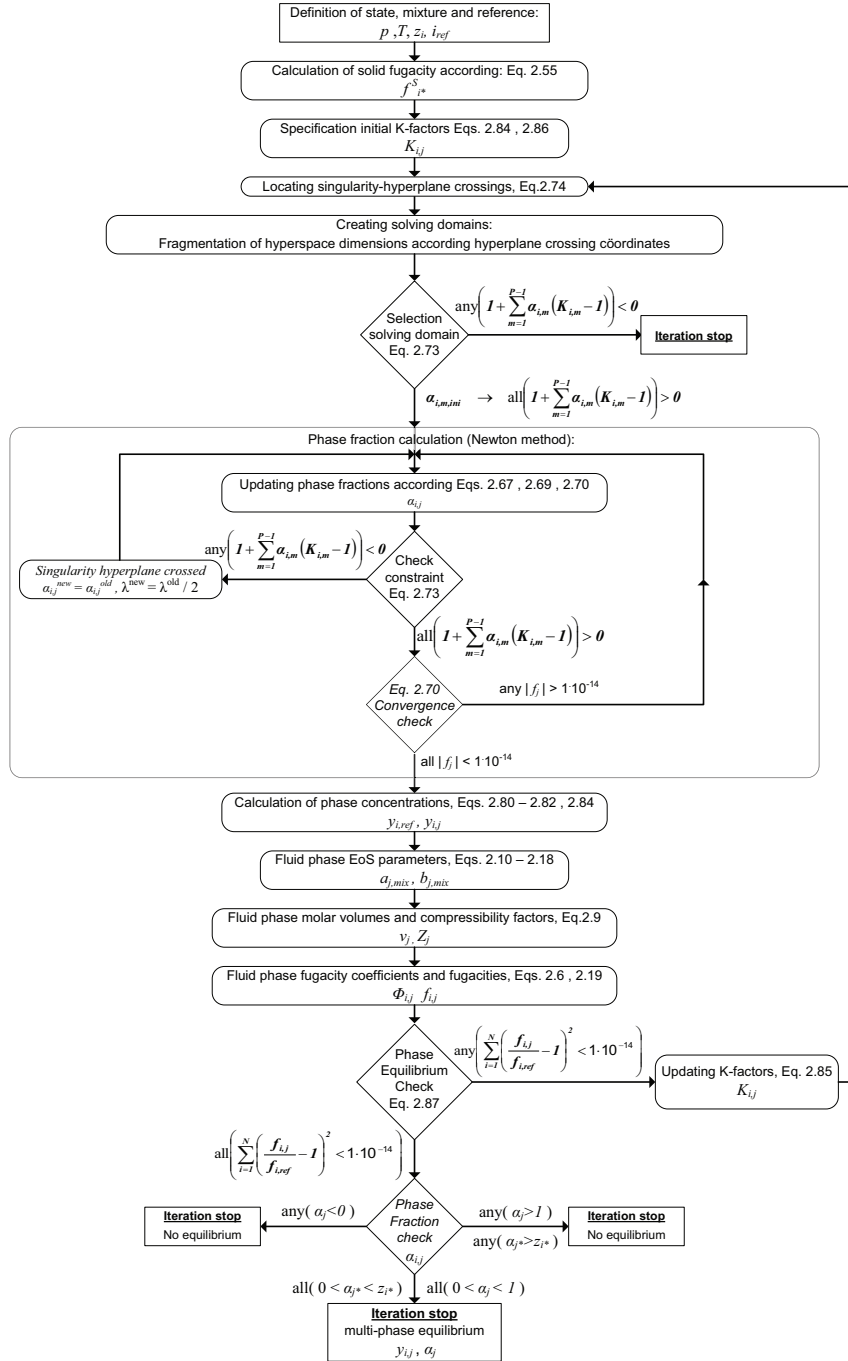


Figure 2.8: Iteration scheme of the Successive Substitution Method for solving the vapor-liquid-solid equilibrium problem.

2.6 Phase Stability

Determination of a phase equilibrium according to the models described in the previous sections, is nothing more than a minimization of mixture Gibbs energy (i.e. solving the describing equations results in conditions for which holds $dG = 0$). Mathematically, different 'physically possible'[‡] phase equilibria might be identified; for example vapor-solid equilibrium and vapor-liquid equilibrium near conditions where in reality a pure solid phase is formed. Each equilibrium corresponds to a local minimum in mixture Gibbs energy. Only one of the mathematically identified equilibria corresponds to the global minimum in Gibbs energy. This equilibrium is denoted as the stable phase equilibrium. Other equilibria for the same conditions (p, T, \mathbf{z}) are denoted as meta-stable or unstable.

Calculation of the mixture Gibbs excess energy for all physically possible phase equilibria allows for selection of the stable equilibrium, but only if all physically possible equilibria (stable, meta-stable and unstable) are identified. In multi-component mixtures, the determination of all (stable, meta-stable and unstable) equilibria requires a tremendous computational effort. The application of stability theory reduces the computational effort and assures identification of stable phase equilibria.

2.6.1 Excess Gibbs energy of a multi-phase mixture

The excess Gibbs energy of a one-phase fluid mixture can be derived from the relation between chemical potential and fugacity (cf. Eq. (2.6)) and is given as:

$$g^E = \sum_{i=1}^N y_i (g_i - g_i^0) = \sum_{i=1}^N y_i RT \ln \left(\phi_i \frac{y_i p}{y_i p^0} \right), \quad (2.88)$$

where g_i refers to the partial molar Gibbs free energy, superscript ⁰ refers to the ideal gas reference state (p_0, T) and superscript ^E refers to the excess property.

The use of Eq. (2.88) for the evaluation of multiple multi-phase mixtures is not possible, as each phase would have its own reference state composition, equal to the actual phase composition \mathbf{y} . Instead of the actual phase composition \mathbf{y} , the overall composition \mathbf{z} can be used as a reference composition, which leads to a reference state equal for all phase compositions and any phase equilibrium solution at conditions (p, T, \mathbf{z}). Using the phase fractions α_j , the multi-phase mixture excess Gibbs energy can subsequently be expressed as:

$$g^E = \sum_{j=1}^P \alpha_j \sum_{i=1}^N y_{i,j} RT \ln \left(\phi_{i,j} \frac{y_{i,j} p}{z_i p^0} \right), \quad (2.89)$$

[‡]Phase equilibrium for which: $0 \leq y_{i,j} \leq 1$ and $0 \leq \alpha_j \leq 1$ for all i and all j .

2.6.2 Tangent plane stability calculations

To locate the stable phase compositions that correspond to the global minimum of Gibbs energy, the rigorous stability analysis of Michelsen [84] is followed. Thereby a Gibbs energy function is defined:

$$G_{\Delta}(\mathbf{y}) = \sum_{i=1}^N y_i (\mu_i(\mathbf{y}) - \mu_i^0) \quad , \quad \mu_i^0 = \mu_i(\mathbf{z}) \quad . \quad (2.90)$$

The Gibbs energy function, Eq. (2.90), describes the difference in molar Gibbs energy at a certain state (p, T) between a tangent hyperplane through a tested phase composition \mathbf{z} and the Gibbs energy surface at an arbitrary composition \mathbf{y} , as shown in Fig. 2.9. In multi-phase equilibrium, evaluation of only one of the phases is sufficient to test for stability, as component chemical potentials of each phase are equal (Eq. (2.3)).



Figure 2.9: The Gibbs energy surface of mixing at 190 K and 40 bar for a binary mixture of H_2S and CH_4 and the tangent hyperplanes of the unstable single-phase and stable two-phase equilibrium.

A phase is called stable if there are no intersections between the Gibbs energy surface and the tangent hyperplane through composition \mathbf{z} , holding that $G_{\Delta}(\mathbf{y}) \geq 0$ for all y_i : $0 \leq y_i \leq 1$. If a tested phase \mathbf{z} is unstable however ($G_{\Delta}(\mathbf{y}) < 0$), there exists a composition \mathbf{y} with a lower molar Gibbs energy that decreases the overall mixture Gibbs energy through the existence of an additional phase. Stability therefore requires all minima of Eq. (2.90), or so-called stationarity points, \mathbf{y}^{SP} to be positive.

The stationarity points, \mathbf{y}^{SP} – see Fig. 2.9 – are found by differentiating Eq. (2.90) towards the $N - 1$ independent phase concentrations y_i :

$$\frac{\partial G_{\Delta}(\mathbf{y}^{SP})}{\partial y_i} = 0 \rightarrow (\mu_i(\mathbf{y}^{SP}) - \mu_i^0) = (\mu_N(\mathbf{y}^{SP}) - \mu_N^0) = k^{SP}. \quad (2.91)$$

If Eq. (2.90) is rewritten in component concentrations and fugacity coefficients, the Gibbs energy function in a stationarity point becomes:

$$G_{\Delta}(\mathbf{y}^{SP}) = RT \sum_{i=1}^N y_i^{SP} (k^{SP}) \quad \text{with} \quad k^{SP} = \ln \frac{y_i^{SP} \phi_i(\mathbf{y}^{SP})}{z_i \phi_i(\mathbf{z})}. \quad (2.92)$$

The stationarity point concentration \mathbf{y}^{SP} in the k^{SP} expression can be transformed by $Y_i = y_i e^{-k^{SP}}$ to result into:

$$\ln \frac{Y_i \phi_i(\mathbf{y})}{z_i \phi_i(\mathbf{z})} = 0. \quad (2.93)$$

The concentrations y_i can simply be derived by normalizing $\sum Y_i$ to unity. Eq. (2.93) is used in a successive substitution scheme to find a local stationarity condition. The iteration steps are:

1. Calculate $\phi_i(\mathbf{z})$.
2. Initial guess for $y_i^{(1)}$. Take $Y_i^{(1)} = y_i^{(1)}$.
3. Calculate $\phi_i(\mathbf{y}^{(t)})$.
4. Check $\left| \ln \frac{Y_i^{(t)} \phi_i(\mathbf{y}^{(t)})}{z_i \phi_i(\mathbf{z})} \right| \leq 10^{-14}$.
5. If 4. not satisfied, set $\ln \frac{Y_i^{(t+1)} \phi_i(\mathbf{y}^{(t)})}{z_i \phi_i(\mathbf{z})} = 0 \rightarrow Y_i^{(t+1)} = \frac{z_i \phi_i(\mathbf{z})}{\phi_i(\mathbf{y}^{(t)})}$.
6. Derive new phase fractions: $y_i^{(t+1)} = \frac{Y_i^{(t+1)}}{\sum Y_i^{(t+1)}}$ and go back to 3.

Some care must be taken in the calculation of the stationarity conditions, as for some concentrations y_i both a liquid and vapor root for molar volume (and compressibility factor) may be found from the EoS (cf. Section 2.3.1). The choice of the correct root in the fugacity coefficient calculation is then determined by the difference in Gibbs energy using the criterion:

$$\sum_{i=1}^N \ln \frac{\phi_i^V}{\phi_i^L} > 0 \rightarrow \text{liquid} \quad \sum_{i=1}^N \ln \frac{\phi_i^V}{\phi_i^L} < 0 \rightarrow \text{vapor}. \quad (2.94)$$

To find all minima of the Gibbs energy function (2.90), the stationarity conditions have to be solved for different initial values $\mathbf{y}^{(1)}$. To assure the identification of all stationarity conditions, the following initial values are used:

- the limits of concentration domain $y_k = 1, y_{l \neq k} = 0$ for each component k ,
- the equivalent concentration condition $y_k = \frac{1}{N}$ for each component k ,
- the tested phase concentration with a small disturbance in both directions for each component k : $y_k = z_k + 0.1(1 - z_k)$ or $y_k = 0.9z_k$, and $y_{l \neq k} = \frac{z_{l \neq k}}{\sum z_{l \neq k}}(1 - y_k)$.

For solid phases, the composition is per definition pure and the Gibbs energy function exists only in one point $y_{i^*} = 1$. The stationarity point of a pure solid phase can therefore be calculated directly as:

$$G_{\Delta}(y_{i^*}) = (\mu_{i^*}^S(y_{i^*}) - \mu_i^0) = \frac{\phi_{i^*}^S}{z_{i^*} \phi_{i^*}(\mathbf{z})}, \quad \text{with } y_{i^*} = 1. \quad (2.95)$$

If all stationarity conditions, Eqs. (2.92) and (2.95), have positive values for the Gibbs energy function, the tested phase equilibrium solution is stable.

2.6.3 The stable phase equilibrium calculation sequence

The capability of a stability analysis as described above is not only limited to the verification of phase stability. Stability analysis provides the locations of stationarity points \mathbf{y}^{SP} which can be used in case of instability to initiate a new phase equilibrium calculation. Interaction between phase stability and equilibrium calculations therefore turns into a recipe that is capable of calculating stable phase solutions without knowing anything about the number of phases, the phase identities or the individual phase compositions. This recipe is discussed next:

A combined equilibrium and stability calculation sequence always starts from a single-phase with composition \mathbf{z} . After determination of the phase identity according to Eq. (2.94), the single-phase stability is checked as described in section 2.6.2. If unstable, new phase compositions are to be selected from the stationarity points. Of interest are the stationarity points with neutral and negative values. Neutral values ($G_{\Delta}(\mathbf{y}^{SP}) = 0$) correspond to phases present in the tested phase equilibrium solution (cf. Eq. (2.90) with $\mathbf{y} = \mathbf{z}$). The location \mathbf{y}^{SP} of a negative stationarity point can be interpreted as a phase composition that may decrease the overall mixture Gibbs energy, compared to the tested phase equilibrium solution.

The stationarity point with the lowest energy (according to Eq. (2.90)) is often present in the stable phase equilibrium solution and therefore initially always selected. Other stationarity points are selected from a Gibbs excess energy analysis, applied to the results of singlestep-iteration equilibrium calculations, performed on all possible unique combinations of the lowest energy stationarity point with a number of residual stationarity points. In rare occasions when three or more component mixtures are involved, it is found necessary to also involve all possible unique combinations of the lowest but one energy stationarity point with a number of residual stationarity points. The minimum number of stationarity points in a combination is restricted to two. The maximum number of stationarity points is imposed by the Gibbs phase rule (cf. Eq. (2.4)) and is restricted to the number of components.

A singlestep-iteration equilibrium calculation for a combination of stationarity points starts with a definition of K-factors as described in section 2.5.1. With use of the corresponding fugacities that result from stability analysis, K-factors are updated by a decelerated successive substitution step, Eq. (2.85), with an acceleration constant $q = 10^{-4}$. Deceleration is required here because stationarity conditions are often close to the stable equilibrium phase concentrations [84]. Therefore K-factors may not be drastically affected. The updated K-factors are used to identify the positive concentration region according to Eq. (2.73), as described in Section 2.5.1. Combinations of stationarity conditions that do not satisfy the positive concentration constraint at all, are discarded from the analysis. Otherwise, a phase fraction calculation is performed and phase fractions, new concentrations, and new fugacities are calculated as described in section 2.5.2.

Unphysical phase fractions, obtained from the singlestep-iteration equilibrium calculations, are not directly discarded from the analysis, as they might converge to small but positive values in the actual equilibrium calculation that follows. Only combinations with the absolute value of the most negative phase fraction greater than the smallest occurring positive phase fraction, are discarded from further analysis. The new fugacities from the remaining combinations are used to determine the excess Gibbs energy, Eq. (2.89), of each combination.

The combination returned from the analysis with the lowest excess Gibbs energy is selected to be solved in an actual phase equilibrium calculation as described in one of the previous sections. If an equilibrium calculation cannot provide a solution or if the solution is outside its physical range, the combination with lowest but one Gibbs energy is selected instead to be solved for equilibrium.

One of the fluid phases resulting from the performed phase equilibrium calculation is to be tested for stability in a new sequence. If stability cannot be verified, the new sequence is continued by definition of new unique combinations from the new stationarity points, followed by new singlestep-iterations, phase selection and a phase equilibrium calculation.

This sequence is repeated until a stable solution is found. Calculations on ternary mixtures of $\text{CO}_2/\text{H}_2\text{S}/\text{CH}_4$ and $\text{CO}_2/\text{N}_2/\text{O}_2$ have shown that it takes usually 2 to 3 sequences, and in rare occasions up to 8 sequences, to find the stable solution with specification of only pressure, temperature and a mixture overall composition.

2.7 Model Verification

To verify correct model predictions, the model results are compared to measured concentrations, temperatures and pressures reported in literature. Phase component concentrations are compared for given conditions (p, T, \mathbf{z}) . Comparison of CO_2 freeze-out is performed for both a prescribed pressure and a prescribed temperature. Selected concentration results are shown in the y_i - p plane, in the solids regime supplemented with a visualization of selected freeze-out lines in the p - T plane.

The model accuracy is presented by the Absolute Average Deviation (AAD) and the Absolute Model Accuracy (AMA), which are defined as:

$$\text{AAD} = \frac{1}{n_{exp}} \sum_{m=1}^{n_{exp}} \left| \frac{y_{m,calc} - y_{m,exp}}{y_{m,exp}} \right| \times 100\%, \quad (2.96)$$

$$\text{AMA} = \frac{1}{n_{exp}} \sum_{m=1}^{n_{exp}} |y_{m,calc} - y_{m,exp}|, \quad (2.97)$$

where n_{exp} is the number of experiments, y a phase component concentration (replaced by p or T in freeze-out comparison), $calc$ corresponds to model calculation for experimental conditions and exp refers to experimental values. Absolute Average Deviations concerning concentrations are calculated per component and shown in the following tables as the root mean square over all the components.

As developments of the CRS process are currently undergoing in natural gas cleanup and flue gas CO₂ capture, the model is compared to literature values of the binary mixtures of CH₄/CO₂ and N₂/CO₂ in respectively § 2.7.1 and § 2.7.2 and the ternary mixture of CO₂/CH₄/H₂S in § 2.7.3.

2.7.1 The CO₂/CH₄ System

The CO₂-CH₄ system is well documented in literature. Good overviews of documented experimental phase equilibria results and their measurement range are given by Swanenberg [125] and Carroll [27]. Results of phase equilibria measurements are available in both the vapor-liquid and fluid-solid region. For comparison in the vapor-liquid regime, the measurements performed by Donnelly and Katz [46], Mraw [87], Neumann and Walch, [92], Davelos [42] and Willems [139] were selected. The accuracy of the model predictions is given in Tab. 2.2. In Fig. 2.10, predicted saturation lines are shown together with experimental vapor and liquid phase data from Davelos and Mraw. Good agreement is found between predicted and experimental results.

Table 2.2: Data sets used for the verification of model predictions of the binary mixture CO₂-CH₄ in the vapor-liquid phase and the accuracy of the model.

reference	year	range	AAD (%)		AMA (% _{mole})	
			vapor	liquid	vapor	liquid
Donnelly & Katz [46]	1954	-1.7 – -73.3 °C 11.1 – 79 bar	4.35	7.36	1.13	2.37
Neumann & Walch [92]	1968	-53.3 – -99.8 °C 6.0 – 66.5 bar	44.02	55.98	0.39	1.53
Davelos et al. [42]	1976	-3.15 – -43.15 °C 8.9 – 85.2 bar	2.50	3.48	1.04	0.71
Mraw et al. [87]	1978	-53.9 – -100 °C 5.8 – 64.5 bar	4.00	7.78	0.74	1.14
Willems [139]	2009	-17.3 – -57 °C 24.7 – 32.6 bar	6.42	12.17	2.71	1.62

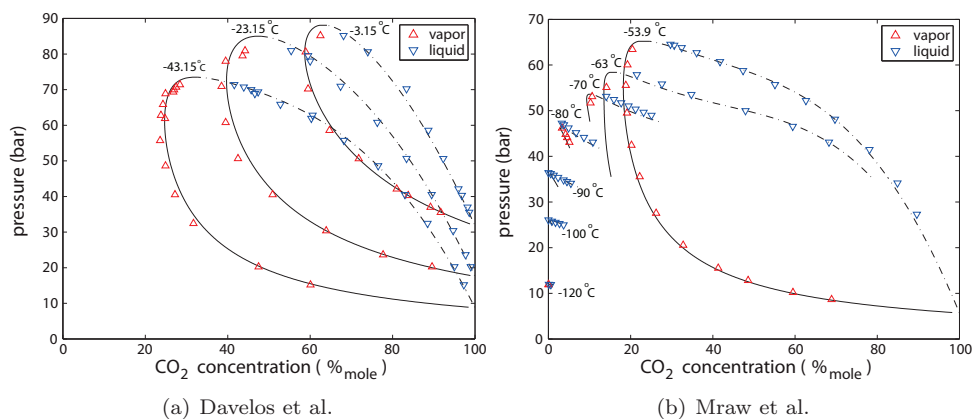


Figure 2.10: Experimental data in the vapor-liquid phase region and model predictions for the CO_2/CH_4 system. The solid and dash-dotted lines represent the saturation lines of the vapor and liquid phase.

The solid-fluid regime is unfortunately not equally well documented. Only four publications were found in literature that contain concentration measurements of the $\text{CO}_2\text{-CH}_4$ mixture in the fluid–solid region of which only two data sets were accessible. These two sets, the sets of Donnelly and Katz [46] and Davis et al. [43], were used for comparison of concentrations in the fluid-solid regime. For the comparison of the freeze-out prediction, see Tab. 2.3, the sets of Donnelly and Katz [46] and Davis et al. [43] are supplemented with the recent data of Le and Trebble [74] and Zhang et al. [147] who measured sublimation lines between the vapor-only and solid-vapor region for different compositions in the lower end of CO_2 concentration.

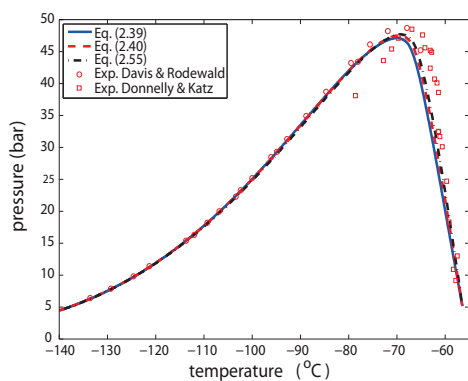


Figure 2.11: The VLS-locus of the $\text{CH}_4\text{-CO}_2$ system and data from Davis et al. and Donnelly & Katz.

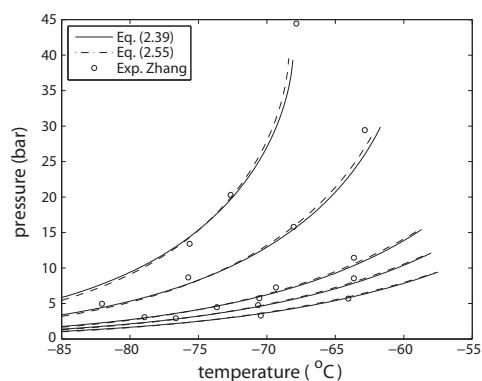


Figure 2.12: Sublimation lines for the $\text{CH}_4\text{-CO}_2$ system with overall compositions z_{CO_2} 10.8, 17.8, 33.4, 42.4 and 54.2 %mole.

The accuracy of concentration and CO₂ freeze-out predictions for the accessed data sets is shown in Tabs. 2.3 and 2.4. Figs. 2.11 and 2.12 show the predicted VLS-locus against data of Donnelly & Katz and Davis et al., and the sublimation lines against experimental data of Zhang et al. Fig. 2.11 contains predictions of the VLS-locus with use of Eqs. (2.39), (2.40) and (2.55). In the prediction of sublimation lines and concentrations in the fluid-solid phase, both Eq. (2.39) and (2.55) were compared.

Table 2.3: Data sets used for verification of predictions of the binary mixture CO₂-CH₄ in the fluid-solid phase and the accuracy of the model for concentration predictions.

reference	year	range	AAD (%)		AMA	
			conc.		conc. (% <i>mole</i>)	
			(2.39)	(2.55)	(2.39)	(2.55)
Donnelly & Katz [46]	1954	-57.8 – -78.6 °C 9.2 – 48.5 bar	24.45(LS)	16.36(LS)	8.58(LS)	5.38(LS)
Davis et al. [43]	1968	-61.4 – -175.6 °C 0.28 – 48.7 bar	14.34(vs) 9.20(LS)	11.74(vs) 17.92(LS)	0.23(vs) 0.34(LS)	0.17(vs) 0.44(LS)
Le & Trebble [74]	2007	-85.4 – -104.6 °C 0.28 – 48.7 bar	-	-	-	-
Zhang et al. [147]	2011	-62.8 – -82.1 °C 2.9 – 44.5 bar	-	-	-	-

The introduction of real gas effects and pressure effects in the pure solid fugacity expression, Eq. (2.55), contributes to a small improvement in the prediction of the VLS-locus and fluid phase concentrations, compared to Eq. 2.39. In the prediction of sublimation lines however, see Fig. 2.12, the use of both expressions becomes comparable as expected since the pressure correction is negligible and the saturated gas phase is close to ideal gas behavior at low pressure (cf. sections 2.3 and 2.4.1).

Table 2.4: Verification and accuracy of freeze-out predictions in the binary mixture CO₂-CH₄, using both Eq. (2.39) and Eq. (2.55).

reference	AAD (%)				AMA			
	P		T		P (bar)		T (°C)	
	(2.39)	(2.55)	(2.39)	(2.55)	(2.39)	(2.55)	(2.39)	(2.55)
Donnelly & Katz [46]	18.62	14.98	4.14	3.32	13.8	10.2	6.3	5.9
Davis et al. [43]	2.38	1.88	0.48	0.47	0.65	0.46	0.41	0.42
Le & Trebble [74]	24.69	20.37	2.01	2.23	3.91	2.87	1.91	2.14
Zhang et al. [147]	6.37	6.44	1.02	1.05	0.56	0.66	0.73	0.74

2.7.2 The CO₂/N₂ System

The vapor-liquid region of the N₂/CO₂ system is at least as extensively documented as the CH₄/CO₂ system. Experimental data in the fluid-solid region is however very scarce. Thorough overviews of published experimental results in the vapor-liquid phase can be found by Yucelen and Kidnay [143] and Weber et al. [135]. For comparison of the whole vapor-liquid range from 0 to -55 °C, the experimental data

Table 2.5: Data sets used for the verification of model predictions of the binary mixture CO₂-N₂ in the vapor-liquid phase and the accuracy of the model.

reference	year	range	AAD (%)		AMA (% _{mole})	
			vapor	liquid	vapor	liquid
Zenner & Dana [146]	1963	0 – -55 °C 12.7 – 138.9 bar	3.06	6.02	1.20	0.98
Weber et al. [135]	1984	0 – -50 °C 50 – 100 bar	1.43	2.22	0.59	0.21
Brown et al. [23]	1989	-3.15 – -53.15 °C 10.1 – 129.6 bar	1.25	3.49	0.52	0.31
Niesen et al.[24]	1989	-3.15 – -23.15 °C 26 – 140.7 bar	1.95	3.15	0.93	0.71
Yucelen & Kidnay [143]	1999	-3.15 – -33.15 °C 16.9 – 130 bar	1.98	6.33	0.86	0.55

from Zenner and Dana [146], Brown et al. [23], Yucelen and Kidnay [143], Niesen et al. [24] and Weber et al. [135] were selected. The results for model accuracy and experimental range are given in Tab. 2.5. With exception of the data of Weber et al. (because of graphical reasons), the data sets and model results are shown in Fig. 2.13.

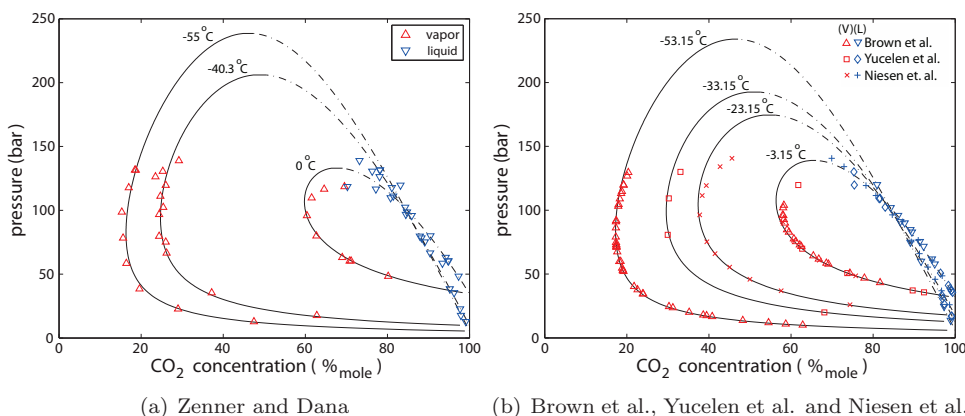


Figure 2.13: Experimental data in the vapor-liquid phase region and model predictions for the CO₂/N₂ system. The solid and dash-dotted lines represent the saturation lines of the vapor and liquid phase.

Typical is the better accuracy of concentration predictions in the sub-critical range ($p/p_{c,mix} < 0.6$), compared to the CH₄/CO₂ system, with predictions of vapor and liquid composition up to 1 and 0.5%_{mole} accuracy respectively. For conditions at elevated pressure ($p/p_{c,mix} > 0.6$) and near the mixture critical point, predictions start to deviate from the experimental results, as can be seen from Fig. 2.13 and is a well known phenomenon in Peng-Robinson EoS based phase calculations of the CO₂-N₂ system [131]. For ($p/p_{c,mix} > 0.6$) the model accuracy is found to decrease to about 5–10%_{mole} for both vapor and liquid composition.

Only one experimental study on the $\text{CO}_2\text{-N}_2$ system in the fluid-solid regime is available that focusses on the region close to the CO_2 freeze-out line [121]. Sonntag evaluated different vapor concentration isotherms from -83 to -113°C . The experimental data and model predictions are shown Fig. 2.14. The experimental range and accuracy of predictions with use of both Eq. (2.39) and (2.55) is reported in Tab. 2.6. Just as in the CH_4/CO_2 system, concentration predictions are more accurate by application of the improved solid fugacity expression (Eq. (2.55)). Again, the accuracy of predictions decreases with increasing pressure and increases for decreasing temperature.

Table 2.6: Data set used for the verification of model predictions of the binary mixture $\text{CO}_2\text{-N}_2$ in the vapor-solid regime and the accuracy of the model.

reference	year	range	AAD (%)		AMA	
			conc. (2.39)	conc. (2.55)	conc. (2.39)	conc. (2.55)
Sonntag [121]	1960	$-83.15 - -113.15^\circ\text{C}$ $5.0 - 101.3 \text{ bar}$	7.83(vs)	3.53(vs)	0.12(vs)	0.07(vs)

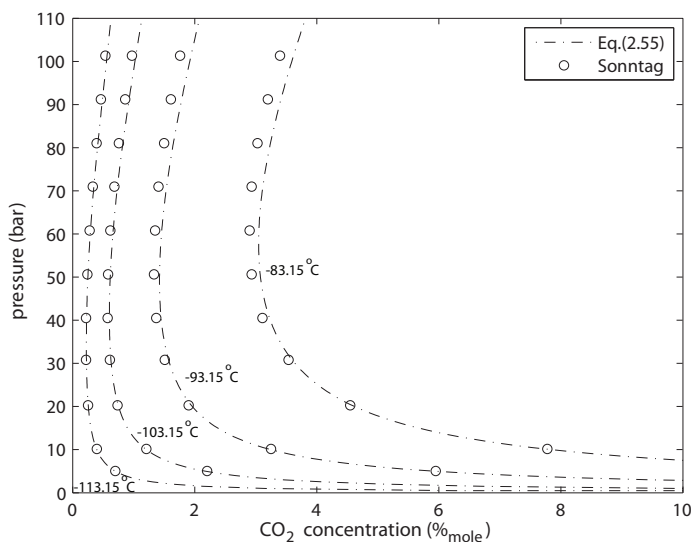


Figure 2.14: Comparison of different experimental isotherms in the vapor-solid regime of $\text{CO}_2\text{-N}_2$.

2.7.3 The $\text{CO}_2/\text{CH}_4/\text{H}_2\text{S}$ System

The ternary mixture of $\text{CO}_2/\text{CH}_4/\text{H}_2\text{S}$ is chosen for comparison as it reflects the main components in heavily contaminated sour natural gas fields. Three published experimental studies exist that deal with phase equilibria of this ternary mixture. An overview can be found in Carroll [27]. Only the data obtained by Ng et al. [93]

Table 2.7: Data set used for the verification of model predictions of the ternary mixture CO₂-CH₄-H₂S. Pressure and temperature are compared for the two- and three-phase fluid boundaries. Concentrations are only compared in the vapor-liquid phase.

reference	year	range	AAD (%)			
			conc.		P	T
			vapor	liquid		
Ng et al. [93]	1985	29.7 – -82.8 °C 15 – 125.5 bar	2.15	6.36	12.70(VL/LL) 3.99(VLL)	30.97(VL/LL) 2.85(VLL)
			(%mole)		(bar)	(°C)
			0.51	1.00	12.4(VL/LL) 2.2(VLL)	4.3(VL/LL) 1.9(VLL)

is usable for model comparison, as also overall composition of the tested mixture is reported.

Tab. 2.7 shows the accuracy of the predictions of bubble and dew pointing lines of the two phase fluid-fluid regime and three phase vapor-liquid-liquid regime, and the concentrations in the vapor-liquid region. The accuracy of the predicted concentrations in the vapor-liquid regime is in line with the binary mixtures. The predicted phase diagram of the studied mixture and the data of Ng et al. is shown in Fig. 2.15.

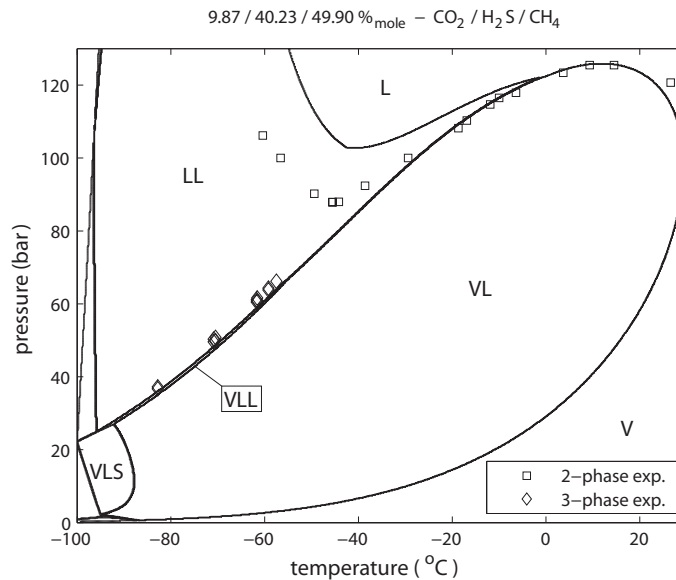


Figure 2.15: Calculated phase diagram of CO₂-CH₄-H₂S compared to experimentally determined bubble and dew point lines of the two and three phase fluid regimes from Ng et al. [93].

The prediction of the liquid side two-phase boundary in the diagram in Fig. 2.15

becomes inaccurate as soon as a second methane rich liquid phase is present (beyond the critical temperature of the three phase VLL region). Prediction of phase component concentrations within the multi-phase regime becomes inaccurate for conditions (p, T) where a vapor phase is absent. Also a mismatch of about two degrees is found in the predicted and experimentally determined location of the VLL region (vapor-liquid-liquid). Comparison between experimental data and model prediction in this region is therefore not possible. The inaccuracy of the model in the regions with two liquid phases can be attributed to two effects.

Firstly, the calculation of fluid fugacity involves the volume or compressibility factor, cf. Eq. (2.19). The Peng-Robinson EoS is known to be less accurate in describing pvT behavior of fluids with dominant presence of polar components such as H_2S . As H_2S is quite dominant in the mixture ($40\%_{mole}$), inaccurate pvT behavior is expected. Prediction of pvT behavior of polar components with the Peng-Robinson EoS might be improved by introduction of temperature dependent binary interaction parameters regressed from experimental data.

Secondly: the Peng-Robinson EoS is known to generally underpredict liquid volumes [131], which influences the calculated liquid fugacities. This may generally play a role in the calculation of equilibria with multiple liquid phases, and can partly be corrected for by the introduction of a liquid volume shift parameter [61].

2.8 Conclusions and Recommendations

In the foregoing sections, we described the tools and algorithms to calculate different kinds of multi-component multi-phase equilibria. We developed numerical models for the determination of two-phase fluid-fluid equilibria, single-fluid–multi-solid equilibria and multi-fluid–multi-solid equilibria, based on the Peng-Robinson equation of state and van-der-Waals mixing rules. By taking into account real gas and pressure effects, an improved fugacity relation for pure solid substances was derived and proven. Stability analysis based on the Gibbs tangent plane criterion was introduced to test phase stability. We managed to establish interaction between phase stability and phase equilibrium calculations to determine stable phase equilibria without any prior knowledge of the number of phases nor of the phase identities present in the stable equilibrium.

Model verification showed that the flash calculation model as described above correctly predicts phase equilibrium for the tested binary mixtures up to an accuracy of $< 2\%_{mole}$. Although qualitatively still correct, prediction of phase equilibria that lack a vapor phase or involve multiple liquid phases is not as accurate ($\mathcal{O}(\geq 10\%_{mole})$). If the model is to be used in such a region, results should first be checked against available experimental data to verify correctness. In case of the tested ternary mixture, reliable results are found in the vapor-liquid region. Care has to be taken in regions that involve only liquid fluid phases. Recommended adjustments to improve prediction in these cases are the correction of liquid volume by application of a liquid

volume shift, and the introduction of temperature depended binary interaction parameters in case of polar components. These regions are however of less interest for the development of Condensed Rotational Separation.

The phase calculation algorithms and stability-equilibrium calculation interaction can be used with any cubic equation of state and any type of mixing rule to possibly improve predictions for mixtures other than the ones of interest for Condensed Rotational Separation.

Preliminary Process Design

The separation and purification achieved by Condensed Rotational Separation relies on partial condensation of a gas mixture to selected pressures and temperatures. Bansal [9] and Willems [139] showed in a small-scale setup operated with binary mixtures of methane and carbon dioxide and nitrogen and carbon dioxide that via expansion cooling, within milliseconds a mixture of vapor and micron sized droplets is obtained, in concentrations according to thermodynamic phase equilibrium. Applications of CRS can therefore be designed and optimized with the use of the phase equilibrium model, discussed in chapter 2.

In this chapter we shall discuss the principles for the locating of optimum CRS separation conditions. We identify the number of separation stages and determine the process layout of the CRS process for applications in natural gas cleanup and flue gas CO₂ capture. We also show how to apply the process of CRS in a narrow vapor-liquid regime and introduce how to use CRS for the separation of multiple components from mixtures.

3.1 Single Stage CRS

The process of Condensed Rotational Separation relies on two principles to achieve selective purification (cf. Section 1.2):

- Fast reduction of temperature and pressure of a gaseous mixture to a temperature and pressure where the contaminant becomes a mist of micron sized droplets.
- Separation of the micron-size droplets from the gas by the unique Rotational Particle Separator (RPS).

A combination of a fast cooling process by heat-exchange and expansion, followed by a Rotating Particle Separator (RPS) is referred to as a 'single CRS stage' and is shown in Fig. 3.1.

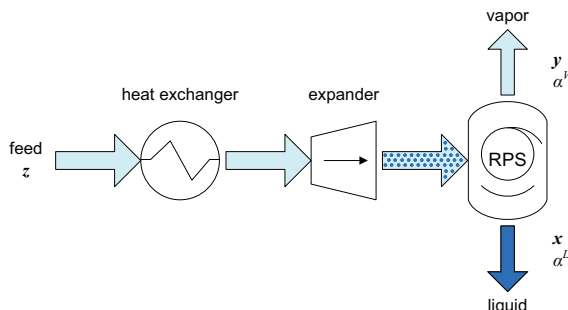


Figure 3.1: Single stage CRS process.

The entering gas with composition z is thereby typically pre-cooled to a saturated vapor condition in a heat exchanger. The resulting saturated gas is expanded over a Joule-Thompson valve or a turbo-expander to reach the preferred separation condition (p, T) . The mist at the separation condition is fed to the RPS, which separates the condensed phase with composition x and molar fraction α^L and the vapor phase with composition y and molar fraction α^V by centrifugal action (cf. Section 1.3).

Drying of the feed gas (water removal) has not been considered so far, but is required for any process that encloses semi-cryogenic and/or high pressure conditions. A high water content under (semi-)cryogenic conditions leads to ice and maybe even hydrate formation, which affects phase behavior and can cause clogging of process components. Because hydrate formation is a slow process (typically minutes to hours) [45, 57, 108] and the gas residence time in the CRS process is small (seconds), hydrate formation is not expected to be an issue in CRS. Apart from condensing, gas drying can be accomplished by conventional technology such as molecular sieves and glycol absorption. In the remainder of this work dry feed gas is assumed unless mentioned otherwise.

3.2 Phase Diagrams

Phase diagrams are effective tools in the design of a phase separation process, as they indicate the boundaries of the different phase regimes by the mixture bubble-point and dew-point lines. Three types of diagrams can be distinguished:

- p - T diagram: Depicts the boundaries of the phase regimes in the dimensions of pressure and temperature for a single overall mixture composition z .
- p - x diagram: Depicts the boundaries of the phase regimes at a single temperature in the dimensions of pressure and mixture composition.
- T - x diagram: Depicts the boundaries of the phase regimes at a single pressure in the dimensions of temperature and mixture composition.

For design and optimization of the CRS process, the p - x diagram is a very powerful tool, especially when applied to binary mixtures. Binary mixtures have the property

to be univariant (can be derived from the Gibbs phase rule, Eq. (2.4)). In practical sense this means that the vapor and liquid phase component concentrations y_i and x_i at two-phase conditions (p, T) are independent from the overall component concentration z_i , for z_i between x_i and y_i (limits of the vapor-liquid two-phase region). This property allows for the use of the lever rule in calculating phase fractions from the diagram [48], and the illustration of process separation paths in a single diagram.

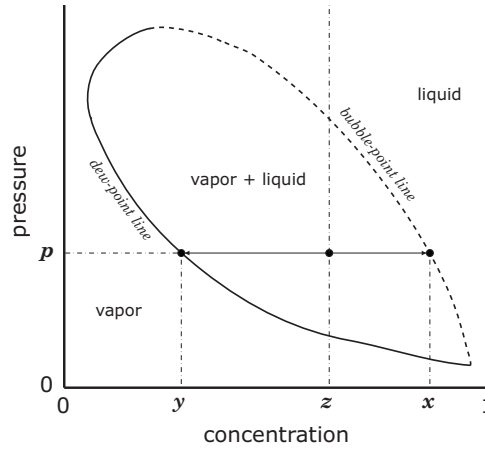


Figure 3.2: p - x phase diagram at constant temperature T .

Fig. 3.2 illustrates a typical p - x phase diagram of a binary mixture at a single temperature T . The vapor and liquid boundaries represent the dew-point and bubble-point line of the mixture. A mixture with a composition z at a condition (p, T) splits into a vapor phase with composition y , indicated by the dew-point line and a liquid with composition x , indicated by the bubble-point line (Fig. 3.2). For a pressure p above the bubble-point pressure or below the dew-point pressure, the mixture is a single-phase liquid or vapor. Similar behavior holds for the T - x diagram of binary mixtures.

3.3 Natural Gas Sweetening

Van Wissen [140] evaluated the separation performance of a single stage CRS process in terms of component recoveries for different separation conditions (p, T) and mixtures (CH_4/CO_2 and $\text{CH}_4/\text{CO}_2/\text{H}_2\text{S}$). The component recovery for the vapor phase is defined as:

$$\mathbb{R}_{i,vap} = \frac{\text{amount of component } i \text{ in vapor phase}}{\text{amount of component } i \text{ in feed}} = \frac{y_i(z_i - x_i)}{z_i(y_i - x_i)}, \quad (3.1)$$

Similarly, the component recovery for the condensed phase is:

$$\mathbb{R}_{i,cond} = \frac{\text{amount of component } i \text{ in condensed phase}}{\text{amount of component } i \text{ in feed}} = \frac{x_i(z_i - y_i)}{z_i(x_i - y_i)}, \quad (3.2)$$

where y_i , x_i and z_i refer respectively to the molar component concentrations in the vapor and condensed phase and in the feed gas (cf. Fig. 3.1). Eqs. (3.1) and (3.2) express the recovery as the fraction of component i that is separated into one of the two phases. The highest recoveries for both vapor methane and liquid carbon dioxide are found in the low-temperature end of the vapor-liquid region, near the freeze-out line of CO₂ [140] (cf. Fig. 3.3 in relation to Eqs. (3.1) and (3.2)).

3.3.1 CO₂ contaminated natural gas

Fig. 3.3 shows the p - T phase diagram of an equimolar mixture of methane and carbon dioxide. The color bars represent the vapor methane concentration (a) and the liquid carbon dioxide concentration (b). Fig. 3.3 shows opposite positions in the vapor-liquid region for high purity liquid CO₂ and high purity vapor CH₄. Separation in a single CRS stage is therefore always a tradeoff between almost pure gaseous methane with a low vapor methane recovery or a high vapor methane recovery and a low purity gas [140].

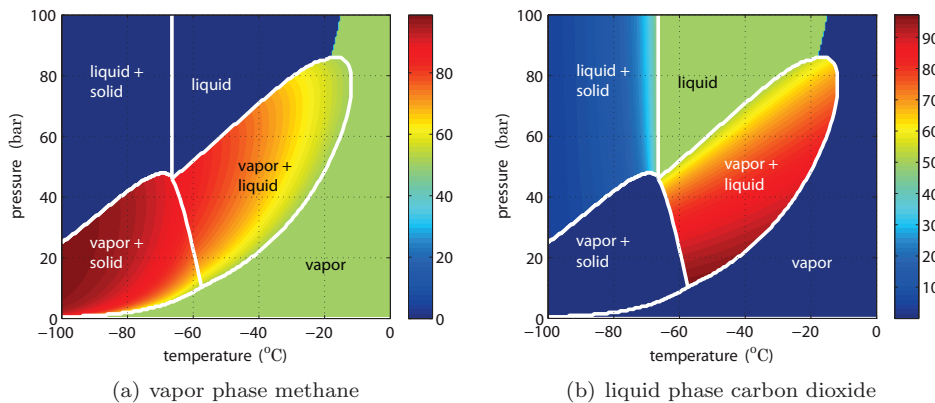


Figure 3.3: Molar concentrations in the two-phase regions of a 50/50%_{vol} CO₂/CH₄ mixture.

Maximum separation of both components requires both high purity gaseous methane and high purity liquid carbon dioxide, which requires at least two stages - one in the upper-left and one in the lower-left corner of the phase diagram shown in Fig. 3.3.

Fig. 3.4 shows the p - x diagram of the binary mixture CH₄/CO₂ for several temperatures. Saturated vapor and liquid concentrations in the two phase region are represented by the solid and dashed-dotted lines, as explained in section 3.2. The dotted lines represent the sublimation and freeze-out line of CO₂. The region enclosed by the vapor and liquid (and solid) boundaries represents the vapor-liquid region. The lowest vapor CO₂ (highest vapor methane) concentrations are found at elevated pressure in the upper left corner of the vapor-liquid region. The highest liquid CO₂ (lowest

liquid methane) concentrations are found at low pressure (lower right corner). A decrease in temperature shows a decrease in CO₂ concentration in both saturated vapor and liquid. For a decreasing temperature in the region $-70^{\circ}\text{C} \leq T \leq -57^{\circ}\text{C}^*$, the CO₂ freeze-out boundary (horizontal dotted line in Fig. 3.4) shifts upward in pressure (see also Fig. 2.11), while the vapor-liquid region shrinks and moves towards low CO₂ concentrations. For a further reduction in temperature, the CO₂ freeze-out line and vapor-liquid region shift down again in pressure, while the vapor-liquid region continues to shrink.

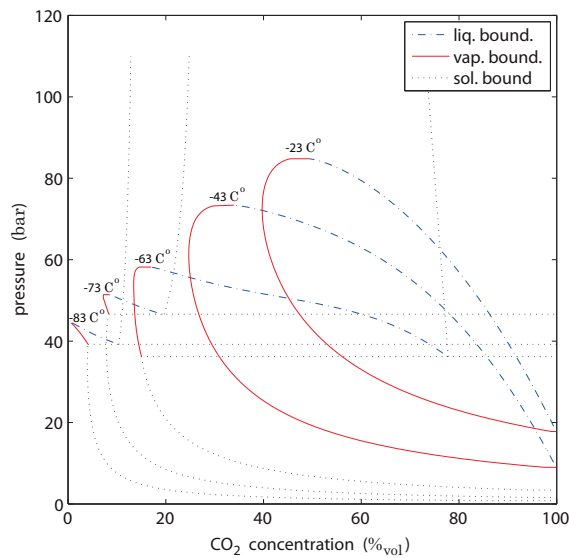


Figure 3.4: P-x diagrams of the methane – carbon dioxide system.

The phase behavior of the binary methane–carbon dioxide system as shown in Fig. 3.4 leads to a two stage CRS process at not only different pressures, but also different temperatures [66]: A lower temperature where high purity vapor methane is separated and a higher temperature where high purity liquid carbon dioxide is separated.

The principle of two stage separation is shown in Fig. 3.5 by means of a process scheme (upper left) and the process separation path. The process separation path is shown simultaneously in the $T-x$ (upper right), $p-x$ (lower left) and $p-T$ (lower right) phase diagram. A mixture of CH₄/CO₂ enters the CRS process and is rapidly chilled by a combination of cooling and expansion to reach the vapor-liquid region (points 'A' in Fig. 3.5). The mixture splits into a liquid 'B', and a vapor 'C'. At this pressure the vapor methane concentration is around its maximum. The saturated liquid, 'B', is however far from pure CO₂. This liquid is flashed by a combination of heating and expansion to a lower pressure (point 'D'), where it splits in high purity liquid CO₂, 'E', and a vapor, 'F', that still contains a considerable amount of methane. Compression and cooling of this saturated vapor 'F' from the second stage to the first

*Triple point of pure CO₂: -56.57°C , 5.18 bar.

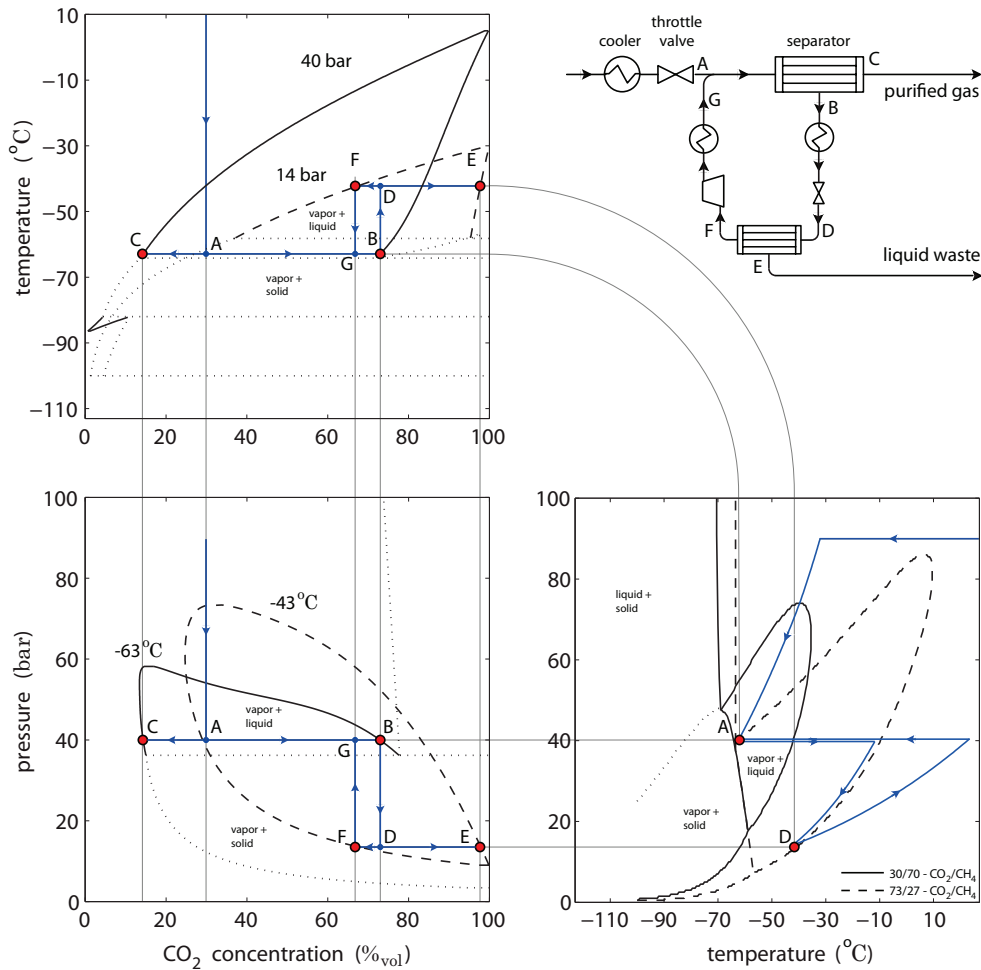


Figure 3.5: Operating principles and design of CRS for CO₂ removal from contaminated natural gas.

stage separation conditions (point 'G') allows for re-feeding of this vapor to the first stage to recover the remaining methane. The result is a two stage looped process that achieves both a maximum purified vapor methane and high purity liquid CO₂.

The temperature and pressure of the first stage 'A-B-C' are determined by the minimum CO₂ concentration that can be reached on the saturated vapor side. The conditions of the second stage are chosen such that the maximum CO₂ concentration on the saturated liquid side is reached. The conditions of both stages are constrained to each other: The second stage pressure must be selected such that the liquid resulting from the first stage, 'B', flashes again into two phases - i.e. 'D' must be in the vapor-liquid region - otherwise there is no phase separation in the second stage.

Practical constraints on the separation conditions are found in the pressure ratio between the two stages and the recycle ratio. The compression ratio should be kept ≤ 4 to overcome the pressure difference in a single compression stage [102, 112]. The recycle ratio is defined as the ratio of re-fed mass flow 'F-G' to process feed mass flow, and is preferably kept small. The recycle ratio becomes high when almost all incoming mixture in the first stage separator is liquefied and almost all mixture entering the second stage separator is gasified, which means that the vertical lines 'B-D' and 'F-G' in Fig. 3.5 approach each other. For the process as shown in Fig. 3.5, the recycle ratio increases from 0.05 at 15%_{vol} CO₂ to 2.2 at 72%_{vol} CO₂ in the feed.

The process shown in Fig. 3.5 can handle contaminated flue gas with levels from 15 up to 72%_{vol} CO₂, given by the saturated liquid and vapor conditions of the first stage 'B' and 'C'. Both stages operate in the optimal regions of the phase diagram, as can be seen from Fig. 3.5 in relation to Figs. 3.3 and 3.4. High purity CO₂ is separated as a liquid at low pressure (14 bar), while high purity methane is separated as a vapor at high pressure (40 bar) close to CO₂ freeze-out. Thereby both the liquid CO₂ recovery as the vapor methane recovery are maximized, giving optimal separation.

The recoveries for both liquid carbon dioxide and vapor methane are shown in Fig. 3.6, and compared against single stage operation. For equal feed mixture composition, the two stage process improves both the vapor methane and the liquid carbon dioxide recovery by a maximum of 90% in the operating range of 15–72%_{vol} CO₂ in the feed.

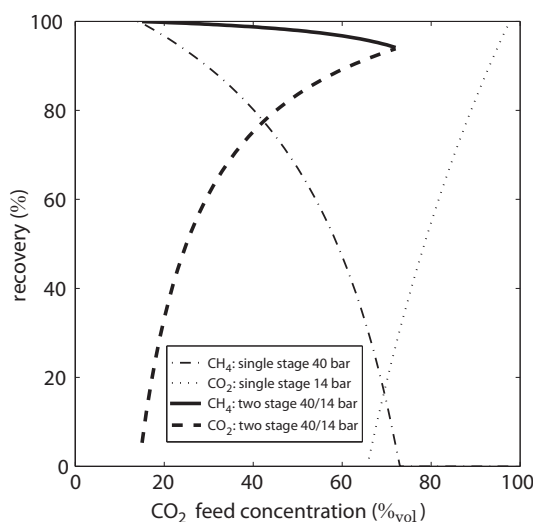


Figure 3.6: Methane and carbon dioxide recoveries for the two stage process of Fig. 3.5, compared against single stage separation for either equal liquid or vapor purity.

The process of CRS as presented here is ideal as a bulk separator for CO₂ removal from heavily CO₂ contaminated natural gas ($\geq 15\%$ _{vol} CO₂). Resulting product gas from CRS containing 15%_{vol} CO₂ can be brought to pipeline specifications, $\mathcal{O}(3\%$ _{vol} CO₂), by traditional methods of CO₂ removal, such as amine absorption [109].

3.3.2 Sour gas

About 40% of the worldwide natural gas reserves is classified as sour, containing both the contaminants carbon dioxide and hydrogen sulfide [26]. Contamination in reported sour gas fields varies from 4 %_{vol} H₂S and 8 %_{vol} CO₂ [2] up to 27 %_{vol} H₂S and 14 %_{vol} CO₂ [21].

The presence of hydrogen sulfide as a third main component in contaminated natural gas has an anti-freeze effect on the freeze-out of CO₂. Fig. 3.7 shows the p - T phase diagram of both a 59/27/14 and a 88/4/8%_{vol}- CH₄/H₂S/CO₂ mixture and the corresponding concentration of methane in the vapor and the liquid phase at -85°C. The presence of hydrogen sulfide shifts the CO₂ freeze-out line by about -20°C compared to a mixture of only CH₄ and CO₂ (i.e. compare the p - T diagrams in Fig. 3.7 and Fig. 3.3). Due to the accompanying extension of the vapor-liquid region towards lower temperatures, very high purities on vapor methane ($\geq 95\%$ _{vol}) and very low purities on liquid methane ($\leq 2\%$ _{vol}) can be achieved in the vapor-liquid region, as indicated via the grey bars in Fig. 3.7.

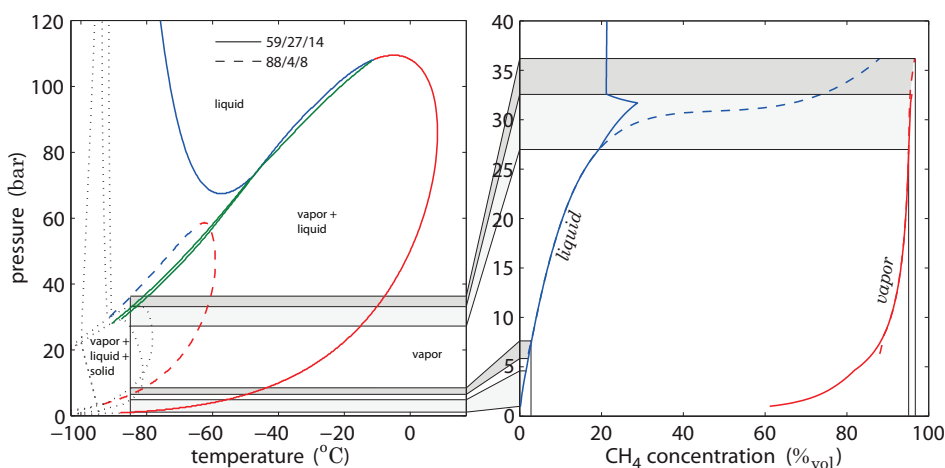


Figure 3.7: Left: The p - T phase diagrams of two ternary mixtures of CH₄/H₂S/CO₂. Right: the methane concentration isotherms at -85°C in the vapor and the liquid phase. The grey bars represent the pressure range at -85°C in which solely vapor and liquid coexist.

If compared to CO₂ contaminated natural gas (section 3.3.1), an improvement in gas sweetening (purification) can be obtained by $\geq 10\%$ _{vol} by the presence of hydrogen sulfide. A two-stage design, as shown in Fig. 3.5, therefore becomes more beneficial if separation conditions are selected close to the freeze-out line of CO₂. In sour gas operation, contaminated gas can be sweetened up to a methane concentration of $\geq 95\%$ _{vol}, thereby reaching a vapor methane recovery of 98-99.9%. Almost all hydrogen-sulfide and a great part of the carbon dioxide is thereby separated into the residual liquid stream [21, 68].

3.4 CO₂ Removal from Combustion Effluent

The application of CRS to CO₂ removal from combustion effluent focusses especially on flue gas from coal-fired power generation. Flue gas resulting from coal-fired power generation generally consists of nitrogen, carbon dioxide, excess oxygen and water and can contain traces of argon, sulphur- and nitrogen-oxides and sometimes heavy metals such as Mercury. For the application of CRS we focus only on the main elements in dry flue gas. Traces of contaminants are primarily neglected because they have only a minor effect on phase separation. The influence of impurities on phase equilibrium and separation performance is studied further on in § 3.4.1. Dry flue gas is essential for any semi-cryogenic CO₂ capture process to prevent freeze-out of water and hydrate formation. In primary design we group nitrogen and oxygen into a nitrogen group, as their volatility is relatively equal compared to the volatility of carbon dioxide.

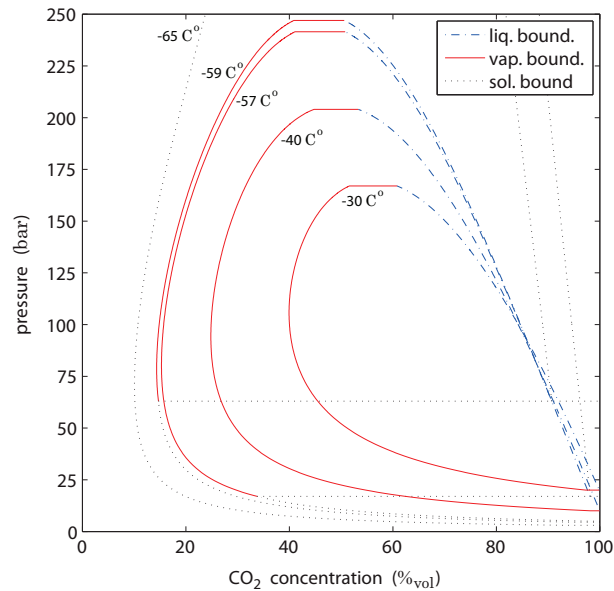


Figure 3.8: P-*x* diagrams of the nitrogen – carbon dioxide system.

Fig. 3.8 shows for different temperatures the *p*-*x* phase diagram of the N₂/CO₂ binary mixture. In contrast to natural gas, the lowest vapor CO₂ concentration is located at elevated pressure (70–100 bar), as indicated by the dew-point line (vap. bound.).

For decreasing temperature, the vapor-liquid region, spanned by the bubble-point (liq. bound.), dew-point (vap. bound.) and CO₂ freeze-out line (sol. bound.), grows and the lowest achievable vapor CO₂ concentration decreases. Simultaneously the bubble line below 100 bar shifts slightly downwards in pressure, resulting in slightly less pure liquid CO₂. Below -57°C, CO₂ freeze-out occurs and the CO₂ freeze-out line starts to rise in pressure. The temperature at which the freeze-out line reaches the pressure of the lowest vapor CO₂ concentration corresponds to the minimum possible vapor

CO₂ concentration that can be achieved in the vapor-liquid regime. This pressure corresponds to about 80 bar and a temperature of -59°C. Achieving a lower vapor CO₂ concentration would require separation in the vapor-solid regime. The liquid phase under this condition still contains about 12%_{vol} nitrogen and can be separated from the liquid by flashing to a lower pressure. To reach a liquid concentration of $\geq 95\%$ _{vol} CO₂, the pressure of the liquid must be reduced to 36 bar or lower, depending on the temperature.

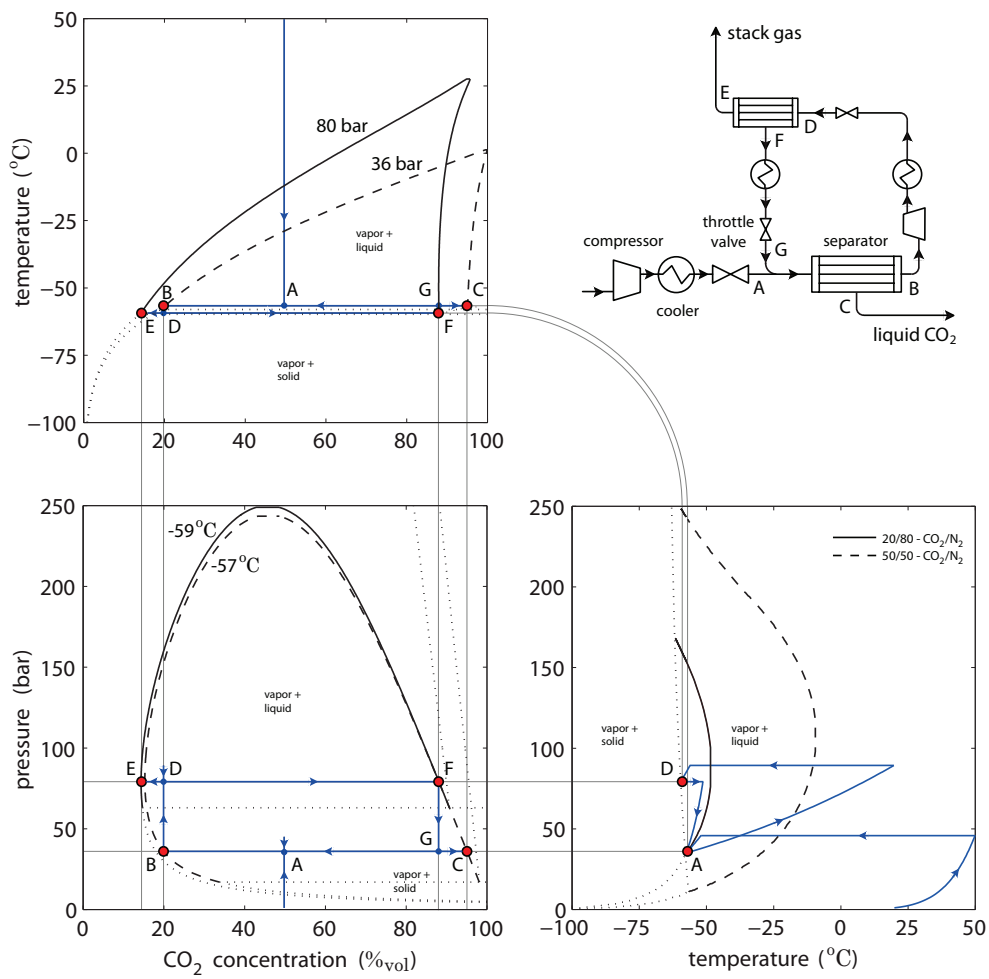


Figure 3.9: The principles and design of the CRS process for the removal of CO₂ from flue gas, with a liquid purity requirement of 95%_{vol} CO₂.

Fig. 3.9 shows the process flow scheme (upper right) and the principles for separating CO₂ from effluent in the $T-x$ (upper left), $p-x$ (lower left) and $p-T$ phase diagram (lower right). An equimolar N₂/CO₂ gas mixture is compressed and chilled by heat

exchange and expansion towards the first separation condition at -57°C and 36 bar, at which it is fed to the first RPS, indicated by 'A' in Fig. 3.9. The final step of expansion cooling is crucial to reach the bulk temperature of -57°C , which is just 1°C away from the CO₂ freeze-out line. Cooling of the bulk towards a temperature this close to the freeze-out line cannot be achieved by isobaric heat exchange alone, because of the temperature difference between heat exchanger wall and bulk flow (see Chapter 4).

In the first RPS the mixture is split in a vapor stream 'B' containing 20%_{vol} CO₂ and a liquid stream 'C' containing 95%_{vol} CO₂. The vapor resulting from the first RPS, 'B', is further compressed to 90 bar, cooled by combination of heat exchange and expansion to -59°C and 80 bar, and fed to the second RPS, indicated by 'D'. In the second RPS, the mixture splits into a vapor stream 'E' containing 16%_{vol} CO₂, and a liquid stream 'F' that still contains an amount of nitrogen that can be separated by flashing back to the first separation condition, indicated by 'G'.

The recycle ratio, which we defined as the ratio of re-fed mass flow 'F-G' to process feed mass flow, is much smaller than in the natural gas application. Comparison of the p - x and T - x diagrams in Figs. 3.9 and 3.5 reveals that the phase split of the recycle stream, 'D', in the flue gas application is relatively close to the single phase region that leaves the process, indicated by 'E'. Application of the lever rule to the second stage phase split in Fig. 3.9, indicated by 'E-D-F', uncovers a large vapor fraction that leaves the process. The phase with the smaller phase fraction is re-fed to the first stage (opposite of the natural gas application), which causes the typically smaller recycle ratio. For the process conditions as shown in Fig. 3.9, the recycle ratio varies from 0.1 at 16%_{vol} CO₂ to 0 at 95%_{vol} CO₂ in the CRS feed stream.

In capturing carbon dioxide from effluent, the amount of CO₂ capture, expressed by the liquid CO₂ recovery, is at least as important as the liquid CO₂ purity. Fig. 3.10 shows the liquid CO₂ recovery as a function of feed composition and compares the two stage design with single stage operation. The improvement in CO₂ recovery by addition of a second stage is not as great as in the natural gas application. The improvement in CO₂ recovery diminishes for increasing CO₂ content in the feed, due to the relatively equal phase split in both stages, cf. points 'B,E' and 'F,G' in Fig. 3.9. Two-stage CRS becomes however more advantageous compared to single stage operation if the first stage pressure is lowered to achieve higher liquid CO₂ purities.

Capturing CO₂ from flue gas by CRS as presented in Fig. 3.9 requires at least a CO₂ content in the feed of 20%_{vol}, resulting in an almost negligible recovery of CO₂. Recovering a decent amount of CO₂ ($\geq 70\%$) requires flue gas with a CO₂ content $\geq 40\%$ _{vol}, as can be found from Fig. 3.10. Flue gas resulting from conventional pulverized coal combustion has only a CO₂ content between 10 and 16%_{vol} CO₂. Application of CRS in effluent CO₂ capture therefore requires a flue gas CO₂ pre-enrichment process upstream of the CRS process. This is further discussed in Chapter 4.

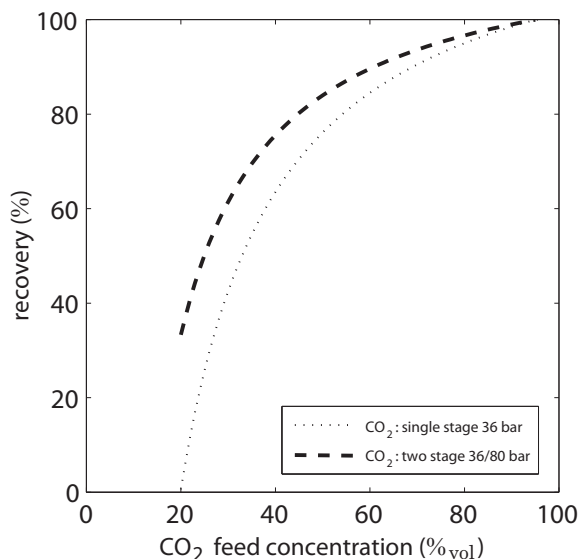


Figure 3.10: Carbon dioxide recovery for the two stage process of Fig. 3.10, compared against single stage separation for equal liquid purity.

3.4.1 Effect of impurities

Impurities in flue gas condensation, such as argon, oxygen and sulphur dioxide, are subject of investigation in several recent studies. Kather et al. investigated the influence of oxygen purity and boiler air ingress on the CO₂ concentration in flue gas from oxy-fuel combustion [64]. Li et al. and Eggers et al. investigated the changes in phase behavior of CO₂ in the presence of argon, nitrogen, oxygen and sulphur-dioxide [49, 78].

Influence of impurities on phase behavior and the separation performance of CRS is only notable when impurities are present in sufficient amounts $\mathcal{O} (> 1\%_{vol})$. In coal combustion such impurities are oxygen and sulphur-dioxide. In absence of flue gas desulphurization, sulphur-dioxide can be present up to a quantity of $2\%_{vol}$ d.b.[†] for sulphur-rich coals such as Illinois#6 [65]; c.f appendix C.

Oxygen is always present in flue gas, due to excess combustion air and ingress of ambient air into the boiler and downstream equipment. For pulverized coal combustion the typical excess oxygen ratio is about 1.5. Air ingress can vary from 3% for new build conventional coal-fired power plants, up to 10% of the flue gas mass flow for existing air blown power plants [64], resulting in a flue gas oxygen content of 3.5–4.5%_{vol} d.b. for air-blown power plants and up to 8%_{vol} d.b. for (partial) oxy-fuel coal-fired power plants. c.f appendix C.

[†]d.b.: dry moist free basis.

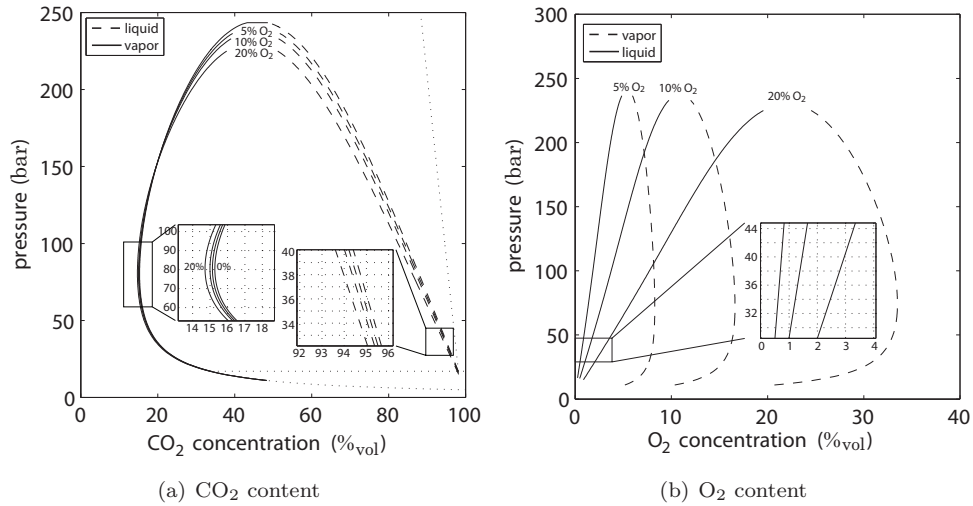


Figure 3.11: Influence of oxygen at -57°C on the phase behavior of dry flue gas (N_2/CO_2) with a constant overall CO_2 concentration, z_{CO_2} , of $50\%_{\text{vol}}$.

The influence of oxygen on the phase behavior of an equimolar mixture of nitrogen and carbon dioxide at the highest separation temperature of the CRS process is shown in Fig. 3.11. In the beginning of Section 3.4 we grouped oxygen and nitrogen into one nitrogen group, since their volatilities are about equal, compared to carbon dioxide. Fig. 3.11 justifies this assumption, since the liquid phase carbon dioxide concentration, 3.11(a), is decreased with less than one percent when the overall O₂ content is increased up to $20\%_{\text{vol}}$. A similar decrease is found for the CO₂ content in the vapor phase. The presence of oxygen contributes furthermore to a negligible shift of the CO₂ freeze-out line towards a lower temperature.

It is inevitable that a small amount of oxygen is always recovered in the liquid phase. For the separation conditions as shown in Fig. 3.9, the liquid oxygen content is small but still goes up to $2.6\%_{\text{vol}}$ for an oxygen content of $20\%_{\text{vol}}$ in the overall composition, as is shown in Fig. 3.11(b). The amount of oxygen in the liquid phase can be lowered by a decrease of separation pressure, which goes along with the increase in liquid phase CO₂ purity.

Sulphur dioxide on the contrary, is a much heavier component with an even lower volatility than carbon dioxide. Therefore sulphur dioxide is almost completely captured in the liquid phase. Fig. 3.12 shows the influence of SO₂ at separation temperature on an N₂/CO₂ mixture:

On the vapor side of the CO₂ concentration diagram, Fig. 3.12(a), the optimum point with lowest CO₂ concentration remains at approximately 80 bar. A minor decrease of the optimum point by 0.4 to $1.5\%_{\text{vol}}$ CO₂ is found for the presence of 2 to $10\%_{\text{vol}}$ SO₂ in the overall mixture. On the liquid side, the CO₂ purity decreases fast with

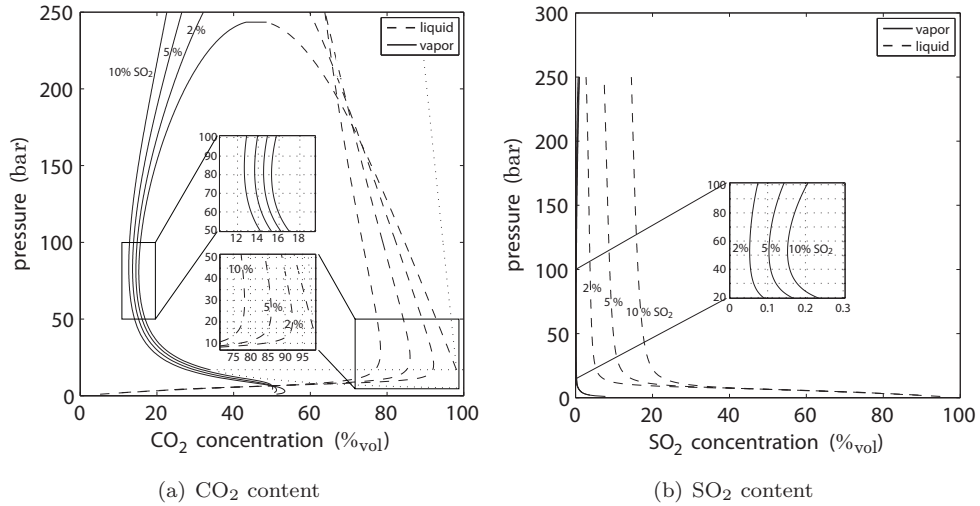


Figure 3.12: Influence of sulphur-dioxide at -57°C on the phase behavior of dry flue gas (N_2/CO_2) with a constant overall CO_2 concentration, z_{CO_2} , of $50\%_{\text{vol}}$.

the increase of SO_2 in the overall mixture and drops below the target of $95\%_{\text{vol}}$ CO_2 for an SO_2 content above $2\%_{\text{vol}}$.

The point of lowest SO_2 content in the vapor phase, Fig. 3.12(b), is also found at approximately 80 bar (the high pressure stage in Fig. 3.9), making effective separation of both sulphur dioxide and carbon dioxide possible.

Sulphur dioxide has, just as the presence of H_2S in natural gas, an anti-freeze effect on

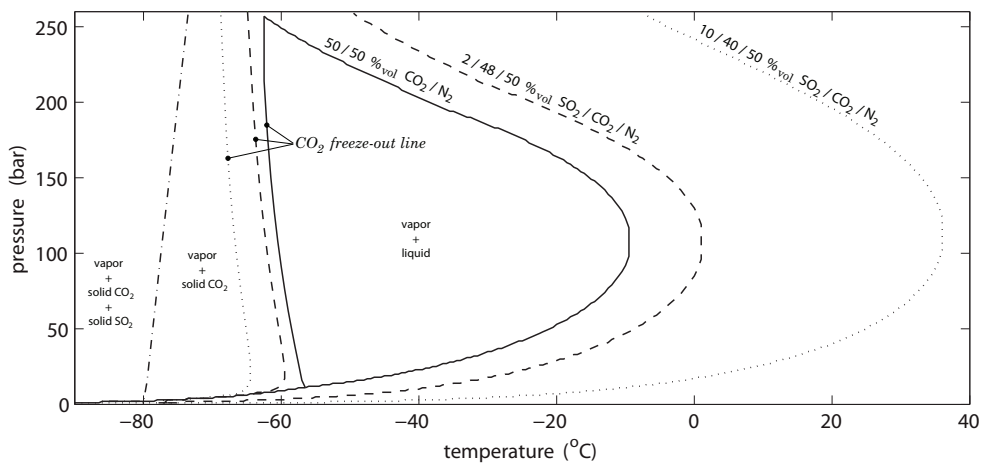


Figure 3.13: Influence of SO_2 on CO_2 freeze-out.

CO₂. At 36 bar, the presence of 2%_{vol} SO₂ lowers the CO₂ freeze-out temperature already by about 2°C. For an overall SO₂ content of 10%_{vol}, the shift is -7°C (Fig. 3.13). In presence of sulphur dioxide, the separation temperature of the low-pressure stage in Fig. 3.9 can therefore be lowered to improve separation. The high pressure stage has no benefit by the presence of SO₂, as SO₂ condenses almost completely in the low-pressure stage.

Fig. 3.14 shows the effect of oxygen 3.14(a) and sulphur dioxide 3.14(b) on the CO₂ recovery for the CRS process of Fig. 3.9. The presence of oxygen in the CRS feed stream has only a very small positive effect on the amount of CO₂ capture. The presence of sulphur dioxide has a greater positive impact on the amount of CO₂ capture. For a low CO₂ content, the presence of 2%_{vol} SO₂ in the feed contributes to an improvement of the recovery by 5%, which decreases to 1% for a high CO₂ content in the feed. Higher feed SO₂ concentrations lead to even greater improvements as shown in Fig. 3.14(b), although in practice they are never encountered.

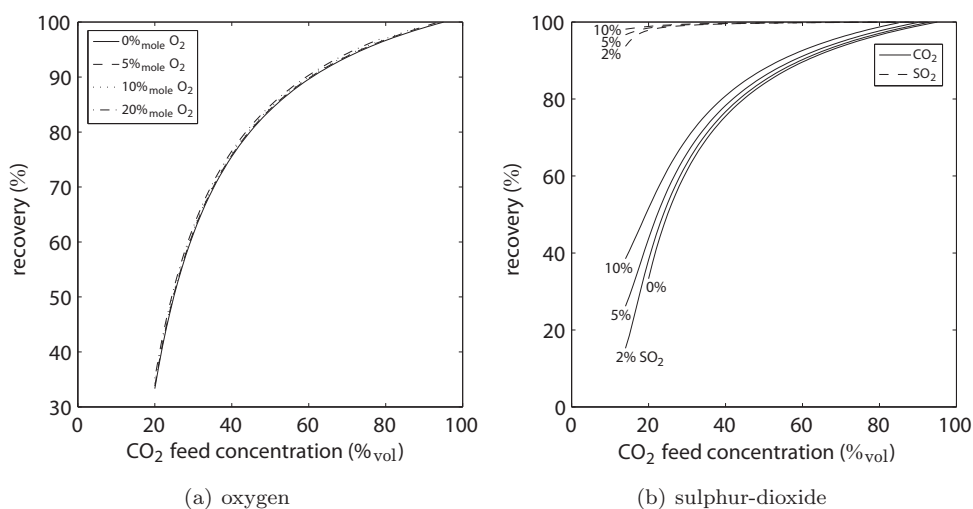


Figure 3.14: Influence by impurities on the recovery of the CRS process in flue gas CO₂ removal as shown in fig. 3.9.

Also shown in Fig. 3.14(b) is the liquid recovery of sulphur dioxide, which is far greater than the liquid CO₂ recovery. For separation conditions as given in Fig. 3.9, a CO₂ concentration of 30%_{vol} and a SO₂ content of 2%_{vol} in the CRS feed, already more than 99% of the SO₂ is captured. CRS thus has the ability to simultaneously capture CO₂ and SO₂ from undesulphurized flue gas. An additional separation process, such as CRS or absorption, might be required in tandem to remove the sulphur dioxide from the liquid CO₂ stream prior to transport, storage or utilization, depending CO₂ stream specifications.

3.5 Separation in a Narrow Vapor-Liquid Regime

Separation of a binary mixture into two essentially pure components becomes impossible with a two stage CRS process when the mixture bubble-point and dew-point lines are close to each other. Examples are the separation of nitrogen and oxygen and the separation of ethane from carbon dioxide. In such cases the vapor-liquid phase only exists in a very narrow region between the pure component saturation lines.

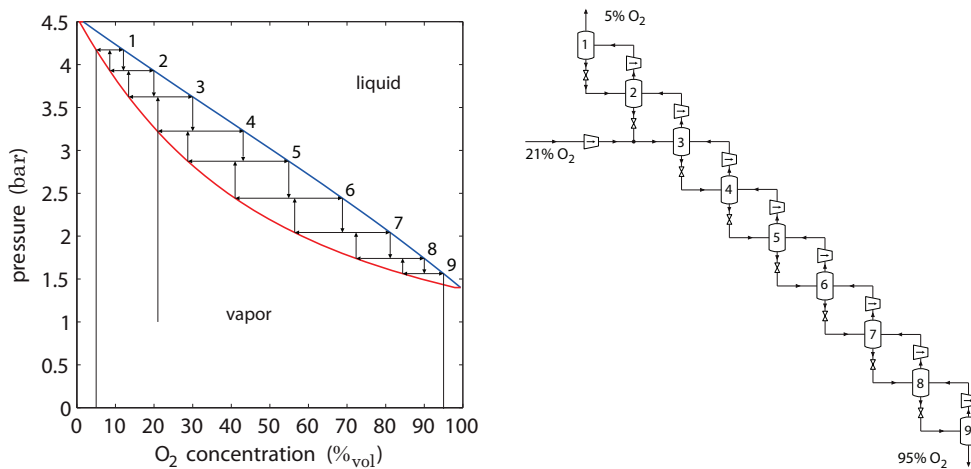


Figure 3.15: Air separation by CRS into 95%_{vol} N₂ and 95%_{vol} O₂.

Fig. 3.15 depicts the pressure-concentration diagram for the nitrogen-oxygen system at -180°C . To separate air into oxygen and nitrogen with purities of 95%_{vol}, a minimum number of 9 CRS stages is required, where the feed enters at the 3th stage. In Fig. 3.15 one can clearly recognize the concept of distillation, however not over a temperature difference, but a dominant pressure difference. The process of CRS can therefore be classified as a pressure distillation process with a freedom to tune the pressure and temperature per stage. In comparison to temperature distillation, each stage in the CRS process, represented by an RPS, is equivalent to a single tray in a distillation column.

The more the mixture pure component volatilities become equal, the narrower the vapor-liquid region. The number of stages required to achieve maximum purities for both components, thereby increases. More separation stages leads to more process equipment (compressors, expanders, heat exchangers and RPS), which diminishes the advantage of CRS as a compact fast distillation technique.

3.6 Separation of Multi-Component Mixtures

Raw gas mixtures encountered in the fields of natural gas sweetening and fossil fuel combustion generally consist of more than two components. Natural gas for example often contains not only CO_2 and/or H_2S , but also amounts of nitrogen and some higher hydrocarbons, such as C_2H_6 . In addition to nitrogen and carbon dioxide in flue gases, water vapor, oxygen, argon and sometimes sulfur-oxide are often present in not negligible amounts.

In contrast to binary mixtures, phase concentrations (\mathbf{x} , \mathbf{y}) in the vapor-liquid regime of multi-component mixtures are overall-composition (\mathbf{z}) dependent, as can be derived from the Gibbs phase rule, Eq. (2.4). The functionality of the pressure-concentration diagram for direct design of the CRS process is therefore lost, and evaluation of phase concentrations per stage becomes a requirement.

3.6.1 Effective separation of a single component

In multi-component mixtures, the design method of a two stage CRS process to effectively separate one component is defined in three steps. In the first step an apparent binary mixture is defined by selection of two key components, as conventional in distillation design [115]. Key components are selected by order of volatility or by importance of presence in a mixture. The component with the highest (or lowest) volatility is always a key component, and corresponds to the required pure component. The component that is dominant under the residual components is selected as the second key component. In case the presence of residual components is comparably equal, the residual component with the highest (or lowest) volatility is appointed as second key component. The resulting apparent binary mixture serves to generate the binary pressure-concentration diagrams, that can be used as described in the previous sections to choose initial separation conditions for both separation stages.

The second step of the design comprises the analysis of phase concentrations of the actual two-phase (or multi-phase) mixture at the separation conditions from step 1. Pressure- or temperature-concentration diagrams can be evaluated at separation conditions of the first stage to find the conditions belonging to either the highest vapor or liquid phase concentration. Alternatively, p - T -concentration plots such as Fig. 3.3 may be evaluated to find the preferred separation conditions. Once first stage separation conditions are re-selected, the phase composition is determined that is fed to the second stage. Evaluation of the second stage conditions is similar to the first phase. The second stage condition is selected or updated such that it comprises the region with the lowest concentration in the phase that leaves the process.

The third and final step comprises of an iterative calculation performed over a range of separation conditions. The range is defined by small variations around the selected first and second stage separation conditions in step two. The iterative calculation contains a flash calculation for the first stage followed by a flash calculation for the second stage and the calculation of mass flows. The residual phase of the second phase

is re-fed to the first separation stage and mixed with the overall feed composition of the process. The new 'entrance' mixture of the first stage is used to repeat the flash calculations for both stages and the calculation of mass flows. The iteration is repeated until convergence of the mass balance over the process is satisfied. Final separation conditions are selected from the resulting separation conditions matrix of the third step.

3.6.2 Separation of two or more pure components

A CRS process applied to a multi-component stream can generally separate only one essentially pure component. The components other than the separated component end up in the residual stream (either the vapor or condensed stream). Effective separation of more than one component with both maximum purities and maximum recoveries requires a sequence of CRS processes, as is shown in Fig. 3.16, which is analogous to having a sequence of multiple distillation columns in a temperature distillation process.

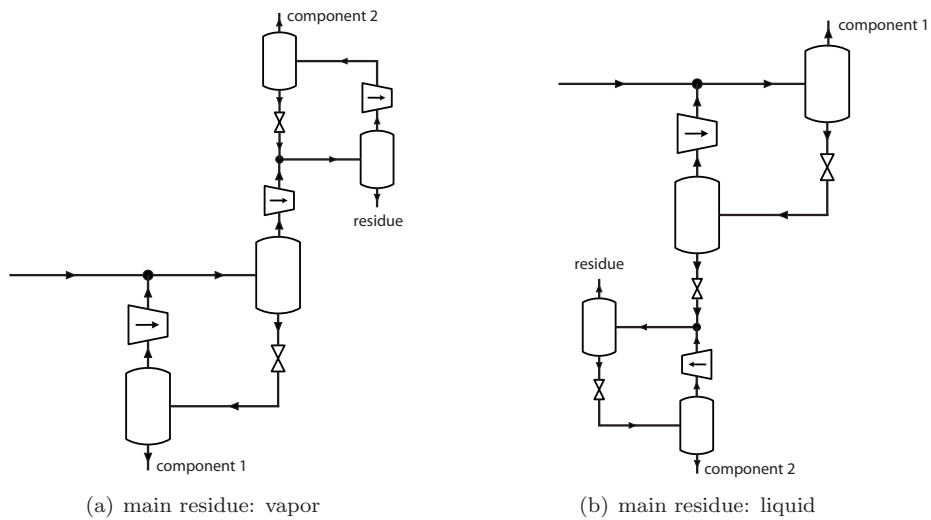


Figure 3.16: Effective separation of two components – most and least volatile – from a multi-component mixture with a double two-stage CRS process.

3.7 Discussion

It has been shown by predecessors of this work that the technique of Condensed Rotational Separation can separate mixtures according phase equilibrium. By rapid cooling, droplet condensation and application of the Rotating Particle Separator, (partially) condensable mixtures can be separated effectively into a vapor and a liquid stream.

With the use of two or more of such separation stages, operated at different pressures and eventually different temperatures, it is possible to separate a binary mixture into essentially pure components at maximum component recoveries. Even separation of mixtures with comparable volatilities is possible, however with a penalty in the number of required separation stages. In multi-component mixtures, CRS is capable of effective separation of the most or least volatile component. By application of multiple multi-stage CRS loops in series, even multiple components can be separated distinctively.

We explained that preliminary design of CRS can be accomplished by the definition of apparent binary mixtures and the evaluation of their phase diagrams in de dimensions pressure and composition ($p-x$). Construction of horizontal tie-lines in the $p-x$ phase diagram for maximum purification of both phases provides a method to determine the number of separation stages (number of separators to be deployed at different pressures and temperatures), the process layout, and the optimum feed stage, for maximum separation.

In comparison to temperature distillation, CRS has freedom in both temperature and pressure. The process of CRS is not constrained to a one direction pressure gradient, whereas in distillation columns a monotonic temperature gradient cannot be omitted. Condensed Rotational Separation as a fast and compact distillation technique therefore offers maximum flexibility to tune separation conditions in the two phase (or multi-fluid phase) region.

Energy and Sizing of Process Equipment:

The benefits of the application of Condensed Rotational Separation are not solely found in separation performance. Fast heat exchange, micron-size droplet condensation and a compact centrifugal separator also result a compact process. For comparison with competitive separation techniques, we estimate the equipment volume and energy consumption of CRS. These represent the capital and operational costs (CAPEX and OPEX) of the process. The first section of this chapter deals with energy calculations for pressure and temperature changers. The second section deals with size determination of radial turbo-expanders, centrifugal compressors, coil-wound heat exchangers and Rotational Particle Separators, which are present in the CRS process.

4.1 Energy

Fast cooling in the CRS process is induced by isobaric heat exchange, followed by expansion and eventually supplemented with compression to reach the different separation stages (cf. 'A-B-C' and 'D-E-F' in Figs. 3.5 and 3.9). Because of high pressure conditions that occur in the CRS process and partial condensation of mixtures, heat of condensation (latent heat) and real fluid behavior of mixtures have to be considered in the determination of process energy consumption.

4.1.1 Entropy and enthalpy

The fluid energy change in process equipment, due to applied heat and work, is thermodynamically expressed by the change in enthalpy h . The amount of heat generated by the process is closely related to the change in entropy s and can be interpreted as a measure for the thermodynamic process efficiency.

Real fluid p v T -behavior of multi-component mixtures is already discussed in Chapter 2, where we introduced the Peng-Robinson equation of state for p v T -behavior of both vapor and liquid. Real fluid behavior of mixtures implies that thermodynamic

properties such as entropy and enthalpy are not only dependent on temperature and composition, but also on pressure.

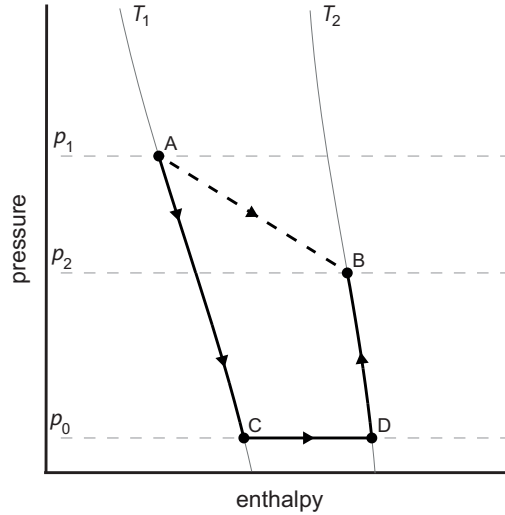


Figure 4.1: Isotherms in a pressure–enthalpy diagram and the path of calculation (A–C–D–B) for the enthalpy difference A–B, corresponding to Eq. (4.1).

Entropy and enthalpy are unique state functions, meaning that for a certain mixture each state (p, T) has its own enthalpy and entropy. The change in enthalpy (or entropy) from state A (p_1, T_1) to state B (p_2, T_2) , see Fig. 4.1, is therefore independent of the thermodynamic path. This allows us to split the calculation of enthalpy (and entropy) change into two pressure dependent parts at constant temperature and a temperature dependent part at constant pressure according to the path A–C–D–B shown in Fig. 4.1:

$$\Delta h_{A-B} = h_2 - h_1 = \int_{p_1}^{p_0} \left. \frac{\partial h}{\partial p} \right|_{T_1} dp + \int_{T_1}^{T_2} \left. \frac{\partial h}{\partial T} \right|_{p_0} dT + \int_{p_0}^{p_2} \left. \frac{\partial h}{\partial p} \right|_{T_2} dp. \quad (4.1)$$

The second term in the RHS (right hand side) of Eq. (4.1) describes the change in enthalpy between T_1 and T_2 at reference state pressure p_0 . p_0 is selected sufficiently low, $\mathcal{O}(1 \text{ Pa})$, such that the reference state obeys ideal gas. This allows the use of the mixture pure components ideal heat capacity correlations $c_p^o(T)$ to replace the derivative $\left. \frac{\partial h}{\partial T} \right|_{p_0}$ [99, 105].

The first and last RHS term are known as departure functions. Due to the simplicity of the Peng-Robinson EoS, it is possible to derive expressions for the enthalpy and entropy departure functions with use of the Helmholtz energy (cf. Appendix A.4).

The departure functions for enthalpy and entropy are given as [99, 105]:

$$\int_{p_0}^p \frac{\partial h}{\partial p} \Big|_T dp' = \frac{1}{\sqrt{8}} \left\{ \frac{a(T)}{b} - \frac{T}{b} \frac{\partial a}{\partial T} \right\} \ln \left(\frac{v + (1 - \sqrt{2})b}{v + (1 + \sqrt{2})b} \right) + (pv - RT) \quad (4.2)$$

$$\int_{p_0}^p \frac{\partial s}{\partial p} \Big|_T dp' = -R \log \left(\frac{v_0}{v - b} \right) - \frac{1}{\sqrt{8}} \frac{1}{b} \frac{\partial a}{\partial T} \ln \left(\frac{v + (1 - \sqrt{2})b}{v + (1 + \sqrt{2})b} \right). \quad (4.3)$$

The parameters $a(T)$ and b are the Peng-Robinson EoS parameters which are specified for mixtures by Eqs. (2.17) and (2.18). v is the molar volume which is calculated from the Peng-Robinson EoS, Eq. (2.9), and v_0 is the molar volume at temperature T and reference pressure p_0 , calculated from the ideal gas law. For mixtures, the EoS parameter partial derivative $\frac{\partial a}{\partial T}$ is given as:

$$\frac{\partial a_m}{\partial T} = \frac{1}{2} \sum_i^N \sum_j^N z_i z_j \left(\frac{1}{(a_i a_j)^{0.5}} \right) \left\{ a_i \frac{\partial a_j}{\partial T} + a_j \frac{\partial a_i}{\partial T} \right\} (1 - k_{ij}), \quad (4.4)$$

where the pure component partial derivatives $\frac{\partial a_i}{\partial T}$, $\frac{\partial a_j}{\partial T}$ are derived from Eqs. (2.11) to (2.12).

In the presence of multiple phases, for example in vapor-liquid coexistence, each phase has its own departure functions. Departure functions for the vapor phase are typically small, as they describe only the effect of compressibility. Departure functions for the liquid phase typically have the order of magnitude of the latent heat, while contribution by compressibility effects is negligible.

In vapor-liquid phase coexistence the departure function at T_1 can be written as:

$$\int_{p_1}^{p_0} \frac{\partial h}{\partial p} \Big|_{T_1} dp = \alpha_1^V \int_{p_1}^{p_0} \frac{\partial h^V}{\partial p} \Big|_{T_1, \mathbf{y}_1} dp + \alpha_1^L \int_{p_1}^{p_0} \frac{\partial h^L}{\partial p} \Big|_{T_1, \mathbf{x}_1} dp, \quad (4.5)$$

where α_1^V and α_1^L are the molar vapor and liquid phase fraction and \mathbf{y}_1 and \mathbf{x}_1 the molar vapor and liquid phase composition at state 1. The change of enthalpy in the reference state for both the vapor and liquid phase can be combined, which simplifies into an expression that is only dependent on overall molar composition \mathbf{z} :

$$\alpha_1^V \int_{T_1}^{T_2} \frac{\partial h^V}{\partial T} \Big|_{p_0, \mathbf{y}_1} dp + \alpha_1^L \int_{T_1}^{T_2} \frac{\partial h^L}{\partial T} \Big|_{p_0, \mathbf{x}_1} dp = \int_{T_1}^{T_2} \frac{\partial h}{\partial T} \Big|_{p_0, \mathbf{z}} dT. \quad (4.6)$$

Combining the result of Eq. (4.6) and twice Eq. (4.5), results in the change in enthalpy of a vapor-liquid mixture:

$$\begin{aligned} \Delta h &= \alpha_1^V \int_{p_1}^{p_0} \frac{\partial h^V}{\partial p} \Big|_{T_1, \mathbf{y}_1} dp + \alpha_1^L \int_{p_1}^{p_0} \frac{\partial h^L}{\partial p} \Big|_{T_1, \mathbf{x}_1} dp \dots \\ &\dots + \int_{T_1}^{T_2} \frac{\partial h^o}{\partial T} \Big|_{p_0, \mathbf{z}} dT \dots \\ &\dots + \alpha_2^V \int_{p_0}^{p_2} \frac{\partial h^V}{\partial p} \Big|_{T_2, \mathbf{y}_2} dp + \alpha_2^L \int_{p_0}^{p_2} \frac{\partial h^L}{\partial p} \Big|_{T_2, \mathbf{x}_2} dp, \end{aligned} \quad (4.7)$$

where $\frac{\partial h^o}{\partial T}$ is the enthalpy change in the ideal gas reference state.

Similarly, for the change in entropy of a vapor-liquid mixture can be derived:

$$\begin{aligned} \Delta s = & \alpha_1^V \int_{p_1}^{p_0} \left. \frac{\partial s^V}{\partial p} \right|_{T_1, \mathbf{y}_1} dp + \alpha_1^L \int_{p_1}^{p_0} \left. \frac{\partial s^L}{\partial p} \right|_{T_1, \mathbf{x}_1} dp \dots \\ & \dots + \int_{T_1}^{T_2} \left. \frac{\partial s^o}{\partial T} \right|_{p_0, \mathbf{z}} dT \dots \\ & \dots + \alpha_2^V \int_{p_0}^{p_2} \left. \frac{\partial s^V}{\partial p} \right|_{T_2, \mathbf{y}_2} dp + \alpha_2^L \int_{p_0}^{p_2} \left. \frac{\partial s^L}{\partial p} \right|_{T_2, \mathbf{x}_2} dp, \end{aligned} \quad (4.8)$$

where ideal gas reference state term $\frac{\partial s^o}{\partial T}$ can be replaced by $\frac{c_p^o(T)}{T}$, which allows for the use of the mixture pure components ideal heat capacity correlations $c_p^o(T)$.

Based on the principles of departure functions, a defined reference pressure and heat capacity correlations, also solid phases can be involved in the calculation of enthalpy and entropy in multi-phase mixtures. The derivation of pure solid fugacity in Section 2.4.1 may function as a guideline to define a pure solid reference pressure and pure solid departure functions. Implementation of solid phases in Eqs. (4.7) and (4.8) is however beyond the purpose of this work, as for CRS the operational domain is limited to the vapor-liquid phase region.

Eqs. (4.7) and (4.8) are used in combination with the phase equilibrium model described in Chapter 2 to calculate enthalpy and entropy changes in turbo-machinery and heat exchangers.

4.1.2 Temperature and pressure changer models

The heat exchanged in a heat exchanger stream can be found directly by application of Eqs. (4.2)–(4.4) and (4.7) to a temperature difference between the stream entrance and exit at constant pressure.

Isentropic and isenthalpic pressure change processes such as compressors, turbo expanders and Joule-Thompson valves can be modeled iteratively, with use of Eqs. (4.2)–(4.4), (4.7) and (4.8) by prescription of either a pressure or a temperature interval from

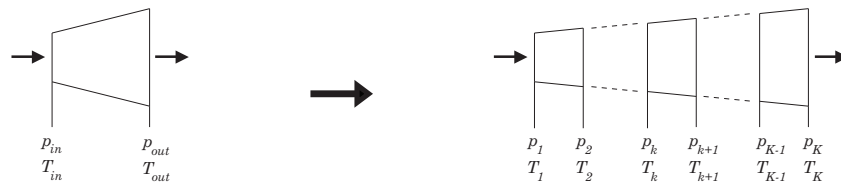


Figure 4.2: Iterative calculation of compression and expansion processes.

inlet to outlet (Fig. 4.2). When prescribing the pressure interval over an expander, the temperature at each pressure step k is iteratively determined by a Newton-Raphson method, such that it fulfils the isentropic or isenthalpic condition:

$$\overbrace{\Delta s \Big|_{(p_k, T_k)}^{(p_{k+1}, T_{k+1})}}^{\text{isentropic}} = 0, \quad (4.9) \quad \overbrace{\Delta h \Big|_{(p_k, T_k)}^{(p_{k+1}, T_{k+1})}}^{\text{isenthalpic}} = 0. \quad (4.10)$$

The iteration scheme for calculation of isentropic (or isenthalpic) expansion paths is shown in Fig. 4.3:

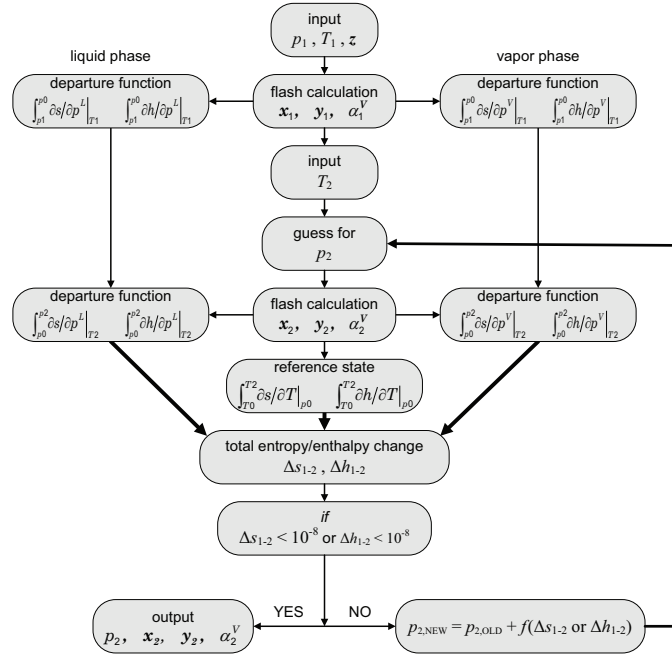


Figure 4.3: Calculation scheme for isentropic or isenthalpic expansion from state k to $k+1$.

Isentropic efficiencies in the compressors and expanders are included in the iterative calculation by:

$$\eta_C = \frac{\Delta h' \Big|_{(p_k, T'_k)}^{(p_{k+1}, T'_{k+1})}}{\Delta h \Big|_{(p_k, T_k)}^{(p_{k+1}, T_{k+1})}}, \quad \eta_E = \frac{\Delta h \Big|_{(p_k, T_k)}^{(p_{k+1}, T_{k+1})}}{\Delta h' \Big|_{(p_k, T'_k)}^{(p_{k+1}, T'_{k+1})}}, \quad (4.11)$$

where $_C$ and $_E$ refer to compressor and expander and where $\Delta h'$ is the enthalpy difference between (p_k, T_k) and (p_{k+1}, T_{k+1}) (Fig. 4.2) such that Eq. (4.9) is obeyed.

In expansion valves a similar but isenthalpic efficiency can be introduced to represent energetic losses by heat and friction:

$$\eta = \frac{\Delta s' \Big|_{(p_k, T'_k)}^{(p_{k+1}, T'_{k+1})}}{\Delta s \Big|_{(p_k, T_k)}^{(p_{k+1}, T_{k+1})}}, \quad (4.12)$$

where $\Delta s'$ is the entropy difference between (p_k, T_k) and (p_{k+1}, T_{k+1}) such that Eq. (4.10) is obeyed.

Calculation of any compression or expansion path starts with the Newton-Raphson based iterative procedure (Fig. 4.3) which calculates temperatures (or pressures) such that for the whole prescribed pressure (or temperature) interval $k = 1, 2, \dots, K$ (Fig. 4.2) Eq. (4.9) or Eq. (4.10) is obeyed.

For $\eta < 1^*$, a second similar iterative calculation follows, which adjusts the temperature (or pressure) interval obtained from the first iteration procedure such that, instead of Eq. (4.9) or Eq. (4.10), either one of the Eqs. (4.11)–(4.12) is satisfied for the whole prescribed interval $k = 1, 2, \dots, K$.

These models are used in the remaining of this work to:

- calculate thermodynamic properties, such as (average) heat capacities and the speed of sound, necessary in the estimation of process equipment size,
- to determine inlet or outlet conditions of turbo-machinery, Joule-Thomson valves and heat exchangers,
- and to determine exchanged heat in heat exchangers and produced or consumed power and heat by compressors and expanders, in order to identify the energy consumption of the CRS process.

* In this work we use the standard $\eta_{isentropic} = 80\%$ and $\eta_{isenthalpic} = 95\%$.

4.2 Equipment Sizing

The process of CRS relies on compressors, expanders, Joule-Thomson valves, heat exchangers, and one or more Rotating Particle Separators. This section discusses the estimation of equipment size for the different devices, with the exception of JT-valves. JT valves are typically small compared to the other devices. Their size estimation is therefore not further discussed.

4.2.1 Expanders

The method of sizing of turbo-expanders uses the coupling of fluid thermodynamics and impeller kinematics and is based on radial expanders. Radial machines can handle low mass flows more efficiently than axial or mixed flow designs [112]. Because of their robustness, compactness and proven reliability, radial expanders and compressors are often preferred in processes such as LNG production and hydrocarbon refining, in which conditions are comparable to the CRS process for coal and gas [7, 36, 37, 54, 55].

Impeller sizing

The main outer diameter or overall package diameter of a radial expander is determined by the impeller tip diameter, the size of the vaneless space, the inlet guide vanes and the inlet volute [80].

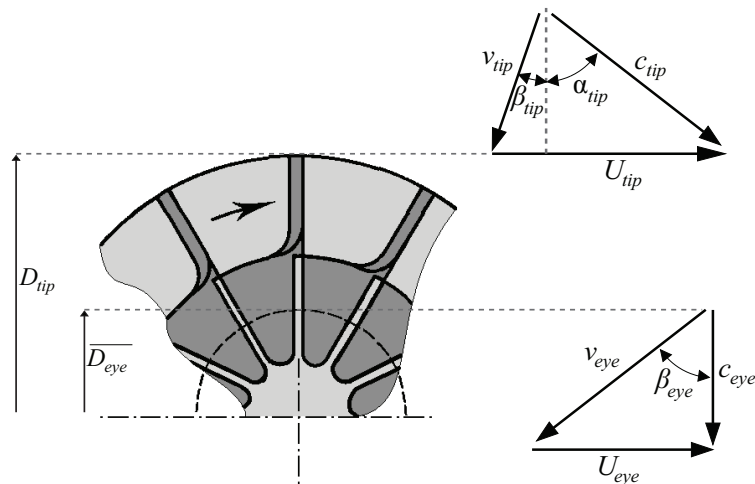


Figure 4.4: Impeller of a radial expander and the corresponding velocity triangles at impeller tip and eye.

Fig. 4.4 shows a typical schematic of a radial expander impeller and the corresponding velocity triangles at impeller tip inlet and impeller eye exit.

Coupling of impeller rotational speed, the change in angular momentum of the fluid and the enthalpic change of the fluid from impeller tip to impeller eye results in a relation between fluid thermodynamics and kinematics over the impeller:

$$h_{0,tip} - h_{0,eye} = (U_{tip}c_{\theta,tip} - U_{eye}c_{\theta,eye}) . \quad (4.13)$$

where c_{θ} is the fluid tangential velocity, U the impeller speed and h the specific enthalpy (here in $\text{J}\cdot\text{kg}^{-1}$). Combined with assumptions of no friction, no slip between the impeller tip and the working fluid and no swirl at the impeller eye exit, Eq. (4.13) turns into a relation between impeller tip speed U_{tip} and the change in stagnation enthalpy of the working fluid over the impeller:

$$h_{0,tip} - h_{0,eye} = U_{tip}^2 . \quad (4.14)$$

Stagnation enthalpy, h_0 ($\text{J}\cdot\text{kg}^{-1}$), is thereby defined as the enthalpy of the fluid if it would be brought to rest both frictionless and adiabatically:

$$h_0 = h + \frac{1}{2}c^2 , \quad (4.15)$$

where h_0 represents the stagnation enthalpy, h the static enthalpy and c is the velocity. The static-to-stagnation entropy change is zero per definition. Therefore the isentropic model (with $\eta_E = 100\%$), described in Section 4.1.2, can be used to relate the fluid velocity c to the static and stagnation condition (p, T) and (p_0, T_0) . By iterative procedure, the static conditions, Fig. 4.5(a), or fluid velocity, Fig. 4.5(b), can be calculated.

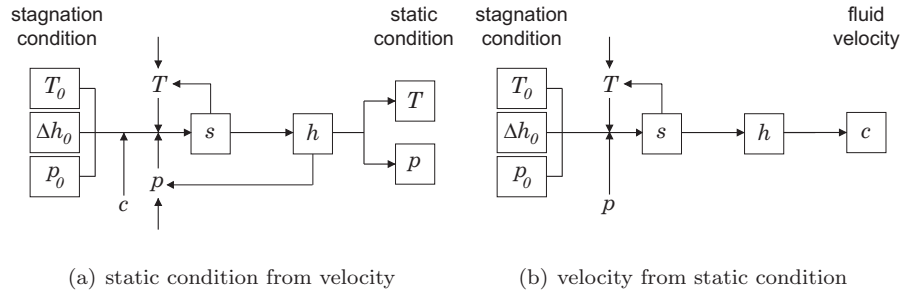


Figure 4.5: Schemes for relating stagnation conditions to static conditions and fluid velocities.

In the calculation of the overall expander package diameter, and compressor package diameter further on, we assume that the inlet volute, inlet guide vanes and vaneless space are frictionless and adiabatic such that stagnation enthalpy is conserved. Stagnation enthalpy only changes from impeller tip to impeller eye. For a specified expander inlet and outlet stagnation condition (p_0, T_0) , the change in stagnation enthalpy over the impeller is calculated from the isentropic model (cf. Section 4.1.2). Isentropic stage efficiencies of $>90\%$ are reported for radial turbo expanders [31, 37]. We however take a conservative estimate of 80% isentropic stage efficiency, η_E , into

account in the calculation of stagnation enthalpy change to cover for fluid friction and adiabatic losses over the impeller.

In turbine operation, high frictional losses and shock formation are undesirable. In design, an aerodynamic design limit is often implemented by keeping the highest Mach number below a level of high frictional losses and possible shock formation. A maximum allowed Mach number of 0.8 is commonly applied in turbine design [112].

In radial turbo expanders, the highest Mach number is encountered at the tip of the impeller, $Ma_{tip} = c_{tip}/a_{tip}$. To estimate the speed of sound, a_{tip} , the static condition at the impeller tip is determined according to the scheme in Fig. 4.5a from:

$$h_{0,tip} = h_{tip} + \frac{1}{2} \left(\frac{U_{tip}}{\sin(\alpha_{tip}) + \cos(\alpha_{tip}) \tan(\beta_{tip})} \right)^2, \quad (4.16)$$

By use of the definition of the speed of sound, the isentropic model and a small disturbance over the isentropic curve at the static condition (p, T) , the speed of sound a can be approached using the density ρ by:

$$a = \sqrt{\left. \frac{\partial p}{\partial \rho} \right|_s} \approx \sqrt{\left(\frac{p(T+\Delta T) - p(T-\Delta T)}{\rho(T+\Delta T) - \rho(T-\Delta T)} \right)_s}, \quad (4.17)$$

The smallest tip Mach number, Ma_{tip} , that can be achieved theoretically, is found for a sum of tip air angle α_{tip} and tip blade angle β_{tip} that equals 90° . A tip blade angle $\beta_{tip} > 0^\circ$ is only applied when the tip Mach number for $c_{tip} = U_{tip}$ exceeds the set limit of 0.8.

With a set value of 0.8 for the tip Mach number, the tip air angle α_{tip} and tip blade angle β_{tip} can be found from an iterative procedure, using the the isentropic model (§ 4.1.2), Eq. (4.16), and Eq. (4.17) to calculate the speed of sound. The iterative procedure matches the static condition and static-to-stagnation enthalpy change to the tip air and blade angle, such that a tip Mach number of 0.8 is found.

The impeller tip air angle is used in combination with the normal volume flow and the static tip condition to calculate the impeller tip diameter D_{tip} :

$$D_{tip} = \sqrt{Q_n \frac{T_{tip}}{T_n} \frac{p_n}{p_{tip}} \left(\frac{\tan(\alpha_{tip}) + \tan(\beta_{tip})}{U_{tip}} \right) \frac{1}{\pi \mathbb{B}}}, \quad (4.18)$$

where \mathbb{B} is the ratio between impeller tip width and impeller tip diameter, Q the volume flow. Subscript 'n' represents the normal conditions[†]. In the sizing of expanders the value of \mathbb{B} is set at 0.1, which is a common value [112].

[†]normal conditions: $T_n = 273.15\text{K}$ (0°C), $p_n = 1.01325 \times 10^5$ Pa.

Inlet guide vanes

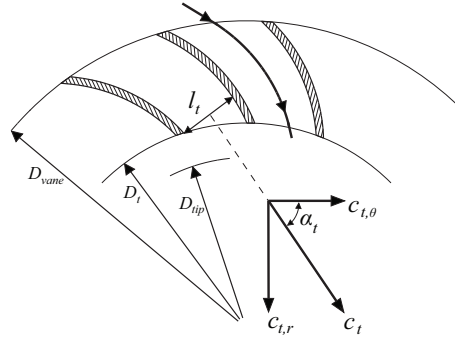


Figure 4.6: Inlet guide vanes and the corresponding velocity triangle.

The fluid at the tip of the impeller is guided by the inlet guide vanes, through a vaneless space onto the impeller tip (Fig. 4.6). The vaneless-space-ratio, defined as the ratio between vane exit diameter D_t and impeller tip diameter D_{tip} , is usually held at 1.05 or less [80]. For straight inlet guide vanes and a chosen guide vane inlet angle of 45° (to match an iso-kinetic volute design) the inlet vane outer diameter D_{vane} can be derived as:

$$D_{vane} = D_t \left(\frac{\sin(0.25\pi - \alpha_t)}{\tan(0.25\pi)} + \cos(0.25\pi - \alpha_t) \right), \quad (4.19)$$

where α_t is the air angle at the vane throat as indicated in Fig. 4.6. Following Subrata [123], the air angle α_t can be derived from the velocity triangle at the vane exit, cf. Fig. 4.6. The radial fluid velocity component at the vane exit, $c_{t,r}$, is calculated from conservation of mass:

$$c_{t,r} = \frac{Q_n}{\pi D_t B} \frac{T_t p_n}{T_n p_t} \frac{1}{D_{tip}}. \quad (4.20)$$

Conservation of angular momentum in free vortex flow over the vaneless space relates the tangential velocity component at the inlet vane throat, $c_{t,\theta}$, to the tangential fluid velocity component at the impeller tip:

$$c_{t,\theta} = U_{tip} \frac{D_{tip}}{D_t}. \quad (4.21)$$

The static condition at the vane throat is determined from the static–stagnation enthalpy relation:

$$h_{0,t} = h_t + \frac{1}{2} (c_{t,r}^2 + c_{t,\theta}^2). \quad (4.22)$$

The procedure for determination of the vane throat static condition is similar to derivation of the static condition at the impeller tip.

The inlet vane throat width is found from combination of mass conservation, the throat static condition and the throat fluid velocity:

$$l_t = \frac{Q_n}{N_{vane} \mathbb{B} D_{tip} c_t} \frac{T_t p_n}{T_n p_t}, \quad (4.23)$$

where N_{vane} represents the number of inlet guide vanes. For straight inlet vanes and a guide vane inlet angle of 45° , a practical limit in the number of vanes can be obtained from the inlet vane entrance and throat angles:

$$N_{vane} \cong \frac{360^\circ}{45^\circ - \alpha_t}. \quad (4.24)$$

Inlet volute

The inlet volute is sized according to a iso-kinetic design as shown in fig. 4.7, resulting in a uniform radial inward flow and a vane inlet radial velocity equal to the volute tangential fluid velocity. For an iso-kinetic volute, the volute collector radius as a function of tangential position is given as:

$$f(\theta) = \sqrt{\frac{D_{vane}}{2\pi} \mathbb{B} D_{tip} (2\pi - \theta)}. \quad (4.25)$$

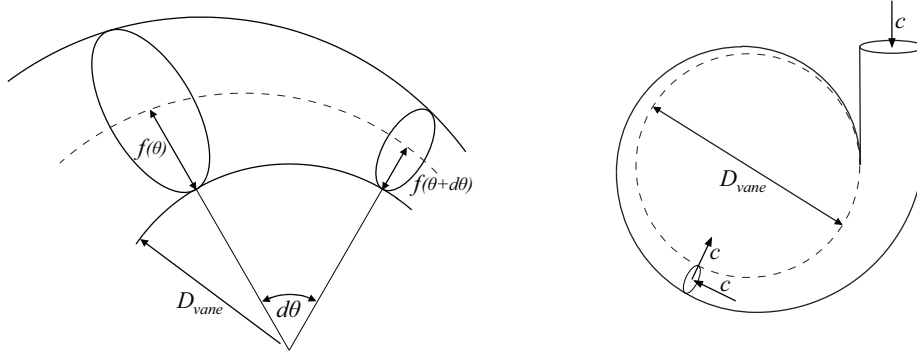


Figure 4.7: Iso-kinetic inlet volute.

Expander package diameter and volume

The expander package diameter is given by Eq. (4.25) as:

$$D_{E,pack} = D_{vane} + (2 + \sqrt{2}) \sqrt{D_{vane} B D_{tip}}. \quad (4.26)$$

The route of overall expander package diameter calculation is shown in Fig. 4.8. The corresponding expander package volume, used for process volume evaluation, is taken as the cubic power of the package diameter.

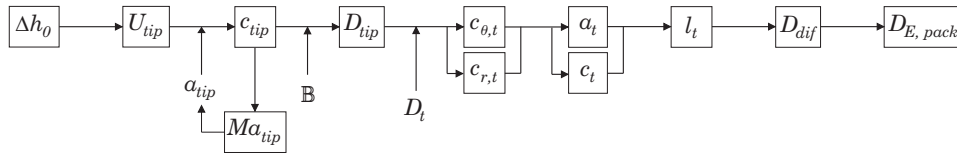


Figure 4.8: Calculation scheme for the overall expander package diameter.

Expander manufacturers often state a limit in expander outlet flow for each expander design. Limiting values of 4.000 to 200.000 nm³/hr [7, 36] and even up to 2.500.000 nm³/hr [36] can be found, dependent on design and pressure drop. In the process of expander sizing, an outlet flow limit of 200.000 nm³/hr is assumed. For higher flows the stream is split and multiple expanders are assumed to be used in parallel.

Typical rotational speeds, found for cryogenic expanders[‡], range from 40000 to 250000 RPM. In the sizing of the expanders, a centrifugal limit is taken in account, given by the product of rotational speed (RPM) and impeller tip diameter (m), which is set constant at 10⁴. If this value is exceeded in the process of sizing, multiple expanders are coupled in series.

4.2.2 Compressors

The sizing of compressors is to some extent similar to the sizing of expanders. The sizing is based on centrifugal compressors. Centrifugal compressors are more compact than the axial or mixed flow designs, have a better resistance to foreign object damage (e.g. solid particles in fluid), are less susceptible to loss of performance by build-up of deposits on the impeller and have the ability to operate over a wider range of mass flow at a particular rotational speed [112]. These advances make centrifugal compressors favorable in fields of natural gas production and transport, LNG production, hydrocarbon refining, and flue gas handling [47, 53, 82, 124].

[‡]http://www.aha.ru/~gmashinf/06_e.html

Similar to radial expanders, the overall package diameter of a centrifugal compressor is determined by the impeller tip diameter, the vaneless space, the diffuser ring and the collector volute.

Impeller sizing

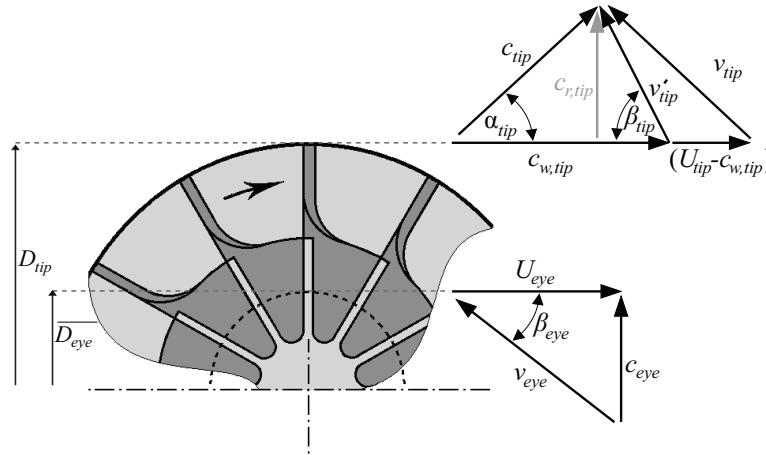


Figure 4.9: Impeller of a centrifugal compressor and the corresponding velocity triangles at impeller tip and eye.

Fig. 4.9 shows a part of a compressor impeller and the corresponding velocity triangles at impeller eye (inlet) and impeller tip (exit). Under ideal circumstances of no slip, the tangential or fluid whirl velocity at the tip would be equal to the impeller tip speed U_{tip} . Due to inertia of the fluid between the impeller vanes, the static pressure on the leading face of a vane is higher compared to the the trailing face. Fluid therefore tends to flow around the vane, causing slip. Furthermore, fluid carried around by the impeller experiences friction with the impeller housing, resulting in a braking effect. Braking effects increase the applied torque requirement on the compressor drive shaft.

For an axial rotation free inlet flow at the impeller eye and coupling of angular momentum, torque and enthalpy change in combination with a slip and applied torque correction, a relation between impeller kinematics and stagnation enthalpy change can be derived:

$$h_{0,tip} - h_{0,eye} = \psi \tilde{\sigma} U_{tip}^2, \quad (4.27)$$

where ψ is the applied torque correction or power input factor and $\tilde{\sigma}$ the slip ratio $c_{w,tip}/U_{tip}$. The slip ratio is experimentally correlated to the number of impeller vanes by:

$$\tilde{\sigma} = 1 - \frac{0.63\pi}{N_{vane}}, \quad (4.28)$$

where N_{vane} refers to the number of impeller vanes [112]. Typical values for the applied torque correction lie in the region 1.035–1.04 [112]. In present-day practice a slip ratio is used of about 0.9, corresponding to 19 to 21 impeller vanes [112].

In contrary to expanders, the fluid velocity at the tip of the impeller is not constrained by the sonic limit. Supersonic diffusion can occur without the formation of shock waves if it is carried out at constant angular momentum with vortex motion in the vaneless space, as long as the radial velocity Mach number at the tip is subsonic. The design constraint by the supersonic limit is therefore imposed on the diffuser throat, to allow for supersonic diffusion in the vaneless space [80, 112]. A Mach number of 0.8 at the diffuser throat is common practice in compressor design.

For arbitrary impeller tip air and blade angles, α_{tip} and β_{tip} , the diameter of the impeller is calculated according:

$$D_{tip} = \sqrt{\frac{T_{tip}}{T_n} \frac{p_n}{p_{tip}} \frac{Q_n}{\pi \mathbb{B} \sigma U_{tip}} \frac{(1 + \tan(\alpha_{tip}) \tan(0.5\pi - \beta_{tip}))}{\tan(\alpha_{tip})}}. \quad (4.29)$$

With the assumptions of an impeller tip width to diameter ratio \mathbb{B} of 0.1, a diffuser throat diameter to impeller tip diameter ratio of 1.05, and a frictionless adiabatic space between the impeller tip and diffuser (vaneless space), the tangential and radial fluid velocity components at the diffuser throat can be calculated from conservation of mass and angular momentum according to Eqs. (4.20) and (4.21). The radial and tangential velocity component at the throat of the diffuser are used to determine the Mach number in the throat and the diffuser throat angle. Mach numbers are derived with use of the isentropic model and Eq. (4.17) as described in Section 4.2.1.

The diffuser throat diameter is calculated in an iterative procedure, see Fig. 4.10, in which the impeller tip air and blade angles are adjusted such that the Mach number at the diffuser throat approaches 0.8 or less in case the radial Mach number at the impeller tip approaches 0.8.

Only for the occasion that the throat Mach criterion cannot be met (if the impeller tip air angle is already small), backswept blades are used and the tip blade angle β_{tip} is adjusted ($\beta_{tip} < 90^\circ$). This adjustment is performed such that the top corner of the velocity triangle $U_{tip} - c_{tip} - v_{tip}$ becomes perpendicular.

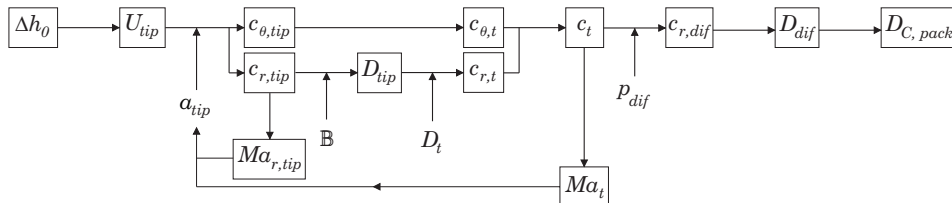


Figure 4.10: Calculation scheme for the overall compressor package diameter.

Diffusor

In centrifugal compressor design it is common that approximately half of the static pressure built-up takes place over the impeller and half of the static pressure built-up takes place in the vaneless space and diffusor [102, 112]. Assuming a negligible impeller eye inlet velocity and conservation of stagnation enthalpy in the vaneless space, the diffusor and the volute, the static pressure at the exit of the diffusor or entrance of the volute can be determined:

$$2p_{tip} - p_{0,eye} = p_{volute} . \quad (4.30)$$

This pressure can serve as a design criterion for the diffusor and can be used to estimate the diffusor exit diameter without information on diffusor vane geometry. Therefore we assume a diffusor exit blade angle of 45 degrees which matches with an iso-kinetic volute design as described in Section 4.2.1. The velocity at the diffusor exit is iteratively derived from the static-to-stagnation enthalpy relation:

$$h_{0,dif} = h_{dif} + \frac{1}{2}c_{dif}^2 , \quad (4.31)$$

the diffusor design criterion and the isentropic model. With use of the conservation of mass and the assumption that the diffusor width increases with the radius by a diffusor angle of 8° [102, 112], the diffusor exit diameter can be expressed as:

$$D_{dif} = \frac{1}{2}D_{tip} \left(\left(1 - \frac{\mathbb{B}}{\tan(8^\circ)} \right) + \sqrt{\frac{\mathbb{B}^2}{\tan^2(8^\circ)} + \left(4 \frac{D_t}{D_{tip}} \frac{c_{t,r}}{c_{dif,r}} \frac{p_t T_{dif}}{p_{dif} T_t} - 2 \right) \frac{\mathbb{B}}{\tan(8^\circ)} + 1} \right) , \quad (4.32)$$

where the radial component of the diffusor exit velocity, $c_{dif,r}$, is derived from the fluid velocity triangle.

Compressor package diameter and volume

With an iso-kinetic volute design described in Section 4.2.1 and Eq. (4.32), the overall centrifugal compressor package diameter is given as:

$$D_{C,pack} = D_{dif} + \left(2 + \sqrt{2} \right) \sqrt{D_{dif} \mathbb{B} D_{tip}} . \quad (4.33)$$

The route of compressor sizing is shown in Fig. 4.8. The overall compressor package volume is calculated as the cubic power of the package diameter.

Similar to expander sizing, a centrifugal limit of 10^4 and a flow limit of $200.000 \text{ nm}^3/\text{hr}$ is taken into account for a single compressor stage, which is an average of limits specified by different centrifugal compressor manufacturers [47, 53, 82]. Flows, larger than $200.000 \text{ nm}^3/\text{hr}$ are split and multiple compressors are assumed to operate in parallel. Exceeding of the centrifugal limit results in multiple centrifugal compressors in series (multiple stages).

4.2.3 Heat exchangers

Heat exchangers are key components in the processing industry. Especially in cryogenic processing, such as LNG production, hydrogen and helium liquefaction, natural gas processing and air separation, efficient heat exchange is of utmost importance. In these fields of application coil-wound heat exchangers, Fig. 4.11(a) or plate-fin heat exchangers, Fig. 4.11(b) are often applied. They are favored because of high heat-exchanging-area to volume ratio, high heat transfer efficiency and capability to exchange heat between up to 10 different fluid streams [79].

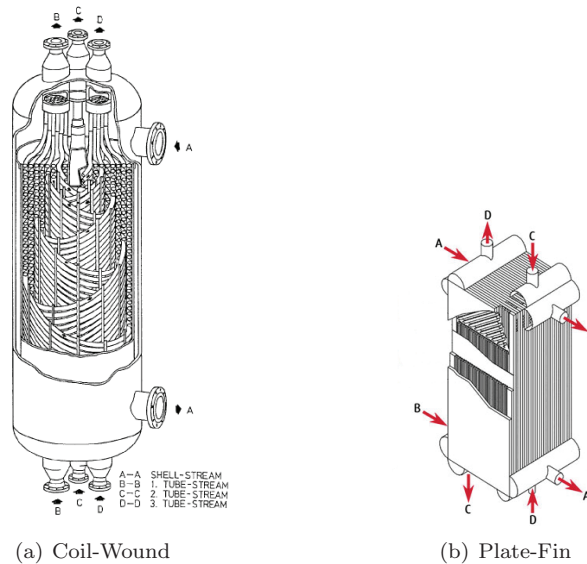


Figure 4.11: Industrial heat exchangers. Reproduced from Neeraas et al. [90] and www.linde-engineering.com

Due to a better vapor-liquid phase distribution on the shell side in condensing/vaporizing mode, a lower sensitivity to fouling and a better resistance to large internal temperature gradients [79], the coil-wound design is considered to be more suitable for application within the CRS process. In CRS, the condensing feed stream (cf. Fig. 3.1) flows through the cell of the coil-wound heat exchanger. The coolant streams (separated single phase streams and external refrigerant; cf. Fig. 5.11) flow through the tubes.

Effectiveness-NTU method

For the size estimation of heat exchangers, we make use of the relationship between the Number of Transfer Units (NTU) and effectiveness. The effectiveness ϵ is given as the ratio of actual transferred heat to the maximum transferrable heat. In relation to

Fig. 4.12, which shows schematically a counter-flow heat exchanger, the effectiveness is expressed as:

$$\epsilon = \frac{q}{q_{max}} = \frac{C_1 (T_{1,h} - T_{1,c})}{C_{min} (T_{1,h} - T_{2,c})} = \frac{C_2 (T_{2,h} - T_{2,c})}{C_{min} (T_{1,h} - T_{2,c})}, \quad (4.34)$$

where q is the transferred power by heat exchange, T the temperature, and C the stream capacity, which is the product of mass flow and specific heat capacity ($\dot{m}c_p$).

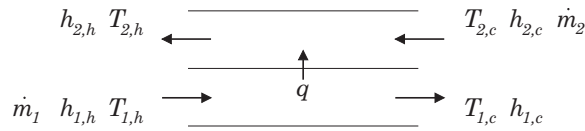


Figure 4.12: Two-stream Counter-flow heat exchanger.

The Number of Transfer Units (NTU) relates the size and geometry of the heat exchanger to the flow through the heat exchanger. Physically, the NTU describes the ratio of energy transferred through the heat exchanger wall per unit temperature and time to the maximum energy that can be transferred from one fluid to another per unit of temperature and time:

$$NTU = \frac{\bar{U}A}{C_{min}}. \quad (4.35)$$

In the NTU expression, \bar{U} is the overall heat transfer coefficient, A the heat exchanging area and C_{min} the smallest stream capacity of both streams.

A number of NTU- ϵ correlations for different heat exchanger configurations are summarized by Bejan et al. [12]. For a counterflow heat exchanger (Fig. 4.13(b)) the ϵ -NTU correlation is given as:

$$\epsilon = \frac{1 - e^{-NTU(1-C)}}{1 - Ce^{-NTU(1-C)}}, \quad (4.36)$$

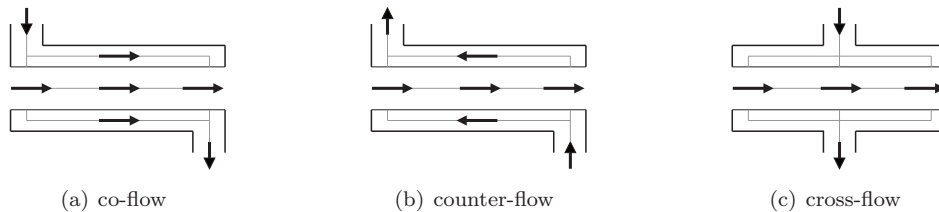


Figure 4.13: Heat exchanger configurations.

with \mathbb{C} the capacity ratio (C_{min}/C_{max}). For a cross-flow heat exchanger (Fig. 4.13(c)) with one mixed stream (stream not divided over multiple parallel crossing tubes or plates; e.g. a shell), the correlations are given as:

$$\underbrace{\epsilon = 1 - e^{\{-2 + e^{(-\mathbb{C}NTU)/\mathbb{C}}\}}}_{C_{min}=C_{mixed}} \quad \underbrace{\epsilon = \frac{1}{\mathbb{C}} \left(1 - e^{(-\mathbb{C}\{1 - e^{-NTU}\})} \right)}_{C_{min} \neq C_{mixed}}, \quad (4.37)$$

In the coil-wound design shown in Fig. 4.11(a), one fluid passes once through the shell from top to bottom. Other streams pass from the bottom to the top through spirally twisted tubes. The coil-wound heat exchanger (Fig. 4.11(a)) is therefore essentially a combination of a counter-flow and a cross-flow configuration with a mixed stream on the shell side.

Fig. 4.14 shows the NTU–effectiveness relationship for counter-flow (a) and cross-flow (b) heat exchangers for different capacity ratios \mathbb{C} . Compact heat exchangers with a small heat exchanging area (low NTU) operate with a large ΔT between both streams 1 and 2 (cf. Fig. 4.12), resulting in a low heat transfer effectiveness. By increasing the area, and thus increasing the NTU, more heat can be transferred which improves the effectiveness. The main increase in effectiveness is found in the lower end of NTU range $0 < NTU < 2$. Heat exchangers with an $NTU > 4$ are rarely encountered, as for $NTU > 4$ there is hardly improvement in heat exchanger effectiveness. Increasing the size of the heat exchanger any further is thus pointless, unless due to process heat integration higher NTU's are unavoidable.

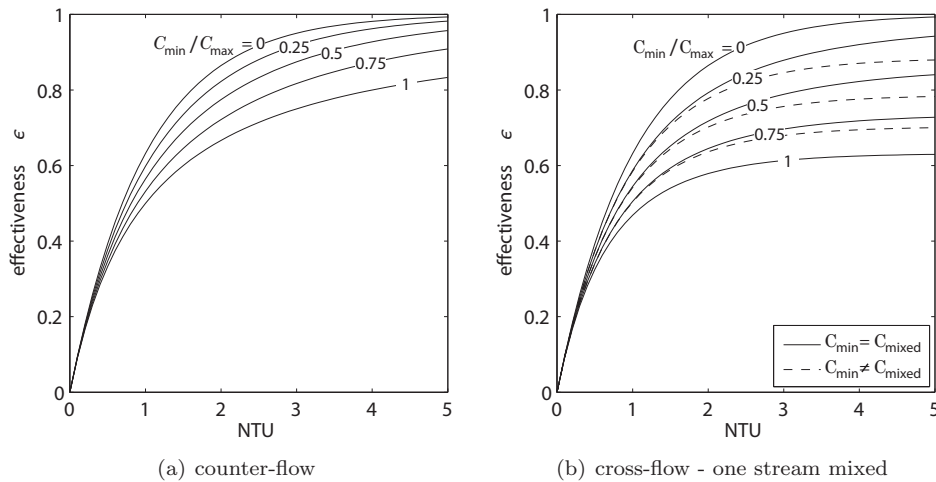


Figure 4.14: ϵ -NTU correlations for different capacity ratios (C_{min}/C_{max})

The sizing of heat exchangers can thus be limited to the range of $2 \leq NTU \leq 4$. For the sizing of the coil-wound heat exchangers in the CRS process we shall strive to a conservative value of $NTU=4$.

Sizing

The sizing of heat exchangers consists of three parts:

1. The derivation of the inlet and outlet temperatures corresponding to NTU=4.
2. Derivation of the overall heat transfer coefficient.
3. Calculation of heat exchanger size and volume.

In setting the temperatures, either the inlet and outlet temperature of stream 1 or 2, or the inlet temperatures of streams 1 and 2 are prescribed; cf. Fig. 4.12. The other temperatures are derived by Newton-Raphson based iterative procedure and the calculation of enthalpy change as described in Section 4.1. To account for (partial) condensation, we re-define in relation to Fig. 4.12 and Eq. (4.34) the effectiveness and the capacity ratio as:

$$\epsilon = \frac{\dot{m}_1 \Delta h_1 \Big|_{T_{1,c}}^{T_{1,h}}}{\min \left(\dot{m}_1 \Delta h_1 \Big|_{T_{2,c}}^{T_{1,h}}, \dot{m}_2 \Delta h_2 \Big|_{T_{2,c}}^{T_{1,h}} \right)}. \quad (4.38)$$

$$C = \frac{\min \left(\dot{m}_1 (\Delta h_1 / \Delta T_1) \Big|_{T_{1,c}}^{T_{1,h}}, \dot{m}_2 (\Delta h_2 / \Delta T_2) \Big|_{T_{2,c}}^{T_{2,h}} \right)}{\max \left(\dot{m}_1 (\Delta h_1 / \Delta T_1) \Big|_{T_{1,c}}^{T_{1,h}}, \dot{m}_2 (\Delta h_2 / \Delta T_2) \Big|_{T_{2,c}}^{T_{2,h}} \right)} \quad (4.39)$$

where Δh corresponds to the specific isobaric stream enthalpy change and ΔT to the change in stream temperature.

For the stream temperatures and capacities corresponding to NTU=4, the overall heat transfer coefficient \bar{U} is determined. The overall heat transfer coefficient is mainly dominated by the resistances due to convective heat transfer. Combined with the conductive heat transfer over the tube, the overall heat transfer coefficient can be approached as [12]:

$$\frac{1}{\bar{U}} \approx \frac{1}{\tilde{h}_1} + \frac{\delta}{\kappa} + \frac{1}{\tilde{h}_2}, \quad (4.40)$$

where \tilde{h} is the convective heat transfer coefficient in a stream, κ the thermal conductivity of the tube material and δ the tube thickness. With use of Nusselt correlations the convective heat transfer coefficients are determined. Appendix D summarizes the Nusselt correlations for shell and tube flow in coil-wound heat exchangers and describes the calculation of the overall heat transfer coefficient.

The overall heat transfer coefficient is determined from an average of three positions in the heat exchanger: The position of average stream temperature, the hot side and the cold side, i.e. $(\overline{T_1}, \overline{T_2})$, $(T_{h,1}, T_{h,2})$ and $(T_{c,1}, T_{c,2})$ in relation to Fig. 4.12.

Using the minimum stream capacity and the average overall heat transfer coefficient, the heat exchanging area is derived from the Number of Transfer Units. With a heat exchanging area to volume ratio of $150 \text{ m}^2/\text{m}^3$ for coil-wound heat exchangers [79], also the heat exchanger packing volume is known.

Multi-stream heat exchangers

The effectiveness-NTU method, described above, works only for two streams. In multi-stream coil-wound designs, multiple tube streams share one shell. In the process of sizing therefore the actual multi-stream heat exchanger is split into a number of 'virtual' two-stream coil-wound heat exchangers equal to the number of tube streams, as shown in Fig. 4.15. The split in shell side mass flow is given by the enthalpy change ratio of the tube streams. In relation to Fig. 4.15 for stream 1:

$$\dot{m}_{sh,1} = \dot{m}_{sh} \frac{\dot{m}_{tu,1} \Delta h_{tu,1}}{\sum_i (\dot{m}_{tu,i} \Delta h_{tu,i})} \quad i = 1, 2, 3, \quad (4.41)$$

where Δh is the stream specific enthalpy change. Subscripts sh and tu refer to the shell or tube side. By summation over all 'virtual' two-stream heat exchangers, the total heat exchanging area and volume is obtained.

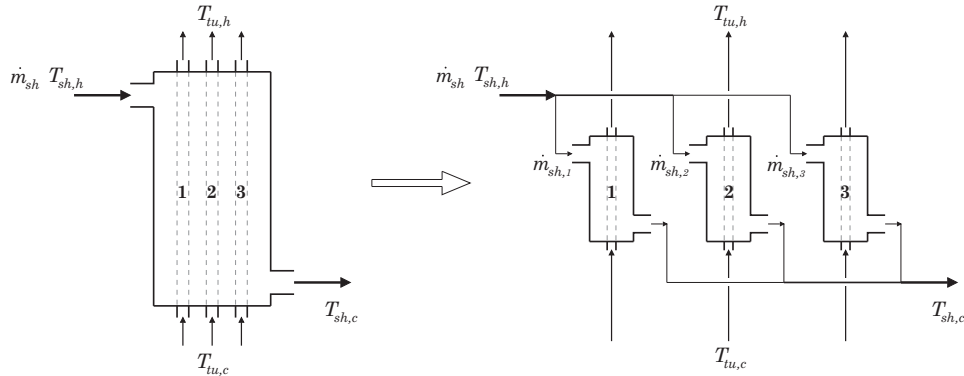


Figure 4.15: Split-up of a multi-tube coil-wound heat exchanger for sizing according to the ϵ -NTU method.

4.2.4 Rotating Particle Separators

The essence of the Rotating Particle Separator (RPS) and its separation principles were already discussed in Chapter 1. General performance indicators for the RPS such as the size of particles, energy consumption per unit flow and size of the unit are discussed by Brouwers et al. [22], Kroes [71] and Willems [139]. Several designs for specific applications have been proposed [13, 20, 25, 66]. In this section we derive scaling laws for the RPS in CRS applications, which are used to estimate the RPS size and apparatus volume.

The scaling laws are applied to the design described by Buruma et al. [25], to which we shall refer to as reference. A schematic of the RPS cross-section is shown in Fig. 4.16. The dimensions of the RPS presented by Buruma are summarized in Tab. 4.1. The pressurized RPS described by Buruma et al. was designed to separate water droplets from a compressed air stream under ambient temperature. The corresponding operational conditions are shown in Tab. 4.2 and compared against typical operation conditions expected in flue gas CO₂ separation.

Table 4.1: Dimensions of the RPS described by Buruma [25]

Total height	L_{RPS}	1.035	[m]
Engine height	L_{motor}	0.530	[m]
Pre-separator height	L_{pre}	0.053	[m]
Pre separator diameter	D_{pre}	0.214	[m]
Filter element height	L_{fe}	0.200	[m]
Filter element diameter	D_{fe}	0.165	[m]
Post-separator height	L_{post}	0.040	[m]
Filter core diameter	D_{core}	0.085	[m]
Inlet/outlet diameter	D_{in}	0.060	[m]
Channel diameter	d_{ch}	1.4	[mm]
Gap size	δ_{gap}	0.1	[mm]
Free space		0.122	[m]
$d_{p50\%,pre}$		7.8	[μ m]
$d_{p50\%,fi}$		1.5	[μ m]
$d_{p,post}$		179	[μ m]

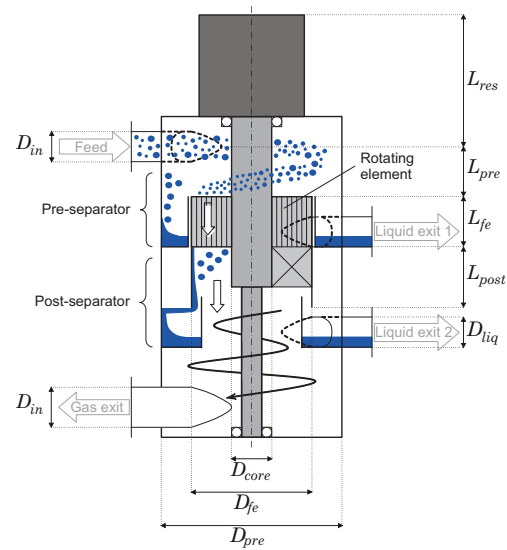


Figure 4.16: RPS cross-section.

There are four essential thermodynamic properties that have to be accounted for in the process of scaling. These four parameters are: volume flow, density, viscosity and surface tension. The scaling can be divided into three parts as shown in Fig. 4.16: the pre-separator, the filter element and the post-separator.

Table 4.2: Fluid properties and flow conditions of the reference RPS and typical conditions of the reference RPS in flue gas CO₂ capture for equal volume flow.

*According to mixture density at normal conditions ($[\text{nm}^3 \cdot \text{s}^{-1}]$).

¹Mixture property, i.e. vapor+liquid. # Vapor property.

Property	Reference [25]	Flue gas CO ₂ capture		Unit
Fluid	19/81 H ₂ O/air	50/50 CO ₂ /N ₂	20/80 CO ₂ /N ₂	[% _{vol}]
Pressure	4	36	80	[bar]
Temperature	20	-57	-59	[°C]
Mass flow ¹	0.35	8.4	12.3	[kg·s ⁻¹]
Density ¹	5.5(4.74#)	131(72.1#)	192(175#)	[kg·m ⁻³]
Volume flow ¹	0.064 (0.256*)	0.064 (5.3*)	0.064 (8.9*)	[m ³ ·s ⁻¹]
Surf. tension [44, 52]	72.88(H ₂ O)	0.015(CO ₂)	0.015(CO ₂)	[mN·m ⁻¹]

pre-separator

The pre-separator is constructed with a tangential inlet to provide a free vortex flow. The diameter of particles that are separated by the pre-separator with a 50% chance, $d_{p50\%,pre}$ is given by Willems [139]:

$$d_{p50\%,pre} = \sqrt{\frac{9\mu_g c_{ax,pre} (D_{pre}^2 - D_{ds}^2)}{8(\rho_p - \rho_g) c_{in}^2 L_{pre}}} \quad (4.42)$$

where μ_g is the dynamic viscosity of the gas or vapor, $c_{ax,pre}$ the axial fluid velocity in the pre-separator, D_{pre} and D_{ds} the diameters of the pre-separator space and the drive shaft, ρ_p and ρ_g the densities from the particles and the gas or vapor, c_{in} the inlet velocity and L_{pre} the height of the pre-separator section.

On the assumption that the $d_{p50\%,pre}$, the axial pre-separator fluid velocity $c_{ax,pre}$, and the inlet velocity c_{in} , are kept constant and that shaft and pre-separator diameter are proportional to each other, i.e. $D_{pre} \propto D_{shaft}$, it can be found that:

$$\overbrace{c_{ax,pre}}^{\text{constant}} = \frac{4Q}{\pi (D_{pre}^2 - D_{ds}^2)} \Rightarrow D_{pre} \propto \sqrt{Q}, \quad (4.43)$$

$$\overbrace{c_{in}}^{\text{constant}} = \frac{4Q}{\pi D_{in}^2} \Rightarrow D_{in} \propto \sqrt{Q}, \quad (4.44)$$

$$L_{pre} = \frac{9}{8} \frac{\overbrace{c_{ax,pre}}^{\text{constant}}}{c_{in}^2 d_{p50\%,pre}} \frac{\mu_g}{(\rho_p - \rho_g)} (D_{pre}^2 - D_{ds}^2) \Rightarrow L_{pre} \propto \left\{ \frac{Q}{(\rho_p - \rho_g)} \right\}, \quad (4.45)$$

with Q the mixture volume flow. The proportionalities given by Eqs. (4.43) to (4.45) are used to upscale the pre-separator and inlet and RPS outlet.

filter-element

Small droplets that are not separated in the pre-separator ($<20 \mu\text{m}$) enter the rotating filter element. The filter element is made up of a large number of axial channels with a channel diameter much smaller than the filter diameter (typically 3 mm). Droplets that enter a channel are centrifuged to the channel wall where they form a small liquid stream. The particles that are collected on the channel wall with a 50% change is given by [139]:

$$d_{p50\%,fe} = \sqrt{\frac{108\mu_g d_{ch} Q}{\Omega^2 (\rho_p - \rho_g) \pi L_{fe} (1 - \varepsilon) (D_{fe}^3 - D_{core}^3)}}, \quad (4.46)$$

with d_{ch} the filter element channel diameter, Ω the angular velocity of the element, L_{fe} the length of the filter element and D_{fe} and D_{core} the filter element outer and core diameter. The correction factor $(1 - \varepsilon)$ is used to correct the axial velocity for the blocked cross sectional area in between channels.

In scaling of the RPS, it is essential for the flow in the filter element channels to remain in the region of (semi-)stability. The region of stability is identified by Kroes [71] and is shown in Fig. 4.17 as a function of the axial (Eq. (4.47)) and angular (Eq. (4.48)) Reynolds number:

$$Re_{ax,ch} = \frac{\rho_g c_{ax,ch} d_{ch}}{\mu_g}, \quad (4.47)$$

$$Re_{\theta,ch} = \frac{\rho_g \Omega d_{ch}^2}{4\mu_g}. \quad (4.48)$$

Stable separation has been proven for both the 'stable RHPF' and 'convective instabilities' region [71]. Also indicated in Fig. 4.17 is the RPS, which is used as reference.

Assuming proportionality between the filter outer and core diameter ($D_{core} \propto D_{fe}$) we obtain:

$$(D_{fe}^2 - D_{core}^2) = \frac{\overbrace{4}^{\text{constant}}}{\pi(1-\varepsilon)} \frac{Q}{c_{ax,ch}} \Rightarrow D_{fe} \propto \sqrt{Q}. \quad (4.49)$$

In case of a natural (flow) driven RPS, conservation of angular momentum from inlet to filter element applies. The angular speed of the filter element can thus be derived from:

$$\overbrace{c_{in}}^{\text{constant}} = \Omega D_{fe}, \Rightarrow \Omega \propto \frac{1}{\sqrt{Q}}. \quad (4.50)$$

If implemented into the angular Reynolds number for a constant filter channel diameter we find that:

$$Re_{\theta,ch} = \frac{\overbrace{d_{ch}^2}^{\text{constant}}}{4} \Omega \frac{\rho_g}{\mu_g} \Rightarrow Re_{\theta,ch} \propto \left\{ \frac{1}{\sqrt{Q}} \frac{\rho_g}{\mu_g} \right\} \quad (4.51)$$

With the assumption of constant axial filter channel velocity, the axial Reynolds number scales as:

$$Re_{ax,ch} = \overbrace{c_{ax,ch} d_{ch}}^{\text{constant}} \frac{\rho_g}{\mu_g}, \Rightarrow Re_{ax,ch} \propto \frac{\rho_g}{\mu_g} \quad (4.52)$$

Because of major differences in kinematic viscosity ($\nu = \frac{\mu}{\rho}$) between the reference conditions and industrial operation (cf. Tab. 4.2), both Reynolds numbers increase significantly by a factor 20–35. The angular Reynolds number however decreases with increasing volume flow. Upscaling therefore follows a line typically steeper than the 45° line indicated in Fig. 4.17. On extrapolation of Fig. 4.17 to higher axial Reynolds numbers, the assumptions of constant axial channel velocity and conservation of angular momentum thus lead to stable separation.

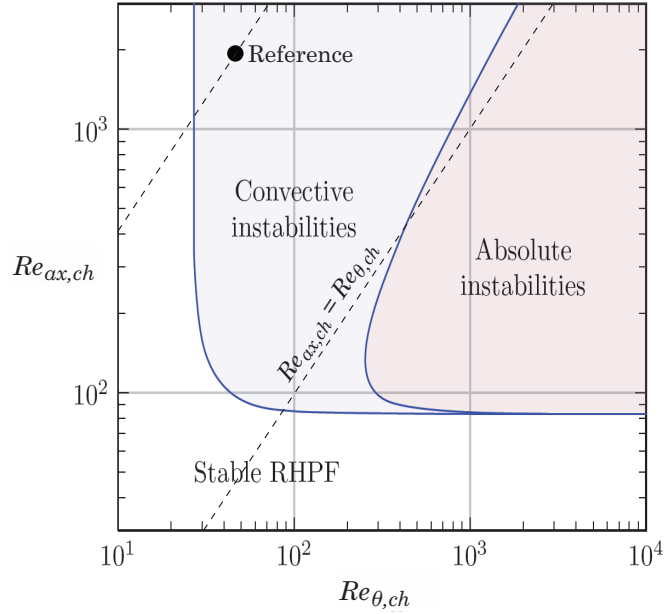


Figure 4.17: Stability of channel flow in the RPS element. Reproduced and edited from [71]

Assuming a constant $d_{p50\%fe}$, we find for proportionality of the filter length:

$$L_{fe} = \frac{\overbrace{108d_{ch}}^{\text{constant}}}{\pi d_{p50\%,fe}^2 (1-\varepsilon)} \frac{\mu_g}{(\rho_p - \rho_g)} \frac{Q}{\Omega^2 (D_{fe}^3 - D_{core}^3)},$$

$$\Rightarrow L_{fe} \propto \begin{cases} \sqrt{Q} \\ \frac{\mu_g}{(\rho_p - \rho_g)} \end{cases} \quad (4.53)$$

post-separator

At the end of the filter element, the liquid stream breaks up in large droplets (typically $\geq 50 \mu\text{m}$). The collection of these droplets occurs in the post-separator, where these droplets are collected on a co-rotating wall with a diameter equal to the filter element outer diameter D_{fe} . The gas in the post separator rotates as a solid body with the angular velocity of the filter element. Droplets in the post-separator move outward due to the centrifugal action and downward with the axial flow. The time it takes for a droplet to move from the filter element inner diameter D_{core} to the outer diameter D_{fe} can be estimated from a radial force balance between the centrifugal force and two counteracting forces, the buoyancy force and the drag force. Willems [139] derived a particle residence time from this force balance on the assumption that the particle acceleration time is very short:

$$\tau_{post} = \sqrt{\frac{3C_D \rho_g D_{fe} \left(1 - \sqrt{\frac{D_{core}}{D_{fe}}}\right)^2}{2(\rho_p - \rho_g) d_{p,post} \Omega^2}}, \quad (4.54)$$

where τ_{post} is the droplet residence time (from filter element to post-separator wall), $d_{p,post}$ the droplet break off diameter at channel exit. C_D is the drag coefficient for flow around a sphere and has roughly a constant value of 0.44 for turbulent flow around the particle; i.e. $Re_p = \frac{\rho_g c_{ax, ch} d_{p50\%, post}}{\mu_g} > 10^3$ [139].

Combination of the post-separator residence time and the axial velocity at filter element exit results in the length required to separate a droplet traveling from channel exit at the filter element inner diameter to post-collector wall. With $D_{core} \propto D_{fe}$, it follows that:

$$L_{post} = \frac{\overbrace{2\sqrt{6}C_D}^{\text{constant}}}{\pi} \sqrt{\frac{1}{d_{p,post}} \frac{\rho_g}{(\rho_p - \rho_g)} \frac{D_{fe}}{\Omega^2} \left(1 - \sqrt{\frac{D_{core}}{D_{fe}}}\right)^2} \frac{Q}{(D_{fe}^2 - D_{core}^2)},$$

$$\Rightarrow L_{post} \propto \begin{cases} d_{p,post}^{-1} \\ Q^{1.5} \\ \sqrt{\frac{\rho_g}{(\rho_p - \rho_g)}} \end{cases} \quad (4.55)$$

In contrary to the pre-separator and the filter element, the post-separator droplet break off diameter $d_{p,post}$ cannot be chosen, fixed or scaled by proportionality. The break off diameter of an upscaled RPS is settled upon determination of the filter element diameter. Willems [139] derived a conservative estimation for the droplet break off diameter at the end of the filter element. The estimation is based on the balance between centrifugal force, shear force and surface tension force, acting on the droplet at channel exit. From this balance the droplet break off diameter can be

estimated as:

$$d_{p50\%,post} = \frac{6}{\rho_p \Omega^2 D_{fe}} \left(\sqrt{\frac{\rho_p \Omega^2 D_{fe} \sigma_p}{6} + \left(\frac{\rho_g C_D c_{ax,ch}^2}{16} \right)^2} - \frac{\rho_g C_D c_{ax,ch}^2}{16} \right), \quad (4.56)$$

where σ_p is the particle(droplet) surface tension σ_p . The drag coefficient C_D is again obtained for flow around a sphere.

The RPS apparatus volume follows from the RPS shell diameter and RPS height. The Shell diameter of the upscaled RPS is given by the diameter of the scaled pre-separator D_{pre} (neglecting shell thickness and bottom and top flanges). The length of the upscaled RPS is calculated according to:

$$L_{RPS} = L_{pre} + L_{fe} + L_{post} + 1.5D_{in} + L_{res}, \quad (4.57)$$

with L_{res} the residual height, which is assumed constant and contains the engine height and the free space that is required for constructional reasons. In upscaling the residual length is kept constant $L_{res} \approx 650\text{mm}$.

4.3 Summary and Conclusions

In this chapter we discussed the tools to determine apparatus volume and apparatus energy conversion or heat exchange. We considered radial turbo-machinery and expansion valves, coil-wound heat exchangers and the RPS, which are all key components in the CRS process.

In the first section of this chapter we discussed the calculation of entropy and enthalpy for real fluids. Calculation of entropy and enthalpy differences between two states (p, T) is performed over pressure at constant temperature, described by departure functions, and over temperature at sufficiently low constant pressure, described by ideal heat capacity correlations. The combination of departure functions and ideal heat capacity correlations provides the means to determine enthalpy and entropy differences. Derivation of an expression for the departure functions from the Peng-Robinson equation of state allowed us to calculate enthalpy changes in both gas and liquid mixtures. Combination with the phase equilibrium model enabled us to determine enthalpy and entropy changes between two states (p, T) regardless of what fluid phase (vapor-only, liquid-only, vapor-liquid) the two states are in.

The calculation of enthalpy and entropy differences is applied to the thermodynamic simulation of temperature and pressure changers (i.e. turbo-machinery, expansion valves and heat exchangers). For the simulation of pressure changers, we developed and briefly described an iterative model to calculate thermodynamic compression/expansion paths and to determine applied/consumed work of turbo-machinery.

In the second part of the chapter we discussed the sizing of expanders, compressors, heat exchangers and the RPS. For radial turbo-machinery, an overall package diameter

is defined, which is regarded as a measure for apparatus volume. Basic turbine theory has been described and applied to calculate the overall package diameter.

The size of heat exchangers is estimated with use of the NTU-effectiveness method. The Number of Transfer Units (NTU) is a measure for size and can be used to derive the heat exchanging area. For estimation of the NTU in condensing/evaporating heat exchangers, we redefined the heat exchanger effectiveness and capacity ratio. Additionally we combined the NTU- ϵ correlations for cross- and counter-flow configurations to represent coil-wound heat-exchangers. We showed that a good balance between heat exchanger size and effectiveness is obtained for $2 \leq \text{NTU} \leq 4$. This range is taken as a design criterion for process heat exchange.

For size estimation of the RPS we made use of a reference design. We formulated new scaling laws, based on existing design equations, whereby volume flow, droplet and gas density, gas viscosity and droplet surface tension were considered.

The methods described for the estimation of equipment volume and the determination of energy consumption/production and/or heat exchange are adequate tools for the evaluation of the CRS process. These methods are applied in the next chapter, where we estimate the size and energy consumption of the CRS process in flue gas CO₂ capture for comparison with competing CO₂ separation technology.

Coal Combustion CO₂ Capture

Almost half of worldwide emitted CO₂ (43.1%) is related to the energy conversion of coal. 62% of the world energy supplied by coal in 2010 was used for electricity production and combined heat and power [69]. The prospect of a significant increase in global coal consumption in the near future caused by developing countries is therefore a big concern towards climate change [141]. CO₂ emissions must therefore be reduced, starting with the major source: coal.

One of the options for near term CO₂ reduction is the capture and storage of CO₂ (CCS). Capture, transport and storage of CO₂ unfortunately comes with a penalty in energy consumption, thereby increasing the price of electricity and decreasing the nett energy production. This penalty makes the application of CCS unattractive, especially for developing countries who want to increase their near term energy production against the cheapest price to feed their emerging economies. To limit global climate change and reduce emissions of CO₂, there is a need for cheap carbon capture technology, especially for application in developing countries such as China and India.

Essentially there are three routes to CO₂ capture: the post-combustion, pre-combustion and oxy-fuel-combustion route. The three routes are depicted in Fig. 5.1.

In the post-combustion system, fuel (coal) is combusted with normal air. CO₂ is removed from the flue gas after combustion. This is the most difficult system, because of the low concentration of CO₂ (typically $\sim 14\%_{vol}$) in the flue gas. In the pre-combustion system, coal is gasified (partially combusted with pure oxygen in a reduced oxygen environment). The resulting gas is shifted in a water/shift reactor to form syn gas (H₂/CO₂) from which the CO₂ is removed. In the oxyfuel system, coal is combusted with pure oxygen to form (almost) pure CO₂. In theory oxyfuel systems do not contain a CO₂ separation process. In practice however, air leakage into the boiler reduces the CO₂ purity to 70–85%_{vol} d.b. CO₂d.b.* (c.f. Appendix C and Tab. 5.2), which requires an additional CO₂ separation process. Oxyfuel can therefore be seen as a special case of the post-combustion system.

*d.b.: dry moist free basis.

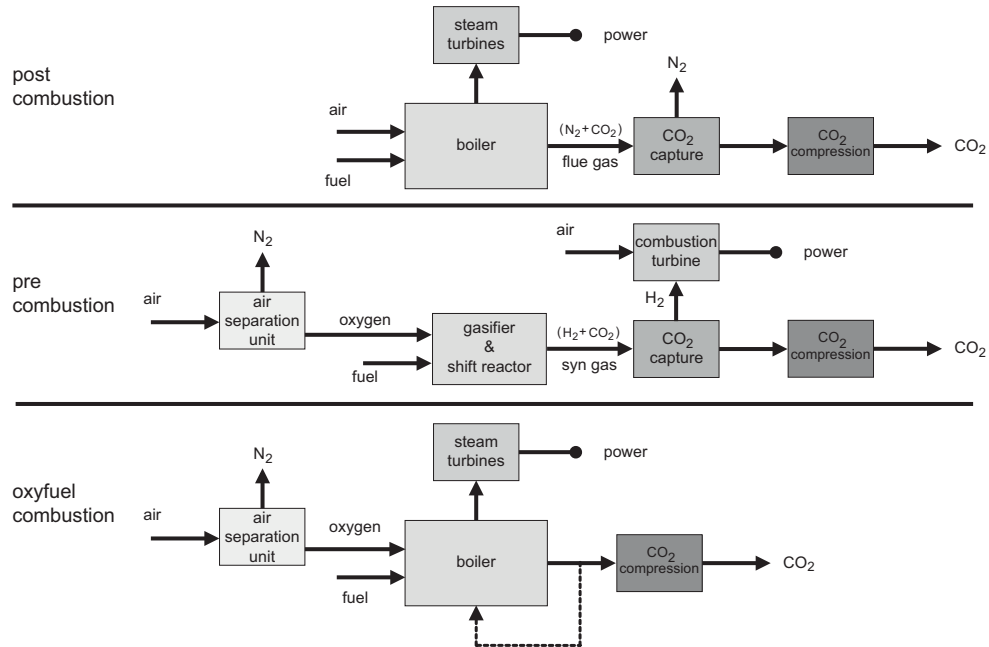


Figure 5.1: Block diagrams of the three routes to CO₂ capture: the post-combustion, pre-combustion, and oxyfuel system.

In this chapter we describe capture targets for CO₂ and discuss the process of Condensed Rotational Separation for the 'post-combustion' capture of CO₂ from flue gas. We focus on coal-fired electricity production, the major source of coal related CO₂ emissions and we compare CRS with conventional CO₂ capture technology to assess the feasibility of CRS in this application.

5.1 Capture Targets

Capture of CO₂ involves two important parameters: the amount of CO₂ captured, which can be defined by the CO₂ recovery (cf. Eq. (3.2)) and the purity of the separated CO₂ stream.

Concerning the stream purity resulting from CO₂ capture processes, there is a lively discussion in literature as to how pure a CO₂ stream should be and whether it can contain impurities, such as H₂O, SO₂, O₂, etc. The final stream purity is however imposed by health, safety and environmental risks, by transport requirements and by utilization (enhanced oil recovery, soda production, welding gas, green houses, etc.) or storage destination (geological or mineral storage).

Proposals for CO₂ stream purity can be found in EU frameworks, which propose a

captured-CO₂ stream purity of at least 95%_{vol} CO₂, [19], by the European DYNAMIS project, which recommend a CO₂ concentration of at least 95.5%_{vol} for transport [134] and by the NETL, who recommend a conceptual design target of at least 95%_{vol} [101].

As described in Section 3.4.1 and Appendix C, the main impurities in flue gas are water vapor, sulphur-dioxide and oxygen. Recommendations on allowed impurity presence can be found from the European DYNAMIS project [134] and the NETL guidelines [101], and are summarized in Tab. 5.1:

Table 5.1: Important recommended targets for the presence of impurities in the transport of captured CO₂. For all targets see [101, 134]. *Based on carbon steel piping. #NO_x

	DYNAMIS[134]	NETL[101]*	unit
CO ₂	≥95.5	≥95	[% _{vol}]
H ₂ O	≤200	≤300	[ppm _{vol}]
O ₂	-	≤4	[% _{vol}]
SO ₂	≤100	≤100	[ppm _{vol}]
NO ₂	≤100	≤100 #	[ppm _{vol}]
N ₂	≤4	≤4	[% _{vol}]
Ar	≤4	≤4	[% _{vol}]
H ₂ S	≤0.02	≤0.01	[% _{vol}]
CH ₄	≤4 (sequestration) ≤2 (EOR)	≤4 (sequestration) ≤1 (EOR)	[% _{vol}]

There are still no clear and strict international guidelines or frameworks that define the amount of CO₂ capture from flue gases. National or local CO₂ reduction policies often describe the targets vaguely as 'the practically and technologically best achievable CO₂ capture rate'. In the setting of flue gas CO₂ capture, the technologically best achievable CO₂ capture rate (CO₂ recovery) is currently believed to be at least 90% [32].

5.2 Post Combustion CO₂ Capture Technologies

A wide range of technologies nowadays exist for the capture of CO₂ from gas streams, although most of them have not been designed for power-plant scale operation [51, 95]. The range of CO₂ capture technologies is depicted in Fig. 5.2 and can be divided into four categories: absorption, adsorption, cryogenics and membranes.

Three of these categories contain technologies that either are currently already commercially available for large scale post-combustion CO₂ capture or are in a stadium of non-commercial small scale testing. These categories are chemical absorption, low temperature processes and membranes. We shall briefly discuss these techniques. For a discussion of all CO₂ removal techniques, the reader is referred to other literature [34, 51, 73, 95].

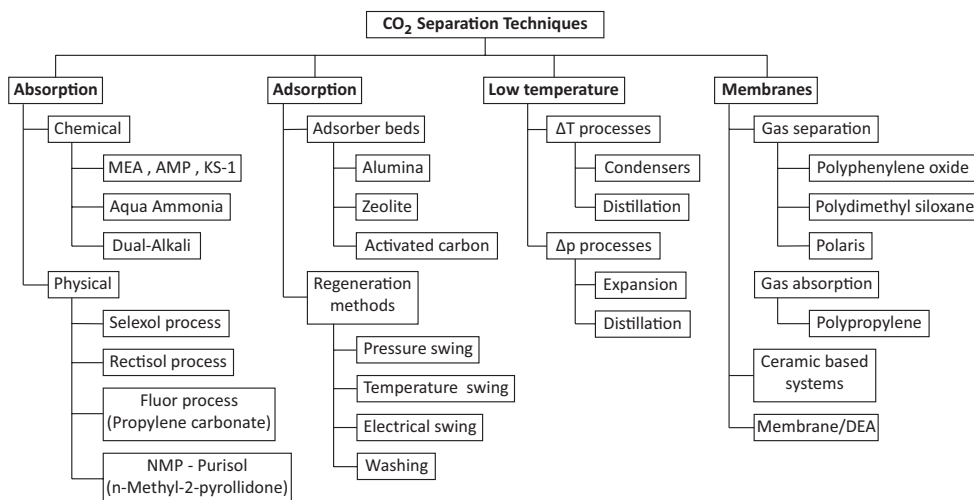


Figure 5.2: Available options for CO₂ removal from gas. In edited form reproduced from [95].

5.2.1 Chemical absorption

Chemical absorption is the standard technology for gases with low to moderate CO₂ partial pressures.

Chemical absorption of CO₂ from gas streams depends on acid–base neutralization reactions, using a base as an absorbent. CO₂ reacts with the absorbent to form a weakly bonded intermediate compound (CO₂ rich absorbent). The weak bond in the intermediate compound can be broken down by application of heat (stripping), resulting in almost pure gaseous CO₂ ($\geq 98\%_{mole}$) and the original (CO₂ lean) absorbent.

A process scheme of an absorption process for the absorption of CO₂ from flue gas is shown in Fig 5.3.

After removal of residual water droplets and some of the remaining particulates in an inlet knockout drum, flue gas is fed to the bottom of the absorber tower (1) where it is brought in contact with the solvent. CO₂ lean solvent (10) is sprayed downward from the top of the absorber tower while flue gas flows upward. During this process, CO₂ is absorbed in the solvent. CO₂ lean flue gas leaves the top of the tower and is led to stack (2). The CO₂ rich solvent at the bottom of the absorber tower (3) is pumped through the lean/rich heat exchanger and fed to the stripper (4).

The rich solvent is sprayed into to the top of the stripper tower, where it contacts with steam. While flowing down in the stripper tower, the solvent heats up and releases the absorbed CO₂. An upward flowing mixture of steam and gaseous CO₂ leaves the top of the stripper tower (6) and is fed to the condenser. In the condenser steam is condensed and separated from the gaseous CO₂ in the reflux drum. Nearly pure CO₂ leaves the reflux drum as a gas (7). Condensed steam is pumped back into the

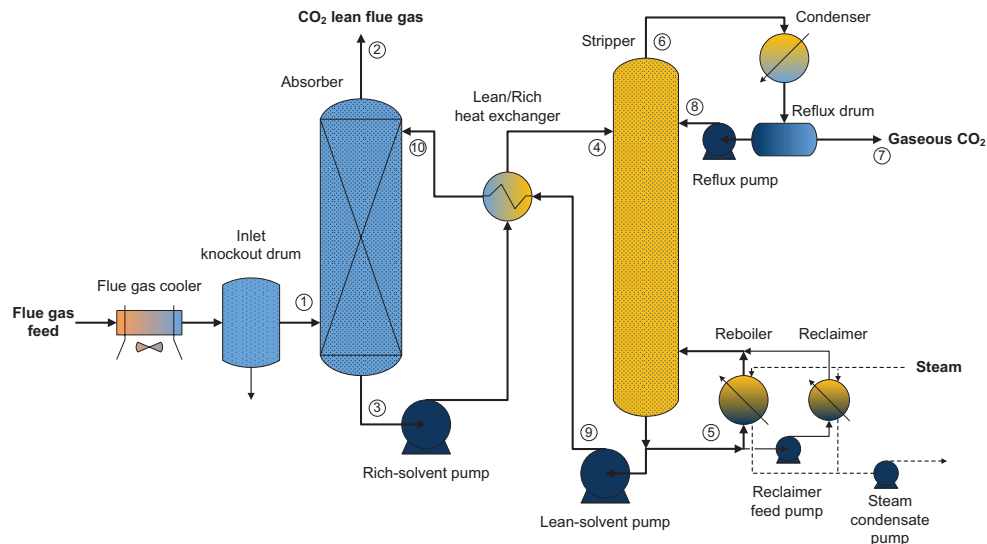


Figure 5.3: A scheme of an absorption process for post-combustion CO₂ removal. Based on the amine absorption process model described by de Rijke [109].

stripper tower (8). At the bottom of the stripper tower solvent is fed to the reboiler and reclaimer (5) where steam from the power plant is used to partially vaporize the solvent into steam. CO₂ lean solvent from the bottom of the stripper tower is pumped (9) through the lean/rich heat exchanger and fed to the top of the absorber tower (10).

The solvent is made up of water and an absorbent. The most conventional absorbent in chemical absorption of CO₂ from gas is monoethanolamine (MEA). MEA is used in the natural gas industry already for more than 60 years and is seen as the most mature technology for removal of CO₂. [95].

Disadvantages in MEA for flue gas CO₂ capture are found in the low CO₂ loading capacity (g CO₂ absorbed/g absorbent), in the severe corrosive character, in amine degradation by flue gas impurities such as SO₂, NO₂, HCl, etc. and by high energy consumption necessary for the high temperature stripping of the CO₂ rich absorbent. By development of new absorbents such as DEA (diethanolamine), MDEA (methyldiethanolamine) and AMP (2-amino-2-methyl-1-propanol), these disadvantages have been reduced to some extent [95].

The technology of chemical absorption by amine based absorbents for post-combustion CO₂ capture is under demonstration at small and large scale coal-fired power plants [34, 91] and is commercially purchasable from major players such as Fluor (Econamine FG Plus) and Mitsubishi Heavy Industries (KM-CDR process) [34, 51, 95].

Absorption processes based on other absorbents, such as aqueous ammonia solvents, do not suffer from degradation by flue gas impurities, do not pose a corrosion problem, and require potentially a lower absorbent regeneration energy. With exception of

the Alstom Chilled Ammonia process based on an ammonium carbonate absorbent [70, 91, 126], these absorption based processes are not yet as far developed as amine based absorption processes for post-combustion CO₂ capture.

The energy penalty for the post-combustion capture of CO₂ is almost completely dominated by the thermal energy required for regeneration of the absorbent. In literature, for 85–90% CO₂ removal from flue gas, numbers are reported for MEA solvents that vary between 3.2–4.0 MJ_{th}/kg CO₂ removed [1, 50, 94, 111] and 2.6–3.2 MJ_{th}/kg CO₂ removed by using amine-based proprietary solvent blends [50, 103].

For simulation of the MEA chemical absorption process, an in-house model was used [109]. This model was constructed originally to serve a feasibility study towards the combination of CRS and amine absorption for the application of CO₂ removal from severe contaminated natural gas fields. The model is constructed on the monoethanolamine (MEA) solvent and has been adapted for CO₂ removal from flue gas. By simulation for 90% CO₂ removal, the thermal regeneration energy of the MEA solvent was found to be 4.2 MJ_{th}/kg CO₂.

In determination of the absorption plant installation size, the size of the absorber, stripper, inlet knockout drum, reboiler, reclaimers, condenser and reflux drum have been taken into account (cf. Fig. 5.3). The energy penalty of the absorption plant, as calculated by the in-house model, covers the heating and regeneration of the MEA solvent and the electric energy consumption of the lean, rich, reflux, steam condensate and reclaimers feed pumps. This adapted in-house model is applied in the comparison with CRS (Section 5.7).

5.2.2 Membranes

A relatively novel capture concept is the use of selective membranes for the separation of CO₂. Membranes are semi-permeable barriers, able to separate substances by various mechanisms (solution/diffusion, adsorption/diffusion, molecular sieve and ionic transport). Membranes can be categorized into two groups, based on material: organic (polymeric) and inorganic (carbon, zeolite, ceramic or metallic). A typical scheme of a cross-flow CO₂ permeable gas-separation membrane is shown in Fig. 5.4:

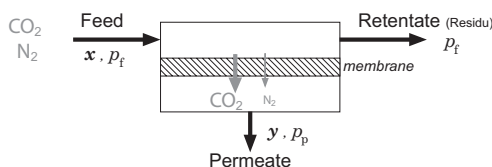


Figure 5.4: Cross-flow CO₂ permeable gas separation membrane.

The performance of membranes is indicated by two properties: permeability and selectivity. Pure component permeability is the membrane thickness scaled molar flux

(flow per area) of a pure component through the membrane material per unit partial pressure drop. The selectivity is the ratio of two pure component permeabilities and indicates the membranes preference to pass one component over another.

In general, membrane transport can be described by the solution-diffusion model [8]. According to the solution diffusion model, the flux through a membrane is given by:

$$\mathcal{Q}_i = \frac{\mathbb{P}_i}{\delta_{mem}} A_{mem} (x_{f,i} p_f - y_{p,i} p_p) , \quad (5.1)$$

where \mathcal{Q}_i is the molar flow of component i through the membrane, \mathbb{P}_i the component permeability, δ_{mem} the membrane thickness, A_{mem} the membrane area, x_i and y_i the molar component feed and permeate concentration and p_f and p_p the feed and permeate pressure.

Membranes are physically limited in the separation that can be achieved. Small membranes are able to produce high purity gas, but at a low flow rate. Increasing the membrane size increases the product (permeate) flow rate but at a penalty of product purity. Post combustion CO₂ capture by membranes requires both a large CO₂ permeate flow and a high permeate CO₂ purity, which requires complex membrane process schemes [95].

Today only one membrane pilot-scale field-application is known for post-combustion CO₂ capture [91]: the membrane system of MTR (Membrane Technology Research). MTR has developed a new polymeric membrane, 'Polaris', providing both high CO₂/N₂ selectivity and a CO₂ permeability about ten times higher than other commercial polymeric CO₂ permeable membranes [83]. Initial field-testing at the Arizona Public Service power plants in the USA has shown good separation performance and minor membrane degradation effects over time [3].

The MTR Polaris typically benefits from the presence of water vapor. Water permeation through a Polaris membrane is even faster than CO₂ permeation [83]. The average partial pressure of CO₂ on the feed/retentate side of the membrane increases due to water presence, while the average CO₂ partial pressure on the permeate side decreases. The CO₂ flux through the membrane thereby increases (Eq. 5.1). The presence of water vapor thus enhances CO₂ separation. The typical membrane size reduction for similar membrane performance by the presence of water in Polaris membranes is 1–10%, depending on feed water content [83].

The MTR system contains a two stage membrane system supplemented with a final hybrid membrane-distillation combination and is shown in Fig. 5.5. In the MTR membrane process, 'cleaned' flue gas from the boiler is led through a cross-flow membrane unit I where a CO₂ rich permeate stream (2) is formed. The CO₂ depleted flue gas from module I (3) is led through a counter-flow/sweep membrane module II, where some of the remaining CO₂ is removed. Separation in membrane unit II is facilitated rather by the air sweep flow (4), than by an absolute pressure difference over the membrane. CO₂ permeated through module II is fed back to the boiler of the power plant by the air sweep flow. The CO₂ rich permeate stream (2) is extracted in module I by a vacuum. After dehydration (7), the CO₂ rich permeate stream is

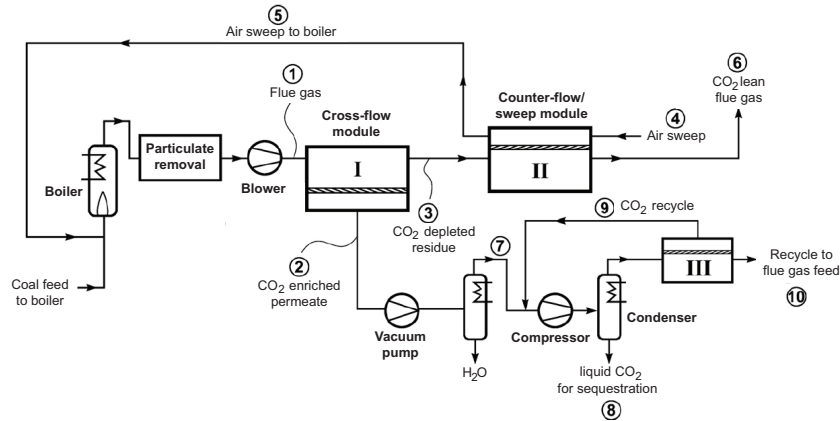


Figure 5.5: The MTR post-combustion membrane CO₂ capture system. Reproduced from [83].

compressed and further purified in a condenser or distillation process, producing high purity liquid CO₂ at elevated pressure (8). Remaining vapor from the distillation process is led through a compact third membrane module III, producing a permeate stream with about the same composition as the distillation process feed (7). Residual vapor from the third module (10) is recycled to the front of the separation process (1).

The process of MTR is capable of separating $\geq 90\%$ of the CO₂, achieving a CO₂ purity in the sequestration stream (8) of $\geq 95\%_{vol}$ at 140 bar and is claimed to consume only 16% of the gross power produced by the coal-fired power plant. Membrane skid costs are thereby claimed to be low by use of low-cost non-corrosive materials, which is possible due to the moderate operating temperature and low operation pressure [83].

5.2.3 Low temperature processes

Low temperature post-combustion separation methods rely on the removal of CO₂ by phase creation and separation. Thereby CO₂ is condensed into a high purity liquid or anti-sublimated into a pure solid. In essence two methods exist: phase creation by temperature change and phase creation by pressure change. The first category contains conventional temperature distillation processes and condensers. The second category contains expansion driven processes and pressure distillation, such as CRS.

Cryogenic techniques are difficult to apply in post-combustion CO₂ capture, due to the low partial pressure of CO₂ in flue gas [14].

Only two cryogenic anti-sublimation CO₂ capture technologies are reported in literature to make their way to field-testing: The Enecogen CO₂ capture process [62, 91] and the AnSu (Anti-Sublimation) process [33, 96]. The Enecogen CO₂ capture project

has lately been canceled. The AnSu process is demonstrated on lab scale, with plans for pilots of 24–120 TPD CO₂ capture [96].

The anti-sublimation process relies on phase separation by freeze-out of CO₂ in two recuperative condensers under near atmospheric pressure at a temperature of -120 – -135°C. In alternating swing operation one condenser freezes CO₂, in the other frozen CO₂ is liquified by heating and pressurization.

Due to the low-temperatures involved, the power consumption of these processes is highly sensitive to the efficiency of the refrigeration cycles. For the AnSu process, the CO₂ capture costs were estimated at 1.2 MJ_e/kg CO₂ removed for 90% CO₂ capture [33, 96]. Anti-sublimation processes for flue gas CO₂ removal are believed to be comparable in energy consumption with chemical absorption and oxyfuel processes [14, 96, 113].

5.3 Oxyfuel CO₂ Capture

Coal-fired oxyfuel combustion relies on the combustion of coal with (almost) pure oxygen. Due to the absence of nitrogen in the combustion air supply, CO₂ rich flue gas is obtained. Combustion with oxygen instead of air results in much higher combustion temperatures. As materials that can withstand these high temperatures are costly, flue gas recycle (FGR) is used (Fig. 5.1) to reduce the temperatures inside the boiler. The amount of recycle can go up to two third of the flue gas mass flow downstream of the boiler [65]. As coal-fired boilers typically operate just below ambient pressure, ingress of ambient air occurs. The amount of air ingress in new-built oxyfuel coal-fired power plants is estimated at approximately 3% of the total flue gas mass flow upstream of the recirculation branch [64]. The typical flue gas CO₂ content in oxyfuel derived flue gas from coal combustion is approximately 70–85%_{vol} d.b. CO₂ (c.f. Tab. 5.3).

Coal-fired oxyfuel technologies are not yet commercially available although a number of smaller pilot scale oxyfuel coal-fired power plants are built. Examples are found by Vattenfall, with the 30MW_{th} coal-fired oxyfuel pilot plant 'Schwarze Pumpe' in Germany [5, 91, 122] and the CS Energy's 30MW_e oxyfuel project at the Callide-A coal-fired power plant in Australia [81, 91] which entered the demonstration phase on December 15, 2012[†]. In addition to existing small-scale pilot plants, a number of large oxyfuel demo plants (100–500MW_{th}) are currently in development [51, 91, 133].

Due to the requirement for high purity oxygen and the need to further purify the CO₂ rich flue gas to meet the capture requirements, the energy penalty involved with oxyfuel CO₂ capture is mainly dominated by air separation and to lesser extent by final CO₂ purification.

[†]www.mitsui.com/jp/en/release/2012/1199411_3607_3607.html

5.3.1 Air Separation

There are essentially four methods to obtain high purity oxygen from air: cryogenics, adsorption swing processes, membranes and chemical absorption methods [28, 86]. Cryogenic air separation is currently the only viable technology capable of producing the enormous amounts of high purity oxygen required for a full scale oxyfuel coal-fired power plant [4]. From the power-plant model, described in Appendix C, the magnitude of oxygen requirement for a 500MW_e coal-fired oxyfuel power plant is estimated at 8200 TPD (tonnes per day).

Tab. 5.2 summarizes selected values for mechanical energy requirement and oxygen purities and reflects the basic magnitude of today's feasible energy costs for large scale cryogenic oxygen production. The energy costs of oxygen purification by cryogenic air

Table 5.2: Reported values in literature on energy consumption and oxygen product purity in large capacity cryogenic air separation processes.

source	year	specific power (kJ _e /kg O ₂)	O ₂ purity (% _{vol})
Castle [28]	2002	767	95–98
Seltzer et al. [117]	2007	792	99
Zanganeh & Shafeen [144]	2007	759	95
Hong et al. [60]	2009	882	99
Darde & Prabhakar [41]	2009	576–846	95–99
Anheden et al. [5]	2011	1177–1206	99.5
Higginbotham et al. [59]	2011	529–684	95
Tranier et al. [128]	2011	576–720	95
Estimated averages		640 900	95 99

separation rise exponentially in the high purity end ($> 90\%_{vol}$ O₂) [41]. In practice air in-leakage requires the application of a final CO₂ purification process. Potential energy savings can therefore be made on oxygen enrichment by using moderate purity oxygen ($\sim 95\%_{vol}$ O₂), instead of high purity oxygen ($\geq 99\%_{vol}$ O₂) [59].

There is one other development in air separation that is worth mentioning: Ionic Transport Membranes (ITM). The ITM is an extremely compact 100% O₂ selective ceramic membrane which, under pressure (~ 35 bar) and high temperature (800–900°C), ionizes and separates oxygen molecules from air. The ITM is under development by Air Products and is currently field-tested in their new 100 TPD ITM test facility in Convent, Louisiana, USA. Air Products hopes to enter commercialization between 2017 and 2020 [106]. Oxygen purities up 99.9%_{vol} on the O₂ rich side and down to 10%_{vol} on the O₂ depleted side (O₂ recovery from air of 58%) have been reported [107]. The ITM is claimed to potentially reduce the energy consumption of oxygen production by 35–60%, compared to cryogenic air separation [6], but requires either a separate fuel combustor or some form of advanced power plant integration to achieve the high temperature ITM feed air.

5.3.2 CO₂ purification

Tab. 5.3 summarizes different raw oxyfuel-derived flue gas compositions encountered in literature. Water is excluded from Tab. 5.3 as its content varies with coal type and its presence is often unwanted in purification. The raw oxyfuel-derived flue gas CO₂ content, found from Tab. 5.3 is typically about 5–25%_{vol} d.b. lower than the transport requirement (cf. Tab. 5.1). If CO₂ is to be transported, utilized or stored final CO₂ purification of the oxyfuel-derived flue gas is a requirement.

Table 5.3: CO₂ Purification island feed stream compositions, reported in literature and Appendix C of this work. Compositions are on a dry basis (d.b.).

	Anheden et al. [5]	Besong et al. [15]		Ritter et al. [110]	White et al. [137]	this work appendix C ASU: 95% _{vol} O ₂
		new plant	retrofit plant			
coal type	Lignite	Bituminous	Bituminous	-	-	Bituminous
CO₂ % _{vol}	90.6	83.5	70.5	77.8	75.7	79.0
N₂ % _{vol}	4.2	9.8	21.3	14.8	15.1	14.7
O₂ % _{vol}	<5.2	3.0	5.0	4.5	6.2	6.3
Ar₂ % _{vol}	-	3.7	3.0	2.8	2.4	-
SO₂ ppm _{vol}	< 42	600	1210	-	4240	-
CO₂ ppm _{vol}	< 190	< 120	485	-	-	-
NO_x ppm _{vol}	< 615	< 120	120	-	425	-

Several CO₂ purification systems have been investigated from simple compressor and single CO₂ condenser or rectification column configurations, to three stage separation processes with intermediate compression and cooling [15, 41, 78, 137, 145]. All systems start with an initial compression and water knockout by molecular sieves, absorption or another water removal technique, after which CO₂ is purified by a condensation/liquefaction section.

Darde et al. [41] compared, for a varying CO₂ content in the CO₂ rich flue gas, flue gas compression without purification to both partial condensation in a cold-box[‡]/flash-separation-vessel and a cold-box/distillation-column combination. Without power plant heat integration, the energy requirement for flue gas compression without purification was estimated between 608 and 311 kJ·kg CO₂ (range: 72 to 100%_{vol} CO₂) [41]. The cold-box/flash-separation-vessel and cold-box/distillation combination without power plant heat integration were found to be comparable but better than flue gas compression. White et al. [137] also suggested a cold-box/flash-separation-vessel combination for oxyfuel CO₂ purification, consisting of two separation stages at different pressures. Besong et al. [15] compared both single stage separation and a two stage separation with a higher and a lower stage temperature, based on the cold-box/flash-separation-vessel combination. Li et al. [78] investigated oxyfuel-derived flue gas impurity effects and compared the CO₂ flue gas purification of a two stage cold-box/flash-separation-vessel process, based on two different stage

[‡]Usually a fin-plate or coil-wound multi-stream heat exchanger.

temperatures, with a distillation column. The distillation column was found to have a 21% energy saving compared to a two stage flash process due to a lower condensation duty.

Vattenfalls pilot-scale oxyfuel power plant Schwarze Pumpe is equipped with a 10 TPD CO₂ purification process, which consists of absorption drying, compression to 15–22 bar, a rectification (distillation) column, a cold-box, a flash-separation-vessel, and a low-purity liquid CO₂ recycle [110, 122].

The typical energy consumption and achieved enrichment/separation of the reported CO₂ purification processes are given in Tab. 5.4. For completeness, the specifications of the CRS process (Section 5.5) are also included.

Table 5.4: Reported values in literature for specific energy consumption of oxyfuel-derived flue gas CO₂ purification. CO₂ stream pressures given between the brackets. ^{1: gas compression}
^{2: liquefaction}

reference		Raw flue gas CO ₂ purity (% _{vol} d.b.)	CO ₂ stream purity (% _{vol})	CO ₂ recovery (%)	Specific energy consumption (kJ _e ·kg ⁻¹ CO ₂)
Darde et al. [41]	1	72–100	72–100	100	608–311 (175 bar)
	2	72–93	95–99	90–95	507–378 (175 bar)
White et al. [137]		75.8	95.9–99.97	87–89	637–606 (110 bar)
Besong et al. [15]		70.5–82.6	98.2–99.2	84.4–93.3	781–594 (150 bar)
Ritter et al. [110, 133]		68–85	95–99.7	84–94	590–460 (110 bar)
this work (CRS)		60–79	95–98	≥ 90%	625–490 (100 bar)

Many of the reported studies not only focussed on CO₂ purification, but also on the further reduction of O₂, Ar, SO₂, NO_x and other impurity traces in the CO₂ stream [15, 78, 137, 144, 145]. Apart from corrosion, environmental and health issues, the requirement for removal of these purities largely depends on the end-destination of the CO₂ and is therefore a site-specific requirement. Performance of impurity removal is therefore not further investigated here.

5.4 CO₂ Compression

For transport and storage of the separated CO₂, a supercritical state is often assumed or recommended to prevent sudden phase transitions caused by changing pressure and/or temperature. The critical point, the lower bound of the supercritical region, varies with flue gas mixture composition. Tab. 5.5 shows the critical point as a function of composition for the binary mixture CO₂/N₂, which represents dry desulpherized flue gas.

Dilution of CO₂ rich flue gas by more volatile impurities raises the critical pressure and lowers the critical temperature, as can be concluded from Tab. 5.5. A supercritical state of 40°C and 100 bar is thus a safe thermodynamic end state for the CO₂ stream, as long as capture target composition is satisfied, i.e. a CO₂ content of ≥ 95%_{vol}.

Table 5.5: Critical conditions of the CO₂/N₂ mixture as a function of CO₂ purity.

CO ₂ content (% _{vol})	Critical point	
	T_c (°C)	p_c (bar)
100	31	74
95	27	79.5
90	23.5	88.5
85	17	96
80	11.5	110

Some CO₂ purification processes proposed for oxyfuel and the MTR membrane CO₂ capture process combine the compression of the final CO₂ stream with liquefaction. Other CO₂ purification processes use the liquid CO₂ for auto-refrigeration, after which compression of the gaseous CO₂ stream follows. CO₂ capture processes such as chemical absorption processes provide a pure gaseous CO₂ stream at near ambient conditions. This pure CO₂ stream must be brought to the transport condition (40°C, 100 bar) by at least a four-stage compression with intercooling as shown in Fig. 5.6.

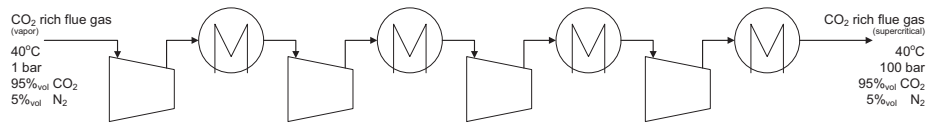
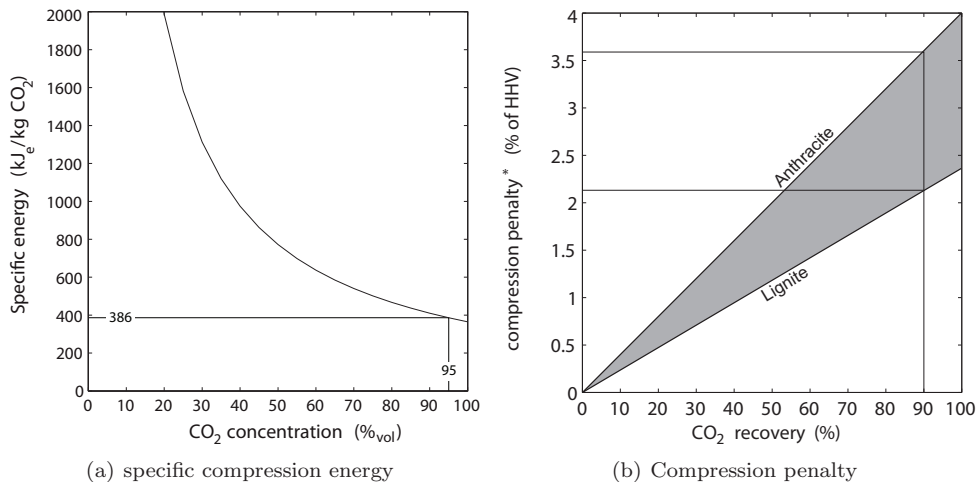
**Figure 5.6:** CO₂ gas compression.

Figure 5.7: CO₂ gas compression penalty. Anthracite: 98% carbon by weight, HHV: 31 MJ/(kg coal). Lignite: 30% carbon by weight, HHV: 18 MJ/(kg coal). * Capture penalty in electric units. For thermal units divide by efficiency; i.e. 0.4. Compressor isentropic efficiency $\eta_C=80\%$.

If a supercritical end-state for the CO₂ stream is required, then gas compression corresponds to the lowest energy penalty that can be achieved for CO₂ capture. Fig. 5.7 shows the specific energy consumption for a four-stage compression with intercooling and the involved energy penalty in % of the HHV of the coal. Assuming no heat-integration with the power plant, i.e. heat removed by intercooling is discarded, and a compressor stage isentropic efficiency of 80%, the costs of compression of a 95%_{vol} CO₂ stream requires 386 kJ_e/kg CO₂ (5.7(a)). This number corresponds to an energy penalty of about 2.2–3.6% HHV at 90% CO₂ removal (5.7(b)).

5.5 Flue Gas CO₂ Purification by CRS

The thermodynamic design of Condensed Rotational Separation is discussed in Chapter 3. A simple process scheme of the two-stage design for flue gas CO₂ separation is shown in Fig. 5.8. Flue gas is compressed to a moderate pressure of 18–36 bar, and cooled by a combination of isobaric heat exchange and expansion to about -55–-57°C – point 'A' in Fig. 5.8 – 1 to 2°C away from CO₂ freeze-out, such that a high purity CO₂ liquid 'C' and a CO₂ lean vapor 'B' are obtained. CO₂ lean vapor from the first RPS is compressed and cooled to a pressure of 80 bar and a temperature of -59°C 'D', 1 to 2°C away from CO₂ freeze-out[§], such that again a CO₂ lean vapor 'E' and a CO₂ rich liquid 'F' are obtained. The CO₂ lean vapor 'E' leaves to stack, the CO₂ rich liquid (< 90%_{vol} CO₂) 'F' is fed back after heating and expansion 'G' to the first RPS. This increases the overall CO₂ content in the feed stream of the first RPS, which enhances the separation in RPS 1.

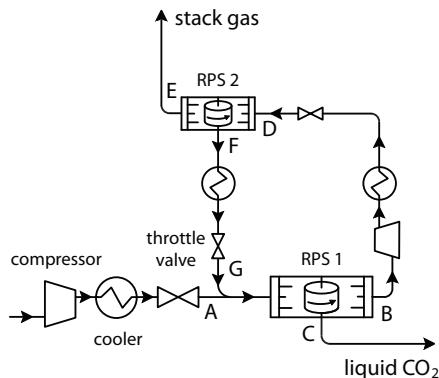


Figure 5.8: CRS process scheme

Table 5.6: Separation conditions

↓ Liq. CO ₂ purity (% _{vol})	RPS 1		RPS 2	
	<i>T</i> (°C)	-57	-59	-57
<i>p</i> (bar)	36	80	36	80
98% _{vol}	<i>T</i> (°C)	-55	-59	-59
	<i>p</i> (bar)	18	80	80

[§]The freeze-out line of CO₂, describing the transition from vapor-liquid to vapor-solid tends to lower temperatures at elevated pressure.

5.5.1 Combined isobaric and expansion cooling

Conditions close to or at the freeze-out line of CO₂ cannot be reached by isobaric heat exchange alone without solid CO₂ (dry ice) formation and clogging of the heat exchanger. To prevent freeze-out and clogging, the wall temperature of the condensing side of the heat exchanger (and thus also the coolant side) is not allowed to be lower than the freeze-out temperature of CO₂. Due to a ΔT between the bulk flow and the heat exchanging surfaces, the bulk flow of (condensing) flue gas cooled by heat exchange can never reach a temperature lower than ΔT above the CO₂ freeze-out temperature. For the cooling/condensing of flue gas (N₂/CO₂) with coil-wound heat exchangers in the CRS process and a coolant of 1°C above CO₂ freeze-out, a ΔT of 1.5 to 5°C is observed, which represents the typical range observed in practice [72].

In the process of CRS, the heat exchanger is supplemented with an isenthalpic expansion of 10 bar, which corresponds to cooling of approximately 2–5°C. Expansion cooling is a homogeneous bulk cooling process. The expander walls have therefore typically the same temperature as the bulk fluid in stationary operation. The freeze-out line of CO₂ can therefore be approached without problems of clogging.

Fast homogeneous cooling by expansion, to a thermodynamic state where vapor and liquid coexist, results in mist formation with droplets in the micron-size range [10]. In droplet condensation (mist formation), the condensing interface (vapor-liquid interface) is much larger than in wall condensation induced by heat exchange. Furthermore, the diffusion distance between condensing matter and the vapor-liquid interface is much smaller in droplet condensation than in wall condensation [68]. Droplet condensation induced by expansion is therefore much faster and vapor-liquid phase equilibrium can be reached within milliseconds [139].

Expansion across the freeze-out line into the region where solid CO₂ is formed has already been demonstrated in CoolEnergy's Cryocell process [56]. Temporary crossing of the CO₂ freeze-out line by expansion of flue gas (caused by unsteady operation or temperature/pressure control) does not necessarily pose a problem. Solid particles that form during non-equilibrium conditions melt partially towards the establishment of thermodynamic equilibrium. In that case, equilibrium establishes at the CO₂ freeze-out condition, where all vapor, liquid and solid coexist. Crossing of the freeze-out line by a small ΔT would yield a mist with CO₂ droplets and some pure solid CO₂ particles. As long as the volume ratio of solid CO₂ particles to liquid CO₂ droplets is small, equipment clogging and separation by the RPS should not be an issue.

5.5.2 CO₂ stream purity

Tab. 5.6 summarizes the separation conditions in RPS 1 and RPS 2, for a liquid CO₂ stream purity of 95 and 98%_{vol} CO₂. Compared to the design value 95%_{vol} CO₂, the first stage pressure is lowered to meet 98%_{vol} purity. The second stage pressure is unaffected because it is defined by the optimum point on the vapor boundary in the p-x phase diagram to achieve maximum separation, cf. Figs. 3.8 and 3.9.

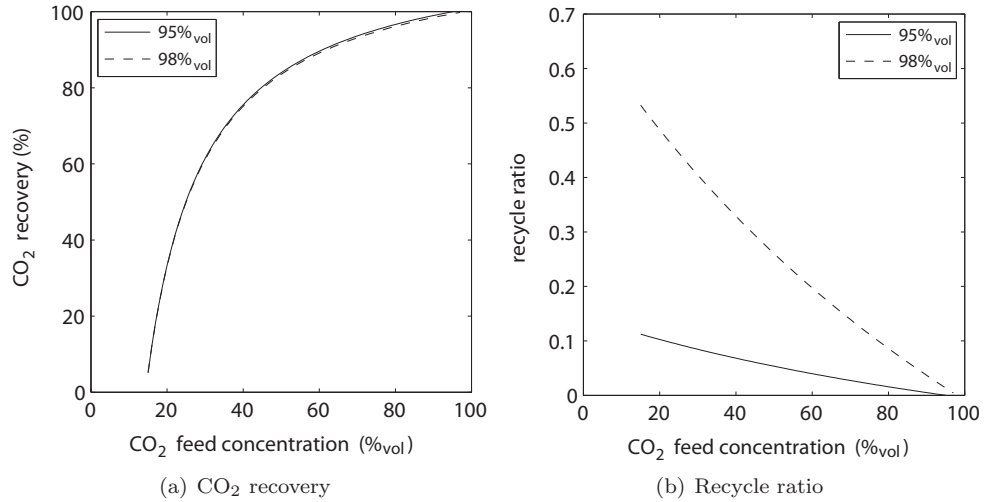


Figure 5.9: Separation performance and recycle ratio for the CRS process for a liquid CO₂ purity of 95 and 98%_{vol}.

The effect on separation performance by increase of the target liquid CO₂ stream purity from 95 to 98%_{vol} CO₂ is negligible as is shown in Fig. 5.9(a). The recycle ratio, which we defined as the ratio of recycle flow 'F-G' to CRS feed mass flow 'A' in Chapter 3, increases however by a factor 5 (Fig. 5.9(b)). The increase in recycle ratio results in an increased energy penalty for the equipment in the recycle loop 'B-D-F-G'.

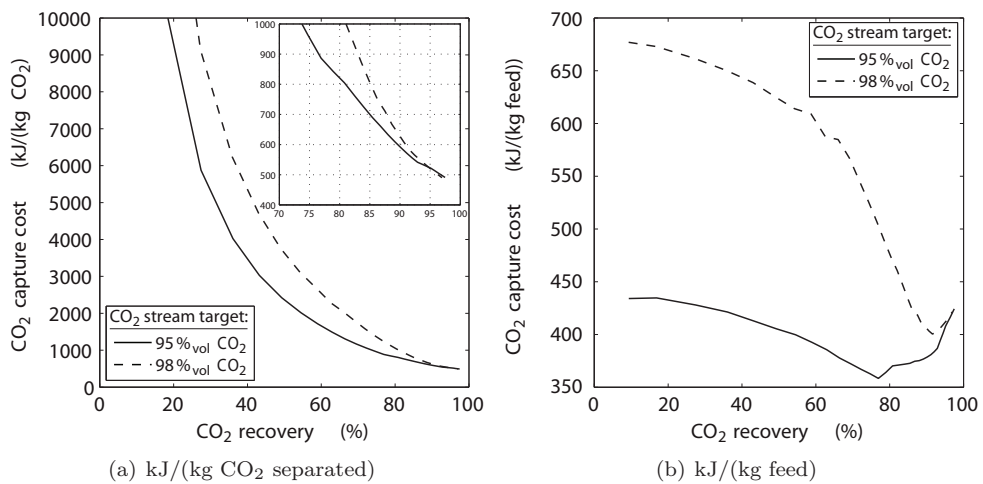


Figure 5.10: CRS energy costs

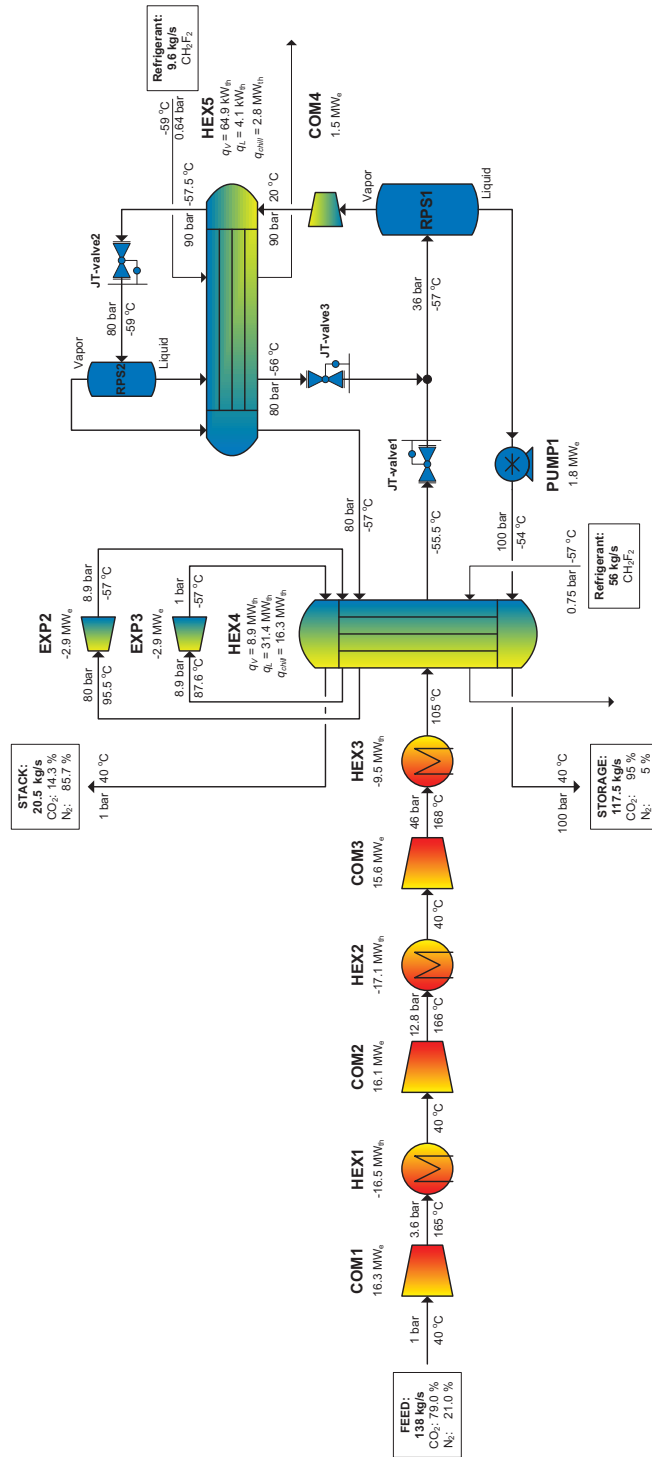


Figure 5.11: CRS process scheme. Presented numbers correspond to oxyfuel derived dry flue gas, cf. Appendix C.

5.5.3 Energy costs and heat integration

The detailed process scheme of the CRS process is shown in fig. 5.11. Refrigeration is provided internally by the cold streams resulting from the separators ('RPS1', 'RPS2') and externally by refrigerant from chiller cycles. By using an appropriate number of turbo expanders in the vapor line to stack, refrigeration is provided to 'HEX4' at the desired temperatures. Liquid CO₂ in the storage stream is pumped to a transport/storage pressure of 100 bar before heat is recovered in 'HEX4'. This saves equipment space compared to the reversed order of heat recovery and gas compression.

The energy consumption of the CRS process is shown in Fig. 5.10 for the two CO₂ stream purities: 95 and 98%_{vol} CO₂. For a high CO₂ recovery (> 90%), the CRS energy costs are equivalent with the lower values reported in Tab. 5.4. The increase in capture cost per kg of separated CO₂ for decreasing CO₂ recovery (Fig. 5.10(a)) is mainly the result of the lower CO₂ content in the feed stream; cf. Fig. 5.9(a), as the CRS energy costs per kg of fluegas (Fig. 5.9(b)) remain of the same order (360–675 kJ/(kg feed)).

Fig. 5.12 shows the distribution of the energy cost per kg of feed gas over the different process elements. With increasing CO₂ recovery the energy cost per kg of feed gas drop. This drop is related to the feed CO₂ concentration; cf. Fig. 5.9a. An increased feed CO₂ content lowers the specific energy costs of feed compression ('COM1', 'COM2', 'COM3') because CO₂ is more dense than N₂ at equal conditions. Secondly, an increased feed CO₂ content reduces the recycle ratio (Fig. 5.9b): More CO₂ is separated in the first stage and less CO₂ is circulated, thus less mass is compressed to the second stage ('COM4'), which reduces the second stage compression costs. Consequently also the vapor mass flow to stack lowers, which reduces again the delivered work by expansion in 'EXP1' and 'EXP2'.

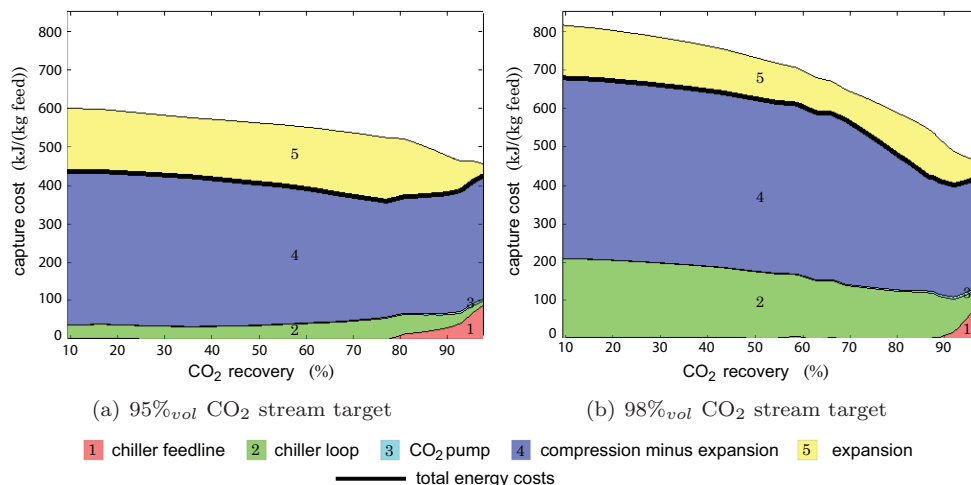


Figure 5.12: CRS energy costs

Due to the heat exchanger limitations imposed by the laws of thermodynamics, $NTU \leq 4$, a minimum ΔT between heat exchanger streams of about 2°C and CO₂ frost prevention[¶], additional cooling by a refrigerant is required in one or both heat exchangers 'HEX4' and 'HEX5'. The vapor mass flow resulting from 'RPS1' is typically smaller than the process feed mass flow, because only a small amount of the second stage feed mixture is recycled (recycle ratio < 1; cf. Fig. 5.9(b)). It is therefore more beneficial to supply additional cooling to 'HEX5' and to minimize the external cooling requirement in the feed flow in 'HEX4'.

For a CO₂ recovery < 77% (< 86% for the 98%_{vol} stream target), an additional third turbo expander is used between 'HEX5' and 'HEX4' to maximize the amount of heat absorbed into the vapor(stack) stream. With only two turbo expanders, a heat absorbing over-capacity would exist in 'HEX4'. The extra turbo-expander generates additional heat absorbing capacity in 'HEX5' and reduces the amount of heat absorbed into the vapor(stack) stream in 'HEX4'.

For a CO₂ recovery $\geq 77\%$ ($\geq 86\%$ for the 98%_{vol} CO₂ stream target; cf. Fig. 5.12), the full heat absorbing capacity of the vapor(stack) stream is required for 'HEX4' and the additional turbo expander becomes superfluous. Consequently, external cooling can no longer be omitted in 'HEX4'. The additional energy required for the feed-line chiller, which supplies the refrigerant in 'HEX4', causes process energy costs to increase, as is shown in Fig. 5.12 by the areas marked by '1'.

The difference in energy costs between the two CO₂ stream purity targets is mainly found in the external cooling requirement by the refrigerant in 'HEX5' and by compression. Although the decrease in separation pressure in 'RPS1' from 36 to 18 bar results in a decrease in compression costs for the feedline compressors 'COM1' to 'COM3', the total compression costs increase. This increase is caused by the larger recycle ratio (cf. Fig. 5.9b) and by the larger compression ratio in 'COM4' in case of 98%_{vol}CO₂ stream purity (cf. Tab. 5.6). The larger compression ratio not only results in increased compression cost for 'COM4' but also in a higher temperature of the gas leaving the compressor, which in turn, in combination with the increased recycle ratio, increases the requirement for refrigerant cooling in 'HEX5'.

For a CO₂ recovery > 90%, the feed flue gas consists mainly of CO₂ (see Fig. 5.9a), which is liquefied and separated in the low pressure stage of the process. The vapor mass flow towards 'RPS2' is therefore small and finally becomes negligible, which reduces the increase in compression and refrigeration cooling costs in 'COM4' and 'HEX5'. In the high CO₂ recovery end, energy costs for both purity targets therefore become comparable.

[¶]Frost prevention is applied by setting the expander outlet temperatures equal to the 'RPS1' inlet temperature, 1 to 2°C above the CO₂ freeze-out temperature

5.5.4 Refrigeration

For additional refrigeration in heat exchangers 'HEX4' and 'HEX5' (Fig. 5.11), a chiller cycle is designed to provide refrigerant of -55 to -57 °C. The chiller cycle is shown in Fig. 5.13 and uses R32 working fluid (CH₂F₂). Tab. 5.7 summarizes the working fluid saturation conditions at the different temperature levels in the CRS process.

Table 5.7: Saturated conditions of the refrigerant R32 (CH₂F₂). * Critical point.

-59	-57	40	78.5*	[°C]
0.64	0.75	24.8	58*	[bar]

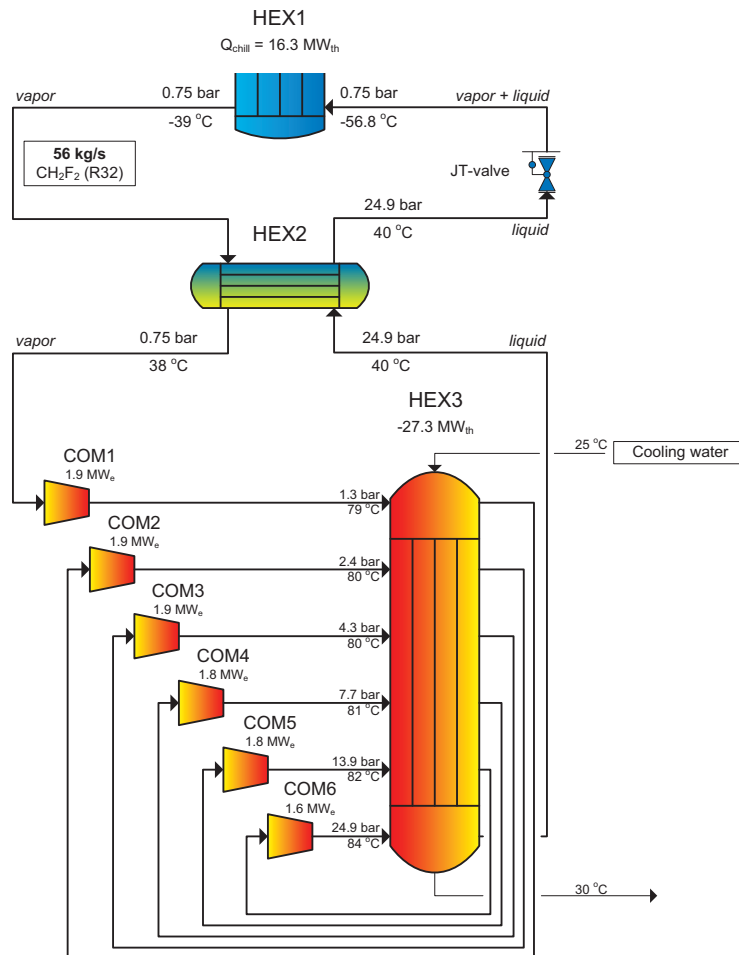


Figure 5.13: Refrigeration cycle. Presented numbers correspond to feedline refrigeration, cf. Fig. 5.11.

Compression of the working fluid occurs in six small stages, 'COM1'–'COM6' (Fig. 5.13) with intercooling, 'HEX3', stage compression ratios ≤ 2 and stage isentropic efficiencies of 90%. After the last compressor, 'COM6', saturated conditions of the working fluid are reached, and the working fluid is totally liquified. The liquified working fluid is further cooled by the returning vaporized working fluid 'HEX2' and expanded over a JT valve to reach the required refrigeration temperature. The refrigeration cycles in the feed line ('HEX4' in Fig. 5.11) and in the recycle loop ('HEX5' in Fig. 5.11) have an effective Coefficient of Performance (COP) of 1.5 and 1.4 respectively. The effective COP of a refrigeration process or chiller is defined as:

$$\text{COP} = \frac{\text{heat transferred from cold side}}{\text{work applied to refrigeration process}} . \quad (5.2)$$

Further optimization of the refrigeration cycle for site-specific operation conditions and the use of optimized refrigeration blends and cascade refrigeration processes have potential to further increase to COP to a value of around 2 [96, 130].

5.5.5 Equipment volume

In addition to operating costs, (i.e. energy consumption), we have to consider the size of the process, as a compact process gives rise to low capital costs.

The equipment size of the different elements within the CRS process and the refrigeration cycles is determined as discussed in Chapter 4. The total volume of the CRS process as a function CO₂ recovery is shown in Fig. 5.14. Fig. 5.14 shows the specific process volume for both separation targets (95 and 98 %_{vol} CO₂). For both separation targets two lines are shown, corresponding to a constant feed mass flow of 140 and 500 kg/s.

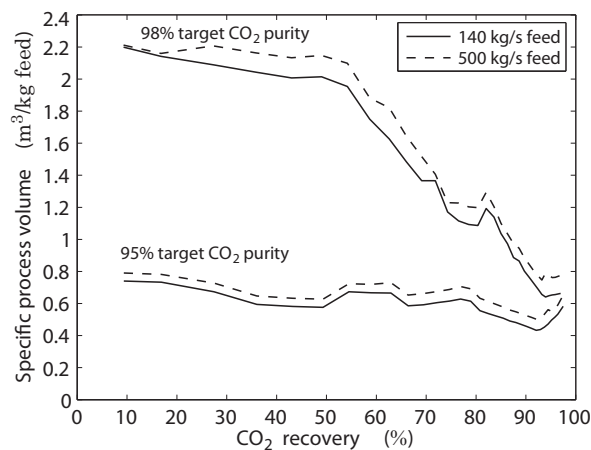


Figure 5.14: Specific process volume of the CRS process, shown for separation targets of 95 and 98 %_{vol} CO₂, and feed mass flows of 70 and 500 kg/s.

500 kg/s. These feed mass flows approximate the dry mass flow coming from either a 500 MW_e oxyfuel or a 500 MW_e conventional airblown coal-fired power plant, cf. Appendix C. The specific process volume for these two mass flows is presented because rotary equipment such as compressors, expanders, RPS (thus also the chiller cycles) do not scale linear with mass flow. The results shown in Fig. 5.14 indicate however that the specific volume of the total CRS process scales only slightly non-linear with massflow. In approximation linear scaling of the total specific CRS process volume as presented in Fig. 5.14 can thus be allowed.

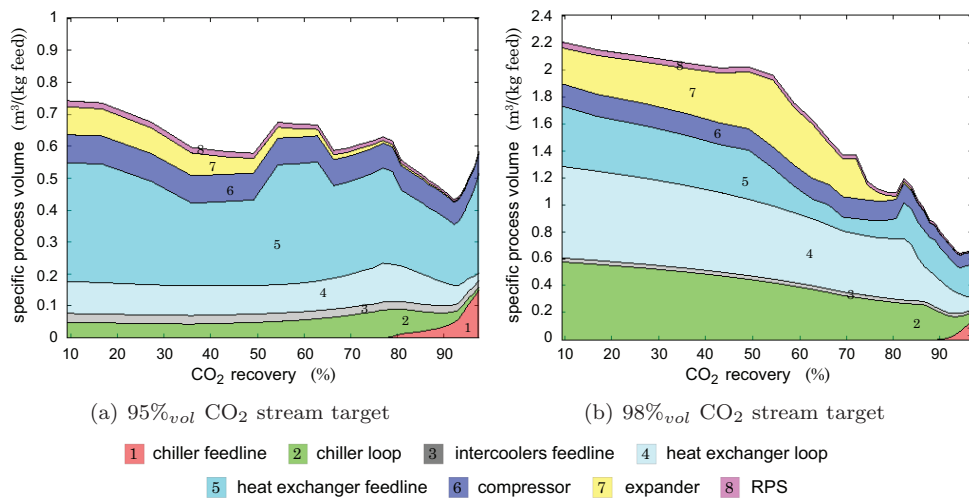


Figure 5.15: Contribution of the different elements to the total CRS process volume.

Fig. 5.15 shows the equipment specific volume distribution of the CRS process. The unsmoothness and the local peaks that occur in the process equipment volume result from the feedline heat exchanger 'HEX4' and are a consequence of a changed heat integration approach necessary to comply with the imposed constraints on heat exchanger design. By shifting up the inlet and exit temperature of the feedline in 'HEX4', the NTU of the heat exchanger set such that $NTU \leq 4$ is accomplished. The range for the temperature shift is limited by the outlet temperature of compressor 'COM3' and the inlet temperature of the expansion valve 'JTvalve1'. Violation of the temperature shift range for $NTU=4$ means that the imposed size constraint $NTU \leq 4$ has to be discarded, which causes variations in the size of the feedline heat exchanger. This occurs for a CO₂ recovery smaller than 80% for the 95%_{vol} CO₂ stream target (<50% for 98%_{vol} CO₂ stream target).

The CRS process volume is mainly dominated by the size of heat exchanger in the feed line (HEX4 in fig. 5.10) and in the recycle loop (HEX5) and to a smaller extent by the compressors (COM1 to COM4) and expanders (EXP1 and EXP2). The size of the water-cooled intercoolers (HEX1 to HEX3) in the feed line, the two separators (RPS1 and RPS2) and the chiller loops in case of the 95% stream target are only small.

The difference in equipment volume between the separation target of 95%_{vol} CO₂ and 98%_{vol} CO₂ is caused by the higher recycle ratio (Fig. 5.9(b)). As explained in the previous section on energy consumption, the circulation flow for the 98%_{vol} CO₂ stream target is larger because more CO₂ is rejected in the first separation stage due to the lower first stage separation pressure. At the high CO₂ recovery end, where the CRS feed gas is almost solely composed of CO₂, nearly the complete CRS feed stream is liquefied and separated in the first stage. The contribution of the second stage then becomes negligible and specific equipment volumes for both CO₂ stream targets become comparable.

5.6 CRS Pre-enrichment

In Chapter 3 and in the beginning of the previous section we have shown that Condensed Rotational Separation as a stand-alone process cannot separate a sufficient amount of high purity CO₂ from a conventional coal-combustion derived flue gas (14%_{vol} CO₂). CRS requires a form of CO₂ enrichment of the effluent prior to the CRS process, to which we shall refer to as CO₂ pre-enrichment in the remainder of this work. Essentially two routes to CO₂ pre-enrichment of flue gas can be distinguished: By removal of some nitrogen and other impurities from the combustion air before combustion, and by removal of some nitrogen and other impurities from the flue gas after combustion. CRS is particularly suited for combination with techniques that cannot meet the separation targets stand-alone. Such techniques are oxyfuel combustion and CO₂ separating membranes. Oxyfuel combustion suffers from leakage of impurities, as explained in section 5.3, and therefore needs additional CO₂ purification. CO₂ separating membranes have their physical limitations in separation performance as explained in Section 5.2.2 and require an additional liquefaction/purification process to become potentially economic.

5.6.1 Partial oxyfuel and CRS

The combination of oxyfuel combustion technology and flue gas CO₂ purification requires only partial oxygen enrichment of the combustion air. For the evaluation of CO₂ capture by the combination of partial oxyfuel combustion and CRS, partially oxygen enriched combustion air is provided to the power plant by mixing of high purity oxygen from a cryogenic air separation unit (ASU) with ambient air.

Fig. 5.16 shows schematically the complete process train for CO₂ capture by the combination of partial oxyfuel combustion and CRS. The energy costs for the cryogenic production of high purity oxygen are already discussed in section 5.3.1. The purity of the ASU supplied oxygen stream is assumed to be 95%_{vol} O₂ and the energy costs of high purity O₂ production by cryogenic distillation are taken as the average, given in Tab. 5.2. The volume of the cryogenic air separation plant has been derived from the Linde GOX6000 ASU at Vattenfall's oxyfuel pilot scale power plant Schwarze

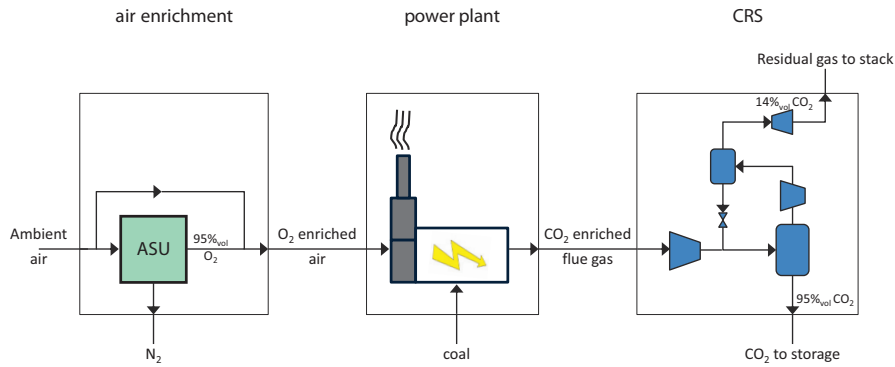


Figure 5.16: Combination of partial oxyfuel and CRS

Pumpe and is estimated at $2 \text{ m}^3/(\text{t. O}_2/\text{day})$ [5, 16]. The power plant is modelled as described in Appendix C.

For a constant gross electric power ^{||} production of 500 MW_e , the energy penalty and the specific installed volume of CO₂ capture by combination of partial oxyfuel and CRS are shown in Fig. 5.17.

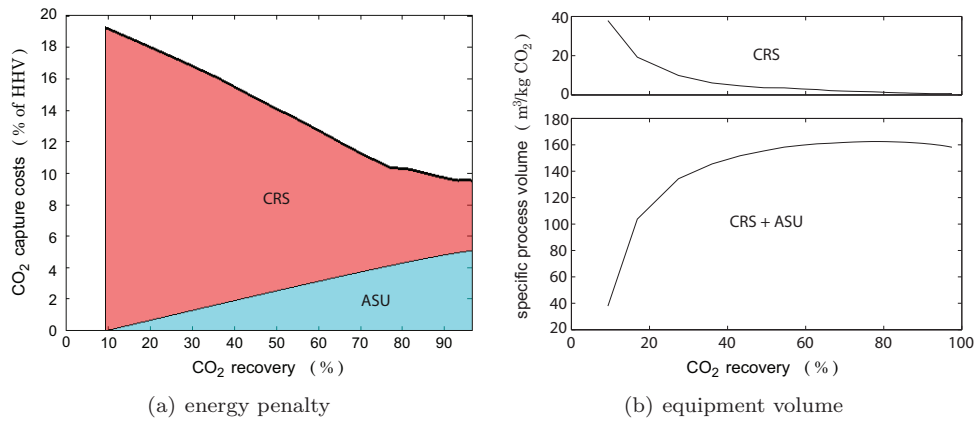


Figure 5.17: Energy penalty and equipment volume for CO₂ capture by combination of partial oxyfuel combustion and CRS. Results are for a 500 MW_e power plant and a CO₂ stream purity of $95\%_{vol} \text{ CO}_2$. Energy penalty (electric energy cost) expressed as percentage of the higher heating value (HHV) of the coal. Equipment volume expressed in cubic meters per separated kg of carbon-dioxide.

It is always more beneficial to enrich the combustion air (and thus the flue gas) as much as possible, as can be concluded from Fig. 5.17 in connection to the relation between the CRS feed gas CO₂ content and the CO₂ recovery (cf. Fig. 5.8a).

^{||}The gross electric power equals the summation of the nett electric power and the CO₂ capture energy penalty.

At a first instance one would expect that for an increase in CO_2 recovery, which requires an increase in combustion air O_2 content, the combined process would become more expensive, due to a larger oxygen demand from the ASU. For constant gross electricity production and an increase in combustion air O_2 content however, the amount of impurities in the resulting flue gas decrease, which causes a reduction in flue gas mass flow. Consequently the CRS process itself becomes cheaper. The nett effect is a decrease in energy penalty as shown in Fig. 5.17a, even though the costs for combustion air O_2 enrichment increase.

The installed volume of the combined process is shown in Fig. 5.17b, for the CRS process itself (upper graph) and the total process (lower graph). The installed volume of the combined process is typically dominated by the air separation unit, because cryogenic separation of oxygen and nitrogen is much more difficult than carbon-dioxide and nitrogen. In the pressure-temperature domain the vapor/liquid saturation lines of pure oxygen and pure nitrogen are much closer to each other than pure carbon-dioxide and pure nitrogen. The vapor-liquid two-phase regime is therefore typically much smaller, which makes separation thermodynamically more difficult (see also Section 3.5). This translates into characteristically large process equipment for O_2/N_2 separation.

5.6.2 Membranes and CRS

Post combustion CO_2 enrichment is more suitable for retrofitting CO_2 capture onto conventional coal-fired power plants. Membranes are particularly suited for this route because of their physical limitations in separation. The membrane system of MTR, see Section 5.2.2, is regarded as feasible state-of-the-art membrane technology in flue gas CO_2 capture and is selected for evaluation in combination with CRS.

The total CO_2 capture train is approximately equal to the system proposed by MTR [83]. Only the latter part (cf. Fig. 5.4), containing the CO_2 condenser and high pressure membrane, are replaced by the CRS process.

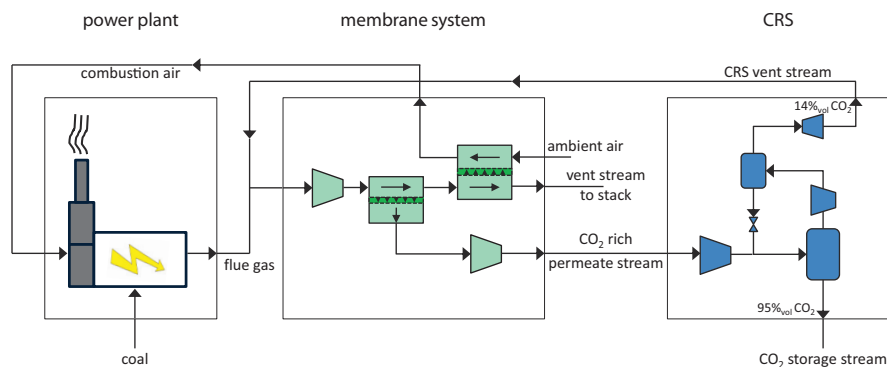


Figure 5.18: Combination of CO_2 permeating membranes and CRS.

The total process train and the membrane system are shown schematically in Fig. 5.18. Dry flue gas from the powerplant is fed to the membrane system. A fan provides a slight overpressure of 1.1 bar to the front end of the first cross-flow membrane. CO₂ enriched flue gas leaves the first membrane on the permeate side with a vacuum of about 0.2 bar, which is provided by the vacuum pump, and is fed to the CRS process. The permeate stream from this membrane typically contains about 78%_{vol} CO₂ for 90% CO₂ recovery and increases for a decreasing CO₂ recovery.

The CO₂ lean residual flow from the first membrane still contains a reasonable amount of CO₂ (typically 16%_{vol} CO₂). This residual stream is fed to a second membrane, which is a counter-flow sweep membrane. The separation in this membrane is not so much driven by pressure difference ($\Delta p = 0.2$ bar), but by the concentration difference between the membrane feed and the sweep stream. Combustion air for the power plant is used as a sweep stream. Some of the CO₂ permeates into the sweep stream and is fed back to the power plant. The residual CO₂ depleted flue gas (typically 2%_{vol} CO₂) is led to the stack.

The combustion air stream CO₂ content goes up to about 12%_{vol} with increasing CO₂ recovery. Due to CO₂ in the combustion air, the CO₂ content in flue gas that leaves the power plant (Appendix C) is slightly increased up to about 24%_{vol} for 90% CO₂ recovery.

CRS processes the CO₂ rich permeate stream, which has a typical CO₂ content of about 78%_{vol}, into a storage stream, containing 95%_{vol} CO₂ and a vent stream containing 14%_{vol} CO₂. Because the membrane vent stream has a much lower CO₂ content, the CRS vent stream is recycled to the inlet of the membrane system.

The cross-flow and counter-flow-sweep membranes are simulated by custom-written elementary membrane models, which are further described in Appendix E. The membrane models determine the separation performance and membrane area for given pressure drop, feed composition, permeate side CO₂ recovery and membrane material properties (selectivity and permeance).

The membranes simulated are MTR Polaris membranes with a CO₂ permeance of 1000 gpu**, a CO₂/N₂ selectivity of 50 and a membrane area to volume ratio of 110 m²/m³ [3, 83]. In simulation of the total CO₂ capture train, the total membrane area is minimized for each CO₂ recovery.

The energy penalty and the installed equipment volume for the combination of the membrane system and CRS are shown in Fig. 5.19. The energy costs of the membrane system and CRS increase with increasing CO₂ recovery and is in contrast to the combination of partial oxyfuel and CRS. To explain this, the flue gas mass flow and composition resulting from the power plant can be regarded as approximately constant. The energy consumption of the fan in the front-end of the first membrane can thus also be regarded as constant. For a low CO₂ recovery, both membranes are small, which results in a high purity permeate stream and a low permeate stream

**1 gpu = 3.35×10^{-10} mole/(s·m²Pa)

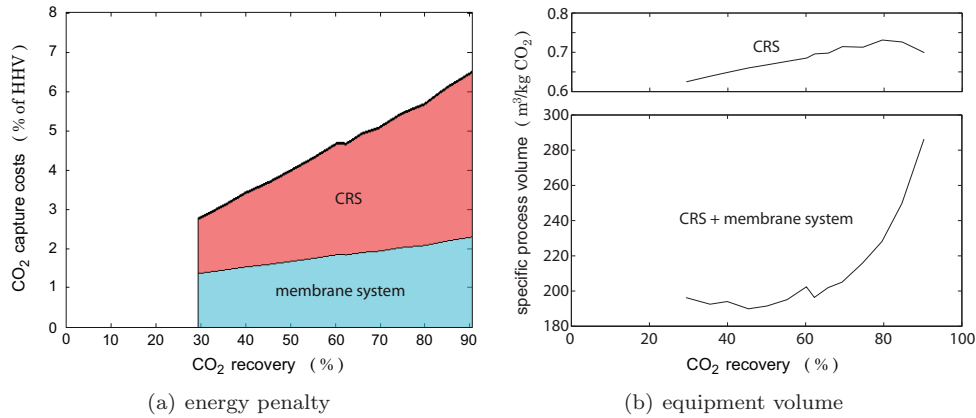


Figure 5.19: Energy penalty and equipment volume for CO₂ capture by combination of the MTR membrane system and CRS. Results are for a 500 MW_e power plant and a CO₂ stream purity of 95%_{vol} CO₂. Energy penalty (electric energy cost) expressed as percentage of the higher heating value of the coal. Equipment volume expressed in cubic meters per separated kg of carbon-dioxide.

mass flow which is fed to the CRS process. The energy requirement of the vacuum pump in the membrane system and downstream CRS process is therefore small.

With the increase in membrane area of both membranes, the CO₂ recovery rises, the permeate mass flow from the first membrane increases and its CO₂ purity drops. Thereby both the energy costs of the permeate side vacuum pump and the downstream CRS process increase.

The installed equipment volume is almost totally dominated by the size of the membrane system and increases approximately exponentially with increasing CO₂ recovery as shown in Fig. 5.19b. CRS typically requires a higher CO₂ content in its feed stream if the CO₂ recovery of CRS is to be increased, cf. Fig. 5.8a. For an increased CO₂ recovery of the total process (membrane system + CRS), a higher permeate mass flow is required from the first membrane. As a consequence, the area of the first membrane must increase, which results in a decrease in CO₂ content on the permeate side of the first membrane, and thus in a decrease in CO₂ content in the CRS feed stream; the opposite of the CRS requirement. To compensate for this decrease in CO₂ content, the area of the second membrane must increase. The recycle of CO₂ to the power plant goes up, which results in a higher CO₂ content in the flue gas from the power plant. The higher CO₂ content in the flue gas increases the CO₂ partial pressure in the membrane system feed gas and enhances the separation in the first membrane.

Increasing the membrane area increases the permeate mass flow from the first membrane. Consequently also more vent gas from the CRS process is recycled, which requires an additional rise in membrane area. These two effects cause the installed membrane volume to rise exponentially with CO₂ recovery.

5.7 Comparison

To assess the application of CRS in coal combustion CO₂ capture, we compare the energy penalty and installed equipment volume to current conventional post-combustion CO₂ capture technology; i.e. chemical absorption. The comparison is performed for a 500MW_e coal-fired power plant, described in Appendix C.

Energetically it is more attractive to apply full oxyfuel combustion instead of partial oxyfuel combustion, as we showed in Section 5.6.1. Therefore the upper limit (95%_{vol} O₂) of the partial oxyfuel case described in Section 5.6.1 is taken for comparison instead of the 90% CO₂ recovery target.

The energy penalty and installed equipment volume of the chemical absorption process (MEA) are determined with use of the in-house model (cf. Section 5.2.1. For an equal comparison, compression of the separated gaseous CO₂ is included in both the energy penalty and equipment volume of the amine absorption plant. The gas compression plant has been discussed already in Section 5.4. For a stream purity of 99.9%_{vol} CO₂, the compression costs have been determined at 369 kJ/kg CO₂, which, for the amine plant, is equal to about 3% of the higher heating value of the coal.

The results of the comparison in terms of energy penalty, installed equipment volume and CO₂ stream purity are shown in Fig. 5.20.

Both the combinations oxyfuel combustion and CRS, and membranes and CRS perform much better in terms of energy consumption, compared to chemical absorption. By implementation of the proposed membrane system in combination with CRS, the saving on operational expenditures is more than a factor two, compared to amine absorption by MEA and CO₂ compression. Even if the regeneration energy of the solvent can be halved by using state-of-the-art amine based solvents (cf. Sec. 5.2.1), the energy penalty of chemical absorption would still be in the same order of the oxyfuel CRS combination. Membranes and CRS must thus be regarded as a serious candidate for CO₂ capture from coal fired power plants.

A penalty is however paid in installed equipment volume. The membrane system in combination with CRS requires about two and a half times more installation volume than a chemical absorption plant and one and a half time more installation volume than a combined oxyfuel CRS process. In terms of capital expenditures, this does not instantly mean that the use of a large membrane separation process is unattractive as membrane skid costs are low (cf. Section 5.2.2).

In terms of CO₂ storage purity, the chemical absorption process, with a CO₂ stream purity > 98%_{vol}, is superior, because impurities in the flue gas nearly absorb or dissolve in the amine solvent. Cryogenic phase separation processes always suffer from impurities such as nitrogen, which dissolve to some extent in the condensed phase. The two hybrid CRS combinations are targeted on a 95%_{vol} CO₂ stream purity, but are able to compete with the achieved purity by chemical absorption. A higher CO₂ stream purity, up to 98%_{vol}, can be accomplished against a negligible increase of the CRS energy penalty and CRS process volume in the high-end of the

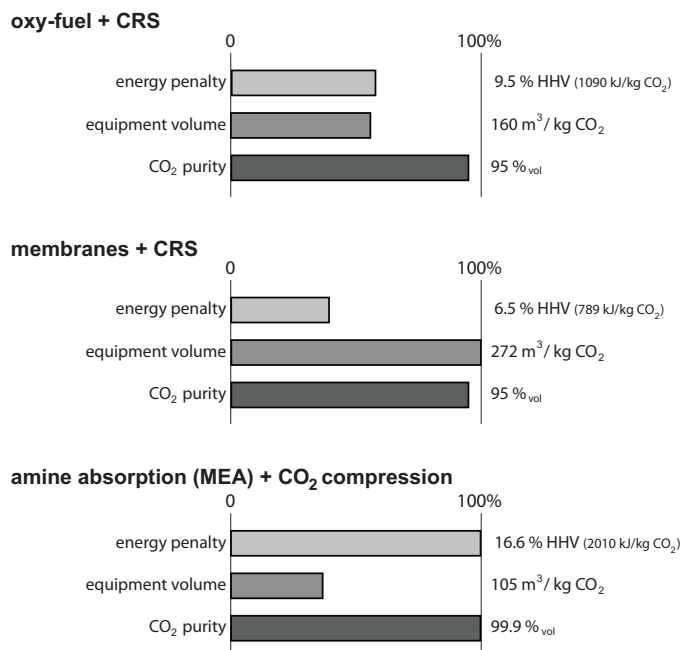


Figure 5.20: Comparison of CRS and flue gas pre-enrichment with amine absorption and CO₂ gas compression.

evaluated CO₂ recovery range, as shown in the Section 5.5.

In total, application of CRS in combination with today's feasible state-of-the-art membrane technology is a serious competitive candidate for CO₂ capture from coal-combustion derived flue gas. A reduction in energy penalty for CO₂ capture by use of different capture routes and processes however comes along with a penalty in installed equipment volume, which is acceptable as long as the capital expenditures for equipment can be kept low.

5.8 Discussion

The comparison is performed only for the Illinois#6 bituminous type of coal. The carbon content and higher heating value of the coal varies with quality. Coal types with a low carbon content (lignite) produce relatively CO₂ lean flue gas in comparison to carbon-rich coals (anthracite). For increasing CO₂ content, CRS in combination with a form of flue gas CO₂ pre-enrichment becomes more favorable, as it enhances the separation performance. For a lower CO₂ content, chemical absorption becomes cheaper and the benefit of CRS reduces. Numbers presented are derived for the

reference coal Illinois#6 and are an indication. A full comparison for the different quality types of coal would give more insight into the effect of coal type.

The analysis of CRS and associated CO₂ capture process trains in this chapter has been performed for dry desulphurised flue gas, represented in the analysis by a mixture of CO₂/N₂. The effect of flue gas impurities such as oxygen and argon is expected to be small and therefore not included.

So far, the removal of water from the flue gas has been omitted. For the CRS process itself it is essential that no water is present in the flue gas, to prevent ice build-up and clogging of heat exchangers. To a certain extent, drying already occurs in the intercooling stages of the CRS feed compressors, where water vapor partially condenses as soon as the water vapor partial pressure in the flue gas reaches the saturation pressure. Further drying after the compressor stages in the CRS process can be performed by mature technology such as glycol absorption dryers or molecular sieves, to reduce the water content in the flue gas to a ppm level. Costs and volume of a drying process have not been included in the analysis.

The comparison of the hybrid CRS combinations with CO₂ capture by amine absorption is performed for a CO₂ recovery of $\geq 90\%$, because this target is believed to be today's best technological practice. In enduring absence of clear CO₂ capture policies another guideline may be followed: Equivalent CO₂ emission per nett produced amount of electricity. Equal CO₂ emissions, from both coal-fired power plants with CO₂ capture and natural-gas-fired power plants without capture, take away the disadvantage of coal being a more CO₂ polluting fuel. The pursuit of a CO₂ emission of about 66 kg/GJ_e (natural-gas-fired electricity production), requires the capture of only 60 to 70% of the CO₂ (depending on CO₂ capture energy penalty). Such an eased capture target reduces the energy penalty of CO₂ capture and lowers the threshold for application of CO₂ capture technology.

CRS with pre-enrichment is not solely applicable to flue gas from coal combustion. It can generally be applied to any flue gas to capture CO₂. CRS is however most advantageous for flue gases with a typically high CO₂ partial pressure, such as encountered in cement and steel production.

5.9 Closure

The application of CO₂ capture from coal-fired electricity generation has been assessed and today's pursued CO₂ capture targets have been identified. Current framework proposals and international CO₂ mitigation projects aim for a capture target of at least 90% of the CO₂ emitted, and a captured stream purity of at least 95%_{vol}.

Different types of CO₂ separation technology have been investigated. Feasible CO₂ capture technologies are chemical absorption, oxyfuel combustion and purification, membrane separation and anti-sublimation. Membrane separation and anti-sublimation are new and promising developments in flue gas CO₂ capture and are still in bench-

scale testing. Oxyfuel combustion and purification and chemical absorption are considered mature technologies. Oxyfuel combustion is currently demonstrated on pilot scale. Chemical absorption is already commercialized technology and regarded as the current standard in post-combustion CO₂ capture.

The detailed process design of CRS was discussed for the application of CO₂ capture from CO₂ enriched flue gases. Separation performance, CO₂ stream purity, CRS installation volume and energy consumption have been investigated. The separated CO₂ stream purity can be increased from 95 to 98%_{vol} CO₂, without significant reduction of the amount of CO₂ capture (CO₂ recovery). For high CO₂ recoveries ($\geq 90\%$), increased product purity can be achieved against neglectable extra energy costs and almost the same installed equipment volume.

For 90% CO₂ recovery, corresponding to a CRS feed CO₂ content of about 60%_{vol}, the energy costs of CRS are found to be about 590 to 625 kJ/kg CO₂ depending on separated CO₂ stream purity (95–98%_{vol}). The corresponding typical specific equipment volume of CRS is small and found to be in the range of 0.6–0.8 m³ equipment per separated kg of CO₂ (cf. §5.5 and §5.6).

CRS in flue gas CO₂ capture is shown to be a very compact 'cherry on the top' process. CRS is well-suited for CO₂ purification of already CO₂ enriched gas streams resulting from flue gas enrichment techniques (other than phase separation) that cannot meet CO₂ capture targets stand-alone.

Two routes have been assessed for the capture of CO₂ from flue gas resulting from coal-fired electricity production: (partial) oxyfuel combustion and CRS, and CO₂ permeating polymeric membranes and CRS. The CO₂ capture energy penalty and installed process equipment volume have been identified and compared against conventional CO₂ capture technology.

The combination of a polymeric CO₂ permeating membrane system in tandem with CRS shows great potential in terms of energy consumption. Energy costs of CO₂ capture are halved in comparison to chemical absorption by MEA with CO₂ gas compression and reduced by 30% in comparison to oxyfuel and CO₂ purification. The reduction comes however at an expense of total equipment volume by about a factor two and a half compared to chemical absorption. As long as space is available and capital expenditures on equipment can be kept relatively low, increased process volume is not an issue. With a CO₂ capture penalty of only 6.5% HHV, application of CRS in combination with today's feasible state-of-the-art membrane technology is thus a serious competitive candidate for CO₂ capture from coal-combustion derived flue gas.

Conclusions

6.1 Modeling of Phase Equilibria

The Peng-Robinson equation of state and the van-der-Waals one-fluid mixing rules were used to construct algorithms for the calculation of different types of phase-equilibria involving vapor, liquid, and solid phases. A refined expression for pure solid phase fugacity has been derived. Stability theory, based on the Gibbs energy of mixing and the tangent plane criterion, has been applied to verify phase stability. We developed an interacting algorithm between phase stability and phase equilibrium calculations to accurately determine the 'nature preferred' stable phase equilibrium for a given temperature, pressure and overall mixture composition, without any prior knowledge of the number of phases and phase identities present.

Model verification has been carried out for binary mixtures CO_2/CH_4 and CO_2/N_2 and the ternary mixture $\text{CO}_2/\text{CH}_4/\text{H}_2\text{S}$. For binary mixtures, phase compositions are predicted up to 2%*mole* accurate. In the case of the evaluated ternary mixture, reliable results are found in the vapor-liquid region. Although qualitatively still correct, prediction of phase equilibria that lack a vapor phase or involve multiple liquid phases is not as accurate ($\geq 10\%$ *mole* deviation from reported experimental values).

CRS design requires accurate prediction of phase compositions in the vapor-liquid region. It also requires accurate prediction of solid phase formation. Improvement of liquid phase pVT behavior is advised for use of the phase equilibrium model in regions with one or more liquid phases in absence of a vapor phase. Improvements in pVT behavior can be accomplished by implementation of a liquid volume shift and/or use of a more accurate (mixture and/or phase specific) equation of state.

The developed phase equilibrium model functions as an important tool in the design and thermodynamic optimization of the CRS process. The model enables construction of different kinds of phase diagrams, is used as a tool in the determination of separation performance of multi-stage looped CRS processes and provides the means to derive thermodynamic properties of multi-phase streams such as enthalpy and entropy.

6.2 CRS: Thermodynamic Design, Energy and Sizing

On the examples of CO₂ removal from contaminated natural gas and CO₂ capture from flue gas, we showed that Condensed Rotational Separation can be considered as a general pressure distillation technique in the semi-cryogenic regime. It can thus serve as an alternative for conventional temperature distillation.

We showed that preliminary design of CRS can be accomplished by the definition of apparent binary mixtures and the evaluation of their phase diagrams in the dimensions pressure and composition ($p-x$). Construction of horizontal tie-lines in the $p-x$ phase diagram for maximum purification of both phases provides a method to determine the number of separation stages (number of separators to be deployed at different pressures and temperatures), the process layout, and the optimum feed stage, for maximum separation. By use of two or more separation stages in a loop, the most or least volatile component can be separated effectively from the mixture. By application of multiple multi-stage CRS loops in series, even multiple components can be separated.

Multi-stage CRS installations typically benefit from the freedom in both stage separation pressure and temperature, whereas in the conventional temperature distillation process (distillation column) the pressure of all separation stages (trays), is equal. CRS therefore offers more flexibility to operate within the two-phase (or even multi-phase) regime.

For determination of the CRS energy consumption and estimation of process size, we introduced the calculation of entropy and enthalpy for real fluids. We discussed the tools to determine apparatus volume and apparatus energy conversion or exchange. We considered radial turbo-machinery and expansion valves, coil-wound heat exchangers and the RPS, which are all key components in the CRS process.

The size of radial turbo-machinery is estimated from an overall package diameter. Basic turbine theory has been described and applied to calculate the overall package diameter. Sizing of heat exchangers is performed with use of the NTU-effectiveness method. For estimation of the NTU in condensing/evaporating heat exchangers, we redefined the heat exchanger effectiveness and capacity ratio. Additionally we combined the NTU- ϵ correlations for cross- and counter-flow configurations to represent coil-wound heat-exchangers. For sizing of the RPS, we formulated new scaling laws, based on existing design equations, whereby volume flow, droplet and gas density, gas viscosity and droplet surface tension were considered.

6.3 CRS in Post-combustion CO₂ Capture

For the application of post-combustion CO₂ capture from coal-combustion derived flue gas, a two stage CRS process was designed and evaluated in detail. Separation performance, CO₂ stream purity, process volume and energy consumption have been determined. CO₂ stream purities up to 98%_{vol} CO₂ are achievable by CRS. The energy consumption of the CRS process is found to be dominated by compression of the flue gas to separation pressure, and to a small extent to external refrigeration. The process volume is mainly determined by the size of the heat exchangers, and to a smaller extent by the size of the refrigeration cycles.

The process of Condensed Rotational Separation in flue gas CO₂ capture is typically a very compact process. It can only separate large amounts of CO₂ if used in tandem with a pre-enrichment technique: a technique that increases the CO₂ content in the flue gas, prior to CRS. The typical required enrichment is from 10–16%_{vol} CO₂ to about 70%_{vol} CO₂ to capture 90% of the CO₂. The CRS process is thus well-suited for final CO₂ purification of already CO₂ enriched gas streams. These streams may result from flue gas enrichment techniques (other than phase separation) that cannot meet CO₂ capture targets stand-alone.

The feasibility of CRS to capture CO₂ from coal-derived flue gas has been assessed for two pre-enrichment techniques: (partial) oxyfuel combustion and CO₂ permeating membranes. The feasibility study was performed for a 500 MW_e coal-fired power plant and was focussed on energy penalty and process volume to represent the operational and capital expenditures of the combined process. The results were reflected against today's mature post-combustion CO₂ capture technology: chemical absorption by MEA.

The combination of a low pressure polymeric CO₂ permeating membrane system in tandem with CRS shows great potential in terms of energy consumption. Energy costs of CO₂ capture are more than halved in comparison to chemical absorption by MEA with CO₂ gas compression. The energy costs are reduced by 30% in comparison to oxyfuel and CO₂ purification by CRS.

The low energy costs come however at an expense of total equipment volume, by about a factor two and a half compared to the process volume of chemical absorption. This is because of the large volume of the membranes. The use of a low pressure membrane system and CRS as a compact distillation technique allows for capital expenditures to be low. With a CO₂ capture penalty of only 6.5% HHV for 90% CO₂ removal, the application of CRS in combination with today's feasible state-of-the-art membrane technology is a serious competitive candidate for CO₂ capture from coal-combustion derived flue gas.

6.4 Outlook for CRS

Throughout this work we showed that it is possible to methodically design the CRS process for maximum separation. Combined with previous work on process details of Condensed Rotational Separation (expansion, droplet formation, separation), the process has evolved to a point where a shift from laboratory research and theoretical simulation to pilot scale is necessary to continue the road to industrial application. Although the main focus of the development of CRS in this thesis is on flue gas, possible applications for pilot scale testing extend to a much broader range. In fact it can be applied to any gas (or liquid) separation that involves phase creation and separation under elevated pressure and any temperature level. A new potentially very interesting field of application is the upgrading of biogas [114]. Other typical fields of interest are the petrochemical sector, LNG and natural gas processing, synthesis gas production, hydrogen production and air separation.

Thermodynamic Derivations

A.1 The Gibbs-Duhem Equation

The first law of thermodynamics applied to an multi-component open system of variable composition holds:

$$\begin{aligned} dU &= dQ - dW \\ \downarrow \\ d(nu) &= Td(ns) - pd(nv), \end{aligned} \quad (\text{A.1})$$

where n represents the total number of moles $n = \sum_{i=1}^N n_i$, T the temperature, p the pressure, u the specific internal energy, s , the specific entropy and v the specific volume. Rewriting Eq. (A.1) with the expressions for the enthalpy $h = u + pv$ and Gibbs free energy $g = h - Ts$ results in the expression for the change in molar Gibbs (free) energy of an open system of variable composition:

$$dg = vdp - sdT + \frac{1}{n} \sum_{i=1}^N (g_i dn_i). \quad (\text{A.2})$$

Relations between the specific and total state functions are:

$$\left. \frac{\partial g}{\partial p} \right|_{T, n_i} = v \rightarrow \left. \frac{\partial G}{\partial p} \right|_{T, n_i} = V \rightarrow \left. \frac{\partial G}{\partial p} \right|_{T, n_i} = n \left. \frac{\partial g}{\partial p} \right|_{T, n_i} \quad (\text{A.3})$$

$$\left. \frac{\partial g}{\partial T} \right|_{p, n_i} = s \rightarrow \left. \frac{\partial G}{\partial T} \right|_{p, n_i} = S \rightarrow \left. \frac{\partial G}{\partial T} \right|_{p, n_i} = n \left. \frac{\partial g}{\partial T} \right|_{p, n_i} \quad (\text{A.4})$$

$$\left. \frac{\partial g_i}{\partial n_i} \right|_{p, T} = \frac{g_i}{n} \rightarrow \left. \frac{\partial G_i}{\partial n_i} \right|_{p, T} = g_i \rightarrow \left. \frac{\partial G_i}{\partial n_i} \right|_{p, T} = n \left. \frac{\partial g_i}{\partial n_i} \right|_{p, T} \quad (\text{A.5})$$

Transformation of the molar state functions g, s, v in Eq. (A.2) into total state functions G, S, V shows that the Gibbs energy is a function of three state variables: $G = G(p, T, n_i)$.

The rigorous result is shown in Eq. (A.6) and is better known as the Gibbs-Duhem equation:

$$\begin{aligned} dG &= V \cdot dp - S \cdot dT + \sum_{i=1}^N (g_i dn_i) \\ &= \left(\frac{\partial G}{\partial p} \right)_T dp - \left(\frac{\partial G}{\partial T} \right)_p dT + \sum_{i=1}^N \left(\left(\frac{\partial G}{\partial n_i} \right)_{T,p,j \neq i} dn_i \right). \end{aligned} \quad (\text{A.6})$$

A.2 Relations between chemical potential, fugacity and activity coefficient

To solve the phase equilibrium problem, an expression for the chemical potential of a fluid in terms of other state variables and state functions is required. For a multi-component ideal gas mixture at constant temperature in a closed system, the chemical potential can be derived from the Maxwell relation [48]:

$$\left(\frac{\partial \mu_i}{\partial p_i} \right)_T = v_i \quad (\text{A.7})$$

The ideal gas equation is used to replace v_i in terms of pressure, temperature and the universal gas constant:

$$d\mu_i = \frac{RT}{p_i} dp_i \rightarrow d\mu_i = RT d \ln p_i \quad (\text{A.8})$$

Integration of Eq. (A.8) between a reference state p^0, T and actual state p, T leads to the expression for the change in chemical potential between the reference and actual state of component i in an ideal gas:

$$\mu_i - \mu_i^0 = RT \ln \left(\frac{p_i}{p_i^0} \right) = RT \ln \left(\frac{p_i}{y_i p^0} \right), \quad (\text{A.9})$$

where R is the universal gas constant. In 1908, Lewis [76] generalized Eq. (A.9) to real gases by defining a 'corrected pressure' function f for each component which he called the fugacity:

$$\mu_i - \mu_i^0 = RT \ln \left(\frac{f_i}{f_i^0} \right). \quad (\text{A.10})$$

When the reference fugacity f_i^0 is replaced by the partial component fugacity ($y_i f_i^{pure}$), the relationship is obtained between mixture component fugacity f_i at conditions (p, T) , the pure component fugacity at reference conditions (p', T) , the molar component concentration y_i and the activity coefficient of component i , γ_i :

$$\Delta \mu_i^{mix/pure} = RT \ln \left(\frac{f_i}{y_i f_i^{pure}} \right) = RT \ln (\gamma_i). \quad (\text{A.11})$$

The reference pressure p' , corresponding to the pure component fugacity f_i^{pure} can be any pressure. It can be equal to p , but it can also be atmospheric. The activity coefficient has therefore only meaning when also the reference pressure is given.

A.3 Fluid Fugacity Coefficient

In calculation of fluid phase equilibria, as described in Chapter 2, the fluid fugacity coefficient is required. Here we derive an expression for the fugacity coefficient in terms of p , V , T and \mathbf{y} .

Starting from the relation between change in chemical potential and fugacity, Eq. (A.10), we assume the reference state to be an ideal gas at same conditions (p, T). For the reference fugacity we then obtain:

$$f_i^0 = y_i p^0 = y_i \frac{RT}{v^0}, \quad (\text{A.12})$$

with v the specific molar volume. If we choose the reference volume equal to the actual volume ($v^0 = v = ZRT/p$), Eq. (A.12) transforms into

$$f_i^0 = y_i p^0 = y_i \frac{p}{Z}. \quad (\text{A.13})$$

Substituting Eq. (A.13) into Eq. (A.10) results into

$$\mu_i - \mu_i^0 = RT \ln(\phi_i) + RT \ln(Z) \quad \text{with} \quad \phi_i = \frac{f_i}{y_i p}, \quad (\text{A.14})$$

where ϕ_i is the fugacity coefficient.

For a very low pressure, or a infinite volume, real gas behavior and ideal gas behavior can be assumed equal. Using the infinite volume as an intermediate state, indicated by v^∞ , the fugacity change can be written as:

$$\begin{aligned} \mu_i - \mu_i^0 &= (\mu_i - \mu_i^{v^\infty}) - (\mu_i^0 - \mu_i^{v^\infty}) \\ &= \int_V^\infty \left[\left(\frac{\partial \mu_i}{\partial V} \right)_{T,n} - \left(\frac{\partial \mu_i}{\partial V} \right)_{T,n}^0 \right] dV. \end{aligned} \quad (\text{A.15})$$

Using the Maxwell relation

$$\left(\frac{\partial \mu_i}{\partial V} \right)_{T,n} = - \left(\frac{\partial p}{\partial n_i} \right)_{v,T,n_{i \neq j}}, \quad (\text{A.16})$$

taking $V = nv = v$, deriving $(\partial p / \partial n_i)_{v,T,n_{i \neq j}}^0$ from the ideal gas equation and substituting Eqs. (A.15) and (A.16) into Eq. (A.14), we obtain for the fugacity coefficient:

$$RT \ln(\phi_i) = - \int_v^\infty \left[\left(\frac{\partial p}{\partial n_i} \right)_{v,T,n_{i \neq j}} - \frac{RT}{V} \right] dV - RT \ln(Z). \quad (\text{A.17})$$

Eq. (A.17) is the workable expression for pressure explicit equations of state such as the Peng-Robinson equation of state in this work.

If we generalize the cubic equation of state into:

$$p = \frac{RT}{v - b_m} - \frac{a_m}{v^2 + ub_mv + wb_m^2}. \quad (\text{A.18})$$

whereby $u = 2$ and $w = -1$ for the PR-EoS, and implement the Van der Waals mixing rules for a_m and b_m as described in Chapter 2, we obtain for $(\partial p / \partial n_i)_{v,T,n_{i \neq j}}$:

$$\begin{aligned} \left(\frac{\partial p}{\partial n_i} \right)_{v,T,n_{i \neq j}} = & -\frac{b_i RT}{(v - b_m)^2} + \frac{RT}{v - b_m} + \frac{a_m b_i (uv + 2wb_m)}{(v^2 + ub_mv + wb_m^2)^2} + \dots \\ & \dots - \frac{2\sqrt{a_i} \sum_{j=1}^N (y_j \sqrt{a_j} [1 - k_{ij}])}{v^2 + ub_mv + wb_m^2}, \end{aligned} \quad (\text{A.19})$$

where k_{ij} is the binary interaction parameter (cf. Chapter 2 and Appendix B).

By Substitution of Eq. (A.19) into Eq. (A.17), the integral over volume can be split into five terms.

The integral over the first and second term hold:

$$\int_v^\infty \frac{b_i RT}{(V - b_m)^2} dV = \frac{b_i RT}{v - b_m}, \quad (\text{A.20})$$

$$- \int_v^\infty \frac{RT}{V - b_m} dV = -[RT \ln(V - b_m)]_v^\infty. \quad (\text{A.21})$$

The third term is the most difficult term to integrate*. We only present the simplified result:

$$\begin{aligned} & - \int_v^\infty \frac{a_m b_i (uV + 2wb_m)}{(V^2 + ub_mV + wb_m^2)^2} dV = -\frac{a_m b_i}{b_m^2} \dots \\ & \dots \left\{ \frac{1}{\sqrt{u^2 - 4w}} \ln \left(\frac{2v + b_m (u - \sqrt{u^2 - 4w})}{2v + b_m (u + \sqrt{u^2 - 4w})} \right) - \frac{b_m v}{v^2 + b_m uv + b_m^2 w} \right\}. \end{aligned} \quad (\text{A.22})$$

Eq. (A.22) can be simplified further by substituting the equation of state into the second right hand term:

$$\begin{aligned} & - \int_v^\infty \frac{a_m b_i (uV + 2wb_m)}{(V^2 + ub_mV + wb_m^2)^2} dV = -\frac{a_m b_i}{b_m^2} \dots \\ & \dots \frac{1}{\sqrt{u^2 - 4w}} \ln \left(\frac{2v + b_m (u - \sqrt{u^2 - 4w})}{2v + b_m (u + \sqrt{u^2 - 4w})} \right) + \frac{b_i}{b_m} \left(vp - \frac{vRT}{v - b_m} \right). \end{aligned} \quad (\text{A.23})$$

*For a detailed derivation of the third and fourth term, the reader can request a copy of the TU/e graduation thesis 'Expansion of Contaminated gas Well streams'; rapport number WPC 2009.01 from the author.

The integral over the fourth term holds:

$$\int_v^\infty \frac{2\sqrt{a_i} \sum_{j=1}^N (y_j \sqrt{a_j} [1 - k_{ij}])}{V^2 + ub_m V + wb_m^2} dV = \frac{2\sqrt{a_i} \sum_{j=1}^N (y_j \sqrt{a_j} [1 - k_{ij}])}{b_m \sqrt{u^2 - 4w}} \ln \left(\frac{2v + b_m (u - \sqrt{u^2 - 4w})}{2v + b_m (u + \sqrt{u^2 - 4w})} \right). \quad (\text{A.24})$$

The last integral term holds:

$$\int_v^\infty \frac{RT}{V} dV = RT [\ln(V)]_v^\infty. \quad (\text{A.25})$$

Combining Eqs. (A.21), (A.25):

$$RT [\ln(V) - \ln(V - b_m)]_v^\infty = RT \left[\ln \left(\frac{V}{V - b_m} \right) \right]_v^\infty = RT \ln \left(\frac{v}{v - b_m} \right). \quad (\text{A.26})$$

Substituting Eqs. (A.20), (A.23), (A.24) and (A.26) into Eq. (A.17) obtains:

$$\begin{aligned} \ln(\phi_i) &= \frac{b_i}{v - b_m} + \frac{b_i}{b_m} \left(\frac{vp}{RT} - \frac{v}{v - b_m} \right) + \ln \left(\frac{v}{v - b_m} \right) - \ln(Z) + \dots \\ &\dots \frac{1}{RT b_m \sqrt{u^2 - 4w}} \left(2\sqrt{a_i} \sum_{j=1}^N (y_j \sqrt{a_j} [1 - k_{ij}]) - \frac{a_m b_i}{b_m} \right) \dots \\ &\dots \ln \left(\frac{2v + b_m (u - \sqrt{u^2 - 4w})}{2v + b_m (u + \sqrt{u^2 - 4w})} \right). \end{aligned} \quad (\text{A.27})$$

With combination of terms one and two and terms three and four, the fugacity coefficient finally becomes:

$$\begin{aligned} \ln(\phi_i) &= \frac{b_i}{b_m} \left(\frac{vp}{RT} - 1 \right) + \ln \left(\frac{RT}{pv - pb_m} \right) + \frac{a_m}{RT b_m \sqrt{u^2 - 4w}} \dots \\ &\dots \left(\frac{2\sqrt{a_i} \sum_{j=1}^N (y_j \sqrt{a_j} [1 - k_{ij}])}{a_m} - \frac{b_i}{b_m} \right) \ln \left(\frac{2v + b_m (u - \sqrt{u^2 - 4w})}{2v + b_m (u + \sqrt{u^2 - 4w})} \right). \end{aligned} \quad (\text{A.28})$$

Conversion of Eq. (A.28) using the compressibility factor and dimensionless EoS parameters

$$Z = \frac{pv}{RT}, \quad b' = \frac{bp}{RT} \quad \text{and} \quad a' = \frac{a(T)p}{(RT)^2}$$

result into the fugacity coefficient as expressed by Eq. (2.19).

A.4 Departure Functions

Calculation of enthalpy and entropy changes in real gases involves the use of departure functions, which describe the change of the property between a reference (ideal gas) and actual (real gas) state at constant temperature.

Starting from specific Helmholtz Energy $A = u - Ts$, substitute $du = dq - dw = Tds - pdv$, assume constant temperature and split the integral using an infinite volume condition such that ideal gas is satisfied, we obtain:

$$dA = -pdv \rightarrow A - A^0 = - \int_{v^0}^v p dV = - \overbrace{\int_{\infty}^v p dV}^{\text{real gas}} - \overbrace{\int_{v^0}^{\infty} p dV}^{\text{ideal gas}} . \quad (\text{A.29})$$

To avoid problems due to the infinity limits, $\int_{\infty}^v \frac{RT}{V} dV$ can be added to and subtracted. Substitution of the ideal gas term ($p = RT/v$) then obtains:

$$A - A^0 = - \int_{\infty}^v \left(\overbrace{p}^{\text{EoS}} - \frac{RT}{V} \right) dV - RT \ln \left(\frac{v}{v^0} \right), \quad (\text{A.30})$$

whereby the p in the integral can be replaced by the pressure explicit equation of state, to describe real gas behavior. Eq. (A.30) describes the departure function for the Helmholtz energy. When a cubic equation of state of the form of Eq. (A.18) is substituted, integrals are solved and the result is simplified, we obtain:

$$A - A^0 = RT \ln \frac{v^0}{v - b_m} + \frac{1}{\sqrt{u^2 - 4w}} \frac{a_m}{b_m} \ln \left(\frac{2v + b_m (u - \sqrt{u^2 - 4w})}{2v + b_m (u + \sqrt{u^2 - 4w})} \right). \quad (\text{A.31})$$

Combined with the Maxwell relation $\left. \frac{\partial s}{\partial v} \right|_T = \left. \frac{\partial p}{\partial T} \right|_v$ and $p = -\left. \frac{\partial A}{\partial v} \right|_T$ derived from Eq. (A.29), the departure entropy can be written as:

$$s - s^0 = \int_{v^0}^v \left(\frac{\partial}{\partial T} \left(- \left. \frac{\partial A}{\partial v} \right|_T \right) \right) dV. \quad (\text{A.32})$$

Working the temperature derivative out of the integral obtains:

$$s - s^0 = - \frac{\partial}{\partial T} \left(\int_{v^0}^v \left(\left. \frac{\partial A}{\partial v} \right|_T \right) dV \right)_v = - \frac{\partial}{\partial T} (A - A^0)_v. \quad (\text{A.33})$$

For the departure enthalpy with $h = u + pv$ we can write:

$$h - h^0 = u - u^0 + RT \left(\frac{pv - p^0 v^0}{RT} \right) = u - u^0 + RT \left(\frac{pv}{RT} - 1 \right). \quad (\text{A.34})$$

A change in specific internal energy u at constant temperature can be written as:

$$du|_T = Tds + pdv = Tds - dA|_T \rightarrow u - u^0 = T(s - s^0) - (A - A^0). \quad (\text{A.35})$$

Substitution of Eq. (A.35) into Eq. (A.34) obtains the departure enthalpy:

$$h - h^0 = T(s - s^0) - (A - A^0) + RT \left(\frac{pv}{RT} - 1 \right). \quad (\text{A.36})$$

Substitution of the departure function for Helmholtz energy, Eq. (A.31) into Eqs. (A.33) and (A.36) obtains the departure functions as expressed in Chapter 4; Eqs. (4.2) and (4.3). For increased the numerical accuracy in modeling, these equations can be transformed in a similar manner as described for the fugacity coefficient, using the compressibility factor and dimensionless EoS parameters.

Binary Interaction Parameters

Table B.1: Binary interaction parameters, k_{ij} , for the Peng-Robinson Equation of State (cf. Section 2.3.2).

interaction	k_{ij}	interaction	k_{ij}
H ₂ -N ₂	0.103	CO ₂ -SO ₂	0.046
H ₂ -CO	0.0919	CO ₂ -CH ₄	0.0919
H ₂ -CO ₂	-0.1622	CO ₂ -C ₂ H ₆	0.1322
N ₂ -O ₂	-0.0119	CO ₂ -C ₃ H ₈	0.1241
N ₂ -CO	0.0307	CO ₂ -C ₄ H _{10n}	0.1333
N ₂ -CO ₂	-0.017	CH ₄ -H ₂ S	0.0789
N ₂ -H ₂ O	-0.2	CH ₄ -C ₂ H ₆	-2.6×10^{-3}
N ₂ -H ₂ S	0.1767	CH ₄ -C ₃ H ₈	0.0140
N ₂ -SO ₂	0.08	CH ₄ -C ₄ H _{10n}	0.0133
N ₂ -CH ₄	0.0311	CH ₄ -C ₅ H _{12n}	0.023
N ₂ -C ₂ H ₆	0.052	C ₂ H ₆ -H ₂ S	0.0833
N ₂ -C ₃ H ₈	0.085	C ₂ H ₆ -C ₃ H ₈	1.1×10^{-3}
N ₂ -C ₄ H _{10n}	0.08	C ₂ H ₆ -C ₄ H _{10n}	0.096
N ₂ -C ₅ H _{12n}	0.1	C ₂ H ₆ -C ₅ H _{12n}	7.8×10^{-3}
CO ₂ -O ₂	0.124	C ₃ H ₈ -C ₄ H _{10n}	3.3×10^{-3}
CO ₂ -H ₂ O	0.12	C ₅ H _{12n} -H ₂ S	0.063
CO ₂ -H ₂ S	0.0974		

Coal-fired Power Plant Model

For the evaluation of the CRS process in coal-combustion derived flue gas, we have created a simple model of a coal-fired power plant. We aimed to predict electric energy production, flue gas composition and mass flow from both conventional air blown and (partial) oxyfuel power plants.

The model incorporates the combustion of coal, boiler air ingress, ash removal by electrostatic precipitation (ESP) and flue gas desulphurization (FGD), see Fig. C.1. The Illinois#6 bituminous type of coal is chosen as a reference fuel [65]. The composition and heating value of Illinois#6 is given in Tab. C.1. Other types of coal, of which the composition is known, can be incorporated later.

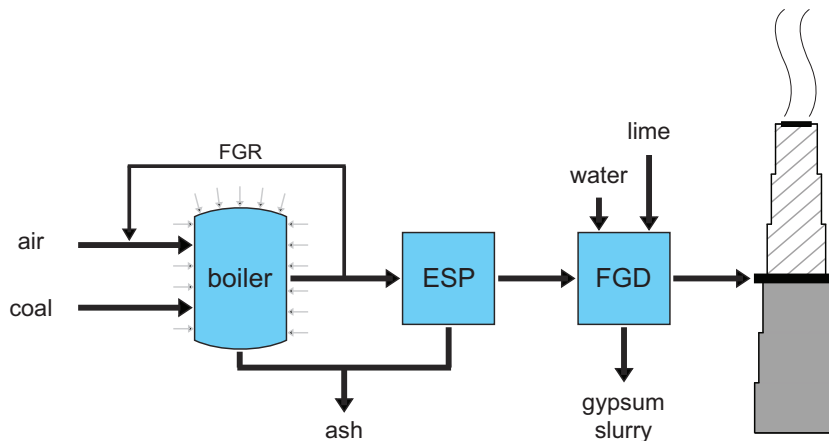
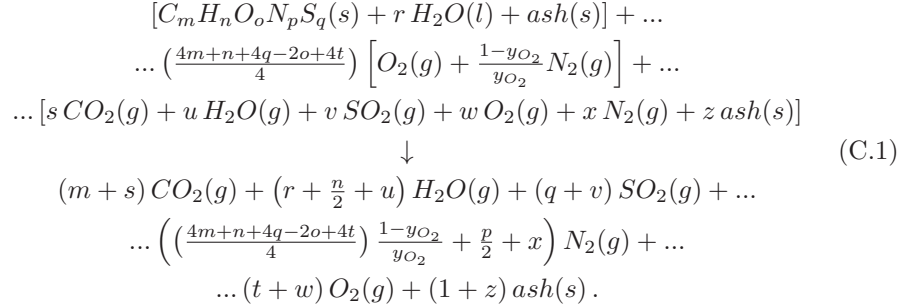


Figure C.1: Universal coal-fired power plant model.

Halogen elements (Chlorine) and heavy metals (Mercury) are neglected, because their presence in coal is negligible. The remaining species are used to describe the ideal

combustion in the boiler according to the following reaction:



The first two reactants (indicated by the rectangular brackets) in Eq. C.1 represent the coal and the (oxygen enriched) combustion air. Also excess combustion air is taken into account. The model operates with an excess oxygen ratio of 1.5 in the boiler [64]. The third reactant term in Eq. C.1 represents the contribution due to flue gas recycle (FGR). FGR is required in the oxygen enriched combustion mode to reduce the increase in combustion temperature. The amount of recycle can go up to two third of the flue gas mass flow in oxyfuel combustion [63].

We assume no recycle for air blown operation ($y_{O_2} = 21\%_{mole}$) and a linear increase with the combustion air oxygen concentration, up to 60% of the flue gas mass flow upstream of the recirculation branch for oxyfuel combustion ($y_{O_2} = 100\%_{mole}$).

Boilers in coal-fired power plants are typically operated just below ambient pressure, which results in ingress of ambient air into the boiler. Air ingress happens at the coal feed openings and is further caused by boiler wall leakage. In new built conventional power plants air ingress corresponds to approximately 3% of the total flue gas mass flow to stack, upstream of the recirculation branch. In air blown power plants this value can rise to 10% in the course of time [64]. Fig. C.2 shows the CO_2 , O_2 and SO_2 content on a dry basis for several values of air ingress. For modeling,

Table C.1: Composition and heating value of Illinois#6 coal, which is used as a reference fuel for comparison purposes [65]. ₁: Contains both bottom ash and fly ash.

Component	Concentration	Low Heating Value	High Heating Value
	[%weight]	[kJ/kg]	[kJ/kg]
Carbon	61.20	24.433	25.350
Hydrogen	4.20		
Oxygen	6.02		
Chlorine	0.17		
Sulfur	3.25		
Nitrogen	1.16		
Ash ₁	11.00		
Moisture	13.00		
Mercury	1.04×10^{-5}		

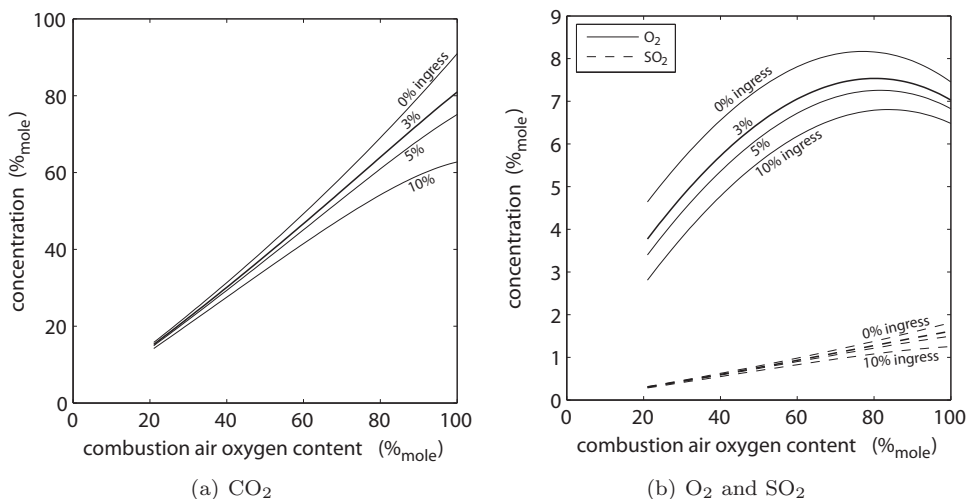
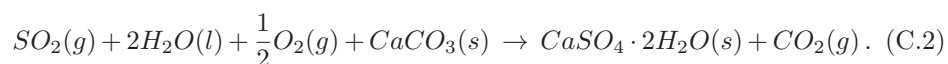


Figure C.2: Concentrations of carbon-dioxide, oxygen and sulphur-dioxide on a dry basis (d.b.) after the ESP for several boiler air ingress rates.

we fix the air ingress of 3% of the total flue gas mass flow upstream of the recirculation branch.

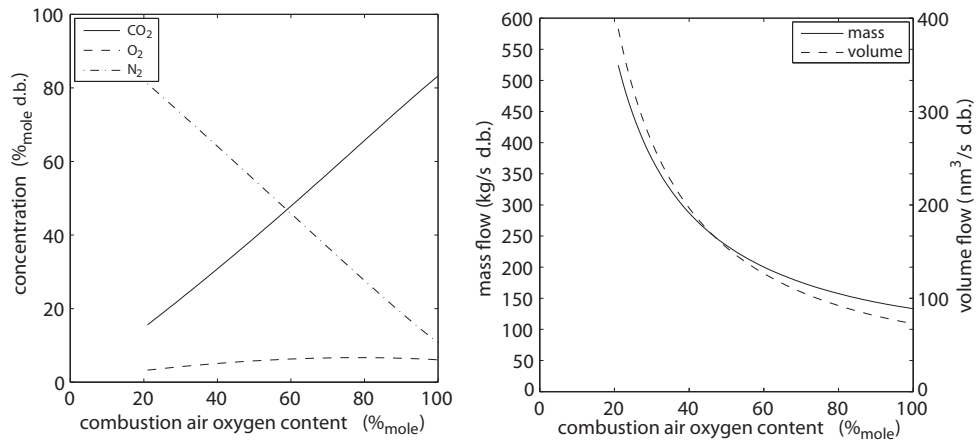
Downstream of the ESP, a wet flue gas desulphurization process (spray absorption tower) is located. The desulphurization process is fed with limestone (CaCO_3) and water to bind sulphur-dioxide into calcium-sulphite. Further oxidation/crystallization of calcium-sulphite results in usable water-bound calcium-sulfate, better known as gypsum. The complete process of absorption and oxydation/crystallization can be summarized in a reaction equation as [17]:



Oxygen, required for the oxidation/crystallization of calcium-sulphite, is supplied by the excess oxygen in the flue gas. The rise in CO₂ content due to desulphurization is small; cf. Figs. C.2(a) and C.3(a). Desulphurization by wet absorption can remove up to 99% of the sulphur-dioxide, resulting in a ppm level content after flue gas desulphurization [17]. A ppm level SO₂ content in the flue gas has negligible effects on thermodynamic properties and multi-phase behavior. This justifies the assumption of 100% SO₂ removal by FGD in modeling. The resulting flue gas (which is led to stack or a to dehydration and CO₂ capture) is solely composed of carbon-dioxide, nitrogen, oxygen and water vapor. The flue gas composition at stack entrance is shown in Fig. C.3(a).

For the conversion of thermal to electrical power, a fixed thermal to electrical efficiency of 38.5% is assumed, which is a common value for both supercritical coal-fired air blown and oxygen blown power plants [65]. The mass and volume flow at stack

entrance as a function of oxygen content in the combustion air are shown in Fig. C.3(b) for a baseline 500MW_e reference coal-fired power plant (without CO₂ capture).



(a) Concentrations (dry basis) after FGD. (b) Mass and volume flow (dry basis) at FGD exit.

Figure C.3: Concentrations and mass and volume flow on a dry basis (d.b.) after the FGD for a 500MW_e power plant with a 38.5% generating efficiency, 3% boiler air ingress and a linear relation between recycle ratio and combustion air oxygen content.

Heat Transfer Coefficients for Coil-Wound Heat Exchangers

Heat transfer in coil-wound heat exchangers as introduced in Section 4.2.3 takes place through the shell and tube fluid, mainly by convection, and through the tube wall by conduction. Without fouling factors, the overall heat transfer coefficient can be expressed as:

$$\frac{1}{\tilde{h}} = \frac{1}{\lambda_{sh}} + \frac{\delta_m}{\kappa_m} \frac{2A_{sh}}{A_{tu} + A_{sh}} + \frac{1}{\lambda_{tu}} \frac{A_{sh}}{A_{tu}}, \quad (\text{D.1})$$

where \tilde{h} is the overall heat transfer coefficient, λ_{sh} the convective heat transfer coefficient for the shell side, λ_{tu} the convective heat transfer coefficient for the tube side, δ_m the tube thickness, κ_m the thermal conductivity of the tube material and A the heat exchanging area. For low tube wall thickness, the heat exchanging area ratio can be neglected.

For sizing of the coil-wound heat exchangers, we assume ASTM A269 welded and bright annealed 316L stainless steel tubing with an outer diameter of 3/4" and a wall thickness of 0.042", corresponding to BWG-19 (pipe thickness standard) and a bursting pressure of about 580 bar, which is commonly applied in heat exchangers *.

The thermal conductivity of 316 stainless steel for cryogenic applications from 0 to 300K as a function of temperature is given by †:

$$\log_{10} \kappa = \sum_{i=1}^9 a_i (\log_{10} T)^{i-1}, \quad (\text{D.2})$$

*webpage: www.webcoindustries.com

†webpage: cryogenics.nist.gov/MPropsMAY/316Stainless_rev.htm

$$\begin{array}{lll}
a_1 = -1.4087 & a_2 = 1.3982 & a_3 = 0.2543 \\
a_4 = -0.6260 & a_5 = 0.2334 & a_6 = 0.4256 \\
a_7 = 0.4658 & a_8 = 0.1650 & a_9 = -0.0199
\end{array}$$

where T is the temperature in K. For applications in the range of 213 to 293K, the thermal conductivity of 316 stainless steel is 13–15.1 W·(m K)⁻¹.

D.1 Shell side

The shell side convective heat transfer coefficient for gas flow is calculated from a method from Gnielinski for tube banks [58] as recommended by Neeraas et al. [90]. The Gnielinski method, Eqs. (D.3)-(D.10), predicts the shell side heat transfer coefficient for gas-only operation within an uncertainty of 10% [90].

$$Nu = \frac{\kappa L}{\lambda_{gas}} = f_A \left(0.3 + \sqrt{Nu_{lam}^2 + Nu_{turb}^2} \right), \quad (D.3)$$

$$Nu_{lam} = 0.664 \sqrt{Re} Pr^{(1/3)}, \quad (D.4)$$

$$Nu_{turb} = \frac{0.037 Re^{0.8} Pr}{1 + 2.443 Re^{-0.1} (Pr^{(2/3)} - 1)}, \quad (D.5)$$

$$L = \frac{\pi}{2} D_{tu}, \quad (D.6)$$

$$Re = \frac{c L \rho}{\gamma \mu}, \quad (D.7)$$

$$Pr = \frac{c_p \mu}{\kappa}, \quad (D.8)$$

$$\gamma = 1 - \frac{\pi D_{tu}}{4 P_r}, \quad (D.9)$$

$$f_A = 1 + \frac{0.7 + \left(\frac{P_l}{P_r} - 0.3 \right)}{\gamma^{1.5} \left(\frac{P_l}{P_r} + 0.7 \right)^2}. \quad (D.10)$$

L is thereby the characteristic length or stream length at the shell side of a tube, given by the half circumference of the tube. κ is the thermal conductivity of the shell fluid, λ_{gas} is the shell side convective heat transfer coefficient, Re the Reynolds number for shell flow, c the average velocity in the empty cross section of the shell as if there were no tubes, ρ the shell fluid density, μ the shell fluid dynamic viscosity and γ the void fraction, used to calculate the average velocity between tubes. Pr is the Prandtl number for shell flow and c_p the shell side fluid heat capacity, which is approached from the isobaric enthalpy change with temperature ($\frac{\Delta h}{\Delta T}|_p$), with ΔT small. f_A is the geometry arrangement factor for in-line tube banks. Finally, P_r and P_l are the radial and longitudinal distances between tubes.

The radial and longitudinal pitch ratios (P_r/D_{tu} , P_t/D_{tu}) are set 1.3 and 1.15 respectively [90], which is in line with common values for multi-tube arrangements in heat exchangers[‡].

For two-phase conditions on the shell side (condensation), a liquid film may form on the tubes. Although the convective heat transfer coefficient of the film is generally much larger than for gas, it may though be included in the derivation of the overall heat transfer coefficient:

$$\frac{1}{\bar{h}} = \frac{1}{\lambda_{sh}} + \frac{1}{\lambda_{fi}} + \frac{\delta_m}{\kappa_m} \frac{2A_{sh}}{A_{tu} + A_{sh}} + \frac{1}{\lambda_{tu}} \frac{A_{sh}}{A_{tu}}, \quad (\text{D.11})$$

Where λ_{fi} is the film layer convective heat transfer coefficient. The shell side heat transfer coefficient for liquid falling film is calculated from a method of Bays and McAdams [11], as suggested by Neeraas et al. [89]: In dimensionless form [89]:

$$Nu = \frac{\kappa\delta}{\lambda_{fi}} = a_1 \left(\frac{D_{tu}}{\delta} \right)^c Re^b Pr^d, \quad (\text{D.12})$$

with δ the reference film thickness

$$\delta = \left(\frac{\mu^2}{g\rho^2} \right)^{(1/3)}, \quad (\text{D.13})$$

$$Re = \frac{4\Gamma}{\mu}, \quad (\text{D.14})$$

$$Pr = \frac{c_p\mu}{\kappa}, \quad (\text{D.15})$$

$$\Gamma = \frac{\dot{m}}{\pi(D_{co} + D_{sh})N_{lay}}, \quad (\text{D.16})$$

where κ is the thermal conductivity of the liquid phase, λ_{fi} the convective heat transfer coefficient of the film layer, μ the liquid phase viscosity, g the gravitational constant and ρ the density of the liquid phase. c_p is the liquid phase heat capacity, approached by $\left. \frac{\Delta h_f}{\Delta T} \right|_p$, with ΔT small. Γ is the characteristic liquid mass flow rate per unit circumferential tube length, \dot{m} is the liquid mass flow, D_{co} and D_{sh} the shell core and outer diameter, and N_{lay} the number of tube layers in radial direction.

The shell core diameter is taken as $D_{co} = 9D_{tu}$ [89]. The number of tube layers and the outer shell diameter are calculated from volume flow at the shell side with the lowest density and a reference flow velocity c_{ref} equal to $1 \text{ m}\cdot\text{s}^{-1}$.

For inline tube banks the relation between the number of tube layers N_{lay} and the inter tube flow area perpendicular to the shell fluid velocity A_{flow} can be approached by:

$$A_{flow} = \pi P_r \sum_{i=1}^{N_{lay}} (D_{co} + 2iD_{tu} + (2i - 1)P_r), \quad (\text{D.17})$$

[‡]webpage: www.engineeringpage.com

The outer shell diameter D_{sh} is then given as:

$$D_{sh} = D_{co} + N_{lay} (P_r + D_{tu}) . \quad (D.18)$$

The constants in Eq. (D.12) are given by Neeraas et al. [89]:

$$\begin{aligned} Re \leq 2000 \\ a = 0.886 \quad a_1 = 0.762 \quad b = 1/9 \quad c = -1/3 \quad d = 1/3 \\ Re > 2000 \\ a = 0.313 \quad a_1 = 0.269 \quad b = 1/4 \quad c = -1/3 \quad d = 1/3 \end{aligned}$$

In estimation of the convective shell side heat transfer, only the equations for gas were applied with average properties in case of two-phase flow. Film thermal resistance is not taken into account.

D.2 Tube side

For laminar single phase tube flow ($Re \leq 2300$) we use the Sieder-Tate correlation [12]:

$$Nu = \frac{\kappa \delta}{\lambda_{tu}} = 1.86 \left(Re Pr \frac{d}{L} \right)^{(1/3)} , \quad (D.19)$$

with

$$Re = \frac{c L \rho}{\mu} , \quad (D.20)$$

$$Pr = \frac{c_p \mu}{\kappa} , \quad (D.21)$$

where L is the characteristic length given by Eq. (D.6), μ , ρ , κ and c_p the dynamic viscosity, density, thermal conductivity and isobaric heat capacity of the tube fluid and c the fluid velocity which is set to $1 \text{ m}\cdot\text{s}^{-1}$ for the side with the lowest density.

For turbulent single phase flow ($Re \geq 10^3$) the Dittus-Boelter correlation is applied for estimation of the convective heat transfer coefficient [12]:

$$Nu = \frac{\kappa \delta}{\lambda_{tu}} = 0.023 Re^{0.8} Pr^n , \quad (D.22)$$

with $n = 0.3$ for cooling and $n = 0.4$ for heating. For the transient regime from $2000 < Re < 10000$, the Nusselt number is derived via interpolation between the Sieder-Tate correlation at $Re=2000$ and the Dittus-Boelter correlation at $Re=10000$.

For two phase flow (condensation) a film layer convective heat transfer coefficient may be included, similarly as described for the shell side.

Neeraas [88] recommends for tube side condensation in coil-wound heat exchangers the method of Boyko and Kruzhilin [18] for calculation of the film Nusselt number and estimation of the film heat transfer coefficient:

$$Nu = 0.024Re^{0.8} Pr^{0.43} \frac{1}{2} \left(\sqrt{\left(\frac{\rho}{\rho_m}\right)_{in}} + \sqrt{\left(\frac{\rho}{\rho_m}\right)_{out}} \right), \quad (\text{D.23})$$

where the Reynolds number is given as Eq. (D.20) with for c the average velocity of the mixture (vapor+liquid) and the characteristic length L given by Eq. (D.6). ρ and ρ_m correspond to the densities of the film and the mixture (vapor+liquid) at the inlet of the tube, in , or exit of the tube, out .

Further corrections may be applied in the estimation of the film heat transfer coefficient as advised by Neeraas [88], but are not considered here.

In estimation of the convective tube side heat transfer, only the equations for single phase flow were applied with average properties in case of two-phase flow. Film thermal resistance is not taken into account.

D.3 Estimation and selection of fluid properties

For estimating the shell and tube side convective heat transfer coefficients, densities, viscosities and thermal conductivities are required. Densities (liquid, gas and mixture) are estimated from the Peng-Robinson Equation of state; cf. Chapter 2.

Viscosities and thermal conductivities for mixture pure components were taken from the NIST Chemistry WebBook [§]. To include to some extent the influence of mixing, viscosities and thermal conductivities for both vapor mixtures and liquid mixtures were estimated according to molar composition; i.e. for dynamic viscosity:

$$\mu_m = \sum_{i=1}^N y_i \mu_i, \quad (\text{D.24})$$

with N the number of components, y_i the component concentration, μ_i the pure component viscosity and μ_m the mixture viscosity. Two-phase viscosities and thermal conductivities are derived equal, with use of molar phase fractions instead of component concentrations.

At thermodynamic state (p, T) a mixture pure component does not always exist in the same phase as the mixture itself. In such case the pure component properties are taken from the pure component saturated condition at mixture temperature and for the actual mixture phase (i.e. saturated vapor if the mixture is in vapor-only phase). If at mixture temperature the pure component would either be a solid or supercritical, the properties are selected at a saturation condition close to the pure component triple or critical point.

[§]<http://webbook.nist.gov/chemistry/>

Membrane Models

In the application of flue gas post-combustion CO₂ capture, CRS is combined with a CO₂ permeating membrane system as proposed by MTR [83]. Models of cross-flow and counterflow(-sweep) modules have been created to assess the membrane-CRS combination. The models make use of the solution-diffusion theory [8].

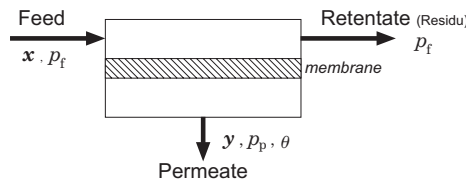


Figure E.1: Membrane.

In the modeling of membranes for process simulation, three membrane material properties are important: The selectivity, permeability and permeance. Pure component permeability is the membrane thickness scaled molar flux (flow per area) of a pure component through the membrane material per unit partial pressure drop. In relation to Fig. E.1, the permeability is expressed as:

$$\mathbb{P}_i = \frac{J_i \delta_{mem}}{(x_i p_f - y_i p_p)}, \quad (\text{E.1})$$

where J_i is the molar flux of component i through the membrane, \mathbb{P}_i the component permeability, δ_{mem} the membrane thickness, x_i and y_i the molar component feed and permeate concentration and p_f and p_p the feed and permeate pressure. The pure component permeance (productivity), \mathcal{P}_i , is the component molar flux through the membrane per unit partial pressure drop and expressed as:

$$\mathcal{P}_i = \frac{J_i}{(x_i p_f - y_i p_p)}. \quad (\text{E.2})$$

The selectivity is the ratio of two pure component permeabilities or permeances and indicates the membranes preference to pass one component over another:

$$S_{i/j} = \frac{\mathcal{P}_i}{\mathcal{P}_j} = \frac{\mathbb{P}_i}{\mathbb{P}_j}. \quad (\text{E.3})$$

The membranes simulated are MTR Polaris membranes with a CO₂ permeance of 1000 gpu*, a CO₂/N₂ selectivity of 50 and a CO₂/H₂O selectivity of 0.5 [83].

E.1 The Infinitely Small Membrane

For an infinitely small membrane (Fig. E.1), compositions on the feed and permeate side and the flux through the membrane can be assumed constant. If we substitute Eq. (E.2) for component i and j into the the selectivity expression we obtain:

$$\mathcal{S}_{i/j} = \frac{J_i (x_j p_f - y_j p_p)}{J_j (x_i p_f - y_i p_p)}. \quad (\text{E.4})$$

With the molar component flux $J_i = \dot{\mathbf{m}}_p y_i / A$, with $\dot{\mathbf{m}}_p$ the molar permeate flow and A the membrane area, the ratio of fluxes equals the ratio of permeate concentrations. Implementation into Eq. (E.4) results into:

$$\mathcal{S}_{i/j} = \frac{y_i (x_j p_f - y_j p_p)}{y_j (x_i p_f - y_i p_p)}. \quad (\text{E.5})$$

For a defined feed composition and selectivity $\mathcal{S}_{i/j}$ in combination with mass conservation $\sum_{i=1}^N y_i = 1$, $\sum_{i=1}^N x_i = 1$, the permeate stream composition can be solved from Eq. (E.5). If we limit ourselves to a CO₂/N₂ binary mixture, a quadratic equation in y_{CO_2} is obtained:

$$y_{CO_2}^2 [1 - \mathcal{S}_{CO_2/N_2}] + y_{CO_2} [r - (1 - \mathcal{S}_{CO_2/N_2}) (1 + r x_{CO_2})] \dots - [\mathcal{S}_{CO_2/N_2} r x_{CO_2}] = 0, \quad (\text{E.6})$$

with r the pressure ratio of feed to permeate pressure ($r = p_f / p_p$). Eq. (E.6) can be solved analytically for y_{CO_2} . The smaller root corresponds to the correct solution:

$$y_{CO_2} = \frac{1 + r x_{CO_2}}{2} - \frac{r}{2(1 - \mathcal{S}_{CO_2/N_2})} - \frac{1}{2} \dots \dots \sqrt{\frac{r^2}{(1 - \mathcal{S}_{CO_2/N_2})^2} + \frac{2r(2\mathcal{S}_{CO_2/N_2} x_{CO_2} - (1 + r x_{CO_2}))}{(1 - \mathcal{S}_{CO_2/N_2})} + (1 + r x_{CO_2})^2}. \quad (\text{E.7})$$

If we consider an N component mixture, the permeate composition is determined by a set of $N - 1$ quadratic equations, given by Eq. (E.5). Analytical solution is not possible for more than two components and requires iterative methods such as a Newton-Raphson method. We constrain ourselves however to binary mixtures.

*1 gpu = 3.35×10^{-10} mole/(s·m²Pa)

E.2 Cross-flow Membrane Modules

A cross flow membrane module can be seen as a series of infinitely small membrane elements coupled together by their retentate and feed streams. We divide the membrane module into a number of K very small membranes (Fig. E.2). Selection of K , such that the size of each element is small, allows for the assumption of a constant permeate flux through the elements membrane and constant feed and permeate side composition. Eq. (E.7) can be used successively to calculate an element's permeate composition.

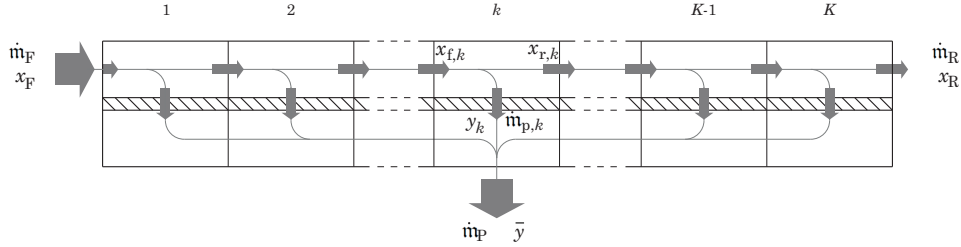


Figure E.2: Cross-flow membrane.

For modeling of membrane modules we neglect feed side pressure drop ($p_r = p_f$) and specify molar feed flow $\dot{m}_f^{(1)} = \dot{m}_F$, feed composition $x_f^{(1)} = x_F$, feed and permeate pressure p_f and p_p , and module permeate CO_2 recovery $\mathbb{R}_{P,\text{CO}_2}$, defined as:

$$\mathbb{R}_{P,\text{CO}_2} = \frac{\dot{m}_P \bar{y}_{\text{CO}_2}}{\dot{m}_F x_{F,\text{CO}_2}}. \quad (\text{E.8})$$

The element permeate CO_2 recovery is set equal for all elements, such that their sum equals the specified module permeate CO_2 recovery. For the first element $k = 1$ the permeate flow is calculated as:

$$\dot{m}_p^{(k)} = \dot{m}_f^{(k)} \frac{x_{f,\text{CO}_2}^{(k)}}{y_{\text{CO}_2}^{(k)}} \frac{\mathbb{R}_{P,\text{CO}_2}}{K}, \quad (\text{E.9})$$

whereby $y_{\text{CO}_2}^{(k)}$ is calculated according to Eq. (E.7). Using Eq. (E.2), the area of membrane element $k = 1$ is calculated as:

$$A^{(k)} = \frac{\dot{m}_p^{(k)} y_{\text{CO}_2}^{(k)}}{(p_f x_{f,\text{CO}_2}^{(k)} - p_p y_{\text{CO}_2}^{(k)})}. \quad (\text{E.10})$$

Mass conservation gives the unknown element retentate flow and composition, which specifies the feed flow and composition of the next element $k + 1$:

$$\dot{m}_f^{(k+1)} = \dot{m}_r^{(k)} = \dot{m}_f^{(k)} - \dot{m}_p^{(k)}. \quad (\text{E.11})$$

$$x_{f,CO_2}^{(k+1)} = x_{r,CO_2}^{(k)} = \frac{\dot{m}_f^{(k)} x_{f,CO_2}^{(k)} - \dot{m}_p^{(k)} y_{CO_2}^{(k)}}{\dot{m}_r^{(k)}}. \quad (\text{E.12})$$

The procedure to calculate element flows, compositions and area, Eqs. (E.9)–(E.12), is repeated to element $k = K$. By summation and averaging the permeate flow, permeate composition and membrane area of the cross-flow module, indicated by P , is determined:

$$\dot{m}_P = \sum_{k=1}^K \dot{m}_p^{(k)}, \quad (\text{E.13}) \quad A = \sum_{k=1}^K A^{(k)}, \quad (\text{E.14})$$

$$\overline{y_{CO_2}} = \frac{1}{K} \sum_{k=1}^K y_{CO_2}^{(k)}. \quad (\text{E.15})$$

E.3 Counter-flow(-Sweep) Membranes

Fig. E.3 shows a counter-flow membrane module which is split into K small elements. The permeate side of the membrane can be swept with a sweep-flow \dot{m}_s . For the evaluated CO_2 permeating membranes, sweeping with a CO_2 lean flow decreases the permeate side CO_2 partial pressure and enhances CO_2 separation. For non-sweep counter-flow membranes this flow is absent.

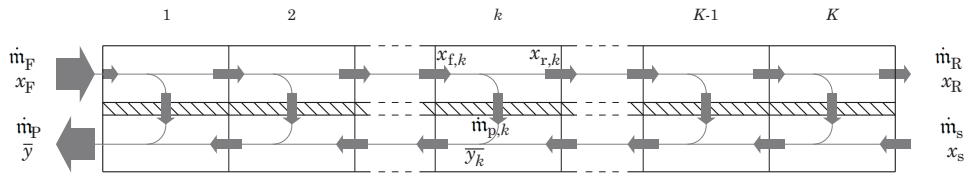


Figure E.3: Counter-flow (sweep) membrane.

Assuming pre-set values in all elements for molar flows and compositions by the cross-flow model, and eventually a prescribed sweep flow \dot{m}_s and composition x_s , the permeate side molar flow for each element k in a counter-flow membrane can be derived from:

$$\dot{m}_{P,i}^{(k)} = \sum_k \dot{m}_{p,i}^{(k)}, \quad (\text{E.16})$$

whereby $\dot{m}_{P,i}^{(k)}$ is the permeate side component molar flow in element k towards the permeate module exit and $\dot{m}_{p,i}^{(k)}$ is the component permeate flow through the elements

membrane (perpendicular to the permeate side molar flow). The permeate side composition in element k is related accordingly as:

$$\bar{y}_i^{(k)} = \frac{\dot{m}_{P,i}^{(k)}}{\dot{m}_P^{(k)}}, \quad \text{with} \quad \dot{m}_P^{(k)} = \sum_{i=1}^N \dot{m}_{P,i}^{(k)}. \quad (\text{E.17})$$

Using the preset feed side compositions and the obtained permeate side compositions $\bar{y}_i^{(k)}$ from Eq. (E.17), the permeate flow through the membrane of each element k is found from:

$$\dot{m}_{p,i}^{(k)} = A^{(k)} \mathcal{P}_i \left(x_{f,i}^{(k)} p_f - \bar{y}_i^{(k)} p_p \right), \quad (\text{E.18})$$

where $A^{(k)}$ is the membrane area of element k , initially obtained from the cross-flow model. The newly gained permeate flows through the membrane give rise to updating the feed side molar flows and compositions using:

$$\dot{m}_{r,i}^{(k)} = \dot{m}_{f,i}^{(k+1)} = \dot{m}_{f,i}^{(k)} - \dot{m}_{p,i}^{(k)}. \quad (\text{E.19})$$

$$x_{f,i}^{(k)} = \frac{\dot{m}_{f,i}^{(k)}}{\dot{m}_f^{(k)}}, \quad \text{with} \quad \dot{m}_f^{(k)} = \sum_{i=1}^N \dot{m}_{f,i}^{(k)}. \quad (\text{E.20})$$

The newly obtained feed side compositions $x_{f,i}^{(k)}$ allow again for the calculation of new membrane permeate flows $\dot{m}_{p,i}^{(k)}$ using Eq. (E.18), the calculation of new permeate side flows $\dot{m}_{P,i}^{(k)}$ using Eq. (E.16) and the determination of new permeate side compositions $\bar{y}_i^{(k)}$ for each element using eq. (E.17).

The sequence of Eq. (E.16) to Eq. (E.20) is repeated until the permeate side compositions converge to stationary values. In each new sequence, newly obtained compositions and flows on feed and permeate side are weighted and averaged with the old values from the previous sequence for reasons of calculation stability.

For the stationary compositions and flows, the permeate CO₂ recovery is determined. Using the difference and between obtained and target permeate CO₂ recovery, the membrane area of all elements k is adjusted by means of a newton method. A quadratic extrapolation function is thereby used for off target permeate CO₂ recovery, and a linear extrapolation function once the target is approached. The sequence and area adjustment is repeated until the target permeate CO₂ recovery is met.

Nomenclature

a	PR-EoS parameter	$\text{kg}\cdot\text{m}^5\text{mol}^{-2}\text{s}^{-2}$
a	Speed of sound	$\text{m}\cdot\text{s}^{-1}$
A	Area	m^2
A	Specific Helmholtz energy	$\text{J}\cdot\text{mol}^{-1}$
b	PR-EoS parameter	$\text{m}^3\text{mol}^{-1}$
\mathbb{B}	Impeller tip width – tip diameter ratio	-
c_p	Specific isobaric heat capacity	$\text{J}\cdot\text{mol}^{-1}\text{K}^{-1}$ ($\text{J}\cdot\text{kg}^{-1}\text{K}^{-1}$)
c	Fluid velocity	$\text{m}\cdot\text{s}^{-1}$
C	Capacity	$\text{J}\cdot\text{s}^{-1}\text{K}^{-1}$
C	Constant	-
\mathbb{C}	Capacity ratio	-
d	Diameter	m
D	Diameter	m
$d_{p50\%}$	Particle diameter separated with 50% change	m
f	Fugacity	Pa
F	Number of thermodynamic degrees of freedom	-
g	Specific Gibbs free energy	$\text{J}\cdot\text{mol}^{-1}$
G	Gibbs free energy	J
G_Δ	Gibbs Energy function	$\text{J}\cdot\text{mol}^{-1}$
h	Specific enthalpy	$\text{J}\cdot\text{mol}^{-1}$ ($\text{J}\cdot\text{kg}^{-1}$)
J	Molar flux	$\text{mol}\cdot\text{m}^{-2}\text{s}^{-1}$
k	Binary interaction parameter	-
K	K-factor (y_i/x_i)	-
L	Length,width or height	m
\dot{m}	Mass flow	$\text{kg}\cdot\text{s}^{-1}$
\dot{n}	Molar flow	$\text{mol}\cdot\text{s}^{-1}$
Ma	Mach number	-
n	Number of moles	mol
N	Number of components	-
p	Pressure	Pa
P	Number of phases	-
\mathbb{P}	Permeability	$\text{mol}\cdot\text{s}^{-1}\text{m}^{-1}\text{Pa}^{-1}$

\mathcal{P}	Permeance (productivity)	$\text{mol}\cdot\text{s}^{-1}\text{m}^{-2}\text{Pa}^{-1}$
q	Transferred heat	$\text{J}\cdot\text{s}^{-1}$
Q	Volume flow	m^3s^{-1}
Ω	Molar flow	$\text{mol}\cdot\text{s}^{-1}$
R	Universal gas constant	$\text{J}\cdot\text{K}^{-1}\text{mol}^{-1}$
\mathbb{R}	Recovery	-
s	Specific entropy	$\text{J}\cdot\text{K}^{-1}\text{mol}^{-1}$
S	Entropy	$\text{J}\cdot\text{K}^{-1}$
\mathcal{S}	Selectivity	-
T	Temperature	K
u	Specific internal energy	$\text{J}\cdot\text{mol}^{-1}$
U	Impeller tangential velocity	$\text{m}\cdot\text{s}^{-1}$
\bar{U}	Overall heat transfer coefficient	$\text{W}\cdot\text{m}^{-2}\text{K}^{-1}$
v	Specific volume	$\text{m}^3\text{mol}^{-1}$
V	Total volume	m^3
w, \mathbf{w}	Solid phase concentration	$\text{mol}\cdot\text{mol}^{-1}$
x, \mathbf{x}	Liquid phase concentration	$\text{mol}\cdot\text{mol}^{-1}$
x, \mathbf{x}	Membrane feed/retentate concentration	$\text{mol}\cdot\text{mol}^{-1}$
y, \mathbf{y}	Vapor phase concentration	$\text{mol}\cdot\text{mol}^{-1}$
y, \mathbf{y}	Membrane permeate concentration	$\text{mol}\cdot\text{mol}^{-1}$
Y	Exponentially transformed concentration	$\text{mol}\cdot\text{mol}^{-1}$
z, \mathbf{z}	Feed (total) component concentration	$\text{mol}\cdot\text{mol}^{-1}$
μ	Chemical potential	$\text{J}\cdot\text{mol}^{-1}$
Z	Compressibility factor	-

Greek

α	Phase fraction	$\text{mol}\cdot\text{mol}^{-1}$
α	Angle (air angle)	rad
β	Angle (blade angle)	rad
γ	Activity coefficient	-
δ	Thickness	m
ϵ	Effectiveness	-
η	Efficiency	-
κ	Thermal conductivity	$\text{W}\cdot\text{m}^{-1}\text{K}^{-1}$
λ	Convective heat transfer coefficient	$\text{W}\cdot\text{m}^{-2}\text{K}^{-1}$
μ	Chemical potential	$\text{J}\cdot\text{mol}^{-1}$
μ	Dynamic viscosity	$\text{Pa}\cdot\text{s}$
ρ	Density	$\text{kg}\cdot\text{m}^{-3}$
σ	Surface tension	$\text{N}\cdot\text{m}^{-2}$
$\tilde{\sigma}$	Impeller slip ratio	-
ϕ	Fugacity coefficient	-
ψ	Applied torque correction	-
ω	Pitzer's acentric factor	-
Ω	Angular velocity	$\text{rad}\cdot\text{s}^{-1}$

Subscripts

0	Reference state, Stagnation condition
ax	Axial
c	Critical point
C	Compressor
$calc$	Calculated from model
$core$	Core
D	Drag
ds	Drive shaft
e, e	Electric
E	Expander
eye	Impeller eye
exp	Experimental
f, F	Feed
fe	Filter element
g	Gas or vapor
i	Component number
in	Inlet
j	Phase number, 2^{nd} component number
m	Mixture
mem	Membrane
n	Normal conditions ($T_n = 273.15K$, $p_n = 1.01325 \times 10^5 Pa$)
p	Particle
p, P	Permeate
$pack$	Equipment package dimension
$post$	Post-separator
pre	Pre-separator
r	Radial
r, R	Retentate
ref	Reference phase
res	Residual
s	Sweep
sh	Shell side
t	Throat/vane outlet
th	Thermal
tip	Impeller tip
tr	Triple point
tu	Tube side
$vane$	Expander inlet or diffuser or impeller vane
θ	Tangential

Superscripts

0	Reference state
$^{(k)}$	Element or iteration number k
*	Solid component
E	Excess property
fus	Pure component fusion condition
L	Liquid phase
o	Ideal
sat	Pure component saturated condition
sub	Pure component sublimation condition
S	Solid phase
SP	Stationarity condition
V	Vapor phase

Abbreviations

AAD	Absolute average deviation
AMA	Absolute model accuracy
CAPEX	Capital expenditures
CCS	Carbon (CO ₂) capture and storage
COP	Coefficient of performance
CRS	Condensed rotational separation
d.b.	Dry basis
DFG	Flue gas desulphurization
EoS	Equation of state
EOR	Enhanced oil recovery
ESP	Electrostatic precipitator
FGC	Flue gas condenser (water removal)
FGR	Flue gas recycle
LHS	Left hand side
LNG	Liquid natural gas
NG	Natural gas
NTU	Number of transfer units
OPEX	Operational expenditures
RHS	Right hand side
RPM	Rounds per minute
RPS	Rotational particle separator
TPD	Tons per day
w.b.	Wet basis

Reference Conditions in this work

Standard conditions	293.15 K	,	1.01325×10^5 Pa
Normal conditions	273.15 K	,	1.01325×10^5 Pa
Normal conditions USA	60 °F	,	14.73 psi (only for conversion MMscfd, kscfd, etc.)

Bibliography

- [1] Abu Zahra, M.R.M. [2009], Carbon Dioxide Capture from Flue Gas, PhD thesis, Delft University of Technology, Delft, NL.
- [2] Alami, I.A. [2010], 'Wasit gas plant: New sour gas developments in Saudi Arabia', *Proc. 6th Sour oil & Gas Advanced Technology, March 28th - April 1st, 2010, Abu Dhabi, United Arab Emirates* pp. 5–18.
- [3] Amo, K., R. Baker, B. Firat-Sercinoglu, J. He, H. Lin, T. Merkel, X. Wei and H. Wijmans [2010], 'An efficient membrane process to capture carbon dioxide from power plant flue gas', *Proc. 27th International Pittsburgh Coal Conference, October 11-14, 2010, Istanbul, Turkey* .
- [4] Anheden, M., J. Yan and G. De Smedt [2005], 'Denitrogenation (or oxyfuel concepts)', *Oil & Gas technol. - Rev. IFP* **60**(3), 485–495.
- [5] Anheden, M., U. Burchhardt, H. Ecke, R. Faber, O. Jidinger, R. Giering, H. Kass, S. Lysk, E. Ramström and J. Yan [2011], 'Overview of operational experience and results from test activities in vattenfall's 30MW_{th} oxyfuel pilot plant Schwarze Pumpe.', *Energy Procedia* **4**, 941–950.
- [6] Armstrong, P.A., D.L. Bennett, E.P. Foster and E.E. van Stein [2005], 'ITM oxygen: The new oxygen supply for the new IGCC market', *Proc. Gasification Technologies 2005, October 9-12, 2005, San Francisco (Ca), USA* .
- [7] Atlas Copco [2012], 'Driving expander technology', PDF-brochure / company website.
- [8] Baker, R.W. [2004], *Membrane Technology and Applications*, 2nd edn, John Wiley & Sons Ltd., UK.
- [9] Bansal, G., M. Golombok, J.J.H. Brouwers and G. Tesselaar [2011], 'CO₂ droplets from condensed natural gas', *Ind. Eng. Chem. res.* **50**(5), 3011–3020.
- [10] Bansal, G.D. [2012], Condensing CO₂ droplets, PhD thesis, Eindhoven University of Technology, Eindhoven, NL.
- [11] Bays, G.S. and W.H. McAdams [1937], 'Heat transfer coefficients in falling film heaters, streamline flow', *Indust. Eng. Chem.* **29**(11), 1240–1246.
- [12] Bejan, A. and A.D. Kraus [2003], *Heat Transfer Handbook*, 1st edn, John Wiley & sons, inc., Hoboken, New-Jersey, USA.

- [13] Benthum, R.J. van, H.P. van Kemenade, J.J.H. Brouwers and M. Golombok [2011], ‘Condensed rotational separation of CO₂’, *Applied Energy* **93**(1), 457–465.
- [14] Berstad, D., R. Anantharaman and Neksa [2013 (accepted)], ‘Low-temperature CO₂ capture technologies – applications and potential’, *Int. J. Refrig.* **xxx**.
- [15] Besong, M.T., M.M. Maroto-Valer and A.J. Finn [2013], ‘Study of design parameters affecting the performance of CO₂ purification units in oxy-fuel combustion’, *Int. J. Greenhouse Gas Control* **12**, 441–449.
- [16] Beysel, G. [2009], ‘Enhanced cryogenic air separation - a proven process applied to oxyfuel’, *Proc. 1st Oxyfuel Conference, September 7-10, 2009, Cottbus, Germany*.
- [17] Bill, A. [2003], ‘Air pollution control - regulatory & technology development’, *Proc. UNECE, November 17-18 2010, Geneva, Switzerland*.
- [18] Boyko, L.D. and G.N. Kruzhilin [1967], ‘Heat transfer and hydraulic resistance during condensation of steam in a horizontal tube and in a bundle of tubes’, *Int. J. Heat Mass Transfer* **10**, 361–373.
- [19] Brockett, S. [2009], ‘The EU enabling legal framework for carbon capture and geological storage’, *Energy Procedia* **1**, 4433–4441.
- [20] Brouwers, J.J.H. and H.P. van Kemenade [2010a], ‘Condensed rotational separation for CO₂ capture in coal gasification processes’, *Proc. 4th Int. Freiburg Conference on IGCC & XtL technologies, 2010, Dresden, Germany*.
- [21] Brouwers, J.J.H. and H.P. van Kemenade [2010b], ‘Condensed rotational separation to upgrade sour gas’, *Proc. 6th Sour oil & Gas Advanced Technology, March 28th - April 1st 2010, Abu Dhabi, United Arab Emirates* pp. 173–187.
- [22] Brouwers, J.J.H., H.P. van Kemenade and J.P. Kroes [2012], ‘Rotational Particle Separator: An efficient method to separate micron-sized droplets and particles from fluids’, *Filtration* **12**(1), 49–60.
- [23] Brown, T.S., E.D. Sloan and A.J. Kidnay [1989], ‘Vapor-liquid equilibria in the nitrogen + carbon dioxide + ethane system’, *Fluid Phase Equilib.* **51**, 299–313.
- [24] Brown, T.S., V.G. Niesen, E.D. Sloan and A.J. Kidnay [1989], ‘Vapor-liquid equilibria for the binary systems of nitrogen, carbon dioxide and n-butane at temperatures from 220 to 344 K’, *Fluid Phase Equilib.* **53**, 7–14.
- [25] Buruma, R.C., J.J.H. Brouwers and H.P. van Kemenade [2012], ‘Rotational Particle Separator as a compact gas scrubber’, *Chem. Eng. Technol.* **35**(9), 1576–1582.
- [26] Candy, D. [2012], ‘United Arab Emirates: E&P profile’, *Arab. Oil and Gas* (10747).
- [27] Carroll, J.J. [2002], ‘Phase equilibria relevant to acid gas injection: Part 1 – non-aqueous phase behavior’, *J. Can. Pet. Technol.* **41**(6), 1–7.
- [28] Castle, W.F. [2002], ‘Air separation and liquefaction: recent developments and prospects for the beginning of the new millennium’, *Int. J. Refrig.* **25**, 158–172.
- [29] Cézac, P., J.-P. Serin, J. Mercadier and G. Mouton [2007], ‘Modelling solubility of solid sulphur in natural gas’, *Chem. Eng. J.* **133**, 283–291.

-
- [30] C.F., Leibovici and J. Neoschil [1992], ‘A new look at the Rachford-Rice equation’, *Fluid Phase Equilib.* **74**, 303–308.
- [31] Chiu, C.-H. and H.E. Kimmel [2001], ‘Turbo-expander technology development for LNG plants’, *Proc. 13th Conference and Exhibition on Liquefied Natural Gas, May 14-17, 2001, Seoul, Korea* (presentation - pdf).
- [32] Ciferno, J. [2009], Existing plants, emissions and capture - setting CO₂ program goals, report DOE/NETL-2009/1366, National Energy Technology Laboratory, USA.
- [33] Clodic, D., R. El Hitti, M. Younes, A. Bill and F. Casier [2005], ‘CO₂ capture by anti-sublimation - thermo-economic process evaluation’, *Proc. 4th Annual Conference on Carbon Capture & Sequestration, May 2-5, 2005, Alexandria, USA* .
- [34] *CO₂ Capture technologies - Post Combustion Capture* [2012], report, Global Carbon Capture and Storage Institute, Australia.
- [35] *Coal in the rich world - The mixed fortunes of a fuel* [2013], *The Economist* .
- [36] Cryostar [2013a], ‘Turbo expander with compressor brake TC’, PDF-brochure / company website.
- [37] Cryostar [2013b], ‘Turbo-expanders for cold production and energy recovery’, PDF-brochure / company website.
- [38] Curtis, H.W. and Michelsen M.L. [1989], ‘The negative flash’, *Fluid Phase Equilib.* **53**, 53–71.
- [39] Danesh, A., D.-H. Xu and A.C. Todd [1991], ‘Comparative study of cubic equations of state for predicting phase behaviour and volumetric properties of injection gas-reservoir oil systems’, *Fluid Phase Equilib.* **63**, 259–278.
- [40] Danesh, Ali [1998], *PVT and Phase Behaviour of Petroleum Reservoir Fluids*, 1st edn, Elsevier.
- [41] Darde, A., A. Prabhakar, J. Tranier and N. Perrin [2009], ‘Air separation and flue gas compression and purification units for oxy-coal combustion systems’, *Energy Procedia* **1**, 527–534.
- [42] Davalos, J., W.R. Anderson, R.E. Phelps and A.J. Kidnay [1976], ‘Liquid-vapor equilibria at 250.00K for systems containing methane, ethane, and carbon dioxide’, *J. Chem. Eng. Data* **21**(1), 81–84.
- [43] Davis, J.A., N. Rodewald and F. Kurata [1962], ‘Solid-liquid-vapor phase behavior of the methane-carbon dioxide system’, *AIChE J.* **8**(4), 537–539.
- [44] Dean, J.A. [1999], *Lange’s Handbook of Chemistry*, 15th edn, McGraw-Hill, Inc., New-York, USA.
- [45] Denderen, M. van, E. Ineke and M. Golombok [2009], ‘CO₂ removal from contaminated natural gas mixtures by hydrate formation’, *Ind. Eng. Chem. Res.* (48), 58025807.
- [46] Donnelly, H.G. and D.L. Katz [1954], ‘Phase equilibria in the carbon dioxide-methane system’, *Ind. Eng. Chem* **46**(4), 511–517.
- [47] Dresser Rand [2010], ‘Bringing energy and the environment into harmony - Products and Services Overview’, PDF-brochure / company website.

- [48] Earth and Mineral Sciences, Pennstate College [September 11th, 2008], *Phase Relations in Reservoir Engineering*, www.e-education.psu.edu/png520.
- [49] Eggers, R. and D. Köpke [2011], 'Phase equilibria measurements and their application for the CO₂ separation from CO₂ rich gases', *Proc. IEAGHG International Oxy-Combustion Network, March 5-6, 2011, Yokohama, Japan*.
- [50] Eswaran, S., S. Wu and R. Nicolo [2010], 'Advanced amine-based CO₂ capture for coal-fired power plants', *Proc. COAL-GEN2010 Conference, August 10-12, 2010, Pittsburgh, USA* pp. 1–8.
- [51] Folger, P. [2010], Carbon capture: A technology assessment, Congressional research Service Rapport 7-5700 / R41325, Congressional research Service.
- [52] Fu, D. and Y. Wei [2008], 'Investigation of vapor-liquid surface tension for carbon dioxide and hydrocarbon mixtures by perturbed-chain statistical associating fluid theory combined with density-gradient theory', *Ind. Eng. Chem. Res.* **47**, 4490–4495.
- [53] GE Power Systems - Oil & Gas [2005], 'Centrifugal & axial compressors', PDF-brochure / company website.
- [54] GE Power Systems - Oil & Gas [2012], 'Turboexpander-generators', PDF-brochure / company website.
- [55] GE Power Systems - Oil & Gas [2013], 'Expanding your plant's succes: Rotoflow turbo expanders for hydrocarbon applications', PDF-brochure / company website.
- [56] Hart, A. and N. Gnanendran [2009], 'Cryogenic CO₂ capture in natural gas', *Energy Procedia* **1**, 697–706.
- [57] Herri, J.-M., A. Bouchemoua, M. Kwaterski, A. Fezoua, Y. Ouabbas and A. Cameirao [2011], 'Gas hydrate equilibria for CO₂-N₂ and CO₂-CH₄ gas mixtures—experimental studies and thermodynamic modelling', *Fluid Phase Equilib.* **301**, 171–190.
- [58] Hewitt, G.F., ed. [1998], *Heat Exchanger Design Handbook*, Begell House, Inc., USA.
- [59] Higginbotham, P., V. White, K. Fogash and G. Guvelioglu [2011], 'Oxygen supply for oxyfuel CO₂ capture', *Int. J. Greenhouse Gas Control* **5S**, S194–S203.
- [60] Hong, J., G. Chaudhry, J.G. Brisson, R. Field, M. Gazzino and Ghoniem A.F. [2009], 'Analysis of oxy-fuel combustion power cycle utilizing a pressurized coal combustor', *Energy* **34**, 1332–1340.
- [61] Hoyos, B. [2004], 'Generalized liquid volume shifts for the Peng-Robinson equation of state for C₁ to C₈ hydrocarbons', *Lat. Am. Appl. Res.* **34**, 83–89.
- [62] Jacobs, J. [2007], 'Enecogen: the cleanest dutch power station', *Proc. 1st Dutch Capture Technology Symposium, March 22, 2007, Petten, NL* (presentation - pdf).
- [63] Kather, A. [2007], 'Oxy-fuel process for hard coal with CO₂ capture', *Proc. International Oxy-Combustion Research Network, January 25-26, 2007, Winsor(CT), USA*.
- [64] Kather, A. and S. Kownatzki [2011], 'Assessment of the different parameters affecting the CO₂ purity from coal fired oxyfuel process', *Int. J. Greenh. Gas Contr.* (5S), S204–S209.

-
- [65] Katzer, J. [2007], The future of coal, Interdisciplinary MIT study, Massachusetts Institute of Technology, Cambridge, Massachusetts, USA.
- [66] Kemenade, H.P. and J.J.H. Brouwers [2012], ‘Hydrocarbon recovery by Condensed Rotational Separation’, *J. Pet. Exp. Prod. Technol.* **2**(1), 49–56.
- [67] Kemenade, H.P. and J.J.H. Brouwers [2013], ‘Comparing the volume and energy consumption of sour-gas cleaning by Condensed Rotational Separation and amine treatments’, *Energy technol.* **1**(1), 392–394.
- [68] Kemenade, H.P., J.J.H. Brouwers and R.J. van Benthum [2011], ‘Condensed Rotational Separation’, *Proc. AFS 24th Annual Conference, May 9-12, 2011, HurstBourne, Louisville(KY), USA* .
- [69] *Key World Energy Statistics* [2012], report, International Energy Agency, Paris, France.
- [70] Kozak, F., A. Petig, E. Morris, R. Rhudy and D. Thimsen [2009], ‘Chilled ammonia process for CO₂ capture’, *Energy* **1**(1), 1419–1426.
- [71] Kroes, J.P. [2012], Droplet collection in a scaled-up rotating separator, PhD thesis, Eindhoven University of Technology, Eindhoven, NL.
- [72] Kuppan, T. [2000], *Heat Exchanger Design Handbook*, Dekker Mechanical Engineering, 1st edn, CRC Press.
- [73] Kuramochi, T., A. Ramérez, W. Turkenburg and A. Faaij [2012], ‘Comparative assessment of CO₂ capture technologies for carbon-intensive industrial processes’, *Prog. Energy Combust. Sci* **38**(1), 87–112.
- [74] Le, T.T. and M.A. Trebble [2007], ‘Measurement of carbon-dioxide freezing in mixtures of methane, ethane and nitrogen in the solid-vapor equilibrium region’, *J. Chem. Eng. Data* (52), 683–686.
- [75] Leibovici, C.F. and J. Neoschil [1995], ‘A solution of Rachford-Rice equations for multiphase systems’, *Fluid Phase Equilib.* **112**, 217–221.
- [76] Lewis, G.N. [1908], ‘The osmotic pressure of concentrated solutions, and the laws of the perfect solution’, *J. Am. Chem. Soc.* **30**, 668–683.
- [77] Li, H. and J. Yan [2009], ‘Evaluating cubic equations of state for calculation of vapor-liquid equilibrium of CO₂ and CO₂-mixtures for CO₂ capture and storage processes’, *Appl. Energy* **86**, 826–836.
- [78] Li, H., J. Yan and M. Anheden [2009], ‘Impurity impacts on the purification process in oxy-fuel combustion based CO₂ capture and storage system’, *Appl. Energy* **86**, 202–213.
- [79] Linde [2009], ‘Looking inside... plate-fin versus coil-wound heat exchangers’, PDF-brochure / company website.
- [80] Logan Jr., E. and R. Ramendra, eds [2003], *Handbook of Turbomachinery*, 2nd edn, Marcel Dekker Inc., New-York, USA.
- [81] Makino, K., N. Misawa, T. Kiga and C. Spero [n.d.], Demonstration project: oxy-fuel combustion at Callide-A plant, report, World Energy Council.
- [82] MAN Diesel & Turbo [2013], ‘Forward thinking - advanced CO₂ compression solutions’, PDF-brochure / company website.

- [83] Merkel, T.C., H. Lin, X. Wei and R. Baker [2010], ‘Power plant post-combustion carbon dioxide capture: An opportunity for membranes’, *J. Membr. Sci.* **359**(1), 126–139.
- [84] Michelsen, M.L. [1982a], ‘The isothermal flash problem part i: Stability’, *Fluid Phase Equilib.* **9**, 1–19.
- [85] Michelsen, M.L. [1982b], ‘The isothermal flash problem part ii: phase split calculation’, *Fluid Phase Equilib.* **9**, 21–40.
- [86] Moghtaderi, B. and T. Wall [2010], ‘A novel chemical looping based air separation technology for oxy-fuel combustion of coal’, *Proc. NSW Low Emissions Coal Technologies Summit, June 8-9, 2010, Sidney, Australia*.
- [87] Mraw, S.C., S.C. Hwang and R. Kobayashi [1978], ‘Vapor-liquid equilibrium of the CH₄-CO₂ system at low temperatures’, *J. Chem. Eng. Data* **23**(2), 135–139.
- [88] Neeraas, B.O. [1994], ‘Tube-side heat transfer of condensing hydrocarbons in coil-wound LNG heat exchanger’, *Proc. 10th International Heat Exchanger Conference, August 14-18, 1994, Brighton, UK I*(The Industrial Sessions Papers), 127–132.
- [89] Neeraas, B.O., A.O. Fredheim and B. Aunan [2004a], ‘Experimental data and model for heat transfer, in liquid falling film flow on shell side, for spiral-wound LNG heat exchanger’, *Int. J. Heat. Transf.* **47**(1), 3565–3572.
- [90] Neeraas, B.O., A.O. Fredheim and B. Aunan [2004b], ‘Experimental shell-side heat transfer and pressure drop in gas flow for spiral-wound LNG heat exchanger’, *Int. J. Heat. Transf.* **47**(1), 353–361.
- [91] *NETL’s carbon capture, utilization and storage database version 4 (last updated 01/2013)* [2013], Google Earth layer / excell spreadsheet.
- [92] Neumann, P.N.A. and W. Walch [1968], ‘Dampf/flüssigkeits-gleichgewicht CH₄-CO₂ in bereich tiefer temperaturen und kleiner CO₂-molenbruche’, *Chem. Ing. Techn.* (40), 241–244.
- [93] Ng, H., Robinson D.B. and A. Leu [1985], ‘Critical phenomena in a mixture of methane, carbon dioxide and hydrogen sulfide’, *Fluid Phase Equilib.* **19**, 273–286.
- [94] Øi, L.E. [2007], ‘Aspen hysis simulation of CO₂ removal by amine absorption from a gas-based power plant’, *Proc. SIMS2007 Conference, October 30-31, 2007, Göteborg, Denmark* pp. 73–81.
- [95] Olajire, A.A. [2010], ‘CO₂ capture and sequestration technologies for end-of-pipe applications – a review’, *Energy* **35**(6), 2610–2628.
- [96] Pan, X., D. Clodic and J. Toubassi [2013], ‘CO₂ capture by antisublimation process and its technical economic analysis’, *Greenhouse Gases Sci. Technol.* (3), 8–20.
- [97] Peng, D.Y. and D.B. Robinson [1976], ‘A new two constant equation of state’, *Ind. Eng. Chem., Fundam.* **15**(1), 59–64.
- [98] Peng, D.Y. and D.B. Robinson [1979], ‘Calculation of three-phase solid-liquid-vapor equilibrium using an equation of state’, *Adv. Chem.* **182**, 185–195.
- [99] Poling, B.E., J.M. Prausnitz and J.P. O’Connell [2007], *The Properties of Gases and Liquids*, 5th edn, McGraw-Hill, Singapore, Asia.

-
- [100] Prausnitz, J.M., R.N. Lichtenthaler and E.G. de Azevedo [1999], *Molecular Thermodynamics of Fluid Phase Equilibria*, Prentice Hall International Series in the Physical and Chemical Engineering Sciences, 3th edn, Prentice Hall PTR, Upper Saddle river, New Jersey, USA.
- [101] *Quality Guidelines for Energy System Studies - CO₂ impurity design parameters* [2012], report DOE/NETL-341/011212, National Energy Technology laboratory, USA.
- [102] Rama, S.R.G. and A.K. Aijaz [2003], *Turbomachinery - Design and Theory*, 1st edn, Marcel Dekker Inc., New-York, USA.
- [103] Reddy, S., J. Scherffius and S. Freguia [2003], 'An enhanced amine-based CO₂ capture process', *Proc. 2th National Conference on Carbon Sequestration, May 5-8, 2003, Alexandria, USA* pp. 1–11.
- [104] Redlich, O. and J.N.S. Kwong [1949], 'On the thermodynamics of solutions. V. an equation of state. fugacities of gaseous solutions.', *Chem. Rev.* **44**(1), 233–244.
- [105] Reid, R.C. [1984], *The properties of gases and liquids*, 4th edn, McGraw-Hill inc.
- [106] Repasky, J.M., E.P. Foster, P.A. Armstrong, E.E. van Stein and L.L. Anderson [2011], 'ITM oxygen development for advanced oxygen supply', *Proc. Gasification Technologies Council, October 12, 2011, San Francisco (Ca), USA* .
- [107] Repasky, J.M., L.L. Anderson, E.E. van Stein, P.A. Armstrong and E.P. Foster [2012], 'ITM oxygen technology: scale-up toward clean energy applications', *Proc. 29th International Pittsburgh Coal Conference, October 15-18, 2012, Pittsburgh (Pa), USA* .
- [108] Ricaurte, M., J.-P. Torr e, D. Broseta, C. Diaz, J. and Dicharry and X. Renaud [2011], 'CO₂ removal from a CO₂–CH₄ gas mixture by hydrate formation: evaluation of additives and operating conditions', *Proc. 7th International Conference on Gas Hydrates, July 17-21 2011, Edinburgh, UK* pp. 1–11.
- [109] Rijke, S.J.M. de [2012], CO₂ removal by amine absorption and Condensed Rotational Separation, Master's thesis, Eindhoven University of Technology.
- [110] Ritter, R., A. Kutzschbach and T. Stoffregen [2009], 'Energetic evaluation of a CO₂ purification and compression plant for the oxyfuel process', *Proc. 1st Oxyfuel Conference, September 7-10, 2009, Cottbus, Germany* .
- [111] Romeo, L.M., I. Bolea and J.M. Escosa [2008], 'Integration of power plant and amine scrubbing to reduce CO₂ capture costs', *Appl. Therm. Eng.* **28**(8-9), 1039–1046.
- [112] Saravanamuttoo, H.I.H., G.F.C. Rogers and H. Cohen [2001], *Gas Turbine Theory*, 5th edn, Pearson Education Limited, Harlow, Essex, UK.
- [113] Schach, M., B. Oyarz'un, H. Schramm, R. Schneider and J. Repke [2011], 'Feasibility study of CO₂ capture by anti-sublimation', *Energy Procedia* **4**, 1403–1410.
- [114] Scholz, M., B. Frank, F. Stockmeier, S. Fal  and M. Wessling [2013], 'Techno-economic analysis of hybrid processes for biogas upgrading', *Ind. Eng. Chem. Res.* (accepted October 23), xxx.
- [115] Seader, J.D. and E.J. Henley [2006], *Separation Process Principles*, 2nd edn, John Wiley & Sons, Inc., USA.

- [116] Sebastian, A. [2001], *A dictionary of the History of Science*, 1st edn, Parthenon Pub. Group.
- [117] Seltzer, A., Z. Fan and Hack H. [2007], ‘Oxyfuel coal combustion power plant system optimization’, *Foster Wheeler N-America Corporation R&D* pp. 1–17.
- [118] Serin, J.-P. and P. Cézac [2008], ‘Three thermodynamic paths to describe solid fugacity: Application to sulphur precipitation from supercritical natural gas’, *J. Supercrit. Fluids* **36**, 21–26.
- [119] Soave, G. [1972], ‘Equilibrium constants from a modified redlich-kwong equation of state’, *Chem. Eng. Sci.* **27**(1197).
- [120] Soave, G.S. [1978], ‘Application of the redlich-kwong-soave equation of state to solid-liquid equilibria calculations’, *Chem. Eng. Sci.* **34**, 225–229.
- [121] Sonntag, R.E. [1960], *The Equilibrium of Solid Carbon Dioxide with its Vapor in the Presence of Nitrogen*, PhD thesis, University of Michigan, Michigan, USA.
- [122] Strömberg, L., G. Lindgren, J. Jacoby, R. Giering, U. Anheden, M. Burchhardt, H. Altmann, F. Kluger and G. Stamatelopoulos [2009], ‘Liquid-vapor equilibrium compositions of carbon dioxide-oxygen-nitrogen mixtures’, *Energy Procedia* **1**, 581–589.
- [123] Subrata, K.G. [2010], ‘A numerical model for the design of a mixed flow cryogenic turbine’, *Int. J. Eng.* **2**(1), 175–191.
- [124] Sundyne [2001], ‘Process gas compressor overview’, PDF-brochure / company website.
- [125] Swanenberg, H.E.C. [1979], ‘Phase equilibria in carbonic systems and their application to freezing studies of fluid inclusions’, *Contrib. Mineral. Petrol.* **68**, 303–306.
- [126] Telikapallia, V., F. Kozaka, J. Francois, B. Sherrick, J. Black, D. Muraskin, M. Cage, M. Hammond and G. Spitznogle [2011], ‘CCS with the alstom chilled ammonia process development program - field pilot results’, *Energy Procedia* **4**(1), 273–281.
- [127] Theunissen, T., M. Golombok, J.J.H. Brouwers, G. Bansal and R.J. van Benthum [2011], ‘Liquid CO₂ droplet extraction from gases’, *Energy* **36**(5), 2961–2967.
- [128] Tranier, J., R. Dubettier, A. Darde and N. Perrin [2011], ‘Air separation, flue gas compression and purification units for oxy-coal combustion systems’, *Energy Procedia* **4**, 966–971.
- [129] Trebble, M.A. [1989], ‘A preliminary evaluation of two and three phase flash initiation procedures’, *Fluid Phase Equilib.* **53**, 113–122.
- [130] Venkatarathnam, G. [2008], *Cryogenic Mixed Refrigerant Processes*, The International Cryogenics Monograph Series, Springer, New-York, USA.
- [131] Vrabec, J., G.K. Kedia, U. Buchhauser, R. Meyer-Pittroff and H. Hasse [2009], ‘Thermodynamic models for vapor-liquid equilibria of nitrogen+oxygen+carbon dioxide at low temperatures’, *Cryogenics* **49**, 72–79.
- [132] Waals, J.D. van der [1873], *De continueit van den gas- en den vloeistoestand*, PhD thesis, Hogeschool Leiden, Leiden, Netherlands.

-
- [133] Wall, T., R. Stanger and S. Santos [2011], ‘Demonstrations of coal-fired oxy-fuel technology for carbon capture and storage and issues with commercial deployment’, *Int. J. Greenhouse Gas Control* **5S**.
- [134] Walspurger, S. and H.A.J. van Dijk [2012], EDGAR CO₂ purity: type and quantities of impurities related to CO₂ point source and capture technology: A literature study, report ECN-E-12-054, ECN - Energieonderzoek Centrum Nederland, NL.
- [135] Weber, W., S. Zeck and H. Knapp [1984], ‘Gas solubilities in liquid solvents at high pressures: apparatus and results for binary and ternary systems of N₂, CO₂ and CH₃OH’, *Fluid Phase Equilib.* **18**, 253–278.
- [136] Wei, Y.S. and R.J. Sadus [2000], ‘Equations of state for the calculation of fluid-phase equilibria’, *AIChE J.* **46**(1), 169–196.
- [137] White, V., R. Allam and E. Miller [2006], ‘Purification of oxyfuel-derived CO₂ for sequestration or EOR’, *Proc. 8th International Conference on Greenhouse Gas Control Technologies, June 19-22, 2006, Trondheim, Norway* **1**, 1–6.
- [138] Whitson, C.H. and M.L. Michelsen [1989], ‘The negative flash’, *Fluid Phase Equilib.* **53**, 51–71.
- [139] Willems, G.P. [2009], Condensed Rotational Cleaning of Natural Gas, PhD thesis, Eindhoven University of Technology.
- [140] Wissen, R.J.E. van [2006], Centrifugal Separation for Cleaning Well Gas Streams, PhD thesis, Eindhoven University of Technology.
- [141] *World Energy outlook 2012* [2012], report, International Energy Agency, Paris, France.
- [142] Yinghui, Li, T.J. Russel and A. Kaveh [2012], ‘A rapid and robust alternative to Rachford-Rice in flash calculations’, *Fluid Phase Equilib.* **316**.
- [143] Yucelen, B. and A.J. Kidnay [1999], ‘Vapor-liquid equilibria in the nitrogen + carbon dioxide + propane system from 240 to 330 K at pressures to 15 MPa’, *J. Eng. Chem. Data* **44**, 926–931.
- [144] Zanganeh, K.E. and A. Shafeen [2007], ‘A novel process integration, optimization and design approach for large-scale implementation of oxy-fired coal power plants with CO₂ capture’, *Int. J. Greenhouse Gas Control* **1**, 47–54.
- [145] Zanganeh, K.E., A. Shafeen and C. Salvador [2009], ‘CO₂ capture and development of an advanced pilot-scale cryogenic separation and compression unit’, *Energy Procedia* **1**, 247–252.
- [146] Zenner, G.H. and Dana L.I. [1963], ‘Liquid-vapor equilibrium compositions of carbon dioxide-oxygen-nitrogen mixtures’, *Chem. Eng. Progr., Symp. Ser.* **59**(44), 36–41.
- [147] Zhang, L., R. Burgass, A. Chapoy, B. Tohidi and E. Solbraa [2011], ‘Measurement and modelling of CO₂ frost points in the CO₂-methane systems’, *J. Chem. Eng. Data* (56), 2971–2975.

Dankwoord

Na bijna vijf jaar, met veel plezier en hard gewerkt te hebben, is het dan eindelijk zover: Het proefschrift is af! Velen hebben hun bijdrage geleverd aan dit succes, waarvoor dank.

Mijn promotie had nooit tot stand kunnen komen zonder de samenwerking met Shell en de inzet en expertise van prof. Bert Brouwers, prof. Michael Golombok en dr. Erik van Kemenade. De vrijheid en eigen verantwoordelijkheid die ik van hen heb gekregen met betrekking tot de inhoud van dit werk heb ik erg gewaardeerd. Bert, ik heb genoten van de verregaande wetenschappelijke discussies, waarbij je probeert met simpele benaderingen de vinger op de juiste fundamentele plek van het probleem te leggen. Het zijn deze discussies die mij iedere keer motiveerden om nieuwe onopgeloste problemen aan te pakken en te evalueren. Dat dit proces niet stopt zodra je van huis bent, heb ik ervaren op de vele reizen die we samen gemaakt hebben, zoals Amerika, alwaar we van 's ochtends aan het ontbijt tot 's avonds laat aan de bar, het gehele CRS proces nog eens samen in detail geanalyseerd hebben. Erik, ik ken niemand die zo snel processen, technieken en problemen kan doorgronden als jij. Dat gaf mij vaak net dat inzicht wat ik nodig had om verder te komen in het oplossen van de tegen het lijf gelopen problemen. Ook voor een goed advies en praktische vragen stond je altijd klaar. Daarnaast zal ik onze reis naar Taiyuan nooit meer vergeten. Niet alleen door de Guinness, of omdat we vierentwintig uur lang gestrand waren op het vliegveld van Beijing, maar ook omdat ik geleerd heb voortaan wandelschoenen mee te nemen als ik met jou op reis ga. Mike, ook al is de deur soms net te smal, we komen er samen toch wel doorheen, zo blijkt. Inhoudelijk was jij minder betrokken bij mijn werk. Je hebt me echter voorzien van de nodige correcties, verbeteringen en tips wat betreft het schrijven van dit proefschrift. Ook al was ik het niet met elke correctie eens, jou bijdrage heeft zeker tot een hogere standaard geleid en ben je daarvoor zeer dankbaar. Ik heb van jullie veel geleerd en ben jullie zeer dankbaar voor jullie input, de opgedane ervaringen en de fijne tijd.

Dan mijn collega AIO'ers. Oud-AIO'ers Guy, Hattie, Gagan, Mart en Nicole, bedankt voor de korte maar gezellige tijd die ik met jullie heb doorgebracht. Tussen alle koffie en de vele discussies door heb ik van jullie in snel tempo de fijne kneepjes van een AIO'er zijn geleerd. Ook collega AIO'ers David, Boaz, Joris, Coen, Julien, Emanuele en Wiktor, bedankt voor jullie gezelschap. Met name tijdens de lunch, de vakgroep uitjes en de twee studiereizen naar Zwitserland heb ik jullie goed leren kennen. David en Boaz, helaas zijn jullie tegenwoordig vaak te vinden bij Shell waardoor het toch wel erg stil is aan het eind van de gang van de 2e verdieping. Ook oud-studenten Steven, Joris en Bob, bedankt voor jullie samenwerking. Steven, jou interne stage liep niet zo lekker, maar je hebt door jou formidabele afstuderen mij voorzien van een degelijk model van een amine absorptie proces. Joris en Bob, zonder jullie had het experimentele condensatie project met de hogedrukcel niet plaats kunnen vinden. Ondanks dat dit deel niet meer is opgenomen in mijn proefschrift, wil ik jullie toch graag bedanken voor jullie samenwerking en input.

Tot slot mijn liefvallige vriendin Laura. Zonder deze promotie had ik je waarschijnlijk nooit ontmoet. We hebben elkaar leren kennen in het eerste jaar van mijn promotie en besloten na een jaar te gaan samenwonen in het pittoreske midden-Limburgse Asenray. Lieve schat, je hebt me gedurende de tijd dat we nu samen zijn altijd gesteund en mij opgevrolijkt op momenten dat het even tegenzat of als iets niet lukte. Ik ben erg gelukkig met jou en ben je zeer dankbaar voor je steun, afleiding en gezelschap.

Rob

Curriculum Vitae

Rob Johannes van Benthum was born in Boxmeer, The Netherlands on the fourth of January, 1984. He attended the Elzendaal Lyceum (VWO) in Boxmeer from 1996 to 2002. In 2002, Rob started his B.Sc. in Mechanical Engineering at Technische Universiteit Eindhoven and began working part-time for the taxi company Maasbuurt Taxi B.V. Rob completed his B.Sc. in 2005 with a graduation project on the prototype design of a novel rotational separator (the RPS).

Rob started his M.Sc. in Mechanical Engineering in 2005, with a specialization in thermodynamics and process technology, while continuing his part-time job. He joined the Formula Student project of the Technische Universiteit Eindhoven in 2006, where he designed the cooling system of the race car. He performed his M.Sc. internship at Mawera Holzfeueranlagen GmbH in Bregenz, Austria in 2007, where he investigated cyclone performance in biomass effluent particulate removal. Rob graduated 'Met Grote Waardering' (with Merit) in 2009 on the topic of gas separation by partial condensation.

From 2009, Rob worked on his Ph.D. project, the last in a series of five funded by Shell on novel CO₂ removal from gas. During his Ph.D., Rob constructed a mathematical phase equilibrium model, developed and optimized the two-stage CRS process and studied the feasibility of its deployment in flue gas CO₂ capture. The results of his work are described in this thesis. Parts of his work have already been published in the journals Energy, Applied Energy and Fluid Phase Equilibria, as well as at the International Pittsburgh and Clearwater Coal conferences, BIT's Clean Coal Technology conference and the Sour Oil and Gas Advanced Technology conference.

